Development and Characterisation of Site-Controlled Quantum Dot Arrays

Charlotte Ovenden

For the Award of Doctor of Philosophy (PhD)
Department of Electronic and Electrical Engineering
University of Sheffield

March 2021

Abstract

The development of methods for the epitaxial growth of semiconductor materials and nano-crystals has revolutionised modern technology. Molecular beam epitaxy (MBE) has allowed ultra-high quality materials to be produced and underpins a vast amount of research in the field of semiconductor photonics. Constant improvements to the technology have meant that the development of quantum circuits and therefore quantum computers has become a realistic goal. Semiconductor quantum dots (QDs) embedded within nanophotonic device structures can form the components of these circuits, which can create or manipulate quantum bits (qubits). A significant challenge remains if this goal is to be achieved, in that the use of randomly positioned QDs in these structures does not easily allow scale-up of the systems. Site-controlled QD growth, where the nucleation position of emitters is deterministically controlled, offers a solution to scale-up challenges. However, the quality of these QDs does not yet match that of randomly grown QDs and best results are often achieved using growth structures that are unsuitable for integration into the single-mode photonic devices that would be the building blocks of these circuits. This work seeks to develop a method for deterministically controlling the growth position of QDs by fabricating regular arrays of nanoholes. Additionally, the fabrication and growth structures must be produced in a scalable manner that facilitates incorporation into single-mode photonic devices.

First, an atomic force microscope (AFM) assisted local anodic oxidation (LAO) nanohole fabrication method will be presented. The nanohole arrays are fabricated on an InP substrate, for the growth of site-controlled InAs QDs that emit in the telecom C-band. Preliminary results for site-controlled droplet epitaxy via MBE are presented, as this growth method has been shown to produce QDs with low fine structure splitting (FSS). An alternative application for LAO structures will be demonstrated, where the oxides are shown to tune to the resonant frequency of a 2D photonic crystal cavity in simulation.

The subsequent parts of this work focus on the development of fabrication, in-situ surface preparation, and MBE growth methods for the site-control of InAs QD arrays on GaAs substrates. Nanohole array fabrication methods focus predominantly on using electron beam lithography (EBL) and inductively coupled plasma – reactive ion etching (ICP-RIE). This method is easily scaled up and produces reproducible results. An atomic hydrogen cleaning method is developed that allows surfaces to be thoroughly decontaminated in-situ, in a manner that preserves the nanohole nucleation sites and does not damage the semiconductor surface. Finally, results demonstrating the production of site-controlled QD arrays are presented. Both optical and AFM imaging measurements are used to characterise the QD arrays, which are grown on nanoholes fabricated using the EBL/ICP-RIE and LAO. The methods are directly compared in the same growth run. Very narrow linewidths for QDs grown on nanoholes fabricated using EBL/ICP-RIE and LAO of 26 μeV and 33 μeV are observed respectively, in addition to low FSS of 16 μeV.

Acknowledgments

I have been very lucky to work with many wonderful and exceptional people in the Semiconductor Materials and Devices (SMD) Group in Electronic and Electrical Engineering, the Low Dimensional Structures and Devices (LDSD) Group in Physics and the National Epitaxy Facility (NEF) at The University of Sheffield. Thank you to the EPSRC for funding my project and Prof. Maurice Skolnick for leading the grant. It has been a great pleasure to be part of the team.

I am very grateful to my supervisor Dr. Ian Farrer for his support, guidance, and good humour throughout my PhD and to my second supervisor Prof. Jon Heffernan for all his guidance, encouragement, and useful discussions.

A big thanks to the MBE growth team Dr. Aristotelis Trapalis, Dr. Edmund Clarke and Dr. Pallavi Patil for growing samples and patiently teaching me over the years. Particular thanks to Aris for doing so much early set-up work on the DCA, and all the time spent together doing site-controlled experiments. Also, thanks to Brett Harrison for buffer growths. Thank you very much to the growth technical team Richard Frith and Stephen Dorward, without whom none of this work would have happened!

Thank you very much to Dr. Ben Royall for taking so much time to train me in all things fabrication related during my first year and to Dr. Paul Fry for initial training in optical measurement and answering my questions throughout the PhD. Also, many thanks for the cleanroom technical staff past and present, Jon Milner, Paul Haines, Saurabh Kumar, Dr. Ken Kennedy, Jon Wall and also to Gordon Askwith.

A special thanks to Dr. Andrew Foster, Dr. Alistair Brash, and Dr. Dominic Hallett for setting up and allowing me to use the PL imaging set-up in D49, which proved to be incredibly useful. In particular, thank you to Dominic for all the assistance with the PL

measurements and for all the time spent on writing code and answering my questions about quantum dots and simulations! Also, thank you to Dr. Maxim Makhonin for the early microPL mapping measurements.

To everyone in LDSD, it has been a pleasure to work alongside you all and see all the interesting things everyone does, and Friday night pub sessions (pre-covid) were always fun! To our collaborators Prof. Dave Richie, and Dr. Lucy Goff from the University of Cambridge, thank you for being such supportive and wonderful work package colleagues. And many thanks must go to those who have supported this work in an administrative capacity, Hilary Levesley, Angela Warren and Sally Greenhough.

To everyone who has made my time at Sheffield such a fun experience, and been great office or lab mates, thanks! Special mentions in no particular order to Lizzy Stark, Dr. Jon Petticrew, Dr. Vladimir Schulyak, Henry Franics, Max Godsland, Henry Worthy, Dr. Lucas Pinel, Dr. Elisa Sala, Dr. Tim Lewis-Roberts, Dr. Joe Maguire, Dr. Dave Hurst, Dr. Tommi Isoniemi, Dr. Catherine Phillips, Dr. Ian Griffiths, Dr. Gau Ragunathan, Dr. Leh Woon Lim, Dr. Ben White, Dr. Jeng Shiuh Cheong, Dr. René Dost, Young In Na, Chufan Wang, Longqi Zhou, Abdul Sharaf, Chak L Chan, Paige Baldwin, Xintao Chen, Dr. Andrey Krysa, Dr. Nasser Babazadeh, Dr. Ofogh Tizno, Dr. Yuefei Cai, Si Chen, Yun Ran Wang, Nada Adham and Wai Ching Lin. To the many others who I haven't named, thank you for making the department such a friendly and great place to be!

A particular thank you to my friends Anna, Andy, Sam, Emma, Tom, Jim, Carly, Alex, Kat, Nat and Mike for being such fantastic people and a great support.

To my parents, Liz and Jeremy. Thank you for always being interested to hear about what I'm doing and lovingly supporting me throughout everything. To my sister Pippa, our chats have always been a fun reprieve from our respective thesis writings. Who would have thought we'd end up finishing at the same time, on opposite sides of the world!

A final but most important thanks must go to Dom, truly without you this wouldn't have been possible. Thank you for being your amazing, hilarious and kind self no matter what and thank you for believing in me every step of the way.

This page intentionally left blank

Presentations

C. Ovenden, I. Farrer, E. Clarke, M. N. Makhonin, B. Royall, A. Trapalis, P. W. Fry, J. Heffernan and M. S. Skolnick, MBE Growth and Characterisation of Site-Controlled InAs Quantum Dots, UK Semiconductors, Sheffield, 2018

C. Ovenden, I. Farrer, M. S. Skolnick and J. Heffernan, Optimisation of local anodic oxidation parameters for site-controlled quantum dot growth, Bruker Users Meeting and Conference, Liverpool, 2019

C. Ovenden, E. M. Sala, I. Farrer, M. S. Skolnick and J. Heffernan, Local anodic oxidation for site-controlled quantum dot growth at telecom wavelengths, Quantum Dot Day, Oxford, 2020

C. Ovenden, I. Farrer, E. Clarke, A. Trapalis, E. M. Sala, M. S. Skolnick, and J. Heffernan, Local anodic oxidation for site-controlled quantum dot growth at 1.55 μm, Quantum Dot 2020 (QD2020), Munich, 2020

C. Ovenden, A. Trapalis, D. J. Hallett, P. K. Patil, E. Clarke, M. S. Skolnick, I. Farrer and J. Heffernan, Growth of site-controlled InAs/GaAs quantum dot arrays for integration into photonic devices, Semiconductor and Integrated OptoElectronics (SIOE), Cardiff, 2021

This page intentionally left blank

Publications

C. Ovenden, I. Farrer, M. S. Skolnick and J. Heffernan, 'Nanoscale wafer patterning using SPM induced local anodic oxidation in InP substrates'. *Submitted.*

C. Ovenden, A. Trapalis, D. J. Hallett, P. K. Patil, E. Clarke, M. S. Skolnick, I. Farrer and J. Heffernan, 'Development of scalable methods for the site-controlled growth of InAs/GaAs QD arrays'. *In preparation.*

C. Ovenden, A. Trapalis, D. J. Hallett, P. K. Patil, E. Clarke, M. S. Skolnick, I. Farrer and J. Heffernan, 'Scalable integration of site-controlled InAs/GaAs QDs into arrays of photonic devices '. *In preparation.*

Contents

1 Introduction **1**

2 Background **5**

2.1 III-V Quantum dots 6

2.2 Nanophotonics 10

2.3 Quantum dot growth 14

3 Methods **35**

3.1 Fabrication 37

3.2 The molecular beam epitaxy (MBE) system 43

3.3 Characterisation 53

3.4 Finite-difference time-domain (FDTD) modelling 58

4 Nanohole Fabrication: LAO **63**

4.1 Nano-feature fabrication 65

4.2 Nanohole positioning accuracy 70

4.3 Oxide growth kinetics 72

4.4 Device simulation 77

4.5 Cavity tuning 80

4.6 Summary 84

5 Nanohole Fabrication: EBL and ICP-RIE **87**

5.1 Development: Electron beam lithography 88

5.2 Development: Etching of nanofeatures 91

5.3 Development: Ex-situ cleaning 96

5.4 Nanohole positioning accuracy 100

5.5 Initial QD growth 108

5.6 Summary 115

6 Atomic Hydrogen Cleaning **117**

6.1 Secondary ion mass spectrometry set-up 118

6.2 Atomic hydrogen cleaning 124

6.3 Summary 141

7 QD Growth and Characterisation **143**

7.1 SCQD sample growth overview 143

7.2 Initial site-controlled QD growths 145

7.3 Optimising nanohole and growth parameters 148

7.4 Characterisation of site-controlled QD arrays 151

7.5 Summary 180

8 Conclusions and Outlook **181**

8.1 Conclusions 181

8.2 Outlook 186

Bibliography **190**

A Appendix **219**

1 | Introduction

The development of the modern computer arose due to demand for process automation and high computation speeds. Through miniaturisation and progressive refinement computing power has grown at a constant rate, as described by Moore's law [1]. However, further miniaturisation of transistors will soon no longer be possible. In 2004 a single atom electrical switch was demonstrated [2], which marks the limit of the technology. Therefore, an alternative solution is required.

The concept of the quantum computer was proposed by Richard Feynman in the early 1980s [3], and the necessary physical requirements for the device were outlined by David DiVincenzo in 2000 [4]. A quantum computer uses quantum bits (qubits), which unlike the bits within a classical computer that can only have a value of 1 or 0, can be in a superposition of the two states. The outcome of this quantum mechanical behaviour is that calculation speed can be exponentially faster for certain problems. More recently, the drive to produce a system for quantum computing has led to research into a number of viable platforms. Semiconductor quantum photonic devices with integrated quantum dots (QDs) are a candidate for the production of quantum computers and fulfil DiVincenzo's criteria [5]. These photonic devices have been shown to effectively control quantum states [6], whilst QDs display many properties that make them excellent qubit candidates. Progress in areas such as device fabrication and QD growth, which are needed to engineer such platforms, have been substantial. However, if the full potential of the quantum computer is to be realised these systems must be fully scalable, and further progress is required in this area.

Molecular beam epitaxy (MBE) is a well established technique that allows growth of very high-quality materials. QDs grown using MBE can give near-transform limited

linewidths [7], high brightness and single-photon purity [8]. Randomly grown QDs are widely used in quantum photonic devices, where the device can improve indistinguishability and single photon purity [9], enhance spontaneous emission rates [10], facilitate interaction between QDs [11], or strong coupling [12], control bunching and antibunching statistics [13], and introduce chirality [14]. However, use of randomly positioned QDs in these systems leads to low device yields, therefore study of a single device is common. Growth of deterministically positioned arrays of QDs could greatly reduce fabrication challenges in the production of scalable quantum circuits, as arrays of devices can be fabricated around known positions. Low numbers of site-controlled QDs have been integrated into photonic devices e.g. optical resonators with high single photon purity [15], nanoscale electronic memory devices [16], and in cavities to demonstrate a photonic crystal molecule [17]. However, the quality of site-controlled QDs does not yet match that of randomly grown QDs.

This work seeks to develop fabrication and growth methods for the production of high quality, deterministically placed indium arsenide QDs that support quantum circuit scalability. An ideal array is composed of a regular array of single QDs that have low linewidths, high brightness, and very similar wavelengths to one another. Particular significance is placed on designing a structure that is compatible with existing photonic devices and allows for detailed characterisation of QDs. Chapter 2 will give background information on and theory on III-V semiconductor QDs, nanophotonics, and give a more detailed overview of site-controlled QD growth via MBE. Chapter 3 outlines the methods for fabrication of samples, growth of site-controlled QDs and the associated in-situ surface preparation processes, characterisation of nanohole arrays and QDs using a range of techniques, and device simulation using a finite-difference time-domain (FDTD) method. Chapter 4 discusses the development of local anodic oxidation (LAO) nanohole fabrication methods on an indium phosphide substrate, and investigates oxide growth kinetics on this material. Initial site-controlled growth of indium droplets is demonstrated. The use of LAO fabricated oxides for photonic crystal cavity mode tuning is then demonstrated in simulation. Chapter 5 goes on to develop an alternative fabrication method on gallium arsenide, where electron beam lithography (EBL) and inductively coupled plasma reactive ion etch-

ing (ICP-RIE) are used. The quality of the nanoholes is assessed and positioning accuracy is tested against simulated nano-photonic devices. Initial site-controlled growth experiments are discussed. Chapter 6 presents the development and characterisation of in-situ atomic hydrogen cleaning processes. The effect of parameter variations is characterised using atomic force microscopy (AFM) imaging, secondary ion mass spectrometry (SIMS), reflection high energy electron diffraction (RHEED) and micro-photoluminescence spectroscopy (μPL). Finally, Chapter 7 presents the development of site-controlled QD growth on atomic hydrogen cleaned nanohole arrays. The QDs are characterised using AFM and μPL, and the results are discussed within the framework of the project aims. Finally, in Chapter 8 concluding remarks are made and directions for future work are proposed.

This page intentionally left blank

2 | Background

This chapter introduces III-V semiconductor QDs, their application within nanophotonics, and site-controlled QD growth via molecular beam epitaxy (MBE). The necessity of creating a method for reliable growth of site-controlled QDs is discussed, within the framework of robust scale up of photonic device production.

The unit cell of GaAs/ InP is shown in Figure 2-1, which has a zinc blende form. The crystal consists of a face centred cubic structure where each arsenic (phosphorous) atom is bonded to four gallium (indium) atoms through a hybridised orbital. The unit cell repeats in this manner throughout the crystal. At the surface, the system seeks to minimise the energetic requirements of surface dangling bonds. This leads to a variety of arsenic or gallium rich configurations, known as reconstructions. It is energetically favourable for unbonded electrons to sit on arsenic rather than gallium atoms, due to their electronic configurations. This behaviour causes a lattice distortion and change in the band structure of the semiconductor near the surface, otherwise known as band bending [18, 19]. The surface reconstruction can be determined using reflection high-energy electron diffraction (RHEED). Additionally, the geometry of the unit cell determines the lattice constant of the material.

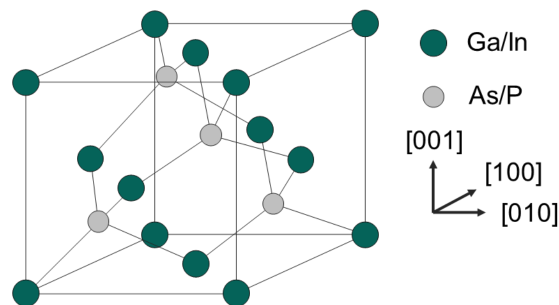

Figure 2-1. 3 dimensional (3D) representation of the unit cell of GaAs or InP.

2.1 III-V Quantum dots

Electronic confinement of carriers can occur when the scale of the confining area is comparable to the de Broglie wavelength

$$\lambda = \frac{h}{p} = \frac{h}{\sqrt{3m_{eff}k_BT}} \tag{2.1}$$

where h is the Planck constant, p the momentum of the electron, m_{eff} the effective mass of the carrier, k_{B} is the Boltzmann constant, and T the is temperature. When confinement occurs in three dimensions a zero-dimensional (0D) structure is produced and the energy levels available are discrete. The degree of confinement determines the density of states (DOS) for the structure, which in the 0D case consist of a series of delta functions. The DOS for varying degrees of confinement is shown in Figure 2-2. To create this 3D confinement, a QD is surrounded by a higher band gap material, e.g. InAs QDs surrounded by GaAs or InP.

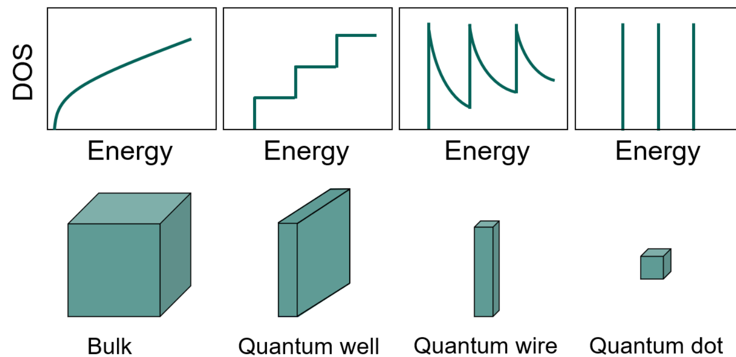

Figure 2-2. The density of states for a range of confinement directions. In the bulk a continuum of states can be seen. The number of states reduces as confinement increases until in the case of the quantum dot, where confinement occurs in three dimensions, energy levels are atomic like and described by delta functions.

QDs are often described as artificial atoms as they possess atom-like electronic structures and exhibit s, p, d and f carrier wavefunction profiles [20], which are analogous to atomic orbitals [21]. A simple visualisation of a QD is the two-level system, which consists of

a ground state and excited state, as shown in Figure 2-3. In this scheme an electron is promoted into the first excited state, which causes an exciton to be generated. The QD will remain in the excited state until spontaneous emission occurs, leading to a population decay rate that is determined by the QD's lifetime. Through this spontaneous emission, the electron and hole recombine to produce a photon. The energy of this photon depends on the energy difference between the confined energy levels in the conduction and valence bands. The size of the QD controls the band gap; a small QD will have a larger band gap than a large QD. Additionally, the composition and strain environment affect the QD energy. The QD is an example of a source of anti-bunched light, meaning that there is a time dependence for the photons being emitted. This behaviour is one of the factors that make it a suitable information generator in a qubit [22].

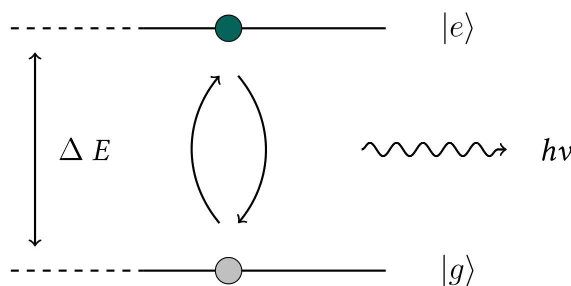

Figure 2-3. A simple two level system representation of exciton formation and subsequent photon emission in a QD, where ΔE is the band gap, hv is the photon energy, $|g\rangle$ is the ground state and $|e\rangle$ is the first excited state of the QD.

In reality, the QD is not an isolated system and its optical properties are affected by the environment surrounding it. As stated, the QD is grown within a higher band gap material. During growth, defects and contaminating species, such as ionic salts or carbon compounds, can become incorporated near the QD. They can act as charge traps that induce a fluctuating charge environment, which can lead to a change the energy of photons emitted by the QD. This unwanted behaviour is termed charge noise and leads to the emission linewidth of the QD broadening [23].

2.1.1 QD transitions

When a transition occurs within a QD a photon can be emitted. A number of charge configurations are possible within the QD, some of which lead to radiative decay. Figure 2-4 demonstrates several of the possible configurations and the corresponding polarisations of emitted photons. The relative electron and hole spins that give rise to each transition are highlighted, where an electron has spin $\pm 1/2$ and the heavy hole spin $\pm 3/2$. A QD can also have a fine structure that is brought about by a lack of symmetry in its shape, which can be caused by strain or the underlying crystal structure. This means that the orthogonal field oscillation directions are not symmetrical and a fine structure splitting (FSS) in the photon energies occurs. A large FSS could mean photons produced by a QD will not be indistinguishable, which would negatively impact on applications that require a high degree of indistinguishability [24]. The QD FSS can be altered by applying a strain field along one axis, which causes a change in the wavefuction of the hole [25].

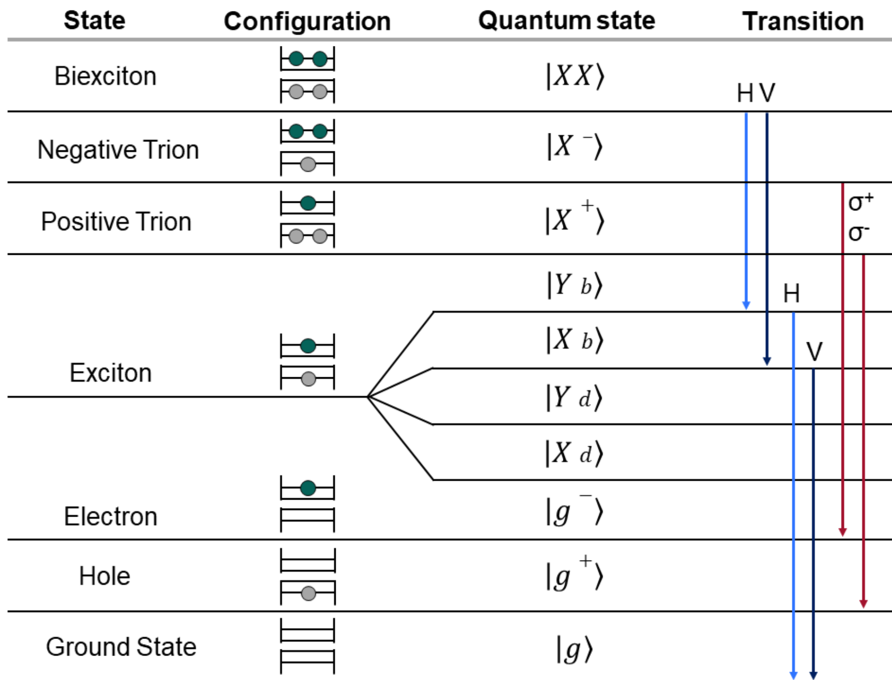

Figure 2-4. The electronic configuration of a QD in a range of confined states for electrons (green) and holes (grey). For radiative (b) recombinations the pseudospin of a circularly polarised photon ($\sigma^{+/-}$) or direction of a linearly polarised photon (H/V) is indicated for each transition. Non-radiative (d) configurations are also shown. Adapted from [26].

2.1.2 QD tuning

The application of an electric field across a QD in a diode can induce electro-luminescence (EL) in forward bias; facilitate emission wavelength tuning via the Quantum Confined Stark Effect (QCSE) [27], which is normally done in reverse bias; and reduce single QD linewidths [28]. This is explained through the reduction in charge fluctuations near the QD as defect states become filled. The diode structure can consist of a positively doped region (p), intrinsic region (i), and negatively doped region (n). The QD is present in the i-region. When a voltage greater than the built-in voltage for the QD is applied, EL can occur. By applying the bias, an electric field is created that causes electrons to move from the n to p region and holes to move from the p to n region, meaning a QD in the central i-region becomes populated. The QCSE can be used as a method of emission wavelength tuning. This tuning occurs when an electric field is applied, causing electrons and holes to be pushed to opposite edges of the QD. The outcome is that the band gap, and therefore photon energies, are altered. A diagram of this process is shown in Figure 2-5. This effect has been used to tune QD emission wavelengths up to 25 meV for InAs/GaAs using an AlGaAs barrier [29] however, without the use of barriers tuning ranges tend to be below 1 meV [30].

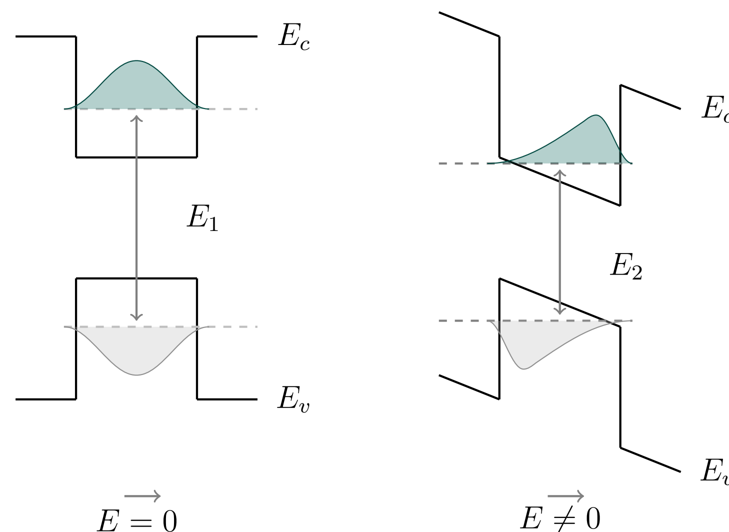

Figure 2-5. A representation QCSE, showing the QD band structure with no electric field applied ($E = 0$), which gives an energy gap of E_1. When an electric field is applied ($E \neq 0$) the energy gap changes to E_2. The valence band energy (E_v) and conduction band energy (E_c) change are indicated.

2.2 Nanophotonics

Nanophotonic structures can consist of a QD embedded within a dielectric material, where the QD acts as a source of quantum light, and loss is minimised by surrounding the device by a low refractive index material. The scale and design of the photonic structures are such that light-matter interactions are controlled, which can affect the emission properties of the QD and the propagation of light. The nanophotonic device has associated modes with corresponding electric field profiles, therefore the position of the QD within the device will determine the coupling strength between the QD and mode. By fabricating many devices around embedded QD sources, a scalable network of qubits can be created, with site-controlled growth of these QDs assisting in their large-scale fabrication. In addition to cavities, that confine light, waveguides control light-matter interaction whilst also guiding a propagating wave. An example of such a device is a nanobeam waveguide (NBW).

Photonic devices with embedded QDs are a promising candidate for quantum information processing and engineering of scalable qubit circuits. A photonic crystal (PC) controls light propagation to varying degrees, depending on its structure and whether it is 1D, 2D or 3D. In each case, the PC consists of a regular lattice of low refractive index areas within a dielectric material, such as an array of air holes fabricated into a semiconductor. The structure creates a photonic band gap, which is analogous to an electronic band gap, in that photons of a wavelength within this energy gap do not propagate in the material. The refractive index difference between the air and dielectric material controls the wavelength of light that is not supported. This is due to the lattice causing reflection and refraction of the electromagnetic waves and subsequent destructive interference at certain wavelengths.

A 1D PC consists of layers of material with different refractive indices, by stacking a number of these layers a structure can be produced which is periodic in one direction. 2D and 3D PCs arise from the same principle, and as suggested are periodic in two or three dimensions. As the dimensionality of the PC increases, the number of degrees to which light propagation is controlled also increases. The focus of this work is on 2D photonic crystal

cavities (PCC), which are created by removing a number of air holes from the PC. This introduces an area where light of all wavelengths can propagate. The resonant mode that is created by the cavity can be manipulated by adjusting the periodicity and dimensions of the air holes, in addition to the refractive index difference between the dielectric and holes. In Figure 2-6 an air clad GaAs L3 cavity is shown where three holes are removed to create the cavity. Simulations using a H1 cavity will be presented in this work, where the H1 cavity is formed by removing only one hole. The air cladding is achieved by growing the slab and imbedded QDs on a sacrificial layer, which can preferentially be removed using an under etch [31].

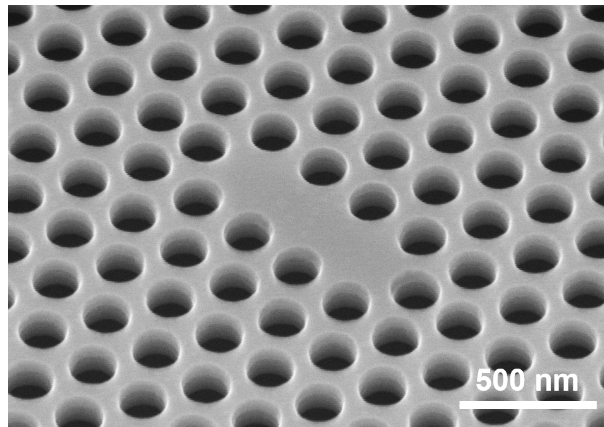

Figure 2-6. A tilted SEM image of a modified L3 PCC. The sample was fabricated and imaged by Dr. Ben Royall.

If a source in a cavity emits at wavelength that lies within the photonic crystal bandgap, the light will be confined within the cavity. The degree to which the light is confined is described by the quality (Q) factor

$$Q = \frac{\omega_0}{\Delta\omega} \tag{2.2}$$

where ω_0 is the cavity resonance and $\Delta\omega$ is the cavity linewidth.

Additionally, the cavity can enhance the spontaneous emission rate of the emitter, which is descibed by the Purcell factor, F_P

$$F_P = \frac{3Q(\lambda/n)^3}{4\pi^2 V_m}\zeta^2 L(\omega) \tag{2.3}$$

where λ is the wavelength of the emitter, n is the refractive index, Q is the Q factor, V_m is the mode volume, ω is the angular frequency of the emitter, L is the Lorentzian lineshape of the cavity, and ζ is the normalised dipole orientation [32].

A narrow cavity mode can be achieved by optimising the PCC design so that losses are minimised. If a QD emits at a wavelength sufficiently close to this mode then the QD is said to be on resonance and coupling can occur. The narrow cavity mode leads to a high density of photonic states being available for the QD to emit into, and accounts for the Purcell enhancement. A faster spontaneous emission rate means the QD's emission lifetime is reduced. This has the effect of increasing its Fourier transform linewidth limit. Where the transform limited linewidth depends only on the QDs lifetime and no dephasing parameters. A QD's measured linewidth can be affected by thermal energy, in the form of phonons, and charge noise, which causes a fluctuation in the electronic environment. The closer a QD can be positioned to the electric field maximum of a device, the better its performance. Good positioning and coupling of a QD to a device has been achieved used a registration technique, where the position of a QD with regard to an alignment mark is found and then a device is fabricated around it. This has been demonstrated with success, with accuracies of 30 nm to 50 nm [33–35]. This method produces good results for low numbers of devices; however, it is less suitable for scale-up as registration and fabrication processes are complex and time consuming. Instead, higher device yields can be obtained by growing arrays of site-controlled QDs and fabricating arrays of devices around them. If the QD arrays are regular enough that no registration would be necessary, device array design would be simplified. Positioning accuracy for site-controlled samples has been reported to be ± 80 nm within the array [36] or < 50 nm with respect to a device [37].

Figure 2-7. A SEM image of a nanobeam waveguide, where the left (L) and right (R) outcouplers are labelled. Reprinted with permission from D. L. Hurst *et al.*, 'Nonreciprocal Transmission and Reflection of a Chirally Coupled Quantum Dot', *Nano Letters*, **18**, 9, 5475-5481, 2018. Copyright (2018) American Chemical Society [38].

A NBW controls the confinement of light in two directions and guides the light in the third. In-plane propagation occurs down the length of a thin wire of air clad semiconductor that has a rectangular cross-section. A SEM image of a NBW is shown in Figure 2-7. A useful property of the NBW is spin dependent chirality [39]. If a circularly polarised QD is placed at the chiral point of a NBW it can couple and emit light into a mode where the direction that the light will propagate in is spin (σ) dependent. In other words, σ^+ light will travel in the opposite direction to σ^- light and the symmetry normally seen for the modes that propagate to the left and right is broken. Applications include, preparation of entangled states in spin networks [40], spin read-out of a QD [41], production of optical isolators [42], and optical circulators [43]. Chiral behaviour occurs through the following mechanism. The NBW supports a mode that contains both transverse and longitudinal electric field components; these components have a phase difference of $\pi/2$. The electric field associated with the transverse (T) mode component is orthogonal, while for the longitudinal (L) component it oscillates in the same direction as propagation occurs in. The contribution proportion is position dependent, as shown in Figure 2-8. In the centre of the waveguide only a linearly polarised, transverse mode component is observed. At the chiral point there is an equal contribution from the transverse and longitudinal parts, which gives rise to circular polarisation. Depending on the relative contribution, linear, elliptical, or circular polarisation is supported. Therefore, a QD must be carefully positioned within the NBW to fully exploit the chiral behaviour.

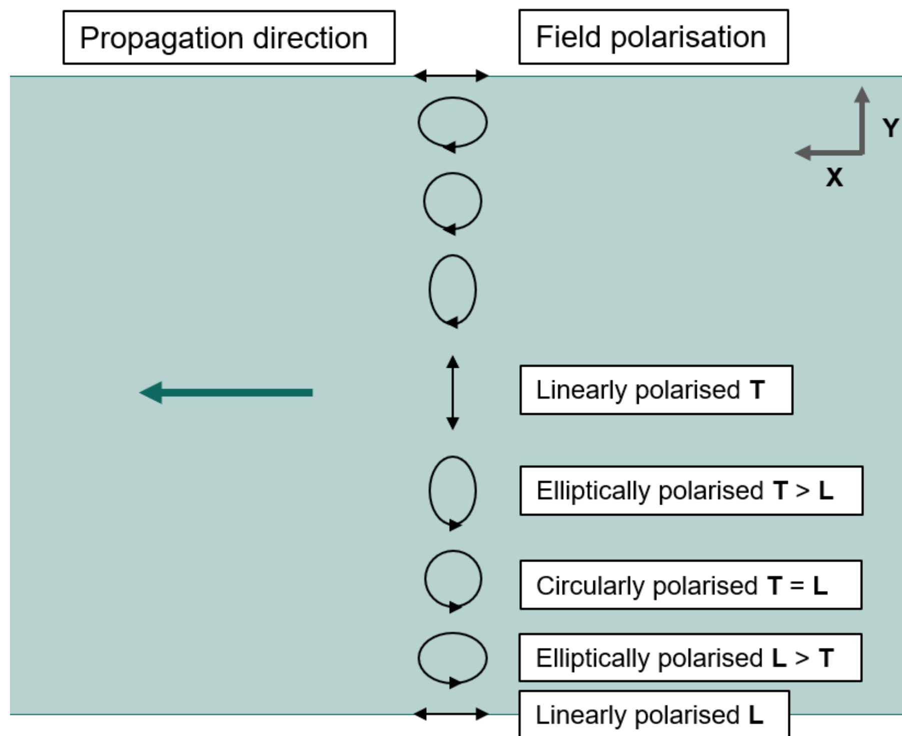

Figure 2-8. Demonstration of the field polarisations at different points in the y direction of a nanobeam waveguide, where circular polarisation is supported at the chiral point.

2.3 Quantum dot growth

The deterministic positioning of a quantum dot (QD) can be achieved via several methods [44]. This work focuses on the use of nanoholes, fabricated on GaAs and InP (100) substrates via two ex-situ methods: electron beam lithography (EBL) in conjunction with inductively coupled plasma – reactive ion etching (ICP-RIE); and atomic force microscope (AFM) assisted local anodic oxidation (LAO). The growth of site-controlled QDs is investigated via the use molecular beam epitaxy (MBE), using a Stranski-Krastanov (S-K) growth mode or droplet epitaxy. MBE is a versatile and widely used technique for growing epitaxial layers. An ultra-high vacuum around 10^{-11} Torr and temperatures around 580 °C to 640 °C for GaAs growth are common [45]. To form a molecular beam, effusion cells are used to generate a flux of elemental group III or group V materials. These materials are evaporated from separate cells and released towards a substrate. On the surface crys-

talline compounds form and epitaxial growth occurs. The process follows three processes, nucleation, steady-state growth, and coarsening. Successful nucleation occurs when a stable nucleus forms. Steady-state growth can then occur, which leads to the formation of clusters that seek to reduce their Gibbs free energy and vary in size. Finally, the clusters coarsen via diffusion, which leads to an increase in size and associated reduction in chemical potential [46].

Molecular beam epitaxy can be used to grow epitaxial material via a variety of growth modes, which are shown in Figure 2-9. These being, Frank-Van der Merwe (FM), which is a layer-by-layer growth of lattice matched materials [47]. Volmer-Weber (VW), where there is a lattice mismatch between the materials and interfacial and strain energies are high, meaning 3D island growth occurs [48]. Finally, Stranski-Krastanov (SK) growth, where again there is a lattice mismatch between the substrate and QD materials. In this case growth initially proceeds layer by layer before 3D island growth takes place. This leads to the formation of 3D islands and a 2D wetting layer (WL) [49]. More specifically, SK growth comes about when there is a large lattice mismatch between the substrate and QD material and small surface free energy. When layers are initially deposited a WL forms, however beyond the critical thickness the strain energy increases until a point where it is energetically favourable for relaxation and bond breaking to occur. This leads to the formation of the 3D islands. A monolayer (ML) is approximately 0.3 nm for InAs or GaAs [50, 51].

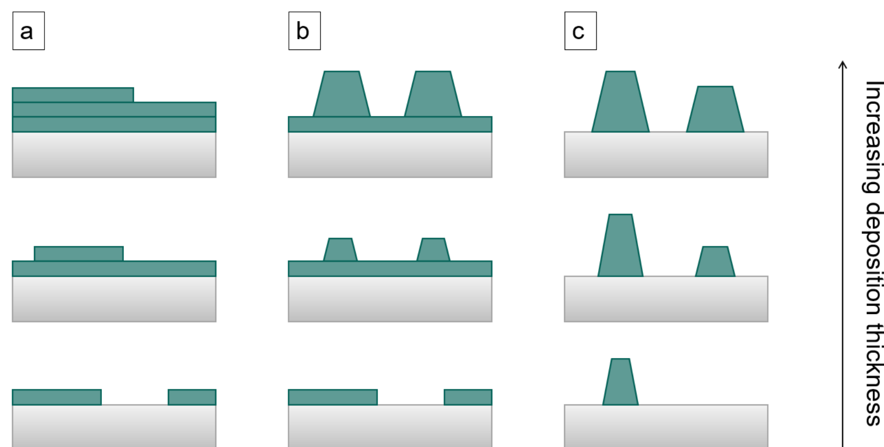

Figure 2-9. Three dimensional island growth modes (a) Frank-Van der Merwe, (b) Stranski-Krastanov and, (c) Volmer-Weber.

Droplet epitaxy (DE) was first experimentally demonstrated in 1991 by Koguchi *et al.* [52]. Metallic droplets are deposited onto the semiconductor surface and subsequently crystalised under arsenic flux; this mechanism is shown in Figure 2-10. DE is not a strain driven process, therefore a wider choice of heterostructure materials are available (lattice matched and lattice mis-matched) and novel structures have been produced [53–55]. The parameters that control SK, such as growth temperature, growth rate, and coverage also affect DE [56, 57].

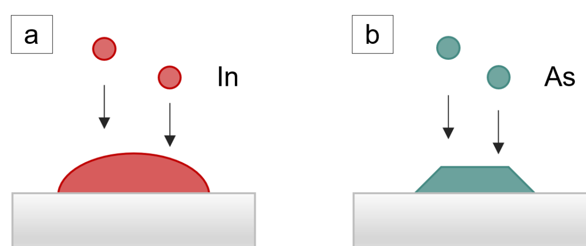

Figure 2-10. Droplet epitaxy quantum dots, (a) first formed through deposition of metalic droplets and then (b) crystalisation under arsenic.

2.3.1 Local anodic oxidation

Local anodic oxidation (LAO) is a chemical oxidation process that can produce nanosized features. A conductive AFM tip is brought into close proximity with a sample surface and negatively biased. Due to water being present in the air from general humidity, a water bridge forms between the tip and sample under these conditions. The bias also induces the formation of anodic OH^- and O^- ions, which are directed by the field towards the semiconductor surface. The anions can then react with the semiconductor material to form a composite oxide, which grows above and below the surface, as shown in Figure 2-11. The voltage supplies the activation energy for ions to move to interstitial reaction sites, however there is a depth at which oxidation is no longer assisted by the tip bias, and so a maximum oxide depth that can be achieved. The nano-size of the tip means a large electric field is generated at its apex and the field directs the anions away from the tip and into the sample [58]. By holding the AFM tip in this manner over a stationary point, an oxide mound can be formed. Or by scanning the tip across the surface oxide lines or more complicated shapes can be produced [59]. The main parameters affecting the dimen-

sions of the oxide formed via LAO and therefore nanohole dimensions are the applied tip voltage [60], and humidity [61], in addition to tip-sample distance [62], tip radius [63] and tip write speed [64]. The oxide features produced via this method can be subsequently removed via wet chemical etching or atomic hydrogen cleaning to form arrays of nanoholes [65]. Fabrication of nanoholes via LAO has an advantage over more commonly used lithographic methods, which use organic resist masks that are a major source of contamination [66]. Instead, LAO is a maskless, one-step, ex-situ process that allows the sample to be transferred immediately into the ultra-high vacuum chamber chamber, where the oxide mounds can be removed via atomic hydrogen cleaning. In previous reports of LAO processing, one major drawback is that nanoholes are shallow [67, 68], and this limits the thickness of the epitaxially grown buffer layer; a critical and effective means of reducing linewidth of site-controlled QDs.

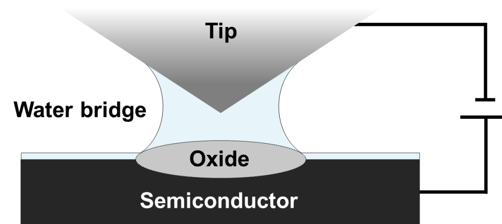

Figure 2-11. A schematic of the local anodic oxidation process, where the close proximety of the biased AFM tip in humid conditions leads to the formation of the water bridge and ogrowth of an oxide above and below the semiconductor surface.

Since the first demonstration of a scanning probe lithography based oxidation technique [69], LAO has been widely studied on metals [70] and semiconductors [71–74]. The kinetics of LAO have been described using the Cabrera-Mott theory [75], or by adaptations of this theory [76]. Using these methods, the activation energy for LAO of GaAs has been found [77]. Additionally, the effect of doping type on oxide growth has been investigated for GaAs [78].

SCQD growth using LAO fabricated nanoholes has been demonstrated successfully using InAs QDs on a GaAs substrate via a SK growth mode, in the literature very low single QD linewidths of 56 μeV have been reported, with 85 % of sites showing PL emission. This

result was achieved through the use of a stacked system growth, where the seed QD layer was grown directly on the fabrication. An observation was reported by Cha *et al.* [60], where the LAO oxides were removed using thermal cleaning in a MBE chamber. At higher tip voltages thermally stable oxides (Ga_2O_3) were formed, which were not fully removed after thermal desorption processes were complete. The oxides formed at lower tip voltages (GaO or Ga_2O) could be thermally removed. In addition to SK SCQD growth, droplet epitaxy growth methods have been used in conjunction with LAO fabricated nanoholes to control the growth position indium droplets on a GaAs patterned surface [79]. Using the same LAO nanohole fabrication technique, InAs SCQDs have been grown on InP via droplet expitaxy, for telecom emission ranges. By growing a single layer of QDs directly onto the fabrication surface, optical activity from QDs was demonstrated with linewidths being reported as 0.8 meV [68]. Although there are a number of literature reports using a LAO technique on GaAs for site-control of QDs, InP has not been widely investigated. Table 2.1 will give an overview of some key results pertaining to GaAs, whilst InP will be discussed in more detail in Chapter 4 as it can be seen that further investigations of LAO on InP are warranted.

2.3.2 QD growth via MBE

On a planar surface, parameters which are commonly used to control QD properties are growth temperature [80, 81], growth rate [82–84], and quantity of material deposited. Growth temperature controls QD brightness [85], emsemble linewidth [86], and QD density and volume [87], where an increase in growth temperature causes an increase in QD volume and decrease in density, as diffusion lengths are increased. A decrease in growth rate has been associated with a red shift in wavelength [88], and a decrease in the inhomogeneous linewidth broadening of the QD ensemble [82]. Additionally, a lower growth rate increases QD size, while reducing size distributions and density [88]. Other control parameters include indium coverage, and arsenic overpressure [89–91].

A broad distribution in QD sizes and emission wavelength ranges is a common outcome

of the growth methods discussed [92]. It has been shown that QD size distribution uniformity and emission linewidths improve with the use of a stacked system, where multiple layers of QDs are vertically strain coupled and a buffer is grown between them [93–96]. The area above the seed QD is at a lower chemical surface potential for subsequent QD nucleation, due to the different lattice constants of the substrate and QD materials, meaning that adatom migration to the area is enhanced [97]. Therefore, the position that bi- to multi- layer QDs grow at is defined by the position of the seed (first layer) QD. A thin spacer layer means bilayer QDs (BQDs) nucleation is dominated by the strain field, whereas as the spacer layer thickness increases the nucleation mechanism switches back to being wholly dominated by the sample growth conditions [98]. Additionally, this results in a reduction in the critical coverage necessary for the nucleation and growth of the 3D islands [99]. The amount of indium deposited must therefore be tuned to the desired emission wavelength, as stacked QD size will increase compared to the seed QD size under the same growth conditions. A TEM image of vertically coupled QD layers is shown in Figure 2-12. The method is commonly used in combination with site-controlled QD growth, where the strain coupling maintains the positioning control through a thicker growth structure than would otherwise be possible.

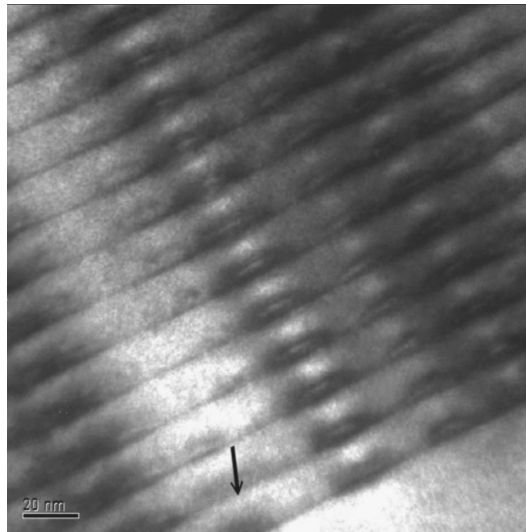

Figure 2-12. A TEM image of stacked QD growth where the strain field leads to vertical positioning coupling between layers of QDs (dark areas). Reprinted with the permission of AIP Publishing from 'Characterization of excitonic features in self-assembled InAs/GaAs quantum dot superlattice structures via surface photovoltage spectroscopy', C. H. Chan *et al.*, Journal of Applied Physics, **101** (10), 103102, (2007) [100].

2.3.3 Site-controlled QD growth

Typically, site-controlled QD (SCQD) growth involves using features, such as nanoholes, to control the position at which a QD grows. The nanohole has a low surface chemical potential that drives indium flux towards the site. A large number of step edges are introduced, which are preferential sites for nucleation, and reduce both strain energy and the surface free energy of the QD [101–103]. This enhances the rate of adatom migration and preferential nucleation, meaning the growth rate at the nanohole site is higher than on planar surfaces and the critical thickness for island formation is reduced. The surface chemical potential can be calculated using the following equation

$$\mu(x) = \mu_0 + \gamma\Omega\kappa(x) + \Omega E_s \tag{2.4}$$

where μ_0 is the surface chemical potential of a flat surface, γ is the surface free energy per unit volume, Ω is the atomic volume, κ arises from the surface curvature, and E_s is the strain contribution energy. In this model, a convex surface has a high chemical potential and a concave surface has a low chemical potential [104]. An island's height increases via the following rate law

$$\frac{\delta h}{\delta t} = D(1 + |\nabla_s h|^2)^{1/2}\nabla_s^2\mu \tag{2.5}$$

where h is the height, t is the time, ∇_s^2 is the Laplacian operator related to the surface, D determines the adatom diffusivity, density and volume, and T is the temperature [46]. The thermodynamic stability of the QDs can be assessed using these contributing factors, in addition to any anisotropic effects from the surface structure e.g., indium tends to incorporate on the B related side wall and directional migrations tends to bring about alignment (and nanohole elongation during buffer growth) in the [110] direction [105, 106].

The use of an Electron Beam Lithography (EBL) with a dry Inductively Coupled Plasma – Reactive Ion Etching (ICP-RIE) fabrication method, allows precise control over nanohole

depth, diameter and pitch (the spacing between nanoholes). Additionally, large numbers of nanoholes and alignment marks can be fabricated rapidly. However, additional challenges arise due to the introduction of a fabrication interface. The interface can be contaminated by processing chemicals, and etching often introduces defects. These sites act as charge traps which broaden emission linewidths and can result in non-radiative recombination [107]. This linewidth broadening can be reduced in several ways including, using thick buffers that move the QD as far from the contaminated surface as possible, growing charge barriers within the structure, the application of an electric field across a diode structure in which the QD is embedded, and the implementation of thorough post-fabrication cleaning process. In-situ fabrication methods do not require the use of organic resists or cleaning chemicals. However, damage can still be caused to the semiconductor surface. Another challenge to overcome is fast in-filling of the nanohole than on the planar surface, which would lead to degradation or complete removal of the preferential nucleation site. Material will grow faster in the nanohole meaning that the buffer growth itself can lead to planarization [108–110]. Therefore, the thickness of a buffer used to move the QD away from the fabrication interface is limited.

Commonly used fabrication methods are as follows: EBL in combination with wet chemical [16,111–113], or ICP-RIE [16,114,115], LAO [116–119], ultraviolet nanoimprint lithography (UV-NIL) in combination with dry etching [120, 121], focused ion beam etching (FIB) [122], in-situ laser patterning [123,124], electron-beam assisted scanning tunnelling microscopy (STM) [125], and a buried stressor approach [126]. High quality results produced by EBL with ICP-RIE or wet etching and LAO are summarised in Table 2.1 The table gives an overview of the parameters used for each SCQD growth, therefore demonstrating conditions where favourable outcomes have been observed. It should be noted that for the majority of reported works, QD wavelength is blue shifted using techniques such as partial capping and annealing [127], which reduces the size of the QD and therefore its wavelength. Additionally, excellent linewidth and occupancy results have been obtained using UV-NIL, with a minimum linewidth of 45 μeV reported with 90 % single occupancy in AFM and PL. The UV-NIL process involves stamping a soft polymer mask to imprint a pattern which can then be transferred to the semiconductor using a plasma

etch. To achieve high occupancy, it was reported that a hot QD growth temperature was used (540 °C). An alternative reported method was the "buried stressor approach" where a buried AlAs stressor layer was used to control the nucleation point of the QD rather than a nanohole. The aim was to reduce linewidths by removing the necessity for a fabrication interface [126]. The method involved the oxidation of the stressor layer, which resulted in the formation of Al_2O_3 The lower volume of the oxide in comparison to the semiconductor lead to a change in the strain field, which drove deterministically positioned strain induced growth. Mean linewidths reported using this method were 120 μeV, with a minimum value of 27 μeV.

A result reported by Schneider *et al.* should be highlighted from the table below as good occupancy statistics, low single QD linewidths, and narrow ensemble wavelength distributions were demonstrated [128]. The results were achieved using nanoholes fabricated using EBL/ ICP-RIE with a pre-growth diameter of 60 nm, depth of 15 to 20 nm and a growth temperature of 545 °C. A stacked QD bilayer was used in addition to an AlGaAs separation layer, which was deposited between the seed and active QD layers. The separation layer acts as a charge trap. A partial cap and anneal was used to truncate the QD heights. The excellent occupancy and linewidth results were attributed by the group to the use of a seed layer.

In addition to nanoholes, arrays of pyramids fabricated on (111)B GaAs substrates have been used to nucleate SCQDs. Photolithography and a wet chemical etch have been shown to produce highly facetted pyramids with sharp tips, which controlled the QD nucleation effectively and gave rise to a very narrow inhomogeneous linewidth of 2.3 meV [129]. Additionally, QD linewidths as low as 18 μeV were achieved [130]. Pyramid arrays have also been shown to control the nucleation position of the QD to $<$ 10 nm [131]. It should be noted that the growth mode for 3D island nucleation on (111)B GaAs can occur by a mechanism that driven by the arsenic terminated 2×2 surface reconstruction and is not strain dependent [132]. Growth temperatures in this mode tend to be lower than those used for SK and excellent QD uniformity has been produced, although growth on this surface orientation does pose additional challenges to a (100) substrate [133].

Table 2.1. A summary of some of the key literature results using electron beam lithography with dry or wet etching and local anodic oxidation nanohole fabrication methods, where temp. is temperature, min. LW is the minimum measured single QD linewidth, and WL is the mean ensemble emission wavelength A [115] B [114] C [106] D [16] E [128] F [111] G [113] H [36] I [119] J [134] K [117].

	Fab. method	QD growth		Buffer growth		Stack	Control parameter	Occupancy		Min. LW	WL (nm)	QD height/ Wavelength distribution
		Rate	Temp. (°C)	Thickness (nm)	Temp. (°C)			AFM	PL			
A	EBL, dry etch	0.031 µm/hr	470	15		N	Buffer thickness			80 µeV		
							Nanohole diameter: 32 nm				1020	
B			500	12	500	N	Nanohole diameter	Best single occupancy 50 % for narrow nanoholes				
							Nanohole depth	Best single occupancy 65 % for narrow, deep nanoholes				
C		0.01 ML/s	470, 500	18 ML	500	Y	Indium coverage: 1.2 ML, 1.7 ML, 2.0 ML	1.2 ML, small double QDs. 1.7 ML, single QDs. 2.0 ML, large single QDs and QDs between nanoholes.				
							1st layer (210 nm / 160 nm pitch)					210 nm = 19.37, 160 nm = 17.8 and 13.73
							6th layer (210 nm / 160 nm pitch)					210 nm = 5.58, 160 nm = 5.29
D	EBL, wet	0.005 to 0.010 nm/s	530	20 nm		Y	Buffer thickness			0.66 meV		
	EBL, dry			34 nm			Buffer thickness			0.6 meV		
E	EBL, wet etch	0.006 nm/s	545	20		Y	Nanohole diameter: 60 nm to 65 nm	77 % single occupancy for 60 nm, 49 % single occupancy for 65 nm	90%	25 µeV	925 (300 nm pitch)	15.9 meV
							Pitch: 200 nm to 350 nm				922 to 927	
F			520	90	550C	N	Buffer thickness, anisotropy			6 µeV	950	
G						Y				43 µeV	925	14.4 meV
H		0.01 ML/s	510	22	510	Y	Stacked system	40 % single occupancy	60%	7 µeV	950	
I	LAO	0.01 ML/s	510	30	450	N	30 nm buffer compared to no buffer	30 nm buffer = multiple/ no occupancy, 0 nm buffer = single occupancy		304 µeV		
				15		Y	15 nm spacer	Single occupancy, 89 %	85%	64 µeV	994	23 meV
				20			20 nm spacer	Unoccupied sites, 75 %				
J				7	480	N	QD growth temperature: 460, 480, 520 °C					520 °C = 3 , 480 °C = 15, 460 °C = 55
K		Varied	510	0		Y	QD growth rate: 0.5, 2 and 3.5 ML/s	90 % single occupancy for 0.5 ML/s and 50 % double occupancy for 3.5 Ml/s	88%	81 µeV	1004	7 nm

A more detailed discussion of some key parameters that SCQD growth should be benchmarked against will now be discussed and a review of the literature presented. These being, single QD linewidth, the linewidth of the QD ensemble, the number of sites occupied by a QD and how many QDs nucleate at each of these sites (occupancy), and the positioning accuracy. In brief, a narrow single QD linewidth is required for photon entanglement, while a narrow ensemble linewidth ensures that there is good reproducibility across the array and improves device yield, as does high single QD occupancy. Finally, good positioning accuracy maximises device properties such as the Purcell enhancement and Q factor.

The required values for each SCQD parameter depend on the application the QDs are used for. The strictest requirements would be associated with creation of entangled states between photons emitted from multiple QDs. This is because all of the emitted photons must be indistinguishable from each other and therefore the same energy. QDs can be tuned into resonance via a number of methods, and these tuning ranges dictate the allowed emission energy range that the SCQDs must fall in. Using a strain tuning method, achieved via atomic layer deposition (ALD) of HfO_2, three QD super radiance was achieved with a tuning range of over 65 meV (QDs emitting at $\sim$ 950 nm) being reported [135]. This range would allow QDs of very different wavelengths to be tuned into resonance and means that results shown in Table 2.1 for references E, G, and I would all be acceptable. However, the method does add a complicated post-growth step, which is less compatible with scalability aims. An alternative tuning method involves electrically tuning QDs, as outlined in 2.1.2, tuning ranges can be as much as 25 meV when AlGaAs barriers are used or below 1 meV if barriers are not used. The scope of this work does not involve the use of AlGaAs barriers, meaning to achieved entanglement between multiple SCQDs either very narrow distributions in the ensemble wavelengths must be achieved (below 1 meV) or post-growth tuning methods must be employed. Similarly, single QD linewidths must be very narrow for entangled states to be created, as significant spectral wandering would cause the photons produced by the QDs to be out of resonance. When assessing the results outlined in Table 2.1, references F and H would give suitably narrow single QD linewidths for applications that reply on entanglement. This work will aim to initially produce ensemble linewidths

initially within the tuning ranges reported using ALD, and then in the range achieved in references E, G, and I. The aim in terms of single QD linewidths will be to initially produce results below reported by reference A, as it is a comparable method of producing SCQDs to the one we employ. The aim will then be to produce single QD linewidths at the resolution of the optical set-up avaible for optical characterisation, which is ~ 25 μeV.

However, some applications are more robust to broader ensemble and single QD linewidths, e.g. chiral coupling a single QD to a nanobeam waveguide, where single QD linewidths of 70 μeV effectively demonstrated directional emission [136]. A more important parameter for this application is the positioning accuracy of the QDs, which will be discussed in more detail in Chapter 5.

The final parameters, number of sites occupied by a QD and occupancy affect applications where a high device yield is required. In the described applications single occupancy is required. For research applications yields of 40 % or above would provide significant benefits. However, when moving towards a scalable, mass produced system it would be preferable to have yields of 70 % or above. When comparing these values to those shown in Table 2.1, references E, H, I and K all reported acceptable results. We initially aim to produce yields of > 40 % single occupancy.

2.3.3.1 Single QD linewidths

Achieving low single QD linewidths is important for a system of qubits as the photons emitted by all QDs must be indistinguishable from one another for entanglement to take place. Therefore, the emission linewidth of QDs must ideally be Fourier transform limited or minimised as far as possible to facilitate the entanglement between photons. This has been shown to be challenging during site-controlled growth due to the introduction of the fabrication interface [115]. Techniques can be used to reduce single QD linewidth broadening, such as use of a thick re-growth buffer or stacked system. Additionally, QDs that emit photons near the band edge of a photonic crystal waveguide enter the slow light regime. This leads to a reduction in the QD lifetime, and so an increase in the Fourier

transform limit. A broader transform limit means mode hopping due to charge noise is more likely to be within the linewidth of the QD, which makes entanglement more likely.

The aim of some groups is to minimise emission linewidths by developing methods that allow site-controlled growth to be maintained far from the fabrication interface. An interesting and novel approach was developed by Yakes *et al.* [111], where the natural anisotropy in crystal growth was harnessed to allow exeptionally thick buffers to be grown. A single layer of site-controlled QDs were grown 90 nm from the fabrication interface and world leading linewidths of 6 μeV were reported using resonance fluorescence PL. An alternative approach to increasing the fabrication interface-active QD distance is through use of a stacked system [119, 137]. The use of a stacked tri-QD system has been shown to significantly reduce single QD linewidths, by a factor of 4 from 2.3 meV for single layer QDs to 600 μeV for the third layer QDs [16]. Additionally, single QD linewidths were reduced when the QD was further from the fabrication interface and a wet chemical etch also gave lower linewidths than a dry plasma etch. The effect these parameters had on single QD linewidths is shown in Figure 2-13.

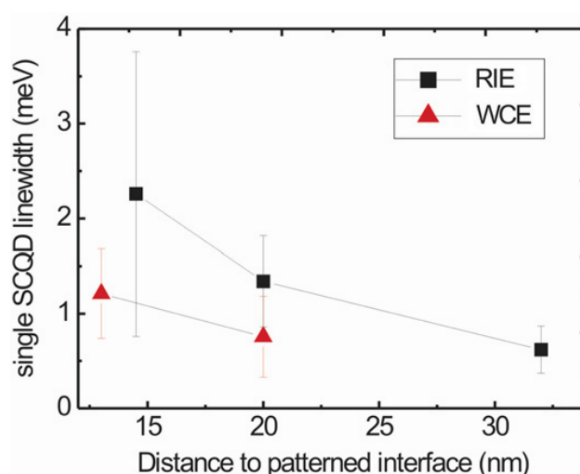

Figure 2-13. The single QD linewidth is shown as a function of the distance between the patterned interface and QD layer for two etch methods ICP-RIE (RIE) and wet chemical etching (WCE). Used with permission of IOP Publishing, from 'Single site-controlled In(Ga)As/GaAs quantum dots: growth, properties and device integration', *Nanotechnology*, C. Schneider *et al.*, **20**, 434012, (2009); permission conveyed through Copyright Clearance Center, Inc. [16].

By using a stacked 2-layer QD system, with 22 nm of buffer from fabrication interface to the active QD layer, an ultra-low hero linewidth of 7 μeV (median 13 μseV of 40 QDs) was produced [36]. A wet chemical etch (WCE) was used, with significance placed on ex-situ removal of the resist, while in-situ atomic hydrogen cleaning was used to remove remaining oxides. An AlGaAs layer was grown directly onto the nanohole array and between the seed and active QD layers. The layer acted as a trap for charge carriers which caused spectral wandering, further reducing linewidth broadening and increasing QD brightness. A spread in QD sizes was observed, which like other groups was attributed to the distribution in nanohole diameterst. An AFM image (a), occupancy statistics (b), and PL image (c) of this result is shown in Figure 2-14. Emission from a regular array of nanoholes was observed at a pitch of 12.5 μm.

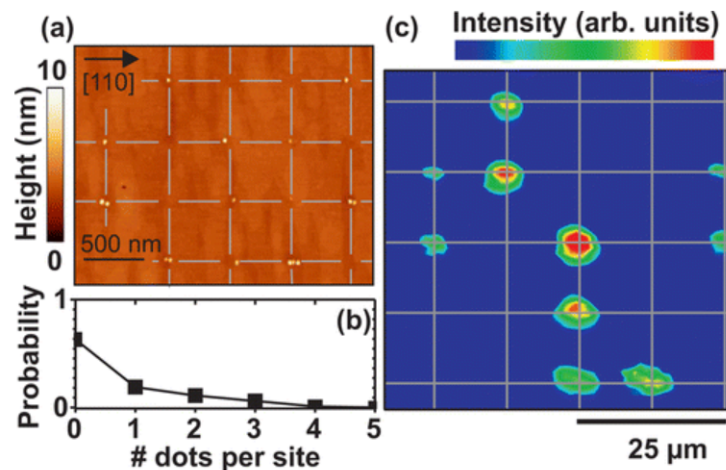

Figure 2-14. For the SCQD array (a) an AFM image shows uncapped QDs, (b) shows the occupancy distribution information for the array and, (c) shows a μPL map for a capped array, where a grid is placed on the images as a guide to the eye. Reprinted with permission from K. D. Jöns *et al.*, *Nano Letters*, **13** (1), 126-130 (2013). Copyright 2013 American Chemical Society [36].

Conversely, other groups have sought to grow low-linewidth QDs very close to the fabrication interface, using a single layer of QDs. The preparation of the fabrication interface becomes even more critical when growing site-controlled QDs in this fashion. Using EBL/ ICP-RIE and a 15 nm buffer, minimum QD linewidths of 80 μeV were produced, with a mean of 132 μeV for 17 QDs [115]. These results demonstrate the importance of well-prepared sample surfaces and show that advanced growth structures can lead to improvements in QD linewidths. It should be noted that the very best reported linewidths

have been for samples where a wet chemical etch has been used, as can be seen in Table 2.1, which is possibly due to reduced damage or contamination levels.

2.3.3.2 Controlling QD size, wavelength distributions, and occupancy

Producing a narrow distribution in SCQD wavelengths across an array increases device yield, where ideally all QDs should emit photons that are of the same wavelength. Therefore, QDs must be of the same size and composition. Wavelength regions often studied in the literature are in the 900 nm to 1000 nm range, or in the telecom O- or C-bands, which centre at around 1300 nm or 1550 nm, respectively. If QDs slightly differ in energy they can be tuned into resonance, using methods such as the Quantum Confined Stark Effect. Occupancy will also be discussed in this section, as the size of a QD that nucleates in a nanohole and the number of QDs that nucleate in the nanohole are often related in the literature. For scalable SCQD growth it is preferable for a large percentage of sites to be occupied by a single QD. This improves device yield, as more devices in the array will contain an active single photon source, that is identifiable and controllable, which might not be the case if multiple QDs are present at a site. However, there is also interest in growing multiple QDs in close proximity, as these systems are analogous to molecules, and are hence referred to as QD molecules. The following parameters will be discussed in relation to controlling QD size and wavelength distributions and occupancy, the nanohole sizes, array pitch, use of a stacked system, indium coverage, growth temperature and growth rate.

The size of the nanoholes used for nucleation have been shown to strongly affect both QD size and occupancy. As the diameter of a nanohole increases, occupancy increases, and as the depth increases single occupancy becomes more prevalent. Using nanoholes $\sim$ 40 nm in depth produced high single occupancy statistics [114, 138]. The type of nanohole etching method also seems to influence occupancy, possibly due to the differing size resolutions of each fabrication method. Nanoholes fabricated via a wet chemical etch possess larger diameters compared to dry etched nanoholes and straighter side walls, using the same electron beam lithography parameters [128].

An AFM study of SCQD growth was reported, where indium coverage was investigated [106]. Three deposition amounts were assessed, 1.2 ML, 1.7 ML and 2.0 ML and the critical thickness was stated to be 1.6 ML. At a thickness of 1.2 ML double dots formed and 74 % of sites were occupied by two QDs. The distance between them was measured to be around 40 nm, therefore it was stated that charge carriers in the QDs could interact with one another meaning that lateral QD bi-molecules had been grown. At 1.7 ML the QD bi-molecules coalesced into larger single QDs, which formed at the centre of the hole, and a low quantity of small QDs nucleated in the planar areas between the nanoholes. For 2.0 ML large numbers of QDs nucleated on the planar surface between nanoholes. Another group showed that by using a stacked system (1.5 ML seed QD, 1.8 ML in subsequent layers), very good single occupancy and size distributions were demonstrated for 2-layer to 6-layer systems. Figure 2-15 shows the beneficial effects of using a stacked system on QD occupancy [139]. It can been seen that when a single layer (a) is compared to a deca-layer (b), the occupancy shifts from being predominantly triple to single (c).

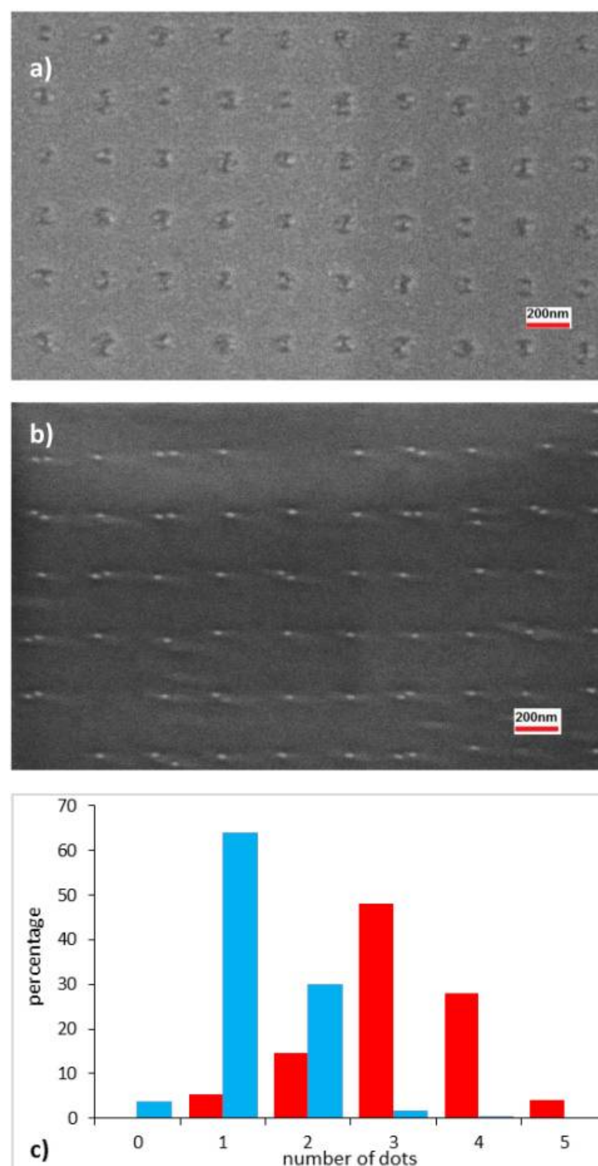

Figure 2-15. SEM images of (a) a single layer of QDs, (b) a 10-layer stack of QDs and, (c) the occupancy distributions for the single- and 10-layer stacks. Reprinted under the terms and conditions of the Creative Commons Attribution license, from reference S. Hussain *et al.*, 'Site-Control of InAs/GaAs Quantum Dots with Indium-Assisted Deoxidation', *Materials*, **9** (3), 208, (2016) [139].

PL and AFM results for a stacked SCQD system were reported, where the effect of altering pitch and using a stacked system vs a single QD layer was observed to affect height and wavelength distributions of the QD ensemble [140]. First for an 11th layer stack, pitches of 210 nm and 160 nm for a patterned sample were compared to each other and an unpatterned sample. For a pitch of 210 nm, the QD heights were 7.56 nm $\pm$ 7.2 %, this increased to 7.76 nm $\pm$ 9.1 % for a pitch of 160 nm, and further still for an unpatterned 11th

layer stack, where it was 8.03 nm $\pm$ 12.2 %. This corresponded to a ensemble linewidth of 22.7 meV for a 210 nm pitch, 37.1 meV for a 160 nm pitch, and 32.8 meV for the unpatterned sample. Pitch was investigated by a different group and was shown to affect the emission energy of QD ensemble [128]. Pitches of 200 nm and 350 nm corresponded to emission wavelengths of around 921 nm and 927 nm respectively. Although this is not a large change in wavelength, it suggests that growth parameter tuning could be required if pitch was varied. Occupancy has been shown to be strongly dependent on pitch. A linear relationship between the two was observed, where the number of sites occupied by at least one QD rose from around 10 % to 90 % when pitch was increased from 0.5 μm to 10 μm for the same growth conditions [141].

The next growth parameter to be discussed is QD growth temperature. Using LAO patterning, growth temperatures of 460 °C, 480 °C and 520 °C were investigated [134]. A higher growth temperature gave favourable results, with a lower distribution in QD diameters and heights, as shown in Figure 2-16. It was noted that at 520 °C QDs were of around the same size as the fabricated nanoholes, and that their size was controlled by the nanohole. At lower temperatures QDs were larger than nanoholes and their sizes and distributions were not well controlled. It was postulated that this behaviour was due to re-evaporation of the indium taking place at the higher temperature. This statement is supported by another observation that site-controlled QD growth temperatures above 530 °C lead to no QD formation, which was explained as being due to indium re-evaporation [117].

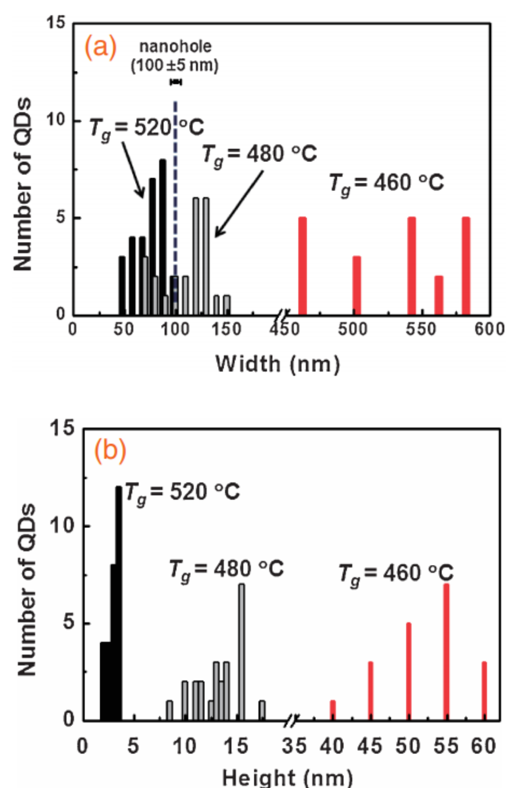

Figure 2-16. The influence of QD growth temperatures, 520 °C, 480 °C, and 460 °C on distributions for (a) QD width and (b) QD height. Reprinted with the permission of The Japanese Society of Applied Physics from 'Size-Limiting Effect of Site-Controlled InAs Quantum Dots Grown at High Temperatures by Molecular Beam Epitaxy', *Applied Physics Express*, Kyu Man Cha *et al.*, **5**, 085501, (2012). Copyright (2012) The Japan Society of Applied Physics [134].

Finally, the effect of growth rate will be considered [117]. Arsenic fluxes equal to 3.5 ML/s, 2.0 ML/s and 0.5 ML/s were seen to produce triply, doubly and singly occupied nanoholes, respectively. The nanoholes in this study were fabricated using LAO and InAs QDs were grown at 510 °C. Another group reported that a change in growth rate from 0.01 ML/s to 0.001 ML/s was observed to increase QD height and improved single occupancy statistics [138]. Additionally, this work reported the same trend in improved single occupancy when increasing growth temperature from 480 °C to 515 °C.

2.3.3.3 Single QD positioning accuracy

Precise control over the position of the emitters within the quantum circuit, and therefore photonic devices, is required to maximise QD and device coupling. Using QD registration

techniques, where the position of a QD is measured relative to an alignment marker and then the device is fabricated around that position, positioning accuracy as low as 30 nm has been achieved [34], although results are more commonly in the region of 50 nm for standard lithographic techniques [137,142]. This method produces good results for a small number of devices; however it is less suitable for scale-up as registration and fabrication processes are complex and time-consuming. Instead, higher device yields can be obtained by growing arrays of site-controlled QDs and fabricating arrays of devices around them. If the QD arrays are positionally regular enough, no registration would be necessary and device array design would be simplified. Positioning accuracy for site-controlled samples has been reported to be $\pm$ 80 nm within the array [36], or $<$ 50 nm with respect to a device [143].

2.3.3.4 Summary

Using the literature reviewed, some conclusions will be drawn with respect to how SCQD growth can be optimised. Firstly, it has been shown that when fabricating nanohole arrays, the best single QD linewidths have been achieved using a wet chemical etch and a stacked growth system. Indeed, stacked growth has improved single QD linewidths in direct comparison to single layer systems, in addition to improving occupancy, size and wavelength distributions. Using a thick re-growth buffer also produced QDs with very low single QD linewidths. Good occupancy and narrow size distributions has been achieved using low growth rates and high QD growth temperatures (520 °C and above), which effectively reduces the growth rate due to indium desorption. However, when too high a temperature is used, it has been shown that no QD nucleation occurs. Occupancy results have been shown to improve when using narrow, deep nanoholes. Additionally, SCQDs tend to emit at longer wavelengths than planar QDs, so size limiting techniques are frequently used to blue shift emission wavelengths.

This page intentionally left blank

3 | Methods

This section will outline the experimental methods that have been used in the project. Firstly, fabrication processes that allowed arrays of nanoholes and alignment marks to be produced will be presented. Next, the principles of molecular beam epitaxy will be outlined, including the in-situ equipment associated with control of the growth process. Techniques for characterising nanohole arrays or QD properties will be described and finally simulation methods will be discussed. Unless stated in the text, fabrication and characterisation of samples and all simulations were performed by the author and the fabrication methods and atomic hydrogen cleaning processes were developed by the author specifically for this project. Growths using the DCA Instruments MBE were performed in collaboration with Dr Ian Farrer and Dr Aristotelis Trapalis and growths using the V-90 MBE were performed in collaboration with Dr Ian Farrer, Dr Edmund Clarke, and Dr Pallavi K. Patil. Buffers labelled TS-XXXX were grown by Brett Harrison. The optical characterisation was performed using a set-up built by Dr Alistair Brash, Dr Andrew Foster and Dr Dominic Hallett. Additional support in the use of the set-up was given by Dr Dominic Hallett.

The literature has demonstrated significant progress in the areas of single QD linewidth, occupancy, positioning accuracy and wavelength distribution. However, if the goal of using site-controlled QDs as in scalable qubit circuits is to be achieved further work is required. This works aimed to develop processes for the growth of arrays of optically active InAs SCQDs on thin buffers, using a scalable and reproducible approach. The structures processed on GaAs were required to be suitable for incorporation into single mode photonic devices, meaning total structure height was limited to 170 nm. The QDs ideally should be in the middle of the device meaning the space for growing doping and spacer

layers, or very thick buffer layers was restricted. To achieve this goal, nanohole fabrication methods were developed using EBL/ICP-RIE and LAO methods and compared. In addition, guide marks suitable for device realignment and sample characterisation were designed. Nanoholes of different sizes (diameter/depth) were produced, to investigate the conditions optimal for SCQD growth, in addition to the positioning accuracy of the nanoholes. EBL with ICP-RIE offers a highly scalable fabrication method, however mitigating the effects of the contamination introduced during this intensive process posed a challenge. Due to the requirements for maintaining a limited structure height, thick re-growth buffers could not be used to improve QD linewidths. Therefore, a robust ex-situ cleaning technique was developed in addition to an in-situ atomic hydrogen cleaning (AHC) method, which both take place at the re-growth interface. Figure 3-1 shows a simple schematic of the growth structure (a) and a simple array (b). Each array contained nanoholes of a certain size and a series of arrays are fabricated, each with different nanohole sizes. The nanoholes were spaced at an appropriate pitch (spacing between the nanoholes from center to center) for characterisation and device integration. Alignment mark crosses of various sizes were required, so that each characterisation process had a marker appropriate to its requirements. The schematic represents a capped sample structure. For AFM analysis no cap was grown, which allowed information to be gathered such as QD size, denisty or nucleation position etc. Images of the EBL patterns used in this work, a list of SIMS ion masses, and samples grown as part of this project can be found in Appendix A.

The fabrication, surface preparation, and growth processes discussed were developed from scratch for this project. Additionally, the DCA Instruments MBE system, introduced later in this work, was installed part way through the project, which allowed access to AHC and further characterisation capabilities (secondary ion mass spectrometry, SIMS). The final aims of this work involved detailed characterisation of SCQD arrays, so to benchmark the QD arrays and single QD properties and inform further developments to this work.

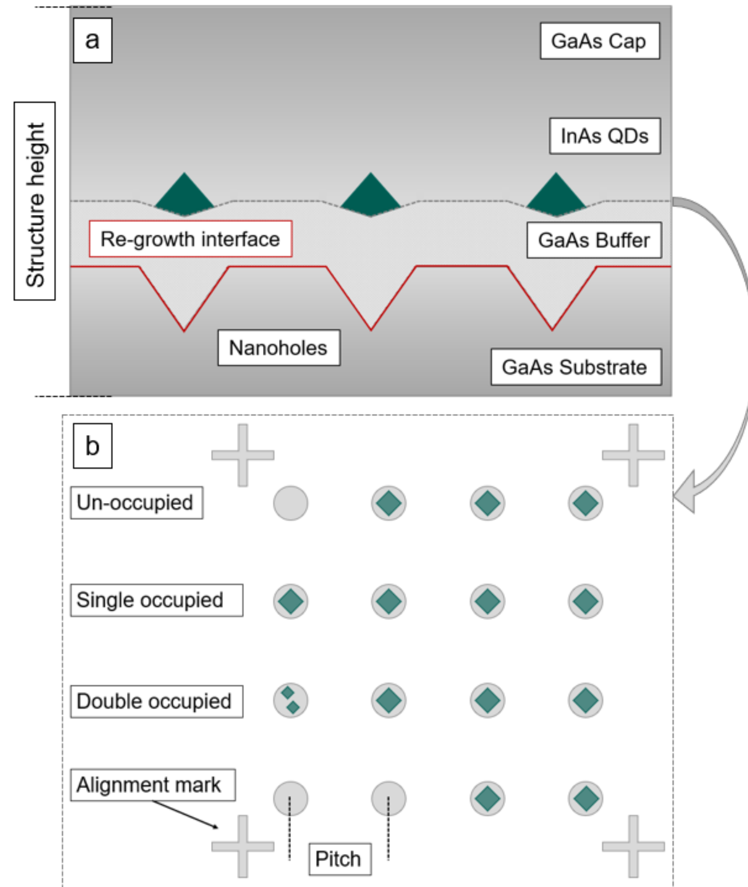

Figure 3-1. Schematic of (a) the structure for SCQD growth of capped samples, where the re-growth interface is highlighted in red and (b) a plan view of SCQDs grown in nanoholes, with examples of un-occupied, single, and double occupied sites. In this case 13/16 sites have at least one QD nucleated, meaning 81 % of sites are occupied and 75 % of sites would be described as singly occupied.

3.1 Fabrication

In this work two distinct nanohole fabrication methods were developed, LAO and EBL/ICP-RIE, results from each will be discussed in Chapters 4 and 5. Samples were patterned with nanohole arrays that ranged in diameter and depth, in addition to sets of alignment marks. In this work GaAs (100) and InP (100) were used at all times. The [110] direction will be referred to as Y and the [1-10] direction as X. In all cases AFM images will be orientated in this manner.

3.1.1 Local anodic oxidation (LAO)

To fabricate oxide lines of varying heights, a conductive AFM tip was scanned across a semiconductor surface in tapping (non-contact) mode while applying a bias between the tip and sample. An example set of oxide lines produced using LAO is shown in Figure 3-2, where the write speed was varied for each line. To create an array of patterned nano-oxide mounds, the AFM tip was rastered back and forward across the sample surface in tapping mode. At pre-programmed positions, nano-oxide mounds were formed by reducing the tip-sample distance, applying the required bias, and holding the tip in a stationary position for 10 s. For all LAO fabrication, a Bruker OTESPA R3 tip, spring constant 26 N/m, drive frequency 300 kHz, tip radius 7 nm was used. To remove the oxide mounds and produce nanoholes samples were acid etch for 2 minutes. A 1:1 solution of HCl/H_2O was used for GaAs and a solution of 4:1:100 $H_2SO_4/H_2O_2/H_2O$ for InP oxides. All GaAs oxides were fabricated at a bias of -22 V, 40 % humidity, temperature of 20 °C, and a peak force amplitude of 8 mV. Investigation into the effect of altering these parameters on nanohole dimensions for InP substrates will be discussed in Chapter 4.

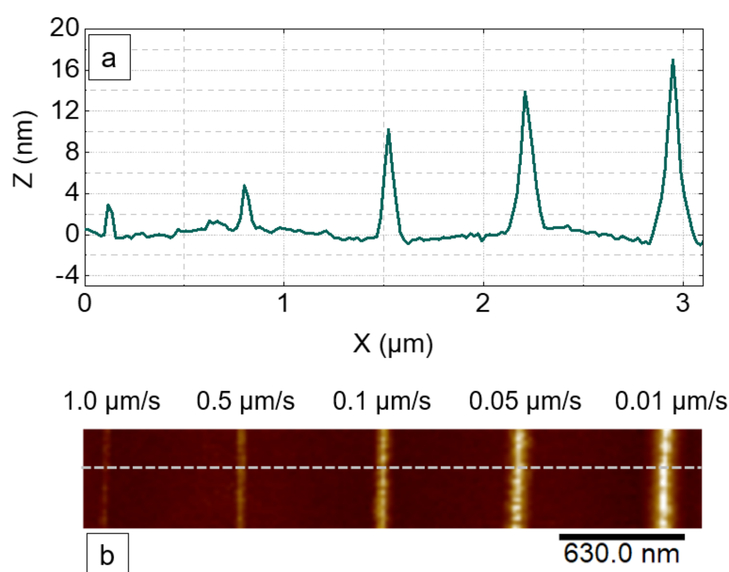

Figure 3-2. Oxide lines fabricated using a LAO process for tip write speeds of 1.0, 0.5, 0.1, 0.05, and 0.01 μm/s (a) a section through the lines is shown and (b) an AFM image of the lines, where the section position is indicated by the dashed line.

3.1.2 Electron Beam Lithography and Inductively Coupled Plasma – Reactive Ion Etching (EBL/ ICP-RIE)

The process flow for the EBL and ICP-RIE will now be outlined and is shown in Figure 3-3. To fabricate the array of nanoholes via this method, a bare GaAs wafer was coated using a resist spinner with a 100 nm layer of positive organic EBL resist poly(α-methylstyrene-co-methyl chloroacrylate) CSAR62. This was achieved using a spin speed of 4000 rpm for 30 s. The resist was chosen as it can produce features with narrow radii and has a resolution enhancement over other commercially available resists, such as poly-methyl methacrylate (PMMA) [144]. In this work two ICP-RIE etchers were used, both of which were Oxford Instruments machines and argon/ chlorine gas chemistry was used. From this point forward they will be referred to as ICP1 and ICP2, and separate etch recipes were developed for each. A schematic of this process is shown in Figure 3-3. Full two inch wafers were processed, or full three inch wafers were processed and then cleaved into quarters for growth experiments.

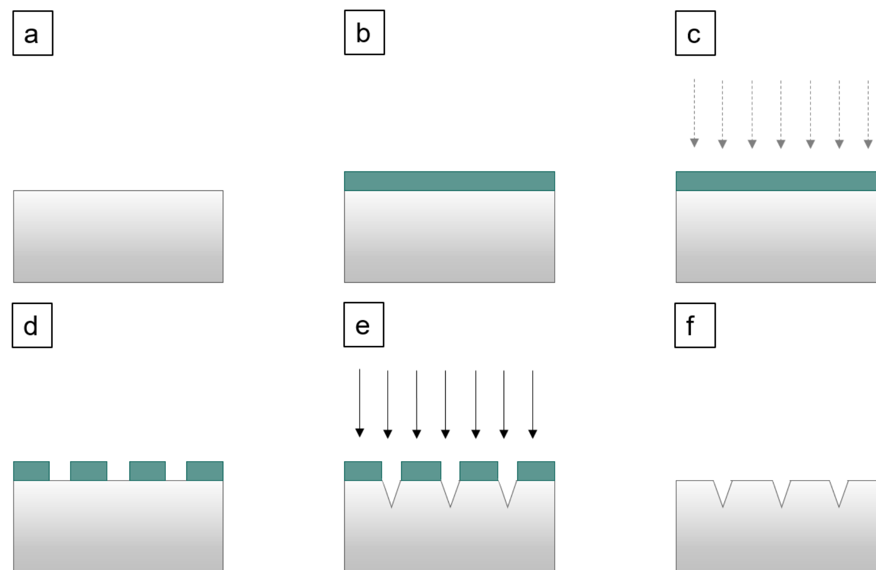

Figure 3-3. A schematic of the main process steps for fabricating arrays of nanoholes are as follows (a) bare semiconductor, (b) the resist is spun onto the wafer, (c) the pattern is defined using EBL, (d) the resist is developed which creates a soft mask, (e) ICP-RIE creates features in the semiconductor and, (f) the resist is removed.

EBL is a commonly used lithographic technique that is used within the semiconductor industry for the production of photolithographic mask plates. Additionally, it can be used pattern nano- or micro-sized features, such as nanohole arrays, photonic crystals, or other photonic devices. During patterning, a beam of high energy electrons is directed at a polymer resist through an aperture. The electrons must carry enough energy to overcome the activation energies needed to initiate bond scission (positive tone) or crosslinking (negative tone) throughout the depth of the resist. If this is successful it can be said that the dose to clear has been achieved. The pattern design can be created using a Graphic Database System II file (GDSII) that directs and controls how the electron beam is applied to the resist, therefore selectively patterning an area. The system allows control over the shape, position and drawn size of the feature in addition to the dose applied, where dose (D) is described by the following equation

$$D = \frac{I.t}{A} \tag{3.1}$$

where I is the beam current, t is the exposure time, and A is the area exposed.

Inelastic collisions of primary electrons with the resist can cause ionisation, which in turn leads to the production of secondary electrons [145]. These secondary electrons negatively impact on achievable resolution as they have energies and cross sections highly appropriate for further bond scission [146]. When fabricating larger features, such as alignment marks, this issue is minimised by running a proximity correction algorithm. As feature size decreases the applied dose must increase as fewer electrons are incident on the region of interest. When features are small and far apart (nanoholes with large pitch) proximity effects are small and little or no correction is needed. In this work a Raith EBL system was used with beam voltage of 50 kV, in a low current mode, with an aperture of 60 μm. This produced a base dose of $\sim$ 240 μCcm^{-2}, from which all doses can be scaled e.g. a scaled dose of 0.5 or 2.0 would give 120 μCcm^{-2} or 480 μCcm^{-2} respectively. Within the text, doses will now on be referred to in terms of their scaled dose with 1.0 being equivalent to 240 μCcm^{-2}. A 500 μm write field was used with a 5 nm step size, 130

ns dwell time, and 38 mm/s beam speed.

The bond scission caused by EBL patterning leads to a reduction in the polymer molecular weight which brings about a change in its solubility. This structural alteration allows a sample to be developed, where the irradiated polymer is dissolved and removed. This was done by submerging the sample in dimethylbenzene heated to 23 °C for 1 minute, before rinsing in propan-2-ol. The mechanism of solid polymer dissolution consists of two processes; the solvent must penetrate the solid polymer before chain disentanglement can then occur. This means that dissolution takes some time. The effectiveness of the solvent will depend on how easily it penetrates the polymer and on the number of interactions between the material and the solvent and the strength of the interactions. These factors must be considered when choosing solvents for development or complete removal of the polymer. In the case of development, areas where chain scission has occurred allow diffusion of the solvent to occur at faster rates, meaning these areas were solvated at an accelerated rate compared to the non-irradiated area.

This process leaves some areas of the wafer free of resist, whilst a soft mask covers the remainder. The areas of the wafer that are exposed can then be etched using ICP-RIE while masked areas are unaffected, meaning the pattern is transferred onto the semiconductor. ICP-RIE is a dry etching technique where ICP power is inductively generated by a radio frequency (RF) source. A magnetic field is generated which in turn produces an electric field. This generates a plasma based on chosen etch gases, where gas composition and pressure can be controlled. The sample table is biased using another RF generator. This power causes the plasma to be accelerated towards the wafer with a controllable kinetic energy. A low energy improves selectivity and causes less substrate damage. Additionally, the nature of the reactive species produced and the ion density are affected, which in turn affect the etch rate. Etching comes about due to ion bombardment, which is a sputtering process, and chemical reaction. Parameters and etch gases can be optimised to produce reasonable selectivity and low sample damage [147]. An advantage of this etch method is that the ion current and ion energy can be independently controlled. A schematic of the chamber is shown in Figure 3-4. Over the course of the project two ICP-RIE machines were

used. Initailly, a single ICP-RIE was avaliable (ICP1) and part way through the project a second machine was installed (ICP2). Etching recipes were developed on both machines. The gasses used were Cl_2 or $SiCl_4$ with Ar. Long periods of equipment downtime occued over the course of the project, which dictated whether ICP1 or ICP2 was used.

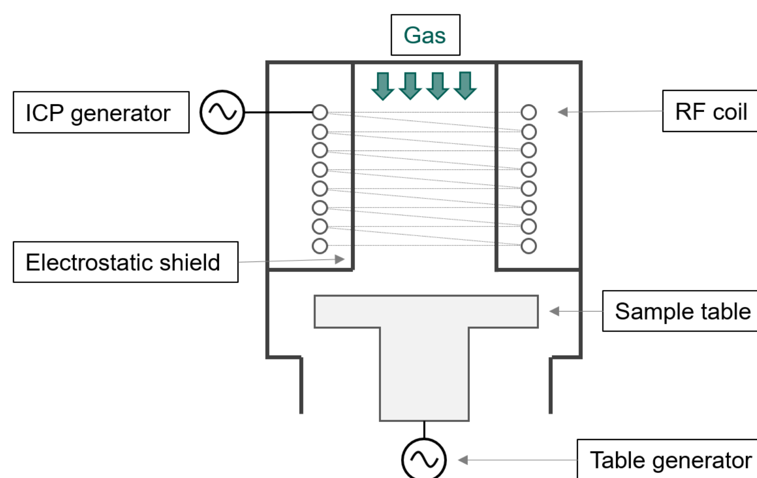

Figure 3-4. A schematic of the ICP-RIE chamber.

Once the wafer is etched the resist must be removed as the surface quality affects QD properties so strongly. A rigorous process was tested and developed, which will be discussed in Chapter 5. The structure of the organic resist poly(α-methylstyrene-co-methyl chloroacrylate) can be seen in Figure 3-5 (a). It contains an aromatic ring, halogen and double bonded oxygen atom, meaning that it can bond via π-π and other weak dispersion interactions, such as those between alkyl chains and polar groups.

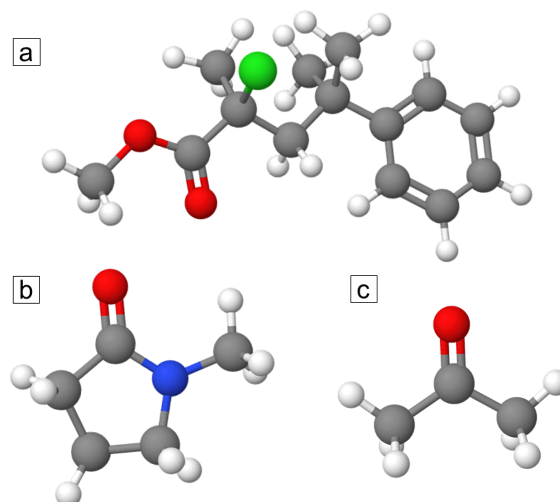

Figure 3-5. Chemical structures of (a) the monomer of CSAR62, (b) NMP and, (c) propanone. The structures were generated using JMol [148]. Elements are as follows, grey = carbon, white = hydrogen, green = chlorine, red = oxygen, and blue = nitrogen.

To remove the resist, two solvents, n-methylpyrrolidone (NMP) and propanone were considered, their structures are shown in Figures 3-5 (b) and (c). They have solubility parameters similar to CSAR62. Both propanone and NMP's interactions are mainly governed by dispersion interactions and polar bonding. The commercially available resist stripper Microposit remover 1165 is 99% NMP, and is commonly used to remove CSAR62 for the reasons outlined above. Propanone in addition to being a suitable solvent for resist removal, also effectively removes general organic contaminants, such as oils and greases, due to its polar nature. Propanone can leave behind drying stains, therefore another solvent is required to remove these and leave no stains once dried. Propan-2-ol is a suitable candidate as it is miscible with propanone and again removes oils and other organics. The final solvent cleaning protocol involved the use of NMP, propanone, and propan-2-ol.

3.2 THE MOLECULAR BEAM EPITAXY (MBE) SYSTEM

MBE is an epitaxial growth method, where accurate deposition on the monolayer (ML) scale can be achieved. Beams of atoms or molecules are directed at the sample surface,

with a certain flux. The flux and therefore growth rate can be controlled. Samples grown in this project use III/V materials, these being gallium or indium and arsenic. These source materials are heated within Knudsen Cells to provide the beam flux, and a shutter can be opened to closed to precisely control the times at which the atomic beams are incident on the sample surface. During growth arsenic is constantly supplied to prevent degradation of the GaAs surface at high temperatures. Gallium and indium adatoms are able to migrate across the sample surface until they reach a nucleation point, arsenic atoms bond to the group III materials and monolayer by monolayer growth occurs. For buffer growth, the gallium shutter is then opened for a short time, which is calculated based on the growth rate and buffer thickness required. A similar approach is taken for QD growth. Indium is supplied for a short time period (the critical thickness is nominally 1.7 ML). The length of time this deposition occurs for can control properties such as QD density and size.

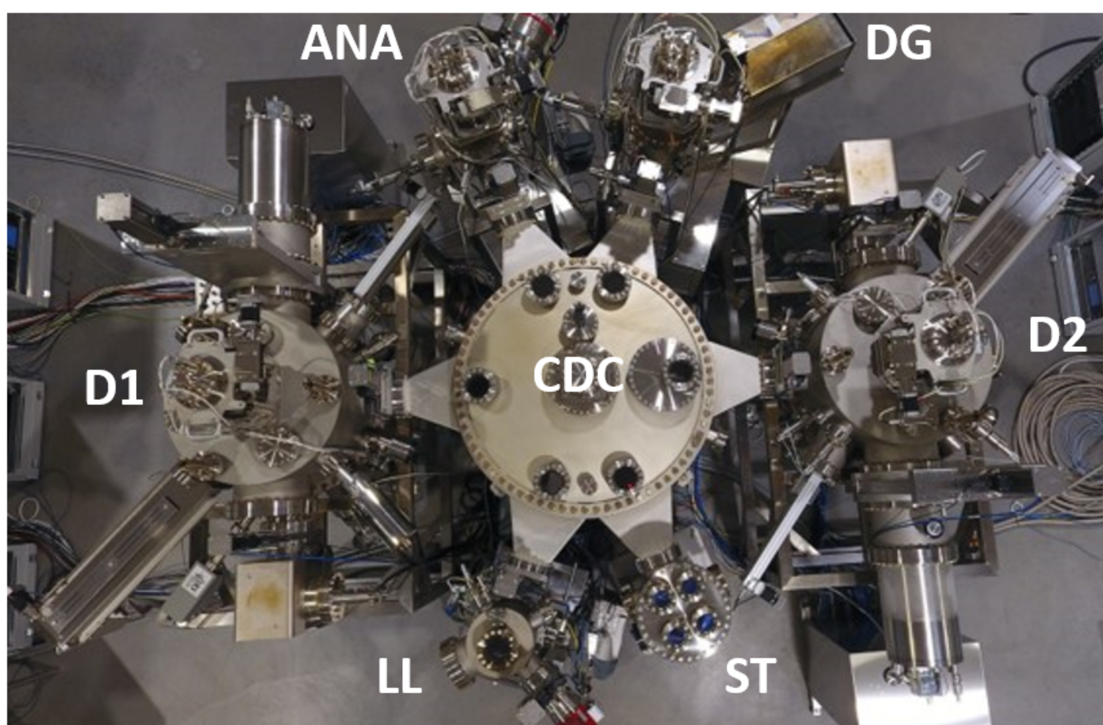

Figure 3-6. An aerial photograph of the MBE system taken using a drone by DCA Instruments, Finland. The chambers of the system are as follows: main growth chamber (D1), atomic hydrogen cleaning chamber (D2), degas chamber (DG), analysis chamber (ANA), which can also degas samples, load lock (LL), central distribution chamber (CDC), and storage racks (ST).

Samples in this work were grown either on a Vacuum generators V-90 machine (SFXXXX

samples) or a DCA Instruments P600 machine (PRXXXX samples). The layout of the DCA MBE system can be seen in Figure 3-6, where a series of chambers are radially distributed around a central distribution chamber (CDC). All chambers, apart from the storage racks, are separated from the CDC by gate valves.

The MBE system is under ultra-high vacuum (UHV) and samples are distributed to each chamber using a robotic arm. Because the load lock is separated from the rest of the system using a gate valve, samples can be loaded and unloaded from the system without breaking the vacuum. The process flow from samples entering to leaving the DCA MBE is shown in Figure 3-7. For DCA samples, degas in the LL took place for 12 hrs at 150 °C and between 8 and 12 hours at 400 °C in DG or ANA. The purpose of the degas was to thermally desorb contaminants and adsorbed molecules. The sample temperature in this case was measured using a thermocouple. Unless stated all other temperature readings will be measured using a k-space Associates Band Edge Thermometer (BandiT) [149].

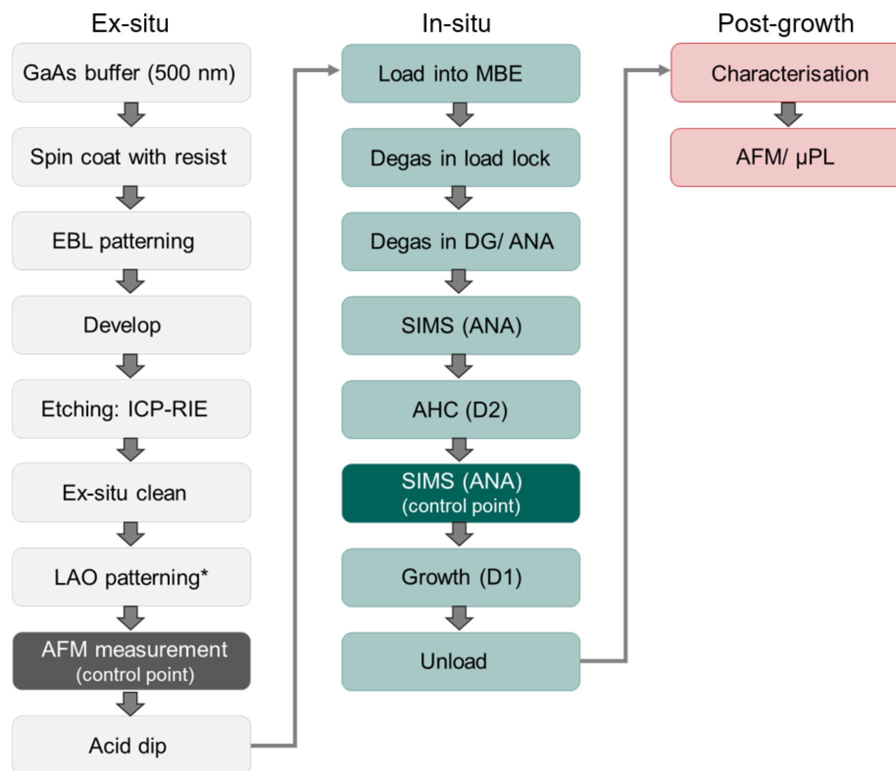

Figure 3-7. The process flow for the fabrication (grey), growth (green), and characterisation (red) of a SCQD sample. Where SIMS is secondry ion mass spectrometry and AHC is atomic hydrogen cleaning. LAO* indicates that this process only occured on some samples and can be skipped. Control points are indicated, at these times the samples are checked to ensure they meet specification and can be removed from the process flow if required.

The stages of buffer or QD growth can be observed using Reflection High-Energy Electron Diffraction (RHEED), which is a technique that provides information on the surface structure. High energy electrons are diffracted from the sample surface at a very shallow angle. The atoms on the sample surface scatter the electrons, which are detected by a phosphor screen. If the sample surface is very smooth constructive interference will take place which gives rise to a clear pattern, as is shown in Figure 3-8 (a). When the sample surface is flat and atomic terraces are present a streaky pattern is observed. However, if the sample surface is rough, i.e part way through buffer growth, where layer by layer growth is occurring, or due to surface oxides, diffuse scatter can reduce pattern intensity. The surface reconstruction can be ascertained from the number of intermediate lines present in the RHEED pattern. The growth of 3D islands has a specific pattern associated with it, shown in Figure 3-8 (b), where additional bright spots appear. These transmission spots are caused by the electrons transmitting through the 3D islands and causing a diffraction pattern. Using RHEED the transition from a 2D to 3D surface can be determined. The growth time at which this occurs is referred to as the 2D to 3D transition time.

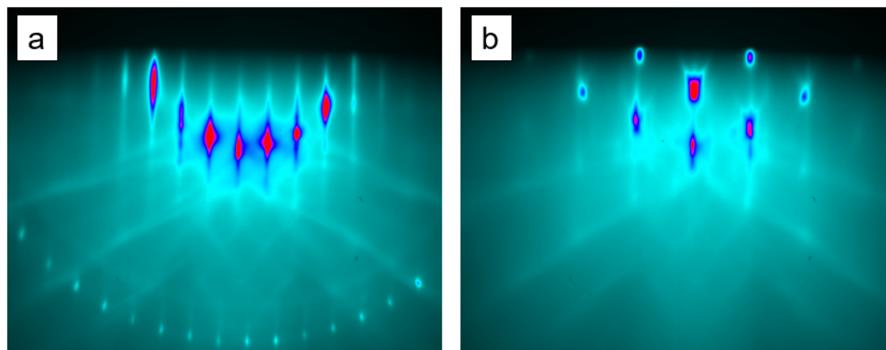

Figure 3-8. RHEED patterns taken in the [110] direction at 500 °C for (a) a smooth GaAs buffer surface and (b) a surface after the growth of QDs, where extra transmission spots can be seen and mark the presence of 3D islands on the sample surface.

The substrate heater is controlled by a feedback loop using a thermocouple which is placed a short distance from the wafer. As this is not in thermal contact with the wafer it is not a true measure of the surface temperature. Instead, the BandiT can be used, which gives real-time temperature information by measuring the optical absorption edge (band edge). The band edge is material and temperature dependent, therefore its movement as

a sample is heated can be precisely mapped onto the sample temperature. However, it is also dependent on the sample size, thickness, polishing and doping meaning that it must be calibrated. A calibration curve for the thermocouple readout against measured BandiT temperature for 2 inch wafers and quarter 3 inch wafers is shown in Figure 3-9. It can be seen that there is a small offset between the D1 and D2 chambers.

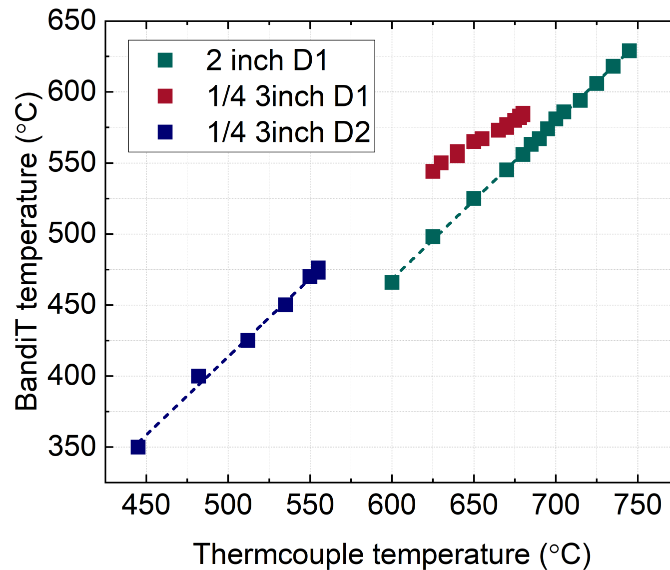

Figure 3-9. BandiT temperature measured for 2 inch and 1/4 3 inch substrates as a function of Thermocouple temperature for chambers D1 and D2.

At the surface, the periodicity of the unit cell can change and a number of arsenic or gallium rich configurations are possible. The notation for the surface reconstruction is written as $(n \times m)$, where the reconstructed cell is n times bigger than the bulk unit cell in x and m times bigger than the unit cell in y. The surface reconstruction can be determined in RHEED from the number of streaks visible in the [110] and [1-10] directions. To check the BandiT temperature results, the GaAs transition from a 4×4 to 2×4 reconstruction was observed using RHEED [150]. This transition should take place at around 515 °C, which as can be seen in Figure 3-10 occurred at the expected BandiT temperature [151].

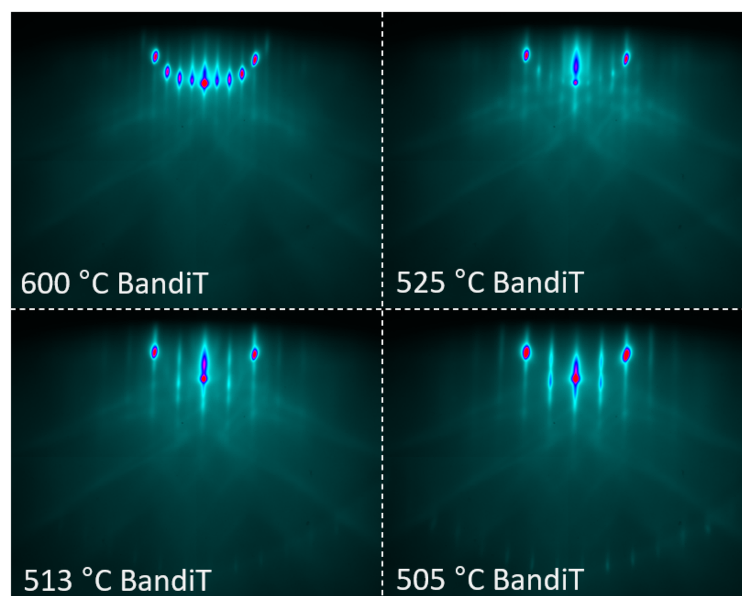

Figure 3-10. RHEED patterns taken in the [110] direction at temperatures of 600 °C, 525 °C, 513 °C and 505 °C while cooling a GaAs substrate, showing a change in surface reconstruction at around 515 °C.

Growths using the V-90 MBE following the same process flow except AHC and SIMS capabilities were not avaliable. To remove surface oxides a thermal desorption process was used. This method involved heating the sample above the temperature at which adsorbed oxides can be thermally removed. The sample was then held at that temperature until oxide desorption was complete. The process was monitored using RHEED.

3.2.1 ANA - secondry ion mass spectrometry (SIMS)

Secondary ion mass spectrometry (SIMS) is a highly sensitive surface analysis technique. A sample is bombarded by a beam of primary ions, in this case argon, which is produced by an ion gun. This splutter beam causes charged fragments to detach from the surface (secondary ions). A schematic of this process is shown in Figure 3-11, where the geometry of the ion gun, sample, and detector is shown for the set-up in ANA. Note, the sample face is positioned so that it is pointing towards the bottom of the chamber. The fragments are guided towards the mass spectrometer by a series of lenses and then analysed to provide information on their composition. This occurs via the use of a quadrupole, where

an alternating RF signal is applied across opposite poles and causes ions to move in a spiralling motion. A DC bias is also applied which drives the ions down the quadrupole. The diameter of the ions spiral will depend on the mass/charge (m/z) ratio in relation to the tuning of the quadrupole, meaning ions of the incorrect m/z ratio will strike the poles rather than move down towards the detector. The quadrupole parameters are swept athrough the m/z range of interest, for both negatively and positively charged ions, meaning quantative data can be collected for surface species. These are referred to as positive and negative modes. The system used in this work was provided and installed by Hiden Analytical.

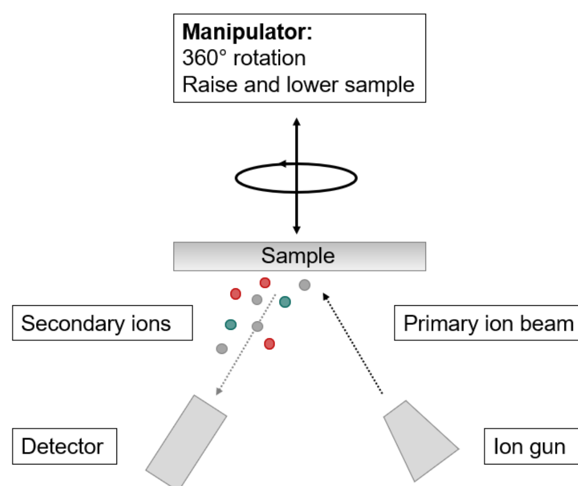

Figure 3-11. A schematic of the SIMS set-up in ANA. Note, the sample is loaded so that it faces towards the bottom the chamber. The black arrows denote the range of motion of the manipulator.

In this work, species with a m/z ratio between 0 and 200 amu were analysed. A list of m/z data associated with fragments in this range is shown in Appendix A, Table A.1. In Figure 3-12 example spectra for negative (a) and positive (b) modes are shown. The species present on the surface can be compared by looking at the intensities of each mass before and after various in-situ processes e.g. atomic hydrogen cleaning.

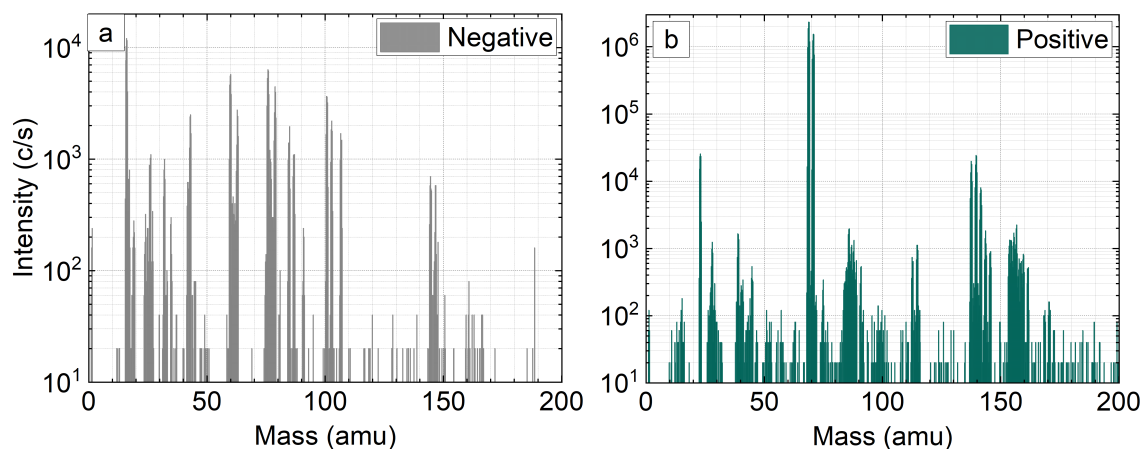

Figure 3-12. Initial SIMS spectra in negative (a) and positive (b) modes for an undoped, epiready GaAs sample.

3.2.2 D2 - Atomic Hydrogen Cleaning (AHC)

Atomic hydrogen cleaning (AHC) is an in-situ surface preparation method that is an effective way of removing native oxides or carbon contamination without causing damage to the semiconductor surface [152]. A temperature of around 400 °C has been shown to effectively remove native oxides, which is significantly lower than thermal desorption or indium assisted deoxidation processes [153]. Chemical reactions taking place between hydrogen and the GaAs oxide surface have been widely studied; with kinetic and thermodynamic considerations being important when describing mechanisms of reaction and predicting the resulting surface reconstructions from said reactions [154]. A hydrogen radical is highly reactive species that bonds to surface oxides and contaminants [155]. The newly formed compounds have a lower desorption enthalpy than the original molecules. Therefore, temperature requirements for desorption are reduced and species can be removed without causing any surface roughening [156]. In addition to a lower substrate cleaning temperature, a number of parameters have been reported to affect the AHC process, these being hydrogen cracking efficiency [157], flux [158], and oxide consistency and thickness [159]. Furthermore, introduction of atomic hydrogen before and during growth has been shown to reduce surface defect density [160]. Surface contamination is removed from the GaAs as described in equations 3.2. The processes that determine the rate of oxide removal are as follows: adsorption of atomic hydrogen radicals, chemical reactions

and adatom diffusion on the GaAs oxide, and chemical desorption of the reaction products. At a low temperature (GaAs substrate T $\leq$ 100 °C) the rate limiting step was reported to be reaction product desorption away from the substrate. Therefore, to ensure complete oxide removal substrate temperatures must be high enough to ensure full oxide removal occurs in an acceptable time frame.

$$H + GaAs(O,C) \longrightarrow GaAs(C) + (Ga, As)H_x \uparrow + H_2O \uparrow, \tag{3.2a}$$

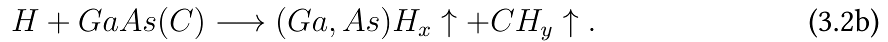

$$H + GaAs(C) \longrightarrow (Ga, As)H_x \uparrow + CH_y \uparrow . \tag{3.2b}$$

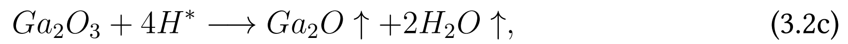

$$Ga_2O_3 + 4H^* \longrightarrow Ga_2O \uparrow + 2H_2O \uparrow, \tag{3.2c}$$

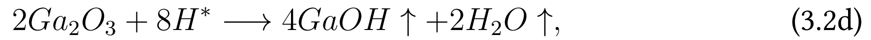

$$2Ga_2O_3 + 8H^* \longrightarrow 4GaOH \uparrow + 2H_2O \uparrow, \tag{3.2d}$$

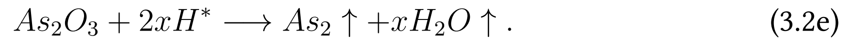

$$As_2O_3 + 2xH^* \longrightarrow As_2 \uparrow + xH_2O \uparrow . \tag{3.2e}$$

A beam of atomic hydrogen is generated by passing H_2 gas over a heated tungsten filament., which is then directed at the sample surface. The hydrogen atomic beam source (HABS) used in this work was manufactured by MBE Komponenten and characterised in the following papers [161–163]. Molecular hydrogen is thermally cracked using a tungsten filament, and the atomic hydrogen produced in this way is directed towards the sample as a beam of gaseous material. The cracking efficiency depends on the filament temperature and the hydrogen flux. The HABS temperature is current controlled, and the relationship between temperature and current is shown in Figure 3-13.

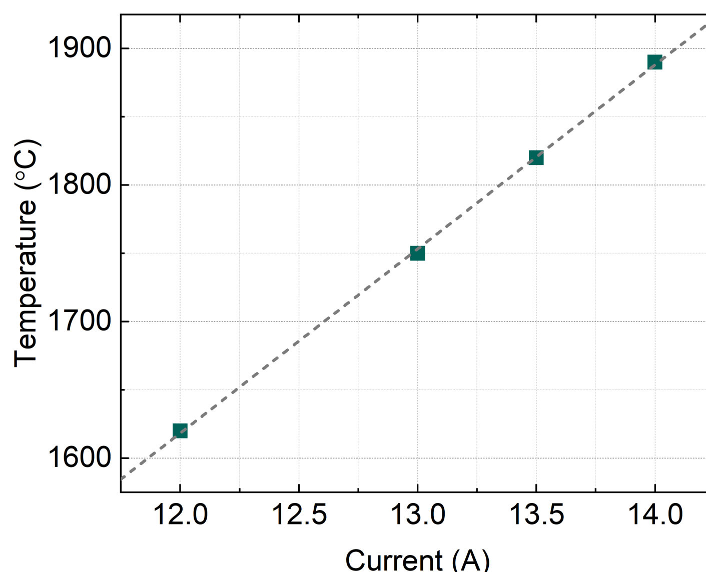

Figure 3-13. HABS temperature as a funtion of supplied current.

A common method for measuring the cracking efficiency involves using a beam flux monitor (BFM). The cracking efficiency and number of hydrogen atoms can be calculated by measuring the change in intensity of the H-2 peak, which is measured as a pressure by the BFM. The system cannot measure the H-1 peak, so instead of seeing an increase in that mass, a fall in intensity should be seen for the H-2 peak. A higher HABS filament temperature will lead to the production of more hydrogen, where cracking efficiency is described by the following equation

$$\eta(T) = \frac{Q_{H_2}^{uc} - Q_{H_2}(T)}{Q_{H_2}^{uc}} \tag{3.3}$$

where $Q_{H_2}^{uc}$ is the uncracked H_2 signal and Q_{H_2} is the cracked H_2 signal [157].

However, due to the geometry of the DCA the cracking efficiency could not be measured in this way, and instead it was estimated using literature values for a range of fluxes. By extrapolating from these literature values and accounting for the chamber size and measured pressures, a flow of 0.5 sccm was calculated to give the highest absolute number of hydrogen atoms [161, 164, 165].

3.3 Characterisation

3.3.1 Atomic force microscopy (AFM)

Atomic force microscopy (AFM) involves using a nanometre scale tip to scan over a sample surface and produce a 3D image of the surface topography to a very high resolution. AFM can be performed on non-conducting and conducting samples, such as polymers (organic EBL resist). The tip is attached to a cantilever, which has a known spring constant, and will respond to changes in surface height by being deflected by a predictable amount. The tip is rastered across the sample surface and a laser is reflected off the back of the cantilever and directed towards a four quadrant photodiode, where the signal changes are converted to an image by the computer. The resolution limit is predominantly defined by the radius of the tip; however, a low vibrational noise environment is also required to visualise very small features such as atomic lattices.

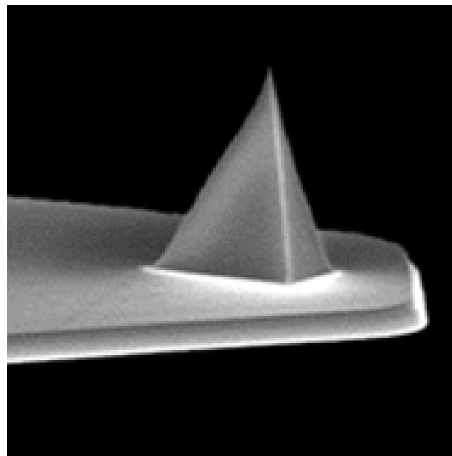

Figure 3-14. A SEM image of a SNL-10 tip, imaged by Bruker. With a tip height of 8 μm, front angle of 15°, back angle of 25°, and side angle of 22.5°.

In this work tapping mode or ScanAsyst tapping mode were used exclusively. In this case the tip is driven at a speed near its resonant frequency, which causes it to rapidly oscillate in the z direction. A Bruker Dimensions ICON AFM was used with a silicon nitride SNL-10 tip, due its super high resolution 2 nm radius, spring constant 0.35 N/m, and frequency 65 kHz. The tip is coated in reflective gold, which due to its chemically inert nature provides

a stable reflection. The AFM model gives sub-angstrom noise levels in z and angstrom levels in x and y, a 90 μm scan size, and drift rates below 200 pm.

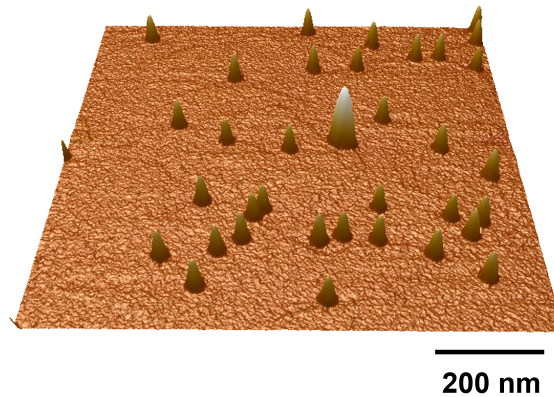

Figure 3-15. A 3D AFM image of a QD sample SF1126, grown by Dr. Edmund Clarke.

AFM is an ideal characterisation method for nanohole and QD samples as it is non-destructive, requires no sample preparation, highly accurate and reproducible, and gives complete 3D information. Software packages Nanoscope Analysis 2.0 (provided as integrated software to the Bruker AFM system), Gwyddion [166], and MATLAB [167], have been used to extract QD and nanohole information (mean size and standard deviation, positioning etc.). Specifically, the positions of QDs within the nanohole presented in Chapter 7 were found using a find and fit code with graphical user interface (GUI), which was written by Dr. Dominic J. Hallett in MATLAB. Surface information such as the root mean square roughness (RMS) were found automatically using the integrated function from Nanoscope Analysis 2.0. The RMS is evaluated by taking the mean squared values for the surface profile, which is found in three dimensions by integrating the height component (Z) across x and y directions. The RMS is described by Gadelmawla *et al.* [168] as follows

$$RMS = \sqrt{\frac{1}{a} \iint_a (Z(x, y))^2 (dx) dy} \tag{3.4}$$

A typical example of a 3D AFM image processed using Nanoscope Analysis 2.0 is shown in Figure 3-15 and examples from 16 nanoholes arrays in Figure 3-16, where different EBL

doses and drawn sizes were used to fabricate nanoholes of varying sizes. An example of no nanohole formation is shown in (a) and (b), where the dose to clear has not been acheived. In Figure 3-17 a section through the nanoholes demonstrates the conical shape, which the high resolution SNL-10 tip is able to resolve.

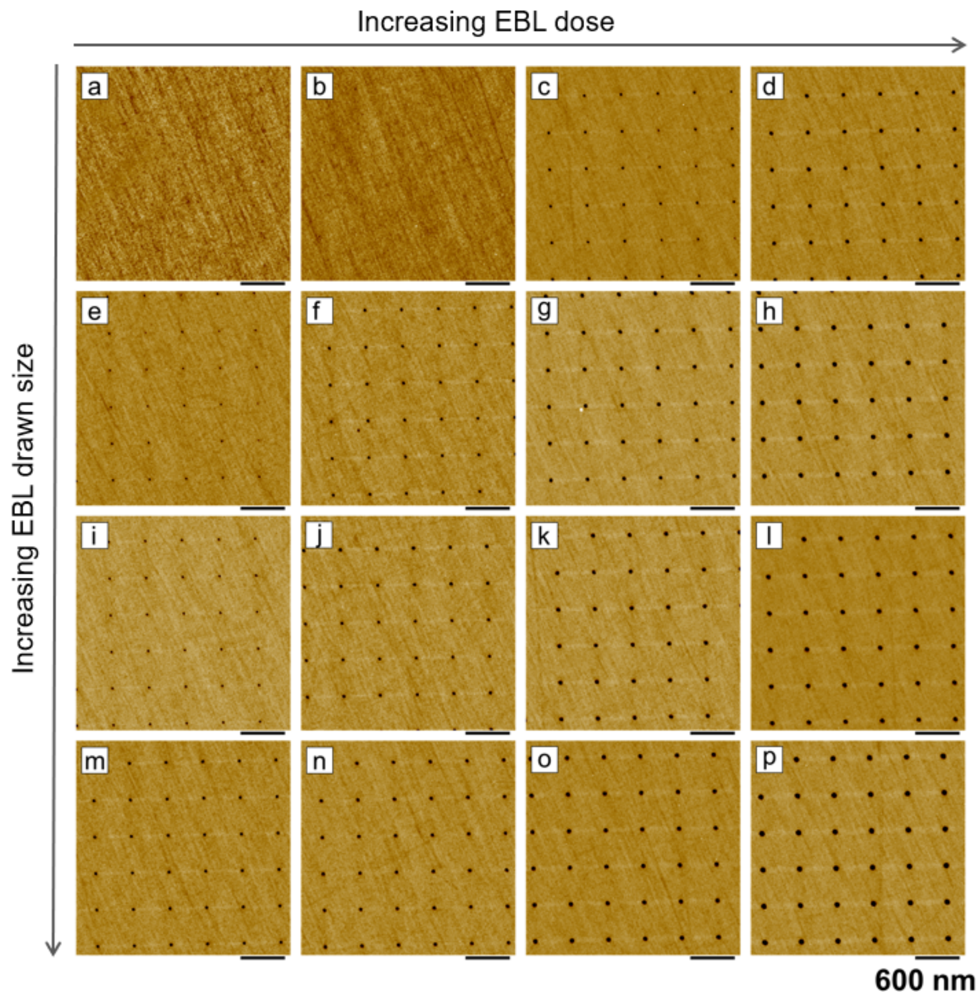

Figure 3-16. AFM images of nanohole arrays with a pitch of 0.5 µm, fabricated on an epiready GaAs (100) surface using EBL patterning and ICP-RIE, where nanohole size is controlled via the EBL dose and drawn size. In (a) and (b) the dose to clear was not acheived meaning no nanoholes were formed, as the dose was increased in (c) and (d) small nanohole formation can be seen. As the dose and drawn size were increased (e) to (p) an increase in nanohole size is observed. A clean, resist free surface is seen for all nanohole sizes.

A closed loop positioning stage allows for reproducible movement to a point on the sample. Alignment marks of a suitable size were incorporated into the sample design, meaning that by using this feature, the same area of a sample could be measured on separate occa-

sions. This allowed the change in specific nanoholes to be monitored at different stages of the process. Of particular interest, was nanohole shape change pre- and post-buffer growth and post QD growth.

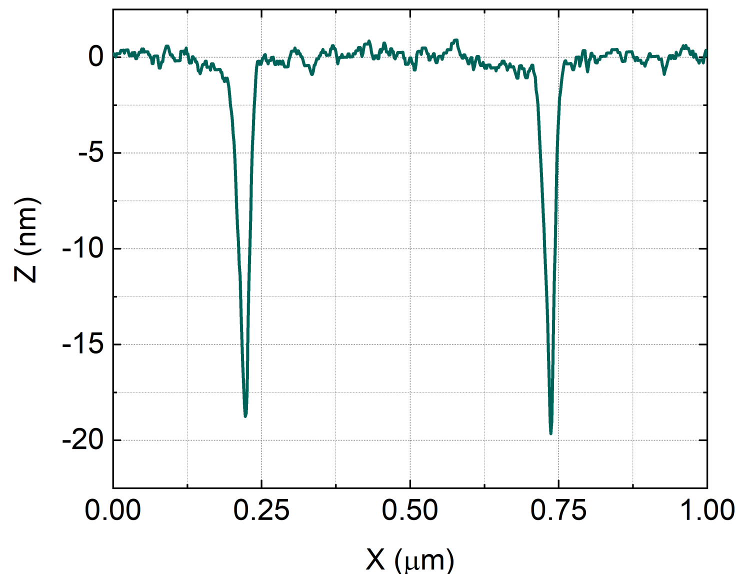

Figure 3-17. A section of an AFM image through x, which corresponds to the [1-10] direction

3.3.2 Photoluminescence (PL) spectroscopy

Micro-photoluminescence spectroscopy (μPL) is a method for optically characterising the emission from single QDs. This project has used a combined imaging and spectrometer set-up, where a large area ($\sim$ 200 x 200 μm) of the sample is illuminated by a 810 nm light emitting diode (LED). A schematic of the set-up is shown in Figure 3-18. The LED induces above-band excitation. A beam splitter directs light through an adjustable filter, which blocks light from the LED travelling to the camera. Light is directed towards a highly sensitive imaging Si CCD camera, and to a spectrometer with a Si CCD detection camera. For fine structure splitting measurements the linear polariser and half wave plate were added to the set-up, and removed at all other times. A closed loop positioning stage allows the sample to be moved under the set-up. This means the μPL of a single QD is acheived by moving the sample into the desired position for light from a specific QD to be focused onto the collection fiber. Spectroscopic information is aquired via this method.

The sample area for which light was collected from was established by shining a laser down the collection path and recording the pixel position on the imaging set-up display. The sample could then be moved using the actuators and μPL data was collected from each area in turn.

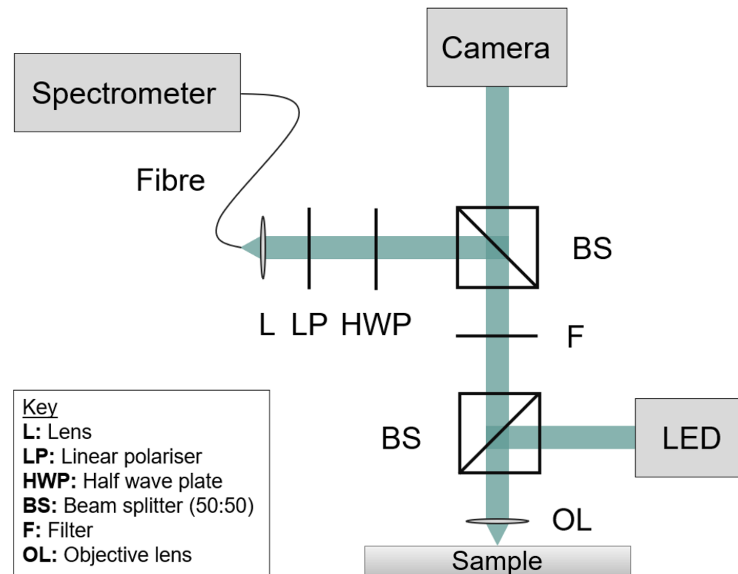

Figure 3-18. A schematic of the μPL imaging set-up used in this project, which is in D49 in the Department of Physics.

The LED excitation source was voltage controlled, and a power meter was used to measure the power under the objective lens. Figure 3-19 shows the measured power at each voltage. The powers are high compared to what would normally be used for a laser as the LED illuminates a large area. A typical laser excitation power, which did not saturate or broaden QD lines, was measured to be from ~200 nW to 500 nW. The associated power denisty was calculated to be ~6.1 W/cm^2. A typical LED power of 2.8 V was roughly equivalent to this laser power, and a power denisty of around 5.9 W/cm^2 was calculated for this voltage.

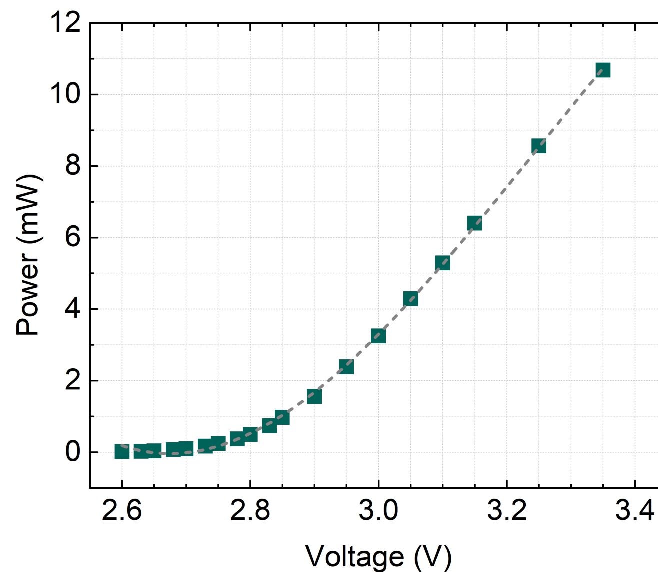

Figure 3-19. The relationship between LED voltage and power measured at the sample.

The samples were cooled to 4 K to reduce QD linewidth broadening from phonon absorption. A continuous flow helium cryostat was used, which cools a cold finger. The samples are mounted on the cold finger using thermal grease, which ensures good thermal contact.

3.4 Finite-difference time-domain (FDTD) modelling

Simulations of nano-optical devices were performed to demonstrate the positioning accuracy requirements in photonic devices in Chapter 5, and the application of LAO for PCC resonant frequency tuning Chapter 4. A finite-difference time-domain method was used via the software package Lumerical FDTD: 3D Electromagnetic Simulator [169]. The method allows the propagation of electro-magnetic fields to be simulated in a device. The simulation area is defined and divided into a 3D mesh. The size of this mesh defines the resolution and speed of the simulation and gives rise to an index map for the dielectric material. An oscillating dipole acts as a source of light and excites supported modes in the device. The electric and magnetic field change over time is provided through solutions to Maxwell's equations, which are itteratively solved over a finite time. Monitors can be

placed at a chosen location in the simulation and parameters such as the Quality factor or mode volume can be calculated. The equation for mode volume is as follows

$$V = \frac{\int \varepsilon(\mathbf{r})|\mathbf{E}(\mathbf{r})|^2 dr^3\mathbf{r}}{max[\varepsilon(\mathbf{r})|\mathbf{E}(\mathbf{r})|^2]} \tag{3.5}$$

where $\varepsilon(\mathbf{r})$ is the dielectric constant and $|\mathbf{E}(\mathbf{r})|$ is the electric field strength. In Chapter 4 where the mode volume was used, Lumerical was able to calculate the mode volume during simulation.

For simulations investigating LAO tuning of a PCC, the oxide mounds were simulated to have a refractive index of 2.0, which matches In_2O_3 [170]. The true composition of the LAO oxides produced is unknown, however this figure was chosen to be a conservative value. The refractive index of $InPO_4$ is 1.8, which would produce a longer tuning range. The refractive index of GaAs was set as 3.4 (920 nm), InP 3.15 (1550 nm) and air was 1.0, at a temperature of 4 K.

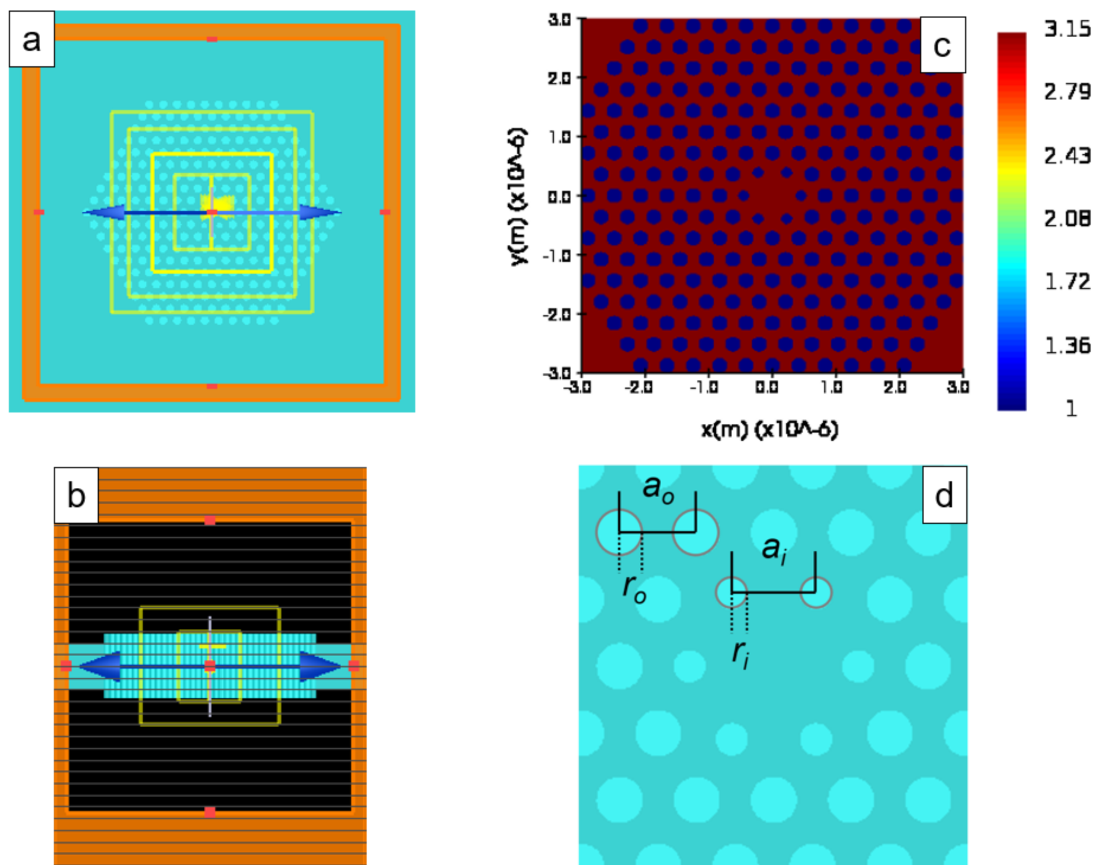

Figure 3-20. Images from FDTD software Lumerical, of the 1550 nm H1 PCC (a) a plan view, (b) a side view, (c) the refractive index profile automatically generated and, (d) the H1 cavity showing the outer hole period a_o, the inner hole period a_i, the outer hole radius r_o, and the inner hole radius r_i.

Figure 3-20 shows an example simulation of an H1 cavity. A plan view is shown (a), where the InP slab and air holes can be seen. The dipole is orientated in the X direction (blue arrow), and various monitors are used (yellow boxes). The boundry of the simulated area is marked by the orange box, a perfectly matched layer (PML) boundry is used which absorbs light and is impedence matched to the material, meaning reflections are minimised [171]. Additionally, it can be seen that the InP slab is extended past the PML layer, again minimising reflections. A side view is shown in (b), where the air holes extend into an air region (black) and past the edge of the slab. This firstly means the slab is entirely air clad, secondly by extending the air holes past the slab no unwanted interface is produced, which could again cause reflections (image cropped, but slab extends past PML boundry). The refractive index map is shown in (c). A fine mesh is used for simulations to give a

high resolution and to have enough points to create round air holes. The parameters for GaAs and InP air clad H1 PCC are shown in Table 3.1. The period of the inner size air holes is denoted by a_i, the period of all outer air holes is a_o, the raidius of the inner air holes is r_i, and the radius of the outer air holes is r_o. These parameters are then varied to optimise the Q factor or emission wavelength of the cavity. The GaAs device parameters for the H1 cavity and the nanobeam waveguide discussed in Chapter 4 were taken from the thesis of Rikki J. Coles [172]. The nanobeam waveguide had a slab thickness of 170 nm and a width of 280 nm. The parameters for the InP devices were determined by through iterative optimisation of a_o, a_i, r_o and r_i, done as part of this work.

Table 3.1. Parameters used in this work for the GaAs H1 PCC (Chapter 5) and InP H1 PCC optimisations (Chapter 4).

Cavity	a_o (μm)	r_o (μm)	a_i(μm)	r_i(μm)	d (μm)	λ (μm)	Q
H1 GaAs	0.24	0.06	0.28	0.062	0.17	0.92	27428
H1 InP (Opt A)	0.452	0.135	0.495	0.094	0.39	1.55	19633
H1 InP (Opt B)	0.445	0.133	0.487	0.093	0.42	1.67	20209

This page intentionally left blank

4 | Nanohole Fabrication: LAO

Improving the scalability and reproducibility of photonic devices with embedded QD single photon sources plays a major role in development of quantum communication technologies. The goal of producing a global quantum network, where information carrying photons are relayed around the world, can be achieved in two ways. Firstly, fibre optics can create a global network for quantum communication. In this case very high-quality single photon sources are required, in addition to quantum memory [173], quantum repeaters [174], and bell state measurement systems [175]. Importantly, the photonic devices and sources must be compatible with current glass fibre infrastructure, which demonstrates low losses in the telecom C-band [176]. Alternatively, low-orbiting and geosynchronous orbit satellites can be used to create a network. The wavelength of light in this system is also of great importance, due to absorption from the atmosphere, background light from the sun causing noise, and Rayleigh scattering. In all cases the best signal is achieved in the telecom C-band, where the background noise is around 3 % of that measured at 800 nm [177]. Therefore, the importance of developing the growth of site-controlled QDs that emit in the telecom C-band (1530-1565 nm) can easily be recognised.

Growth of randomly positioned InAs/InP QDs that emit at 1550 nm has been achieved via SK or droplet growth methods, as discussed in Chapter 2. Emission at or near 1550 nm is more easily achieved for InAs/InP than for InAs/GaAs. The QDs in a InAs/GaAs structure normally emit below 1 μm, however strain reducing layers can be used to red shift their emission wavelength to around 1.3 μm [178, 179]. Emission wavelengths can also be altered by using a stacked system. The ensemble linewidth for a single QD layer has been reported to be 35.5 meV, which was reduced to 16.7 meV for the second QD layer [94].

Very recently telecom C-band emission has been demonstrated for a InAs/GaAs system through the use of a superlattice InGaAs capping layer [180]. QD emission wavelengths for InAs/GaAs are normally shorter than for InAs/InP without the use of these described measures. This is due to the large lattice mismatch between InAs and GaAs of 7 % compared to the mismatch of 3 % in the InAs/InP system, which results in a greater degree of strain in the QD. Therefore, there is a subsequent shift in the QD bandgap, and shorter emission wavelengths are observed for GaAs [181]. However, the small lattice mismatch between InAs and InP can lead to the growth of quantum dashes rather than QDs during SK epitaxy, which have larger than ideal FSS [182]. The FSS has been reduced using droplet epitaxy, which does not rely on a strain mechanism [183, 184].

LAO has been used as a nanohole fabrication method for site-controlled QD growth on GaAs with QDs emitting in the 900 to 950 nm region, however not as extensively as EBL based methods [117, 119, 134]. However, the LAO of InP has not been widely studied. LAO offers advantages as a fabrication method as it is a one step process which takes place under ambient conditions and does not require the use of organic EBL resists or complicated cleaning procedures. Early reports of site-controlled InAs/ InP QD growth via droplet epitaxy have reported single QD linewidths of 0.8 meV [68]. In this report the nanoholes used were < 5 nm in depth meaning that indium droplets were deposited directly onto the fabricated surface and and no re-growth buffer was used. Nanoholes fabricated via LAO on InP have often been shallow in nature or of poor shape uniformity, meaning the thickness of a re-growth buffer is limited. Therefore, improvement in nanohole properties is a desirable step towards improving QD properties. For a thick re-growth buffer to be used, which can assist in reducing spectral wandering of a QD's emission, fabricated nanoholes must be deep. This work succeeded in producing deep, circular and well defined nanoholes, with a maximum depth of 15.6 nm.

This chapter will discuss the development and characterisation of high-quality LAO fabricated nanoholes on InP. The aim of producing deep nanoholes was successfully achieved. The literature has shown that QD properties for an InAs/GaAs system can be controlled via nanohole diameter, therefore the control parameters of applied tip bias and humid-

ity were investigated and a range of nanohole dimensions were fabricated. The accuracy with which each nanohole is positioned compared to an ideal array will be mapped. Early results for the site-controlled QD growth via indium droplet deposition on InP will be presented. Additionally, the kinetics of InP will be investigated to further understand the material properties and the activation energy for LAO on InP is calculated, which is yet to be reported on in the literature. Finally, an alternative application of LAO fabrication will be presented via simulation; the tuning of PCC resonant frequencies using LAO oxides, which has been experimentally demonstrated using a GaAs PCC, but as yet has not been investigated for InP PCCs. For this purpose, an H1 PCC that has a resonant frequency of 1550 nm was designed.

4.1 Nano-feature fabrication

The development of a controllable nanohole fabrication method on semi-insulating InP will now be presented. Figure 4-1 shows an example of an array of 25 oxide mounds. The oxides were removed to produce the corresponding array of nanoholes using a solution of 4:1:100 $H_2SO_4/H_2O_2/H_2O$, which preferentially etches the oxide over the semiconductor [185, 186]. Prior to any LAO process, the sample was acid dipped to thin the native oxide to a minimum. It can be seen that the oxides and nanoholes are well defined and homogenous.

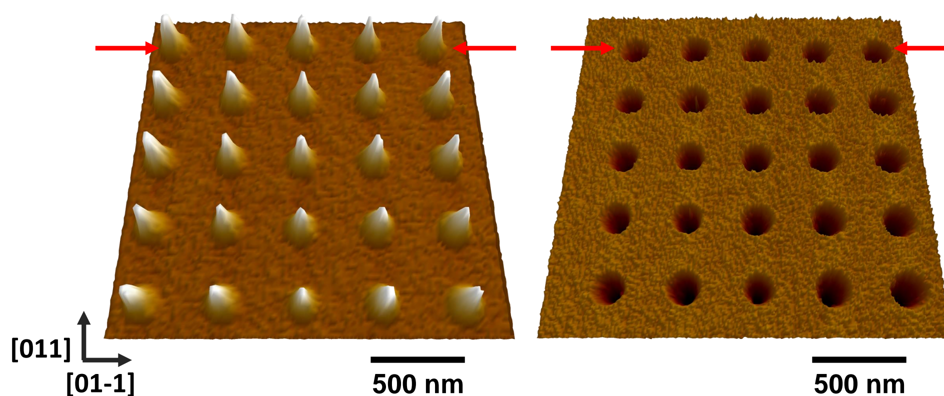

Figure 4-1. 3D AFM images of oxide mounds fabricated via LAO at a voltage of -22 V and at 40 % humidity, and the corresponding nanoholes formed by acid etching away the oxides.

Sections through corresponding nano-features are marked by arrows and shown in Figure 4-2. It can be seen that the oxide grows above and below the surface in a roughly equal manner and produces a conical feature shape, which is suitable for nucleating QDs.

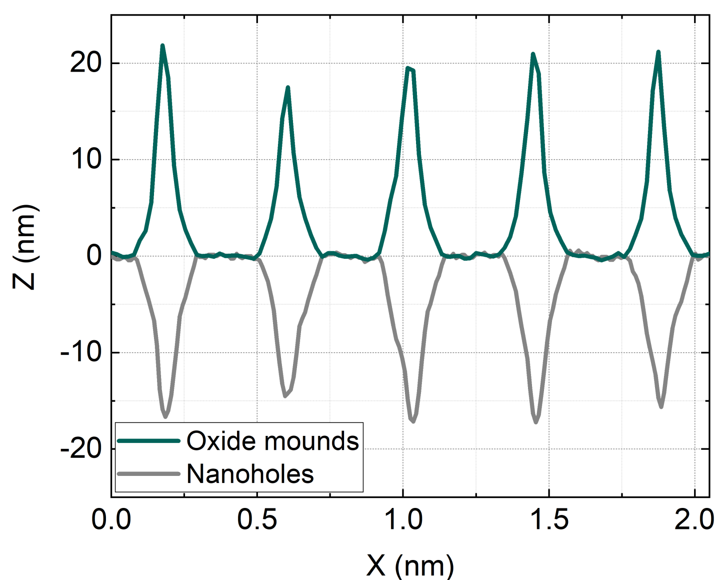

Figure 4-2. A section taken through corresponding oxide mounds and nanoholes from Figure 4-1.

Arrays of 25 features were fabricated under ambient conditions (26 °C, 40 % humidity) at a tip bias of -22 V. For each set of oxide mounds and nanoholes, the mean and standard de-

viations in diameter and height/depth were measured, whilst the amplitude setpoint was varied (Figure 4-3). The amplitude setpoint controls the tip-surface separation; a smaller value corresponds to a smaller separation. A range from 4 to 7 mV was investigated in detail, as much below this range nanomound circularity deteriorated, and above the range oxides were not formed reliably. Significant changes in either diameter or height over the range were not observed. However, to fulfil the aim of fabricating deep, reproducible nanoholes, an amplitude set-point of 7 mV was chosen as the deepest nanoholes were fabricated at this setpoint (16 nm $\pm$ 1.153 nm), which had a mean radius of 213 nm $\pm$ 7.7 nm.

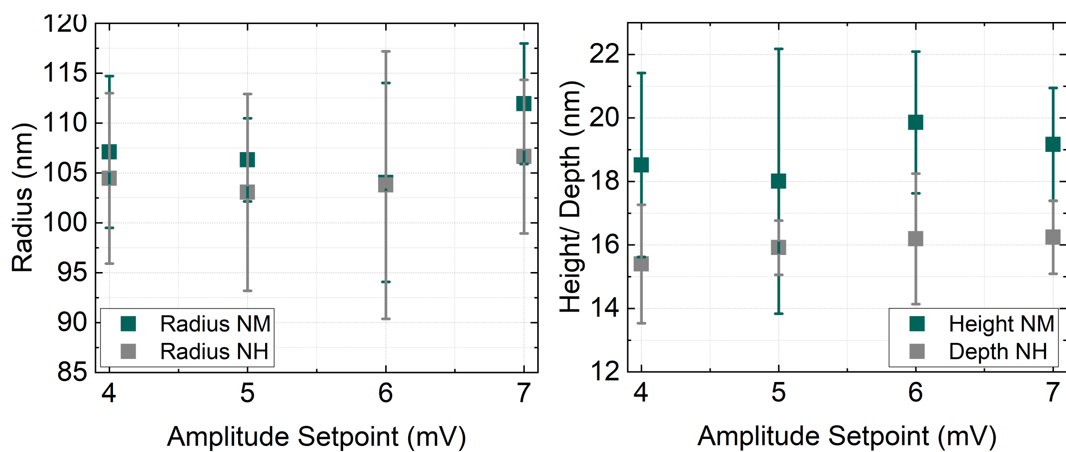

Figure 4-3. The oxide (nano) mound (NM) and nanohole (NH) radius and height/depth, found from AFM images of 25 feature arrays, as a function of the amplitude setpoint.

Once initial oxidation had been demonstrated and an amplitude setpoint value chosen, humidity and bias conditions were investigated. These parameters have been shown to strongly influence nanomound and nanohole diameter and depth [60,61] . Arrays of nanofeatures were fabricated, whilst altering the applied tip bias and humidity for each array. Figures 4-4 (a) and (c) show nanomound and nanohole radius as a function of tip bias respectively, which was measured at the feature base, whilst (b) and (d) show the corresponding nanomound height and nanohole depth. With increasing bias, both the height and radius of the features increased in a linear manner. This is because the increased bias forms a larger electric field at the tip, which increases both the radius of the feature and the penetration depth of the ions. When a constant voltage is applied between the tip and sample for an extended period of time (> 0.1 s) space-charge builds up as the oxide

grows. This effect leads to some preferential oxide growth in a lateral direction, which in turn causes the increase in the oxide radius. The humidity has a strong influence over the nanohole radius, which again increased with increasing humidity. The nanohole depth was less strongly affected by the humidity, however there was a slight increase in depth as humidity was increased. This is because the humidity affects the size of the water bridge much more significantly than the penetration depth of the ions. The maximum average depth for an array of nanoholes was 15.6 nm $\pm$ 1.2 nm with a corresponding average radius of 104 nm for array 40 %, -22 V. The applied tip bias and humidity provide control parameters for nanohole size, where nanohole diameter and depth can be controlled in a reproducible and predictable manner.

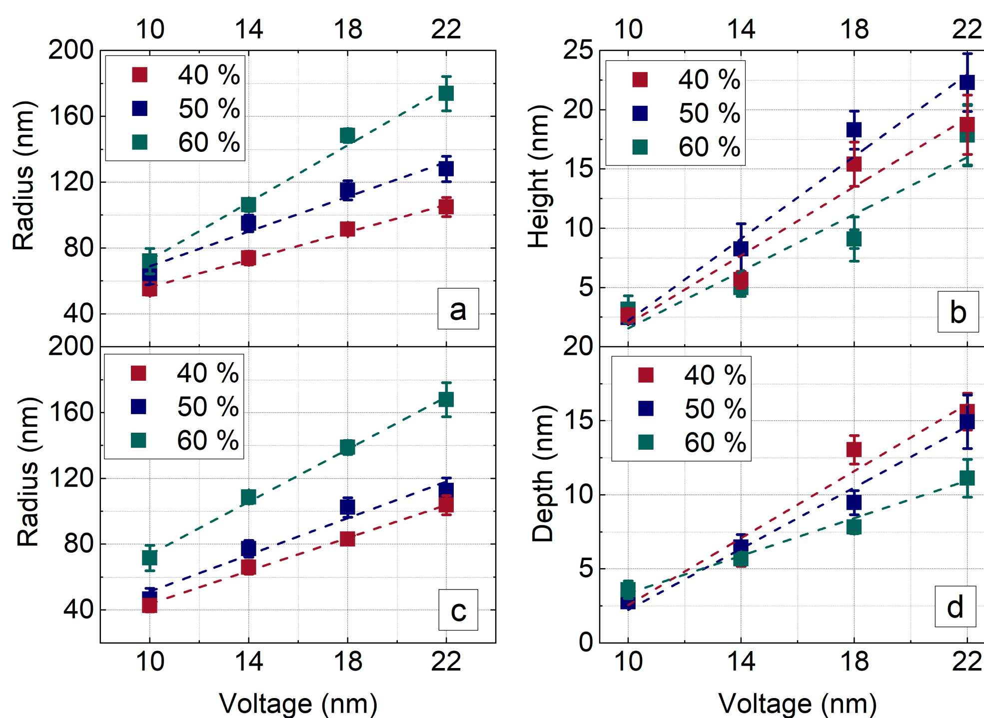

Figure 4-4. Feature size dependence on (negative) voltage and humidity for (a) oxide mound radius, (b) oxide mound height, (c) nanohole radius and, (d) nanohole depth. Mean values and standard deviations were calculated from arrays of 25 nano-features for each parameter.

The LAO process often describes the oxide growing equally above and below the surface, however this is an oversimplification and in practice the oxide can grow in a non-symmetrical manner. The ratio of the oxide height (h) above the surface and oxide depth (d) below the surface has been shown to be related to the density of the oxide material

grown

$$\frac{h}{d} = \frac{(1 - \frac{M_s}{\rho_o}\frac{\rho_s}{M_o})}{(\frac{M_s}{\rho_o}\frac{\rho_s}{M_o})} \tag{4.1}$$

where M_s is the molar mass of the substrate, which is 145.792 g/mol for InP, r_o is the oxide denisty, r_s is the substrate denisty, which for InP is 4.81 g/cm^3, and M_o is the molar mass of the oxide [187].

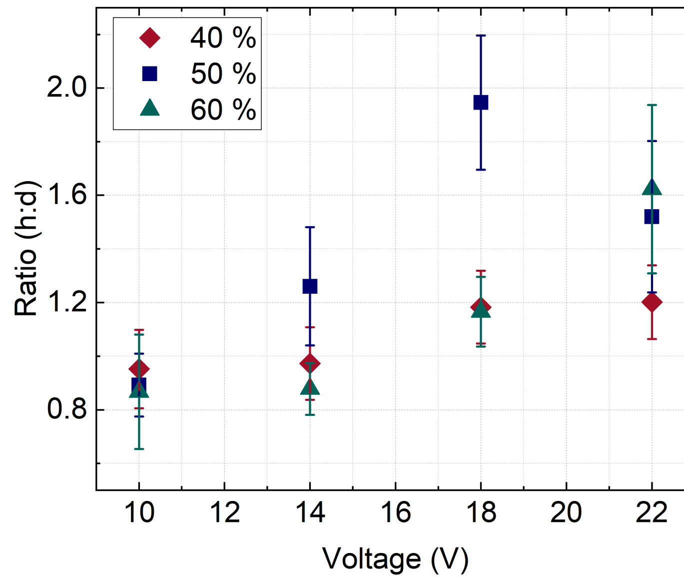

Figure 4-5. Oxide mound height to nanohole depth ratio as a function of applied bias at varying humidities. The ratio for each corresponding nanomound/ nanohole pair was found and the mean and standard deviation for 25 features are shown.

The h/d ratio as a function of applied tip bias is shown in Figure 4-5. The ratio of mean h/d for the 25 features increased for all humidities as the height of the oxide feature increased. In other words, as a larger voltage was applied the oxides preferentially grew above the semiconductor surface. Humidities of 40 % and 50 % gave a similar ratio value as one another, however 50 % humidity at -18 V showed an uncharacteristically high h/d of 1.9. Using equation 4.1, the h/d for a particular oxide type and density can be predicted. If it were assumed that LAO followed the path of an electrochemical anodization reaction, the reaction product would be $InPO_4$ [67]. If the oxide were pure and crystalline then the h/d would be 0.37. The h/d for pure, crystalline In_2O_3 would be 1.75. A report in the literature

of LAO on GaAs showed that the voltage applied affected the type of oxide formed. A higher bias led to the formation of the more stable Ga_2O_3, whilst at a lower voltage Ga_2O or GaO was formed. The oxide composition was confirmed using x-ray photoelectron spectroscopy (XPS) [60]. A further study identified Ga_2O_3 and As_2O_3 using XPS [188]. It is therefore likely that the oxide formed on a InP surface is neither pure or fully crystalline. Some question of the oxide type is still present, which could be resolved experimentally through XPS analysis.

4.2 Nanohole positioning accuracy

Now the regularity of nanohole array will be characterised in terms of the position of each nanohole. A grid of x, y coordinates relating to the position of each nanohole in the array was found and compared to a grid of positions for a generated ideal array, which had been used to fabricate the oxides. The deviation in x and y was found, in addition to the total deviation, which was the distance between the 'fitted' nanohole and ideal 'generated' nanohole. A diagram of these measurements is shown in Figure 4-6

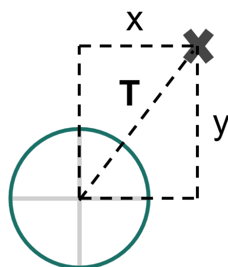

Figure 4-6. A diagram showing the difference between the intended position (green circle) and the measured nanohole position (cross) for the lateral displacements x and y and the overall displacement (T).

An AFM image of a typical LAO fabricated nanohole array is shown in Figure 4-7 (a) and the generated and fitted arrays in (b). The deviations were found for each nanohole array fabricated as part of Figure 4-4. The largest deviation was 3.8 nm $\pm$ 2.8 nm, which was associated with the array fabricated at 60 % humidity and -22 V. No relationship between nanohole diameter or depth and positioning accuracy was observed, and all other mean positioning deviations were below 3.8 nm.

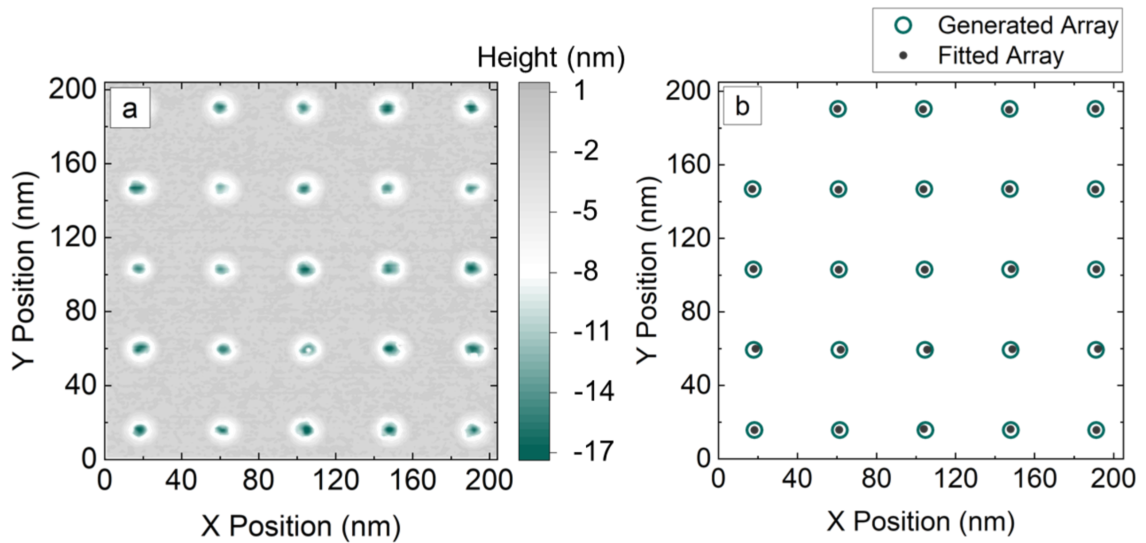

Figure 4-7. For a nanohole array fabricated at 40 % humidity and -22 V (a) is an AFM image of array (b) is a fitted array shows position of each nanohole in the AFM image and generated array shows each ideal nanohole position if the array was completely regular.

Figure 4-8 shows histograms of the errors in x (a) and y (b) and the total deviation (c) for array 40 %, - 22 V. The low positioning errors observed demonstrate the effectiveness of the technique in producing a high quality array of regular nanoholes. The impact of this positioning error on device operation is further discussed in Chapter 5.

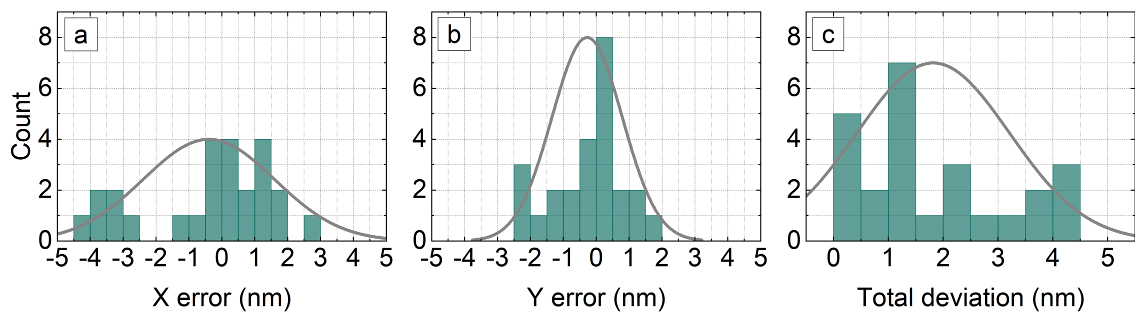

Figure 4-8. Histograms for the x and y lateral displacements, and total displacement for 25 nanoholes for the array shown in Figure 4-7.

4.2.1 Site-controlled QD growth

To assess the suitability of the LAO fabricated nanoholes for site-controlled growth of QDs, an initial MBE droplet epitaxy (DE) experiment using indium was performed. A

nanohole array was fabricated on an epiready semi-insulating InP substrate at a humidity of 40 %, a bias of -22 V at 20 °C. These conditions were chosen as they produced deep and relatively narrow nanoholes. The sample was acid dipped prior to loading into the V-90 MBE. The development of the DE growth parameters was performed by Dr Pallavi Patil and Dr. Edmund Clarke with some input from the author. The native oxide was removed in-situ using a thermal desorption process, at a temperature of 520 °C under arsenic flux. Once an oxide free surface was observed in RHEED, the substrate temperature was lowered to 250 °C (the arsenic shutter was closed at 400 °C). Indium was deposited directly onto the nanohole patterned sample before the it was cooled and removed for analysis. Figure 4-9 (a) shows an AFM image of low density site-controlled indium droplets on LAO fabricated nanoholes. A section through the droplets (b) shows the droplets are large and well positioned at the defined nanohole sites. No droplets nucleated between nanoholes. Further development of growth parameters is required to increase the density and reduce the droplet size, however the nanoholes have clearly demonstrated their ability to control the droplet growth position.

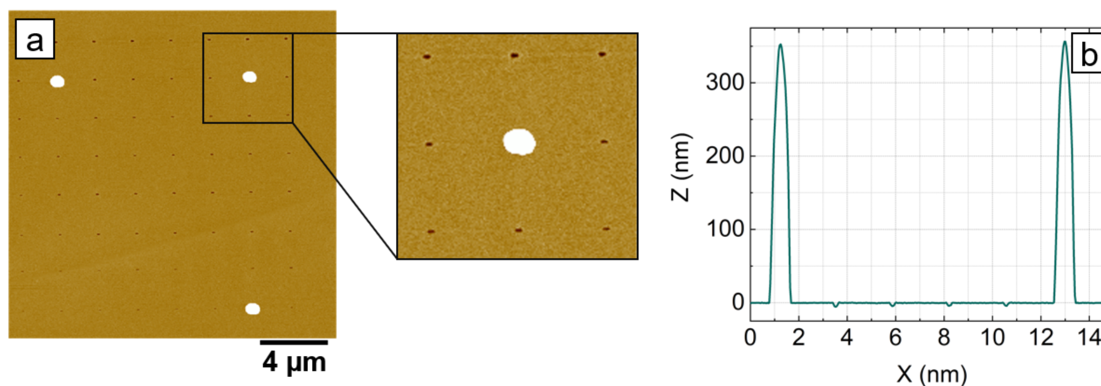

Figure 4-9. (a) AFM image with a zoom in of site-controlled indium droplets on a semi-insulating InP substrate with LAO fabricated nanoholes (40 % humidity, -22 V, 20 °C) and (b) a section through the droplets and nanoholes. Indium was deposited for 120 s, at a rate of 0.012 ML/s.

4.3 Oxide growth kinetics

As well as its potential for use in site-controlled QD formation, LAO has been used to create functional components in heterostructures, where fabrication of oxide lines granted

electrical control over a QD [189]. The LAO process on n-type, p-type and semi-insulating InP is compared while varying tip write speed. Figure 4-10 shows the height of the oxide mounds as a function of log(1/write speed). For all samples, the AFM tip was scanned across the surface in a line at a tip bias of -22 V. Reducing write speed, which is equivalent to a longer dwell time, produces a larger oxide. A linear relationship between the oxide line height and log(1/write speed) was demonstrated for all substrates. This behaviour has previously been observed on silicon [71]. The large standard deviation in oxide height arose from fluctuations in the water bridge as the tip was scanned across the surface [190]. These observations show that LAO fabrication can be undertaken on all doping types, however there is some difference in height produced for each material. Reports for the LAO of GaAs showed that p-type materials produced larger oxide lines than n-type materials, which was attributed to different oxide types forming in the two doping types [78]. The observations in this work are consistent with those seen for GaAs substrates.

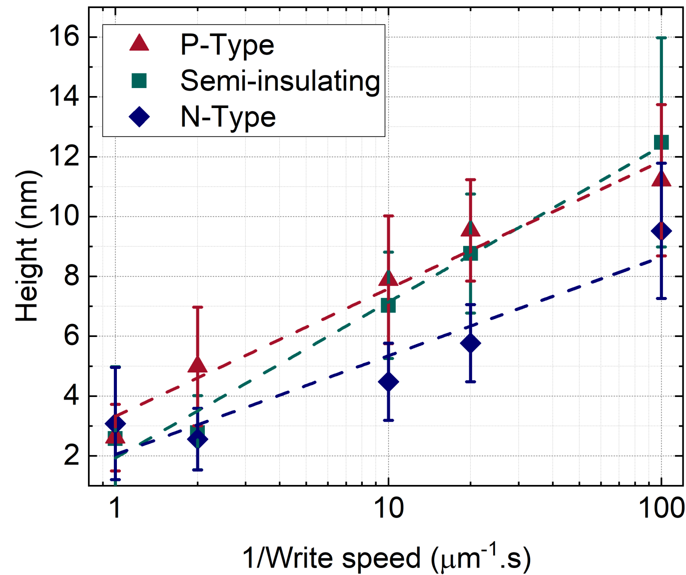

Figure 4-10. Oxide lines fabricated by scanning the AFM tip across p-type, semi-insulating, and n-type InP while varying the tip write speed. The gradient of each line is equal to $1/h_1$.

Models that describe the growth kinetics of LAO oxides formed on semiconductor surfaces are often based upon or adapted from the Cabrera-Mott model [75]. In this section such a model is used to calculate the activation energy for semi-insulating InP, which was

developed by Stiévenard *et al* [76]. The following growth rate equation is used

$$\frac{\delta h}{\delta t} = u\; exp\left(\frac{h_1}{h}\right) \tag{4.2}$$

where h is the height of an oxide, t is time, u is a rate constant, and h_1 is described in the following manner:

$$h_1 = \frac{qaV}{kT} \tag{4.3}$$

where q is the charge of an electron, a is half the width between reactive sites on the lattice, V is the tip voltage, k is Boltzmann's constant and T is temperature. To find h_1 experimentally the following equation is used

$$\frac{1}{h} = \frac{1}{h_1}\; log\nu + \frac{1}{h_1}\; log\frac{h_L^2}{h_1 u W_{ox}} \tag{4.4}$$

where ν is the tip write speed, h_L^2 is the square of the maximum oxide height possible, and W_{ox} is the full width half maximum diameter of an oxide. At a constant tip write speed the rate constant, u can be found in the following manner

$$h = \frac{\frac{qa}{kT}}{log\;(\frac{h_L^2 \nu kT}{u W_{ox} qa}) - log\; V}\; V \tag{4.5}$$

which allows the activation energy, W to be calculated

$$u = u_o\; exp\; \frac{-W}{kT} \tag{4.6}$$

where u_o is in the order of 10^4 cm/s.

The graph of *1/h* as a function of *logv* for a range of tip biases is shown in Figure 4-11. The oxidations were carried out at 18 °C.

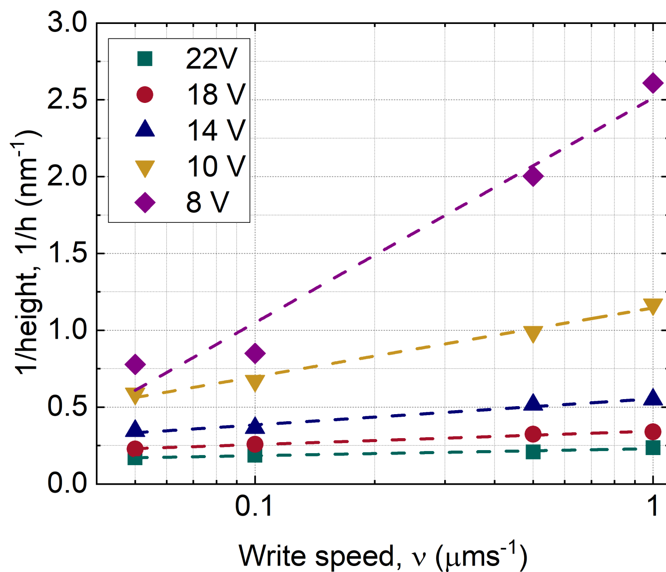

Figure 4-11. A plot of log tip write speed against 1/oxide line height shows a linear fit for each voltage.

The slope of each line in Figure 4-11 was found and using equation 4.4, h_1 was found for each voltage. A graph of h_1 against V is shown in Figure 4-12. The slope was found to be 1.46 nm/V, this allows a to be calculated for each voltage using equation 4.3.

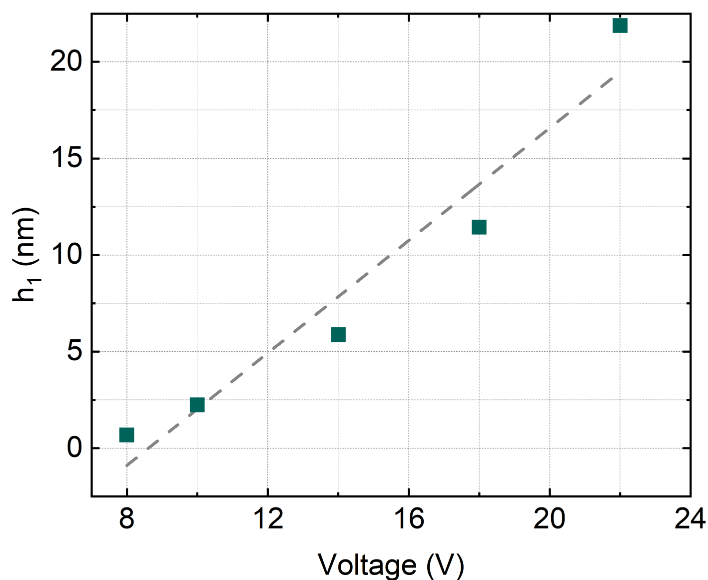

Figure 4-12. A plot of voltage against the slope of log write speed vs 1/height, where the gradient is equal to qaV/kT .

Next, by plotting a graph of h against V equation 4.5 can be solved to find u for each voltage. The graph is shown in Figure 4-13. The slope of V against h for tip write speed 0.1 μm/s was 0.300 V/nm. The mean slope of h/V for all write speeds was 0.301 V/nm $\pm$ 0.02 V/nm. Finally, this allows equation 4.6 to be solved for W.

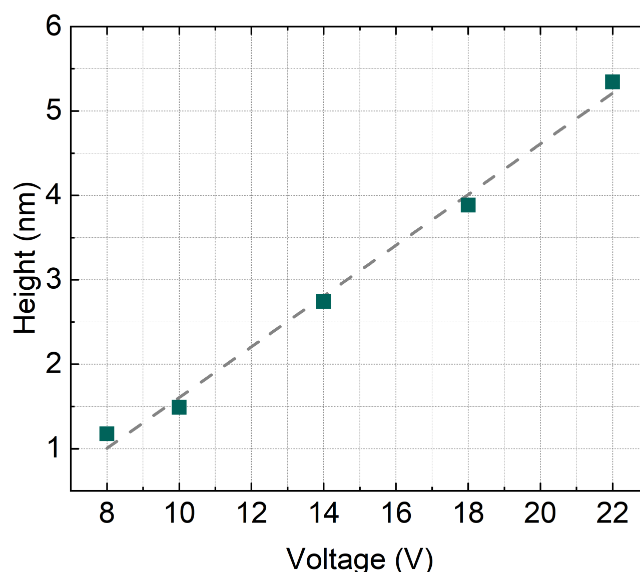

Figure 4-13. Voltage plotted against the mean height of each oxide line for a tip write speed of 0.1 μm/s.

The activation energy, W is then plotted as a function of voltage. A linear relationship between activation energy and voltage was observed, where the activation energy ranges from 0.39 eV for -8 V to 0.46 eV for -22 V. The increase in activation energy as tip bias was increased implies that more energy was required at higher tip voltages, however the difference between lowest and highest voltages was relatively small at 0.06 eV. The small increase could be explained through build-up of some point charge. Stiévenard *et al.* applied their model to several literature works and calculated results for the activation energy of silicon to be between 0.1 and 0.4 eV [191–193]. Variation can be explained due to differences in set-up and experimental parameters, such as temperature. Červenka *et al.* reported activation energies for GaAs, using the same method of calculation, of 0.05 eV for -6 V and 0.02 eV for -8 V [77]. This work has shown that the activation energy for LAO of InP is similar to that required for silicon oxidation.

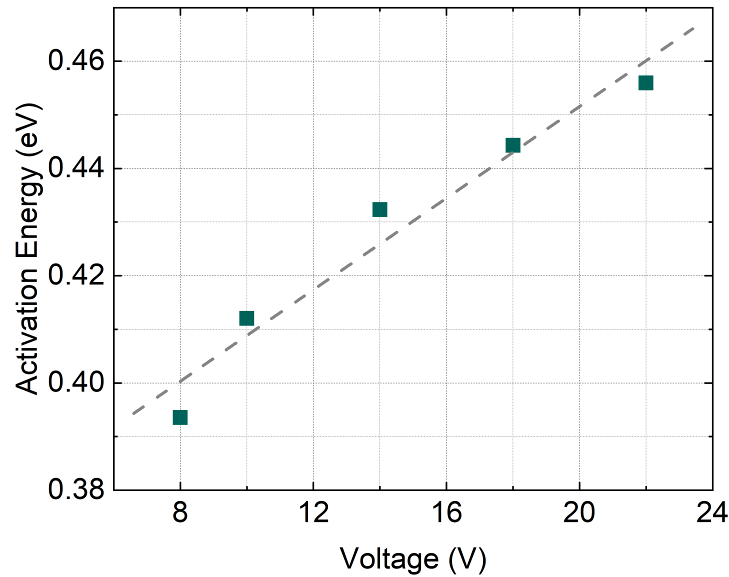

Figure 4-14. Activation energy for LAO of semi-insulating InP as a function of applied tip voltage at a write speed of 0.1 μm/s.

4.4 Device simulation

The next section will introduce an alternative application for LAO fabricated nano-features, that being altering, or tuning, the resonant frequency of a PCC. A tuning shift of up to 2 nm has been reported for a GaAs PCC, which was resonant at around 900 nm [194]. Oxides were fabricated on the cavity using a LAO technique. Due to the refractive index difference between the GaAs slab and GaAs oxide, there was a change in the near field geometry and a slight change in cavity volume due to the growth of the oxide above the surface. The oxides were reported to be 4 nm high and were fabricated at positions designed to overlap with areas of high field strength. It was reported that a small amount of tuning could be produced by fabricating oxides that interacted with a portion of the cavity mode, and more complicated oxide designs that overlapped with a larger proportion of the mode yielded the greatest tuning values, as is shown in Figure 4-15. This work seeks to use investigate the tuning range that can be achieved using an InP PCC via FDTD simulation.

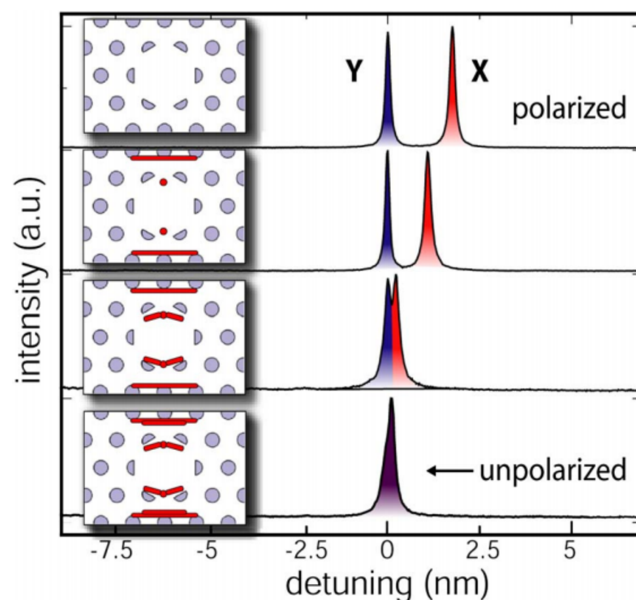

Figure 4-15. The tuning of the PCC X mode with respect to Y mode as a function of the LAO fabricated oxide design. Reprinted from 'Tuning photonic nanocavities by atomic force microscope nano-oxidation', *Applied Physics Letters*, K. Hennessy *et al.*, **89**, 041118, (2006), with the permission of AIP Publishing .

To investigate LAO tuning of an InP PCC, a H1 cavity was designed using Lumerical FDTD simulation to have a resonant frequency of 1550 nm. The basic cavity design and the simulations and device parameters are discussed in Chapter 3. Due to the increased surface roughness of the oxide it is desirable for the QD to be as far from the fabrication interface as possible. To this end, the cavity was optimised using a 380 nm InP slab. A cavity design with large radius air holes was used as this reduces fabrication challenges and means any deviations in hole size have less of an impact on the cavity mode. A side view of the cavity is shown in Figure 4-16.

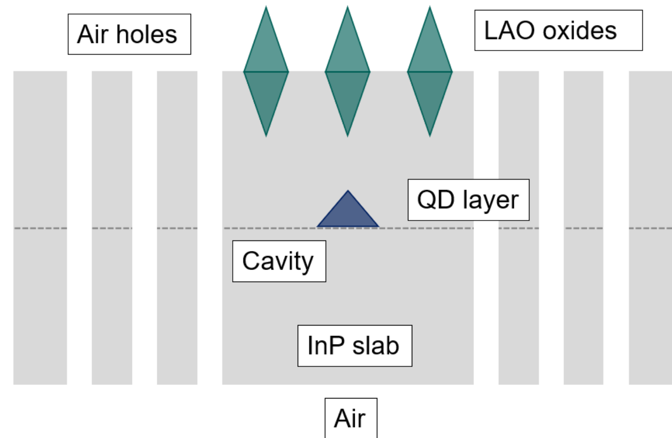

Figure 4-16. A side view of the H1 cavity layout for LAO oxide tuning experiments.

The initial PCC design 'optimisation A' and wavelength corrected design 'optimisation B', which have the same a to r ratios and are simply scaled in size Q factors and resonant frequencies were found and are shown in Figure 4-17 as a function of the slab depth. The periodicity, a hole radius r, and slab thickness t were optimised for telecom wavelength resonance. Figure 4-17 (a) shows that for the initial optimisation A, the highest Q factor (20 200) was observed at a thickness of 420 nm. However, the cavity mode was at 1667 nm for the design at that slab depth. By using the slope of optimisation A in Figure 4-17 (b), new values for a and r that would give an optimised Q at 1550 nm were found. These new values produced the radius and periodicity values for optimisation B. A slab thickness of 380 nm was shown to give an optimised Q factor (19 600), which intersected with a cavity mode of 1550 nm. This optimised cavity geometry will be used to demonstrate cavity tuning.

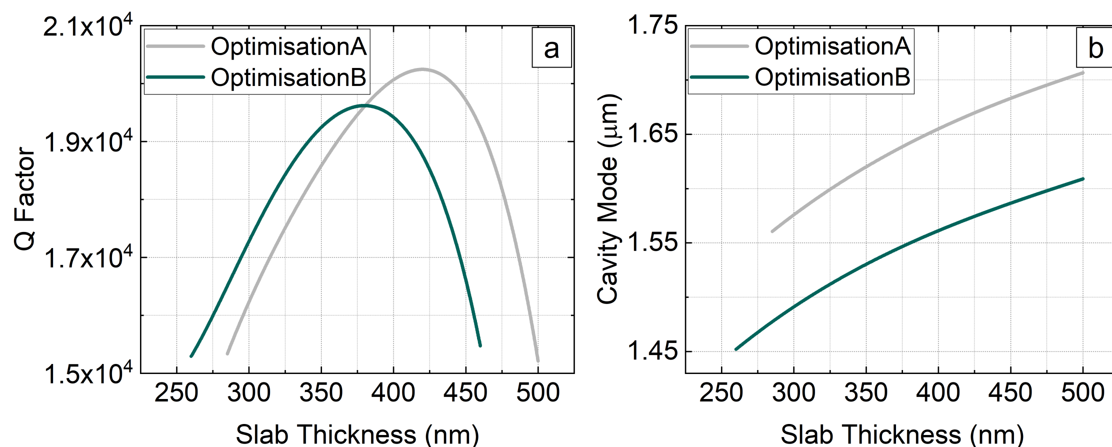

Figure 4-17. Using 3D FDTD simulation the relationship between (a) the slab depth and Q factor and (b) slab depth and cavity mode was found for two H1 PCC designs, optimsation A and optimisation B.

4.5 Cavity tuning

If a QD is to efficiently couple to the cavity the QD must emit light of a wavelength that is in resonance with the mode. This means that its emission wavelength must be as close to the resonant frequency of the cavity as possible. Therefore, QD growth is tuned so that there will be good coupling to the cavity system. However, small fabrication imperfections easily lead to a shift in the resonant frequency of the cavity and often only a percentage of grown QDs will be precisely at the engineered wavelength. To overcome these issues, methods of tuning the QD into resonance with the cavity have been reported, such as atomic layer deposition and laser tuning of QDs [135,195], or QCSE tuning [30]. The LAO method instead tunes the cavity resonance. An advantage of the LAO tuning method is that each cavity can be tuned individually under ambient conditions, with the possibility of in-situ measurement and near field visualisation being demonstrated [196].

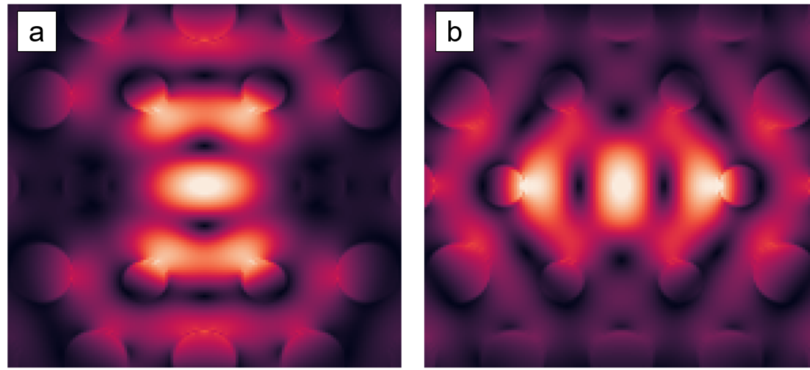

Figure 4-18. Electric field profiles for modes generated using an (a) E_x and (b) E_y dipole source in FDTD simulation, where a lighter colour indicated a larger field strength.

Figure 4-18 shows the mode profile generated from a x-dipole (a) and y-dipole (b) source. To investigate the placement of the oxide with regards to the mode for each dipole orientation, oxide designs in Figure 4-19 (b) to (h) (E_x and E_y) were simulated, where either oxide mounds or oxide lines were used. The patterns were designed with the aim of overlapping strongly with either the x-dipole (E_x) or y-dipole (E_y) mode, or with both, so to investigate the independent or combined tuning of both cavity modes. Additionally, the effect on the Q factor of the cavity will be calculated, as this has yet to be discussed in the literature.

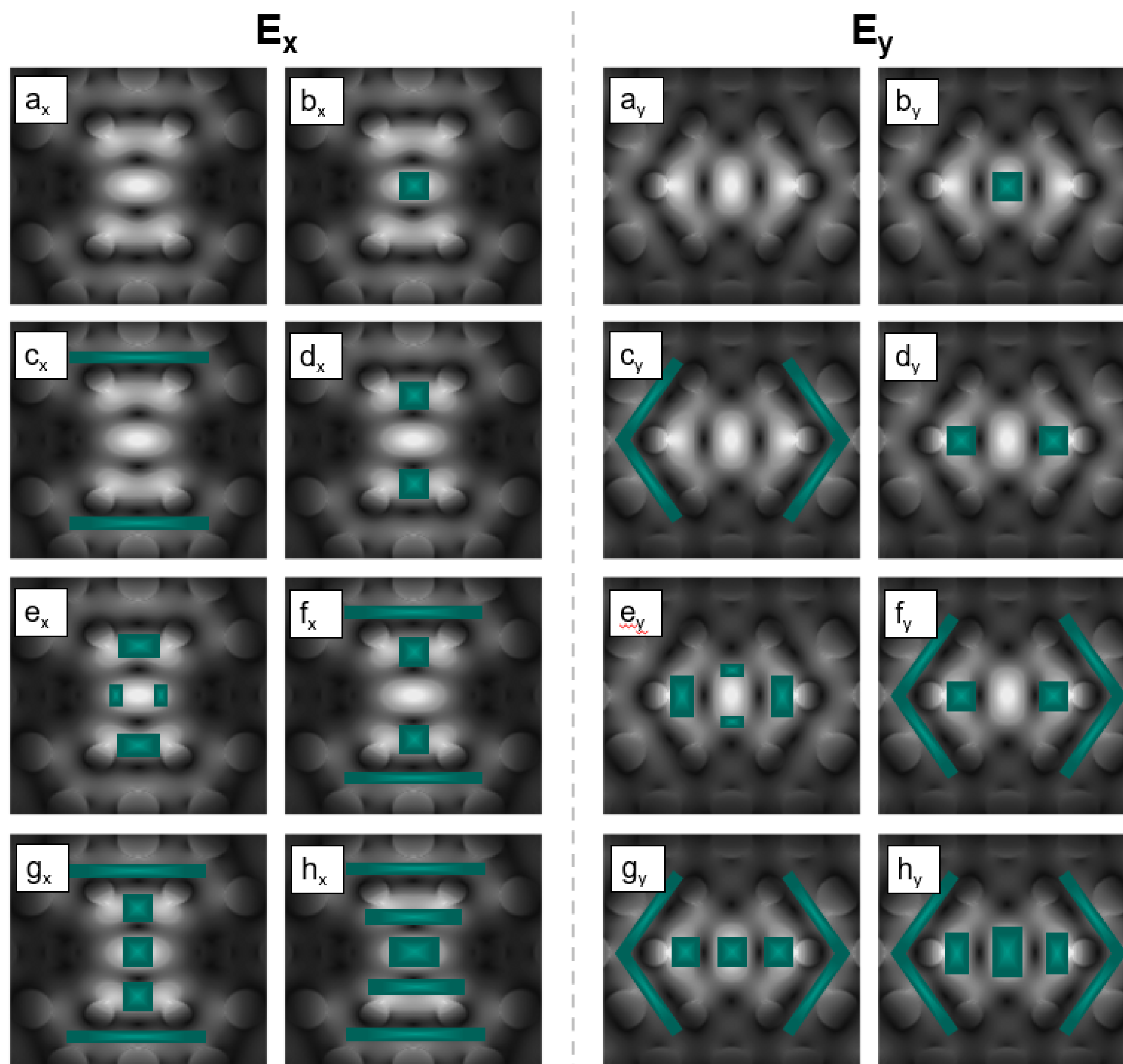

Figure 4-19. LAO oxide structure representations (a_x) to (h_x), indicated in green, optimised to overlap with the E_x mode and structures (a_y) to (h_y) optimised to overlap with the E_y mode. Oxides are simulated as areas of lower refractive index compared to the InP slab.

Figure 4-20 shows the shift in the cavity resonance (a) and Q factor (b) for oxide patterns a_x to h_x, which were in general designed to overlap more strongly with the E_x mode. For each structure, the E_x and E_y mode was simulated. The resonant frequency of the cavity was altered by differing amounts depending upon the oxide pattern simulated. For pattern b_x, the modes were both tuned by around 0.5 nm as the oxide pattern overlaped with both to a similar degree. However, for pattern d_x, the oxide overlapped strongly with the E_x mode only, therefore that mode was tuned by around 0.75 nm whilst the E_y mode showed almost no tuning. The largest tuning range was observed for pattern h_x, which had the

largest volume of oxide patterned, and demonstrated over 2 nm of tuning for the E_x mode and 1 nm for the E_y mode. The Q factor was variable, however remained reasonably high for all patterns and both modes.

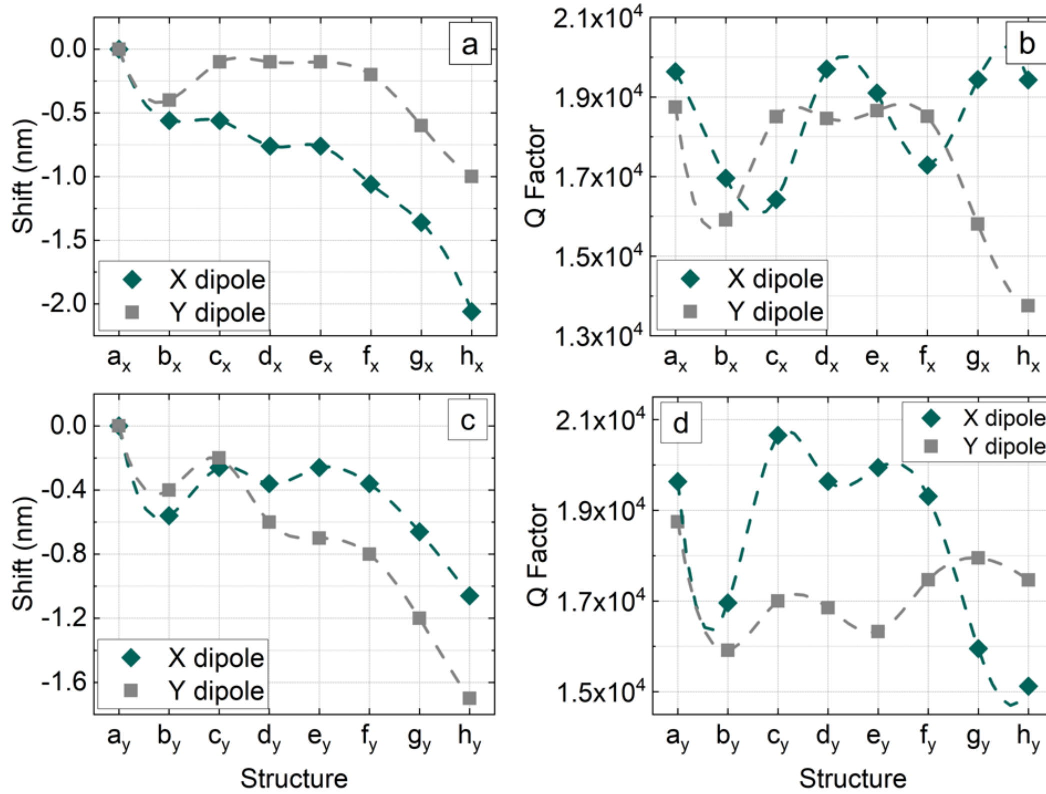

Figure 4-20. The relationship between structure type for structures (a_x) to (h_x) optimised for a E_x mode for X orientated and Y orientated dipoles and (a) the cavity mode shift and (b) Q factor and the relationship between structure type for structures (a_y) to (h_y) optimised for a E_y mode for X orientated and Y orientated dipoles and (c) the cavity mode shift and (d) Q factor.

The cavity tuning and Q factor were also calculated for structures a_y to h_y, which were optimised to overlap strongly with the E_y mode. Again, the simulation results are shown for both the E_x and E_y modes in Figure 4-20 (c) and (d). The behaviour in cavity tuning was very similar as that seen for structures a_x to h_x. The maximum tuning was again seen for the largest volume of oxide; however, the range was slightly smaller at around 1.6 nm for the E_y mode and 1.2 nm for the E_x mode. The Q factor again varied depending on the structure. However, in all cases the oxide patterns did not adversely affect the Q factor to a large degree.

Finally, the effect of change the oxide size is shown in Figure 4-21. The oxide structure h_x

was used and its size was varied between ± 10 nm above and below the InP surface to ± 50 nm above and below the InP surface. The shift in the cavity resonance and Q factor is shown for the E_x and E_y modes. Generally, the tuning range increased as the oxide size increased and the Q factor fell. A significant increase in shift was observed when the size was increased was 0 nm to 10 nm, however there was a plateau from 20 nm to 30 nm, before the shift again increased. The maximum simulated shift was – 5 nm. The largest oxides produced experimentally were around ± 20 nm above and below the InP surface. This means to improve the tuning range a method for increasing the oxide size could be sought, such as pulsing the tip bias to reduce the build-up of charge or increasing the experiment temperature. It was observed that for the mode that the oxide was designed to overlap with (E_x), the drop in Q factor was not large. However, there was a significant decrease in the Q factor for the degenerate mode.

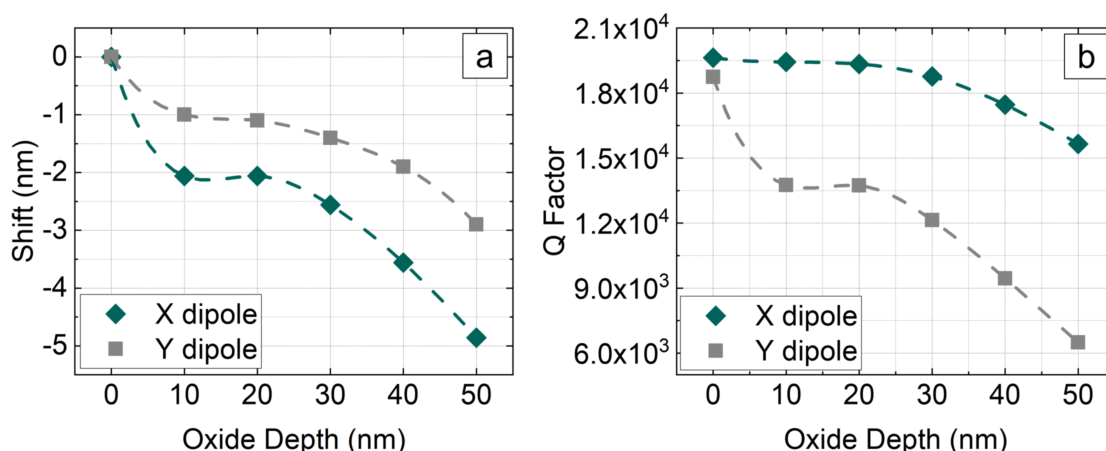

Figure 4-21. The relationship between structure size for structure (hX) optimised for a E_x mode for X orientated and Y orientated dipoles and (a) the cavity mode shift and (b) Q factor. Oxide size varies between ± 10 nm above and below the InP surface and ± 50 nm.

4.6 SUMMARY

In summary, deep and reproducible nanoholes, with maximum mean depths of 15.6 ± 1.2 nm have been fabricated using LAO on InP substrates. The dimensions of the nanoholes were controlled via applied tip bias and humidity. The deep nature of the nanoholes will allow re-growth of thicker epitaxial layers, which should assist in reducing QD linewidths.

The nanoholes were very well defined in shape, which would help maintain QD spectral homogeneity. Additionally, the nanohole arrays were highly regularly positioned. Initial site-controlled droplet epitaxy experiments showed excellent site-control of the droplets. However, further work is required to optimise droplet size and density. Due to Covid-19 restrictions experimental continuation of this work was not possible. LAO was demonstrated on n-type, p-type, and semi-insulating InP, with a faster growth rate associated with p-type substrates compared to n-type substrates. The semi-insulating InP and p-type growth rates were comparable. The kinetics of LAO were investigated for semi-insulating substrates and the activation energy for LAO was found to be ~ 0.4 eV. Finally, 3D FDTD was used to demonstrate the tuning of a H1 PCC with a resonant mode at 1550 nm. For oxide sizes in the range that were achieved experimentally, maximum tuning was ~ 2 nm. LAO has been demonstrated to be a simple fabrication method for the production of regular, high quality nanohole arrays, without the need for organic EBL resists. However, the method is slow and alignment marks for device fabrication cannot be produced. Therefore, the method is suitable for fabrication of small arrays, but not fully scalable systems e.g. a 30×30 array of oxides with a pitch of 2.4 μm would take around 3 hours to write. For comparison, an array of this type would take seconds to pattern using EBL. The process could be made more scalable by improving the technology, e.g., by using an AFM probe with multiple tips so more nano-oxides could be fabricated at once [197].

This page intentionally left blank

5 Nanohole Fabrication: EBL and ICP-RIE

Fabrication of nanohole arrays for the site-control of QDs has been achieved using the highly scalable EBL and ICP-RIE method. As discussed in Chapter 2, literature reports have shown that nanohole diameter and depth can control QD properties, such as emission wavelength and occupancy. This chapter will present the development of a nanohole array fabrication method using EBL and ICP-RIE on a GaAs substrate, including an ex-situ cleaning method. The remainder of this thesis will focus on the use of an InAs/GaAs material system, which as outliner in Table 2.1 typically produces SCQDs with emission wavelengths between 920 nm and 1020 nm. Specifically, this work aims to develop processing and growth methods to produce SCQDs that emit between 900 nm and 1000 nm. These wavelengths are suitable for fundamental physics experiments of the type performed in the group. Additionally, it allows samples to be characterised using the available silicon CCD detectors, which have a detection cutoff of around 1000 nm. The research outcomes that come from developing SCQD growth using these materials can be adapted and applied to a system more suitable for telecom communication wavelengths, such as InAs/InP. A range of nanohole diameters and depths were fabricated. In addition, alignment marks suitable for characterisation and fabrication re-alignment were designed and produced. The regularity of the nanohole arrays was tested against simulated devices to show the highly accurate nature of the fabrication method. Finally, some initial SCQD growths will be presented. A summary of the requirements the nanohole arrays and alignment marks must meet is as follows:

- Controllable diameter, depth, and pitch.

- Good reproducibility for nanohole diameter and depth across the arrays.

- Nanoholes within an array must be regularly positioned.
- Suitability for incorporation single mode photonic devices must be considered.
- Alignment marks and labels must be fit for purpose i.e.
    1. allow each QD across the sample to be easily located in AFM and PL
    2. be of a suitable spacing and size for the PL camera's field of view
    3. be deep enough that they will be clearly visible after re-growth and when covered in resist for subsequent device fabrication.

5.1 Development: Electron beam lithography

An initial EBL pattern was designed to benchmark the effects of drawn size and dose and to test ex-situ cleaning methods. Arrays of nanoholes were drawn inside a grid of boxes, which acted as alignment marks, as seen in Figure 5-1. Each column of the pattern (B to N) changed in dose from 0.6 to 5.8 times the base dose 240 $\mu C/cm^2$. Nanohole drawn size increased for each row (2 to 11) from 10 nm to 100 nm diameter. Each array of nanoholes had a pitch of 0.75 μm and was 150 $\times$ 150 μm in size. The box around each array was 500 $\times$ 500 μm, meaning the space between the array and each individual box was 175 μm. The run time for each pattern was 54 minutes.

This EBL pattern was used to test initial etch parameters and their suitability for SCQD growth. A number of issues were found with the pattern. Firstly, the arrays and alignment boxes were found to be very large compared to the field of view of the μPL set-up. This was a particular issue if using a solid immersion lens (SIL) during PL measurements, as only one array could be characterised at once. To characterise another area, the cryostat was vented and the SIL moved to a new position. This problem was exacerbated by the low number of labels and their distance from some arrays. Additionally, it was decided that there were a large number of array parameters that produced nanoholes much too large in diameter to be suitable for the site-control of the QDs.

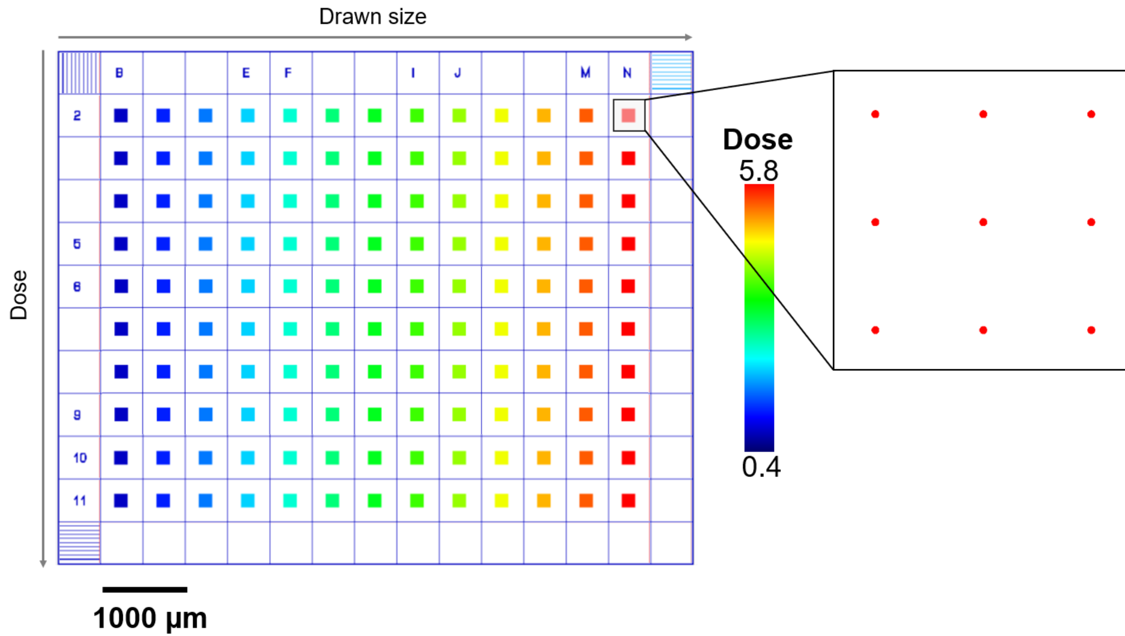

Figure 5-1. EBL 'pattern 1'. Each coloured square is an array of nanoholes where dose and drawn size is varied in x and y respectively. The grid of boxes are alignment marks.

A new pattern was designed with the aim of solving these problems. All subsequent patterns (2 to 5) were slight adjustments of the new pattern design, as further data and information became available from SCQD growths. Pattern 5 is shown in Figure 5-2 and all patterns can be found in Appendix A. The parameter differences for patterns 2 to 5 are shown in Table 5.1. A dedicated area for LAO patterning was introduced once SCQD growth on LAO patterned GaAs commenced.

The layout of patterns 2 to 5 meant there was a significant reduction in overall pattern size, and pitch was introduced as a variable parameter. This eased characterisation via AFM and PL, that otherwise required movement across large areas. Additionally, the alignment marks in pattern 1 consisted of long lines surrounding arrays. This was found not to be necessary for alignment and increased patterning time. The patterning time was significantly reduced to 20 mins for a 6×6 grid of patterns. The introduction of the LAO area in pattern4, which consisted of alignment marks around an area designated for LAO fabrication allowed comparison between LAO and EBL fabricated nanoholes to be made.

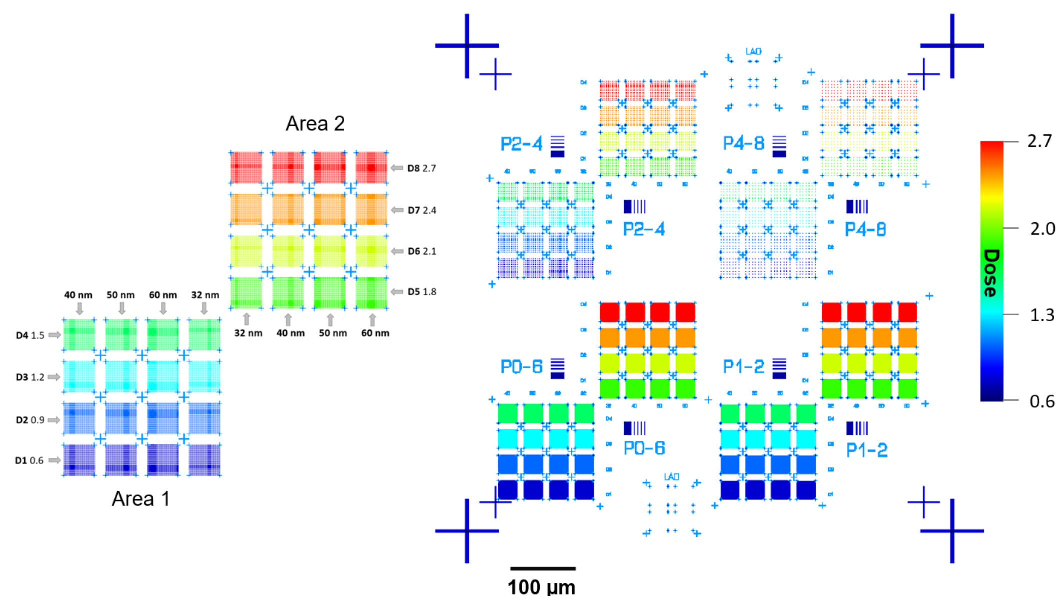

Figure 5-2. Layout of the updated EBL pattern, which for patterns 2 to 5 has the same basic layout (pattern 5 shown) with some minor adjustments between iterations. Each pattern consists of four quadrants, which are identical except pitch is varied. A blow up of the quadrant for 0.6 μm pitch (P0.6), is shown. Dose and drawn size are varied, for area 1 and area 2. Pattern 4 and 5 also include alignment crosses that mark out a designated area for local anodic oxidation patterning. Images of all patterns can be found in Appendix A.

Nanohole drawn size and applied dose was slightly altered between patterns, this allowed fine control over small nanoholes. The larger nanoholes formed in area 2 of Figure 5-2 were found to nucleate multiple QDs and are not discussed in detail in this chapter. A table with growth parameters and the EBL pattern used for all samples discussed in this work can be found in Appendix A.

Table 5.1. EBL dose and drawn size parameters for patterns 2 to 5, where pitch is varied for the four quadrant.

Pattern	**Area 1**								**Area 2**								LAO Region
	Drawn size (nm)				Dose				Drawn size (nm)				Dose				
					D1	D2	D3	D4					D5	D6	D7	D8	
2	40	50	60	70	0.6	0.9	1.2	1.5	40	50	60	70	1.0	2.6	4.2	5.8	No
3	32	40	50	60	0.6	0.9	1.2	1.5	40	50	60	70	1.0	2.6	4.2	5.8	No
4	32	40	50	60	0.6	0.9	1.2	1.5	40	50	60	70	1.0	2.6	4.2	5.8	Yes
5	32	40	50	60	0.6	0.9	1.2	1.5	32	40	50	60	1.8	2.1	2.4	2.7	Yes

5.2 Development: Etching of nanofeatures

Initially, a $SiCl_4$ and Ar etch was investigated as these gasses were reported in the literature to be suitable for processing GaAs [115]. Figure 5-3 (a) shows the effect of changing RF power on the etch rate, measured using reflectivity with a AlGaAs/GaAs wafer chip, while using 5 sccm of $SiCl_4$ and 0 sccm of Ar. The reflectivity measurement gave the bulk etch rate rather than the nanohole etch rate, which was around 7 times slower for ICP1, due to competition between the incoming etching ions and etch products. Figure 5-3 (b) shows the etch rate as a function of Ar flow under constant $SiCl_4$ flow of 5 sccm. These slow etch rates were suitable for fabricating very shallow nanoholes however, the $SiCl_4$ gas flow was found to be unstable due to the ICP-RIE configuration. This would affect nanohole fabrication, in particular as the holes are so shallow that small differences in depth could have a large impact on growth experiments. Therefore, it was decided to move to using an Ar/Cl_2 mixture, which was more stable.

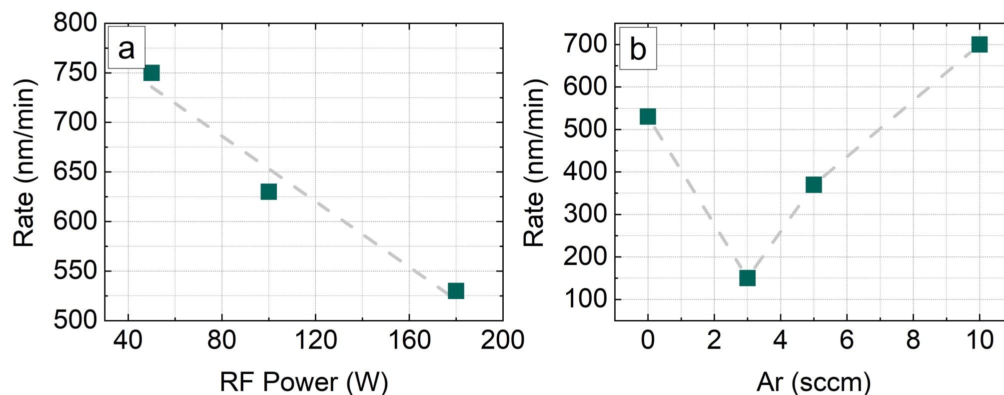

Figure 5-3. Etch rate measured for a $SiCl_4$ and Ar recipe using reflectivity to measure the rate, while varying (a) RF power and (b) argon flow.

Etch rates for a range of ICP-RIE recipes were investigated and are shown in Table 5.2. The etch rates were established using a reflectivity measurement. ICP1 etch: 1 was a recipe already programmed on the machine. It was designed for etching of photonic crystals and produced a very fast etch rate of $\sim$ 800 nm/min. For ICP1 etches: 2 to 5 the RF power was reduced, causing a reduction in the ion energy. Additionally, the amount of Cl_2 in the etch gas mixture was reduced. These changes led to a significant reduction in the

reflectivity measured etch rate. Nanohole samples were then fabricated, and it was found that Etch ICP1: 2 produced very small and shallow nanoholes. The smallest nanoholes were measured to be 38.6 nm $\pm$ 2.7 nm in diameter and 10.2 nm $\pm$ 3.7 nm in depth. During the project a second ICP-RIE was installed (ICP2), due to alternating equipment downtime an etch recipe was also established on ICP2 and depending on equipment availability either ICP1 or ICP2 was used. The ICP2 recipe in Table 5.2 shows the final etch recipe for this machine.

Table 5.2. Etch rates measured for bulk samples using reflectivity for Ar/Cl_2 etch recipes. The etch rate for ICP2 was not measured and instead the nanohole etch rate was established, which is shown in Figure 5-6.

Etch #	Ar (sccm)	Cl_2 (sccm)	RF Power (W)	ICP Power (W)	DC Bias (V)	Rate (nm/min)
ICP1: 1	10	20	200	300	500	800
ICP1: 2	20	5	100	300	350	190
ICP1: 3	25	5	100	300	350	190
ICP1: 4	12	3	100	300	350	170
ICP1: 5	15	10	100	300	350	170
ICP2	25	2	48	240	150	NA

Before the final recipe was established for ICP2, the effect of altering gas mixtures on nanohole depth and diameter was investigated. The mean nanohole depths and diameters as a function of Ar flow are shown in Figure 5-4 (a) and (b) respectively. The general effect of increasing Ar flow was to increase nanohole depth and decrease nanohole diameter, while an increased Cl_2 flow caused an increase in both nanohole depth and diameter. The increase in diameter when a larger amount of Cl_2 was used was explained by it anisotropically etching the semiconductor via a chemical reaction, whilst the Ar gas could not underetch the resist in this manner as it is a bombardment ion. The decrease in nanohole diameter seen when Ar flow was increased could be attributed to the high plasma density inhibiting removal of etch products, which effectively slowed the etch. The gas mixtures chosen for ICP2 etching were 25 sccm and 2 sccm, as a good balance between slow vertical etching and maintaining narrow nanohole diameters was achieved.

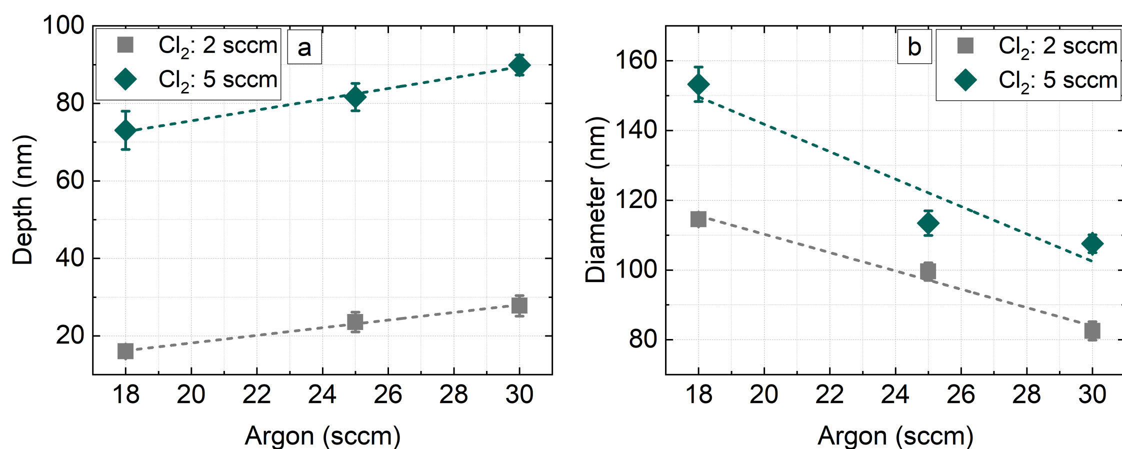

Figure 5-4. The relationship between Ar flow and (a) nanohole depth and (b) nanohole doammeter is shown for Cl_2 flows of 2 sccm and 5 sccm. Samples were fabricated using ICP2 with a RF power of 48 W, ICP power of 240 W, and an etch time of 25 secs.

The effect of varying EBL drawn size and dose was investigated for ICP1 and ICP2, using pattern 3 and pattern 2 respectively. This allowed a comparison to be made between the machines. Figure 5-5 (a) shows the nanohole etch depths for ICP1 (EtchA) and ICP2 (EtchB). In both cases it can be seen that there was an increase in etch depth with drawn size, with a linear dependency. EtchA gave a slightly faster etch rate meaning that to achieve the same nanohole depth on ICP2 etching time should be slightly increased, on average nanoholes were 6.8 nm deeper for doses 2 to 4. Figure 5-5 (b) also shows a general increase in nanohole diameter for etch A and B as drawn size increased, again with a linear dependency. Diameters were similar for both etches with ICP2 producing slightly wider nanoholes, which were on average 8.5 nm larger for doses 2 to 4. This was expected as the etch predominantly affects the nanohole depth. These results demonstrate good reproducibility on both systems and allow nanoholes of various dimensions to be fabricated. Therefore, the effect of growing QDs in nanoholes that range in size can be investigated.

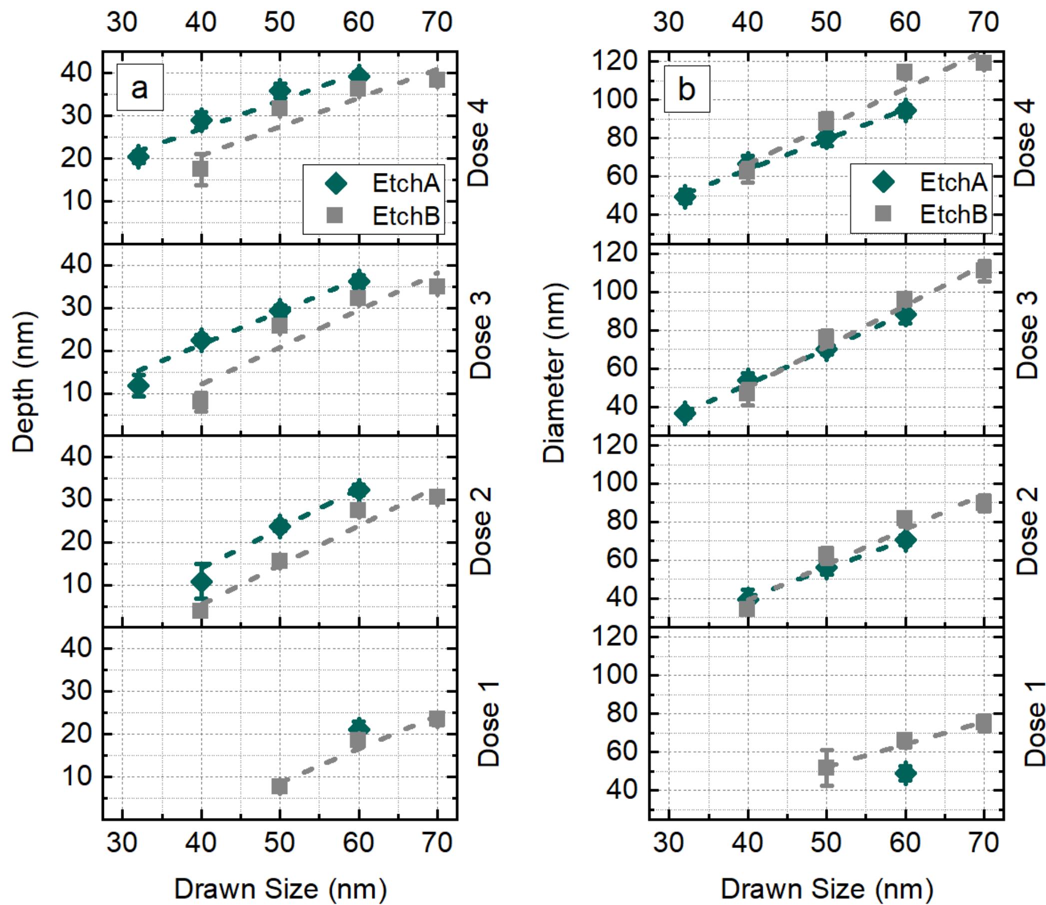

Figure 5-5. The effect of EBL dose and drawn size on (a) nanohole depth and (b) nanohole diameter, using the standard etch developed for ICP1 (ICP1:2) for 'EtchA' and ICP2 standard etch for 'EtchB', where samples were patterned using EBL pattern 2 and 3 respectively and etched for 40 s.

The nanohole depth dependency on etch time was established by fabricating six samples whilst varying the time used for each sample. All other parameters were kept constant. Times of 10 s to 60 s were investigated, with results being shown in Figure 5-6. Firstly, in (a) it can be seen that the nanohole depth and diameter were coupled, meaning that as nanohole diameter increased so did nanohole depth. Secondly, the nanohole depth increased as etch time increased, while diameter stayed roughly constant. In (b) a linear dependency between etch time and nanohole depth was observed. An outlying data point was associated with a 50 s etch and was discounted from the fit calculation, which could be explained by machine instability. This experiment shows that by changing the etch time the depth of nanoholes can be controlled somewhat independently of the nanohole diameter.

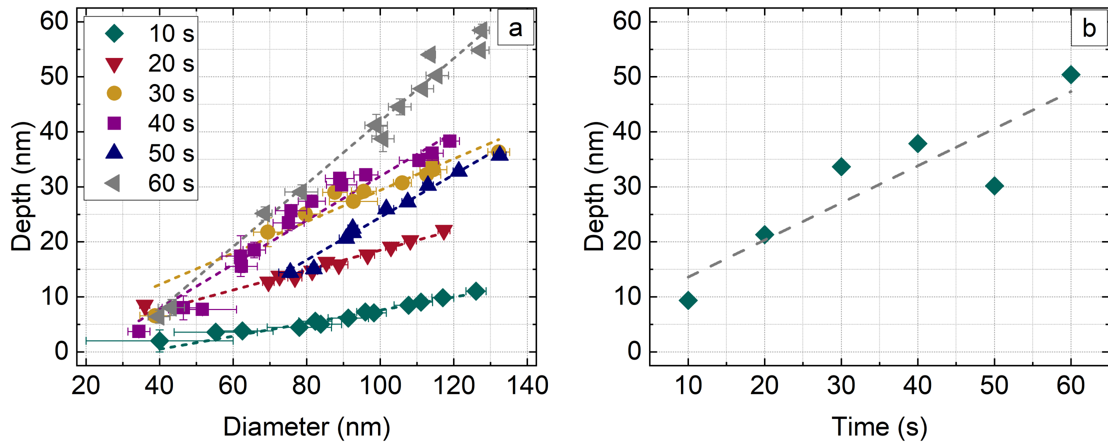

Figure 5-6. The relationship between (a) nanohole diameter and depth while varying etch time and (b) nanohole depth as a function of etch time for samples fabricated using EBL pattern 3 and ICP2.

Figure 5-7 shows the diameter and depth relationship for nano- and micro-sized features, which become de-coupled once features are above $\sim$ 500 nm in diameter for ICP1 and $\sim$ 300 nm in diameter for ICP2. This behaviour is useful as it means alignment marks, which are wider than nanoholes are deeper and so more visible during characterisation.

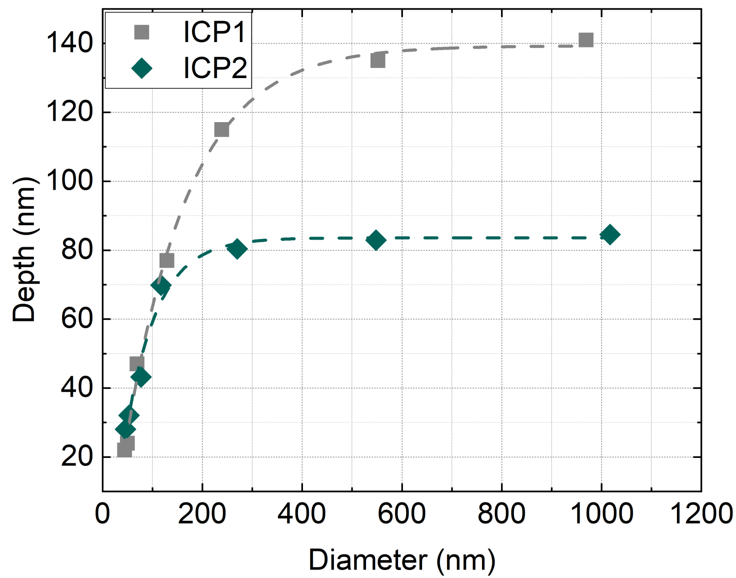

Figure 5-7. The relationship between diameter and depth for nano- to micro-sized lines, fabricated using ICP1 and ICP2 and etched for 60 s.

5.3 Development: Ex-situ cleaning

By aiming to produce a surface free from organic resist and other contaminants linewidth broadening caused by these species acting as charge traps may be reduced. This behaviour can be mitigated to some extent through the use of a re-growth buffer layer, meaning that the QD is grown some distance from the fabrication interface. The ex-situ cleaning process is not only necessary to maintain high sample quality, but it also reduces contamination of the growth chamber. To check the surface cleanliness ex-situ characterisation methods were first used. These were AFM and Nomarski microscopy, the in-situ characterisation method SIMS will be discussed in Chapter 6. An example of a Nomarski image of a clean sample (pattern 2) is shown in Figure 5-8. However, only gross contamination can be seen by such a method and samples which appear clean initially can be dirty when characterised via AFM.

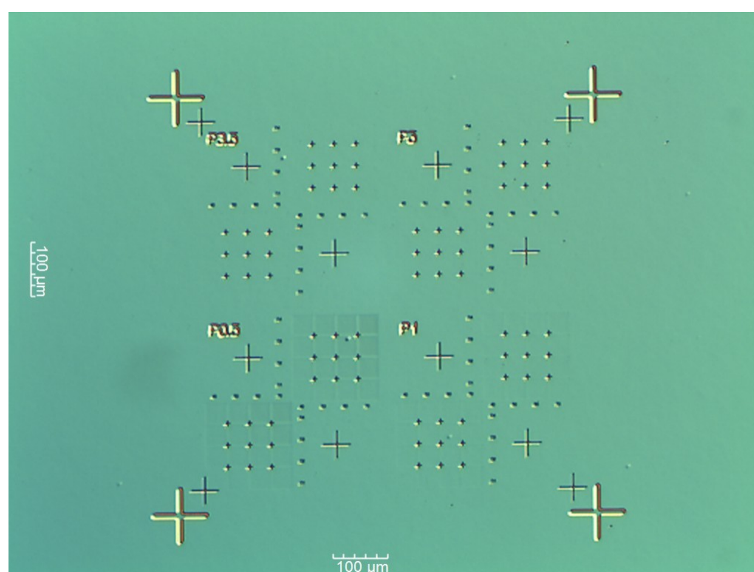

Figure 5-8. A Nomarski microscope image of a resist free epiready GaAs substrate patterned using EBL pattern2 and ICP1.

A cleaning procedure was developed with the aim of producing a surface with the same properties as before fabrication, that is free of contaminants and of low roughness. Figure 5-9 (a) is an AFM image of an epiready GaAs surface, which underwent no processing. Some minimal roughness was seen due to polishing marks, with a RMS value of 0.474 nm. A series of cleaning recipes were tested with the outcome of each attempt being shown in

Figure 5-9. The processes used for each sample are shown in Table 5.3. For samples (b) and (d), hardened material was observed on the flat surface and residue was left around the nanoholes. While, for (c) hardened material was present on the flat surface only and for (e) round the nanoholes only. The process used to clean sample (f) successfully removed all contamination from the flat surface and from around the nanoholes.

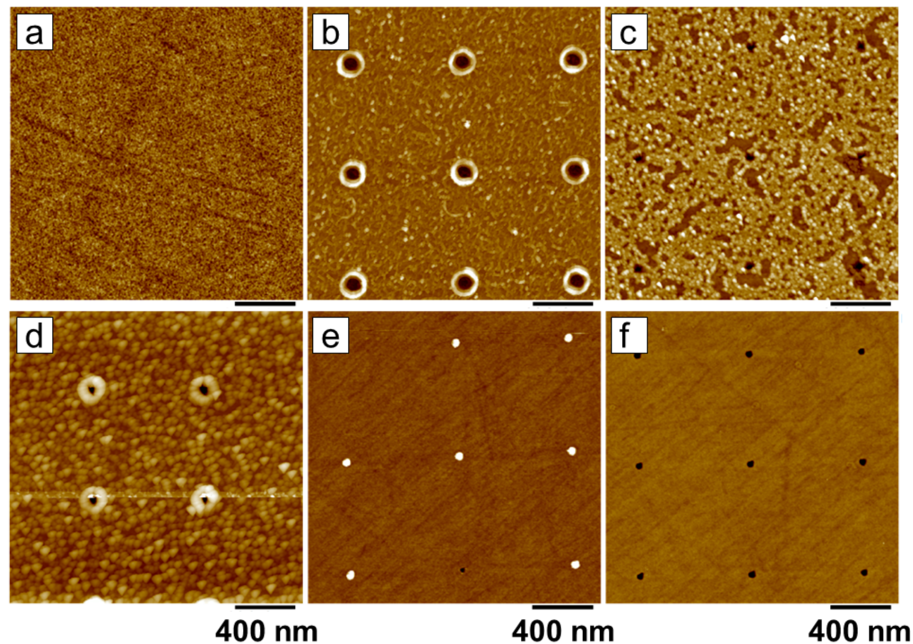

Figure 5-9. AFM images of (a) an uprocessed epiready GaAs substrate and (b) to (f) nanohole patterned samples after undergoing the cleaning procedures outlined in Table 5.3.

The cleaning procedure for each sample is shown below.

Table 5.3. The steps used for cleaning tests of epiready GaAs samples (a) to (f).

Sample	Step 1	Step 2	Step 3	Step 4	Step 5
a	-	-	-	-	-
b	plasma ash	sonicate in propanone	sonicate in propan-2-ol	-	-
c	plasma ash	sonicate in propanone	sonicate in propan-2-ol	HCl dip	-
d	plasma ash	1165 stripper (NMP)	sonicate in propan-2-ol	HCl dip	-
e	1165 stripper (NMP)	sonicate in propan-2-ol	plasma ash	HCl dip	-
f	1165 stripper (NMP)	sonicate in propanone	sonicate in propan-2-ol	plasma ash	HCl dip

The cleaning process used in (f) produced a sample clean in appearance using AFM, with a RMS of 0.298 nm (the RMS value was collected from a single scan, discluding the

nanoholes). These tests were initially performed using 1×1 cm chips. However, the recipe was refined for use with 3 inch wafers, which required larger solvent volumes. The 1165 resist stripper was in all cases pre-heated before cleaning of the sample took place. The final cleaning method used with 3 inch wafers is as follows:

1. On a 100 °C hotplate heat the sample in 1165 stripper for 10 minutes
2. Sonicate for 10 minutes in 1165 stripper at 80 °C at a frequency of 37 kHz
3. On a 100 °C hotplate heat the sample in 1165 stripper for 10 minutes (fresh solvent)
4. Sonicate for 10 minutes in 1165 stripper at 80 °C at a frequency of 37 kHz
5. Sonicate for 3 minutes in 1165 stripper at 80 °C at a frequency of 80 kHz
6. Sonicate for 10 minutes in room temperature propanone, 37 kHz
7. Sonicate for 10 minutes in room temperature propan-2-ol, 37 kHz
8. Blow dry sample thoroughly with N_2 gas
9. Bake on hotplate for 1 minute to drive off remaining solvent
10. Oxygen plasma ash for 2 minutes
11. Dip for 3 minutes in 1:1 HCl/H_2O
12. Rinse for 1 minute in H_2O
13. Blow dry sample thoroughly with N_2 gas
14. Inspect the sample using an optical microscope

At this stage if the sample appeared clean it was checked using AFM. Samples that had small areas of resist remaining on the surface would undergo the whole process for a second time, which would be sufficient to fully clean the surface. Once the 3 inch wafer

was approved for growth, it would be cleaved into quarter pieces and a second HCl/H_2O dip would be performed immediately prior to loading into the load lock chamber of the MBE system.

Once a cleaning method was established on an epiready sample, the method was used on an epitaxial grown buffer to check that clear atomic steps were still visible post ex-situ cleaning. It can be seen from Figure 5-10 (a) that good quality atomic steps were visible. However, an intermittent issue was observed, in that some samples showed surface roughening and apparent etching around nanoholes, as shown in Figure 5-10 (b).

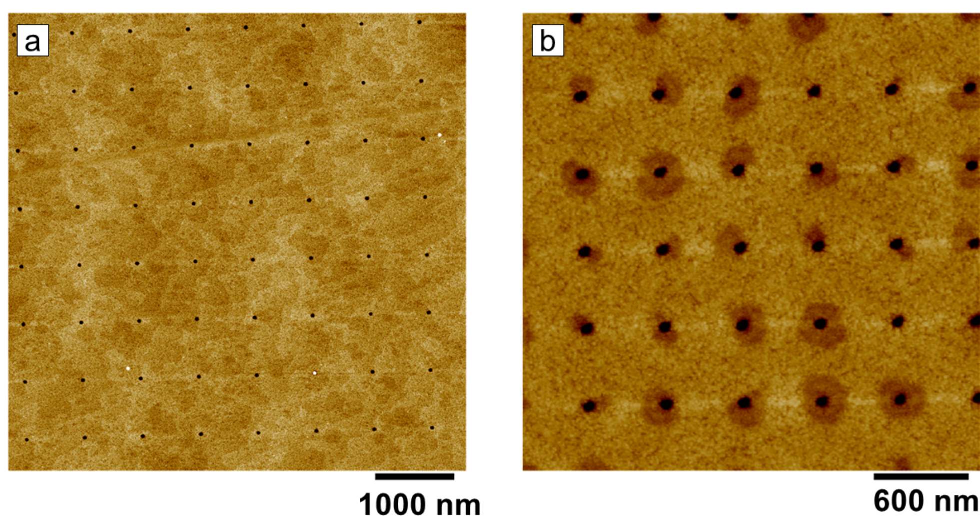

Figure 5-10. AFM images of samples after undergoing all cleaning steps excluding step 9, bake on hotplate showing (a) a smooth sample surface with very minimal levels of contamination and (b) a roughened sample surface.

It was ascertained that this behaviour occurred after the acid dip stage and was due to etching rather than contamination. HCl does not etch GaAs, therefore this etching was explained due to some propan-2-ol being left in nanoholes when the acid dip stage was conducted. Propan-2-ol and HCl form an alkyl chloride, where the Cl^- is free to react with GaAs and the enthalpy of re-formation of 2-chloropropane does not out complete that of enthalpy of formation of the etch products. When only HCl is present at temperatures below 500 °C, H^+ and Cl^- recombination is more energetically favourable than $GaCl_2$ or As_2 product formation [198]. Therefore, HCl can only etch GaAs at high temperatures,

however the mixture of HCl and propan-2-ol allows the etching mechanism to occur at room temperature. The reaction coordinate diagram for this is shown in Figure 5-11. The negative impact of this behaviour was overcome by heating the sample to 100 °C on a hotplate for 1 minute to drive off any remaining solvent prior to the acid dip (cleaning step 9).

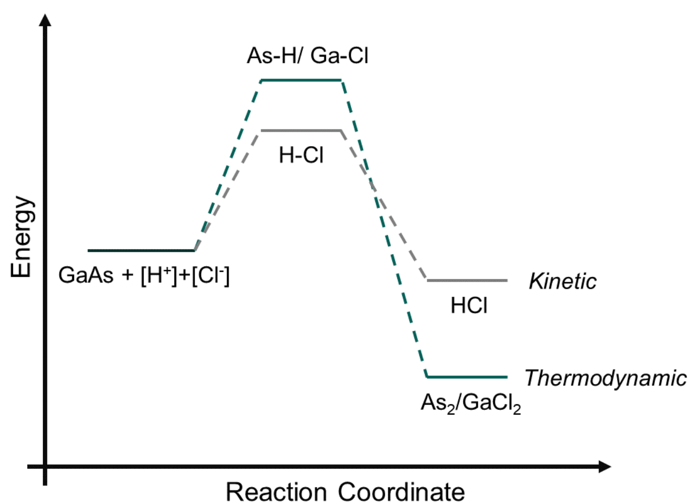

Figure 5-11. A reaction coordinate diagram (not to scale) showing the products when propan-2-ol and HCl mix (thermodynamic product) and without the presence of propan-2-ol (kinetic product).

5.4 Nanohole positioning accuracy

Characterisation of the regularity of the nanohole arrays will be discussed. A 10 $\times$10 μm AFM image was taken, which contained 169 nanoholes. Figure 5-12 shows the fitted x, y positions for the nanohole array and the coresponding ideal (generated) array.

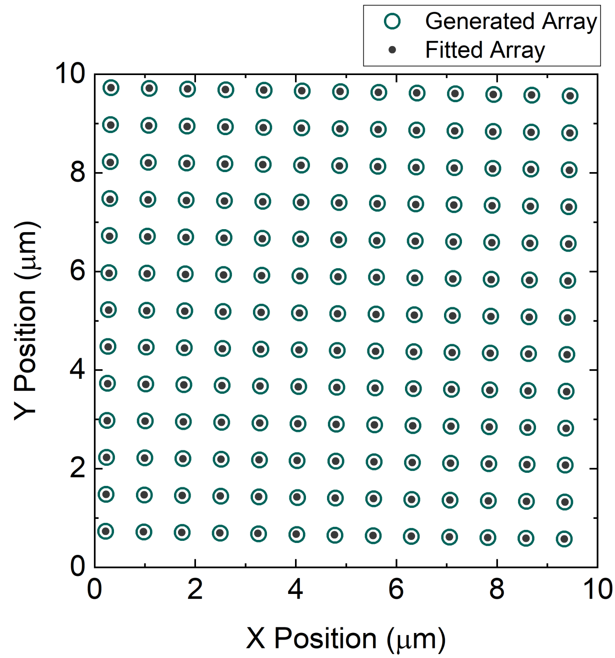

Figure 5-12. Position map marking the x, y coordinates of the fabricated nanoholes 'fitted array' and the x, y coordinates of an ideal array 'generated array' for a 10 x 10 μm AFM image, total of 169 nanoholes.

The offset between the fitted and generated arrays was then found to assess the degree of regularity in the fabricated array. A histogram of the offsets is shown in Figure 5-13. The mean offset across all 169 nanoholes was 8.5 nm $\pm$ 3.8 nm.

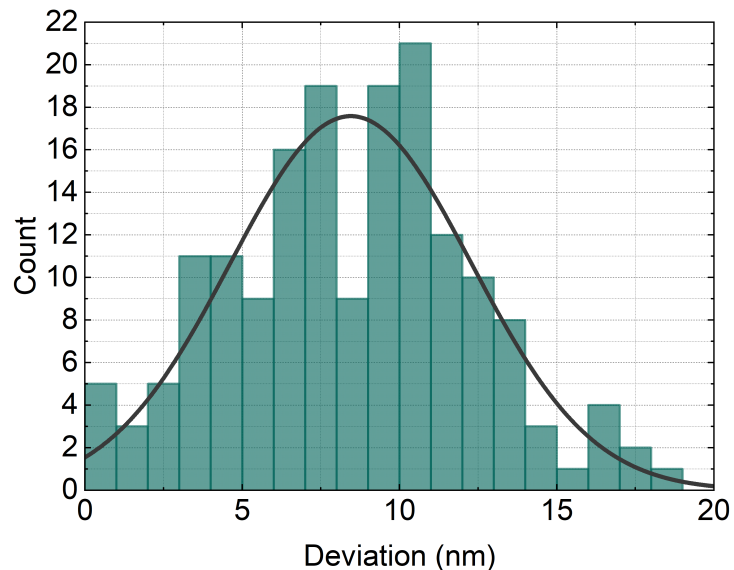

Figure 5-13. A histogram of the deviation in positions for the 169 nanoholes in Figure 5-12.

The distributions for the nanohole positioning regularity and nanohole diameters are im-

portant as they may affect a nucleated QD's position and size. Using 3 × 3 μm AFM images, histograms of nanohole diameter for dose 1, 2, 3 and 4 at 60 nm drawn size were plotted and are shown in Figure 5-14. The spread in diameters slightly reduced as dose increased, with the standard deviation in diameter being 2.55 nm, 2.18 nm, 1.56 nm and 1.47 nm for doses 1, 2, 3 and 4 respectively. Although this is a small change in deviation, it does show that to obtain the most reproducible nanohole arrays, it is preferable to use larger nanoholes. This trend is explained by the smallest nanoholes being produced at EBL doses that approach the 'dose to clear'. At this dose nanoholes can still be fabricated as the etch gases quickly remove the small amount of remaining resist, however any small deviation in smoothness of the resist surface, etch or EBL beam becomes more significant. In the literature it has been reported that the etch chemistry used to fabricate nanoholes not only affects the diameter and depth of the nanoholes but can also affect the deviation in nanohole sizes [199]. Additionally, it was shown that a wet chemical etch produced nanoholes of a more uniform diameter that nanoholes fabricated using identical EBL parameters in conjuncture with a dry etch. However, the nanoholes were widened due to anisotropy in the wetc chemical etch meaning that the narrowest nanoholes can be produced using a dry etch. The deviation in nanohole diameters using EBL and an ICP-RIE etch were very low and deemed suitable for the purpose of growing SCQDs. The impact of nanohole dimensions on QD size will be discussed in Chapter 7.

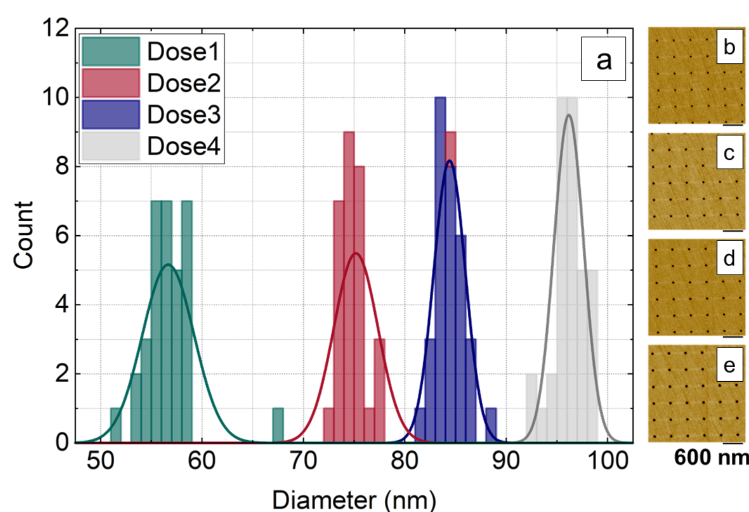

Figure 5-14. (a) Nanohole diameter distributions for arrays 60 nm drawn size, dose 1 to 4 etched using ICP2 with EBL pattern 3 for 25 s and corresponding AFM images for (b) dose 1 (c) dose 2 (d) dose 3 and (e) dose 4.

The positioning regularity of each nanohole array as a function of EBL dose is shown in Figure 5-15. The errors in positioning for x, y, and the total deviation are compared for doses 1 to 4 for 60 nm drawn size and are shown in Figure 5-15. In all cases the nanohole positioning deviation was very small, with no significant coupling between the dose and positioning accuracy being observed. The deviations for EBL/ICP-RIE fabrication are slightly lower than for LAO nanohole fabrication. To assess the impact of such a deviation, devices that would benefit from the use of site-controlled QD growth were simulated.

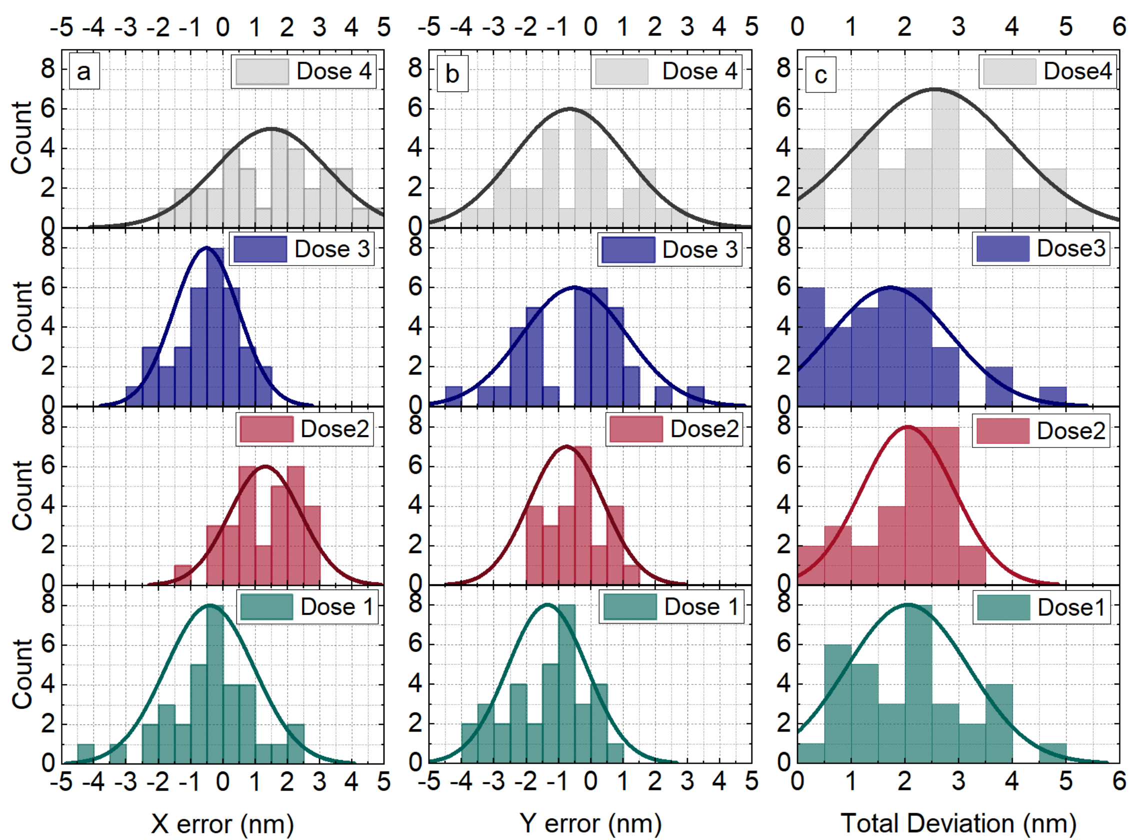

Figure 5-15. Positioning errors in (a) x, (b) y and (c) the total deviation as a function of dose, for 60 nm drawn size, dose 1 to 4 etched using ICP2 with EBL pattern 3 for 25 s.

5.4.1 Device simulation

Precise control over the position of a QD is necessary if a device is to function as efficiently as possible. Using the measured positioning deviations for the 10 $\times$ 10 μm array, the

impact of a dipole light source being positionally shifted from the centre of a cavity, where the field is strongest, and in a nanobeam waveguide will now be discussed. 3D FDTD simulations are used to analyse the position dependence on device properties and quantify the effect the experimentally measured deviation would have on device functionality. The simulation and device parameters used were outlined in Chapter 3.

First, a H1 cavity with a resonance mode of 920 nm (air clad GaAs) was simulated. The position dependent Purcell Factor (F_P) was assessed for this device, which had a simulated Q factor of 27 000. The mode volume was found to be 0.05 μm^3. The effect on the F_P of moving the dipole from the centre of the device was then determined by finding the field intensity at each grid point and normalising it to the centre field strength. The normalised dipole orientation was accounted for. This gave a quantitative value for Purcell enhancement for each coordinate in the cavity. The F_P at the centre of the cavity for the E_x mode was 848 and E_y mode is 794, which is a result in the range that is commonly acheived in simulation [10]. A 2D heat map of the F_P as a function of dipole position is show in Figure 5-16 (a) for the E_x mode and (b) E_y mode.

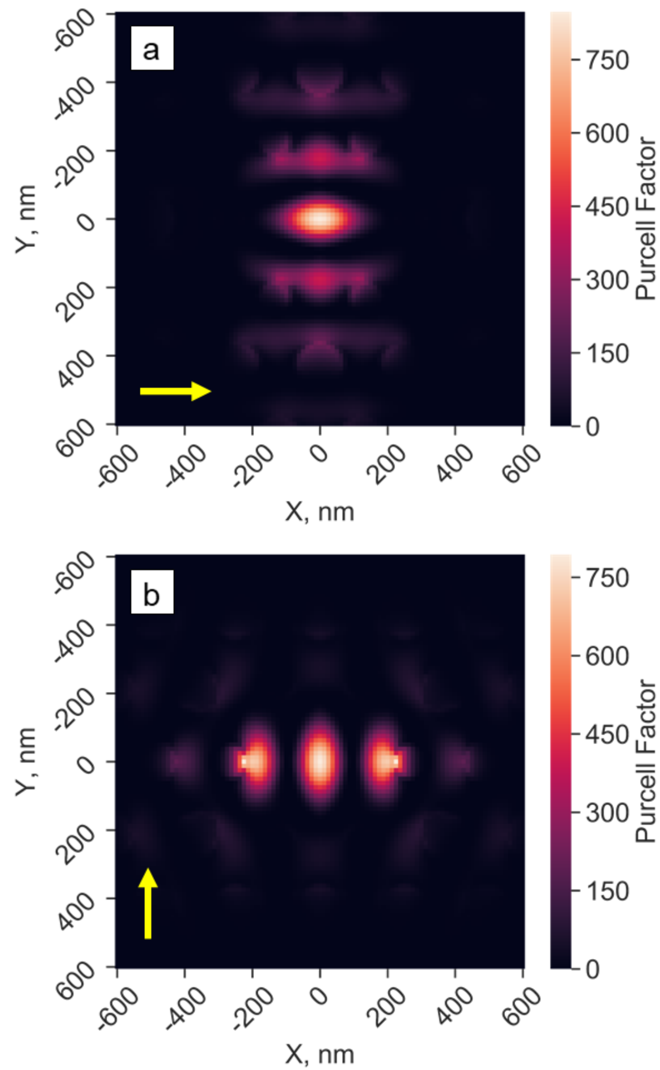

Figure 5-16. A 2D heat map of the position dependent F_P for an air clad H1 cavity with a GaAs slab and resonant frequency of 920 nm showing (a) the E_x mode and (b) the E_y mode. The arrow represents the oscillation direction of the dipole source.

Sections were taken in both x and y directions through the centre of the device and the F_P as a function of the position offset from the cavity centre is shown in Figure 5-17. This result demonstrates that the regularity of nanohole positioning is very good, as the F_P remains above 95 % of maximum.

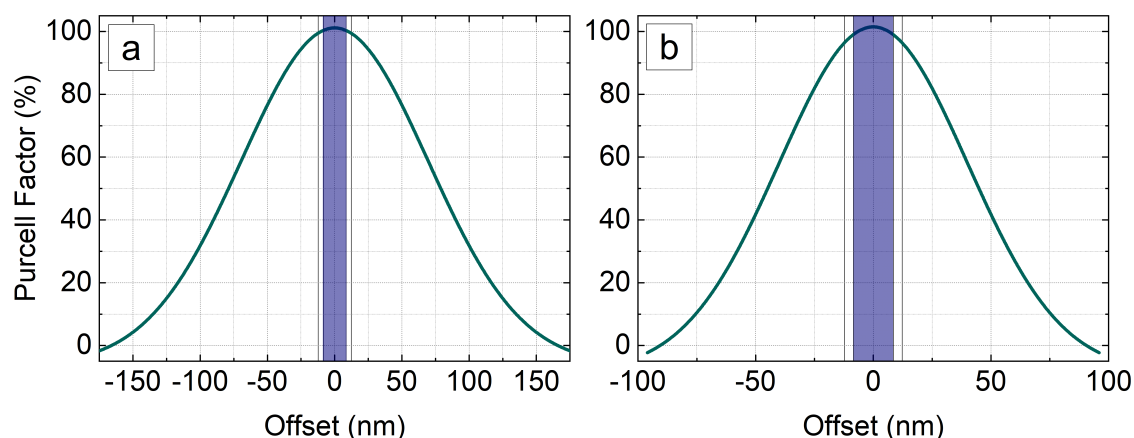

Figure 5-17. Cross sections of the F_P as a function of dipole position for (a) mode E_x using a x-normal section or mode E_y using a y-normal section and (b) mode E_x using a y-normal section or mode E_y using a x-normal section, which are equivalent. The blue area is the mean deviation value that was measured for a 10×10 μm array (Figure 5-13) and the black line is the standard deviation for the position deviation.

As discussed in Chapter 2, a chiral point in a waveguide can alter the direction of light propagation. The effect of placing the source at various positions across the y direction of the nanobeam waveguide was simulated. The electric field amplitudes, monitored in the z-normal direction, are shown in Figure 5-18. At the centre of the waveguide (b) the guided modes travelled in both directions with a 50:50 split. As the dipole was moved off centre the directionality of propagation became more apparent. At the chiral point, which was +90 nm offset (a) from the centre 89.4 % the guided light travelled left if the source was R polarised and 10.6 % travelled right if the source was L polarised. The opposite behaviour was observed at the other chiral point at −90 nm offset (c). The percentage of light that was coupled to any non-guided mode was not measured.

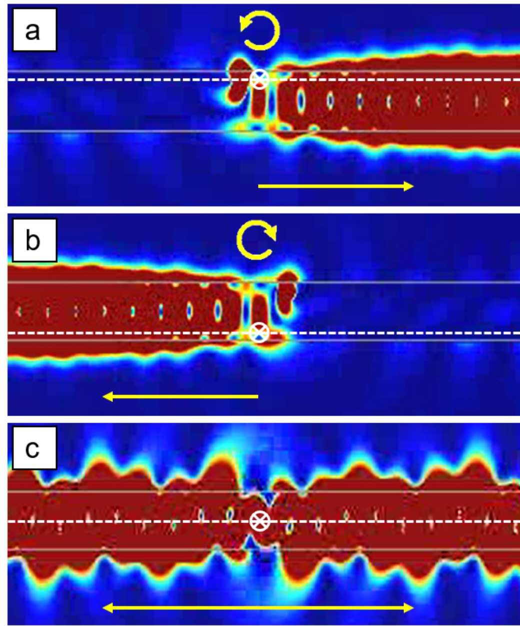

Figure 5-18. A simulated GaAs air clad nanobeam waveguide showing spin dependent chiral behaviour at (a) the +90 nm chiral position, where the σ^+ photons travel to the right, (b) the -90 nm chiral position, where the σ^+ photons travel to the left and, (c) at the waveguide centre (0 nm) where the spin dependent chiral behaviour is not present and there is a 50:50 probability of photons of either spin travelling in either direction. The yellow arrows indicate propagation direction and the white circle/ dashed line indicates dipole position.

The degree of chirality that was maintained when moving the dipole in the y direction away from the chiral point was measured and plotted in Figure 5-19. Moving the dipole 8.5 nm from the chiral point reduced the directionality from 89.4 % to 84.9 %. The impact of the slight irregularity in positioning of the nanoholes within the array would therefore be minimal and not significantly impact device functionality.

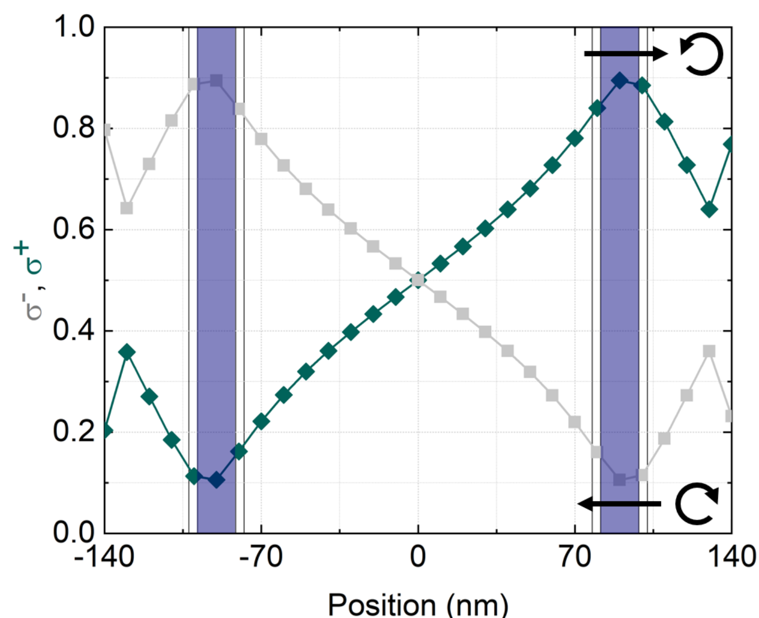

Figure 5-19. Simulated spin dependent directional coupling as a function of dipole position in the waveguide. The mean nanohole positioning deviation of 8.5 nm is marked in blue and the first standard deviation is marked by black lines.

5.5 Initial QD growth

Initial site-controlled QD growth was attempted using the V-90 MBE using 2 inch GaAs buffer samples. In addition to the fabrication challenges, good quality buffer material must be grown directly onto a smooth oxide-free GaAs surface. Although the HCl acid dip removes the majority of the oxide, once exposed to air a native oxide immediately grows on the semiconductor surface to a self-limiting thickness. This oxide must be removed prior to growth and for these growths this was done using a thermal desorption process. The temperature at which the oxide desorption occurred was found to be 609 °C using RHEED. To remove the oxide from the patterned samples the wafers were heated to 609 °C and the temperature was maintained for 15 minutes before being held for a further 5 minutes at 614 °C. A list of samples that will be discussed are part of this section are shown in Table 5.4.

Table 5.4. Fabrication and growth parameters for samples grown using the V-90 MBE for initial site-controlled QD experiments. For all samples the QD growth rate was 0.01 ML/s and the QD and buffer were grown at 475 °C.

Sample	EBL pattern	Indium coverage (ML)	Percentage of 2D to 3D time (%)	Buffer thickness (nm)	Cap
SF1457	1	1.6	94	15	No
SF1458	1	1.6	94	30	No
SF1475	1	1.6	94	15	Yes
SF1535	1	1.53	90	30	Yes
SF1558	2	1.5	88	20	No
SF1559	2	1.41	83	20	No

Once the oxide desorption process was complete the sample was cooled to growth temperature. The buffer, QDs and cap were all grown at 475 °C. It was decided to investigate indium deposition amounts, as a percentage of the 2D to 3D time and GaAs buffer thickness. Indium coverage amount was varied to optimise QD size and buffer thickness was varied to investigate the effect on surface and QD quality. Additionally, a growth interrupt was included, meaning that after the indium shutter was closer the substrate temperature was held constant for 80 s before the next stage was started (cooling or capping). The interrupt allowed time for further diffusion to take place and material to gather in the nanoholes. A coverage 94 % of the 2D to 3D time, which was found to be 3 minutes and 25 seconds, was chosen for initial SCQD growth as no QD nucleation was observed in RHEED at the point the indium shutter was closed, and very low density QD growth started to appear in RHEED after 80 s. Thin re-growth buffers were grown so to ensure nanohole sites would not be completely planarised and that the growth structure would be suitable for incorporation into devices with limited structure heights.

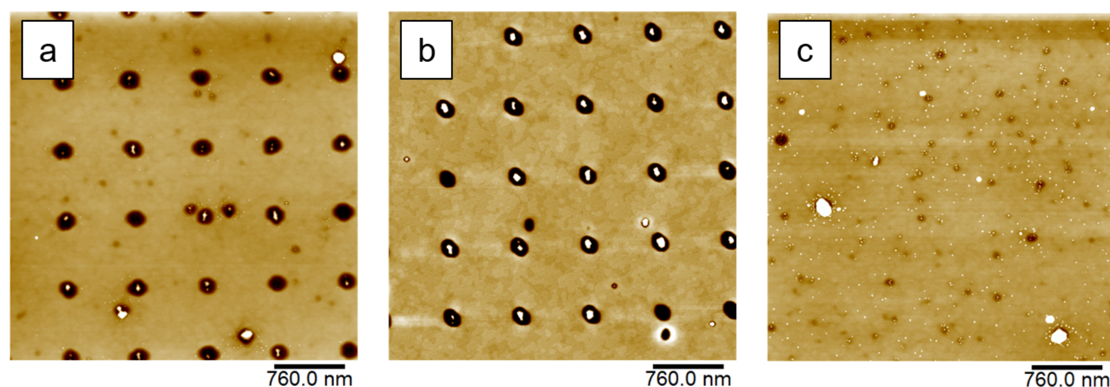

Figure 5-20. AFM images of initial SCQD growths on the V-90 MBE, using a deposition amount 94 % of the 2D to 3D time for sample (a) SF1457, 15 nm buffer (b) SF1458, 30 nm buffer and, (c) off pattern area of SF1457.

The first SCQD growth attempts are shown in Figure 5-20, where buffer thickness was varied for two samples and images on a patterned array and off-pattern are shown. SCQD growth was achieved for both samples. A large number of small QDs were observed in the off pattern area, in addition to a low number of larger QDs or defect sites. For sample SF1457 (a) five large unwanted, 'parasitic' pits, which were comparable in size to the patterned nanoholes, were observed in a 3.8 μm AFM scan. Additionally, there were a large number of larger parasitic pits across the surface. For sample SF1458 (b) very few small parasitic pits were observed and three medium. The RMS for the samples, measured on pattern, was 0.499 nm and 0.434 nm for SF1457 and SF1458 respectively. This suggests that roughness introduced during the oxide desorption step was more effectively smoothed by using a thicker buffer. The effect of the parasitic pits was to act as preferential nucleation sites, meaning QDs grew in these areas. Although the same indium coverage was used for both samples the mean QD heights were different. They were measured to be 7.9 nm $\pm$ 10.2 nm and 27.8 nm $\pm$ 5.8 nm for samples SF1457 and SF1458 respectively. This difference in QD height was caused by a larger number of QDs growing in parasitic pits for sample SF1457 compared to SF1458. It was estimated that nanoholes decreased in depth by around 5 nm when a 15 nm was deposited and by around 10 nm when a 30 nm buffer was deposited.

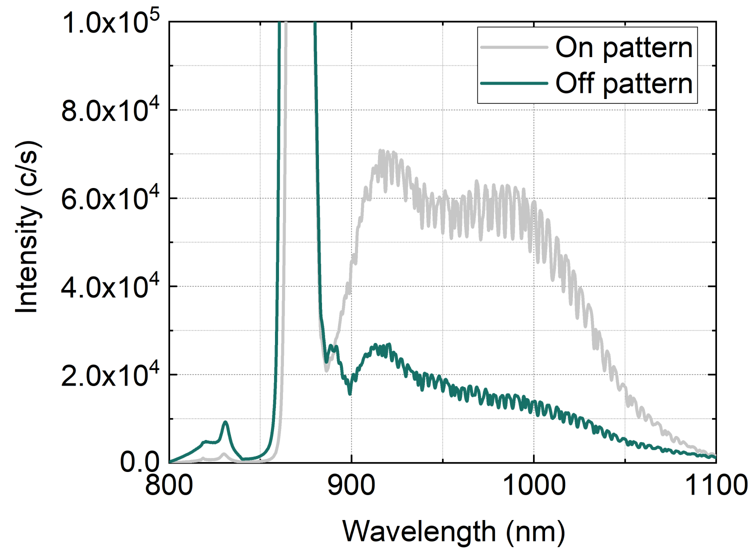

Figure 5-21. Low temperature (4 K) PL spectra measured using 0.1 mW power and a silicon CCD for sample SF1457, on the patterned nanohole area and off the patterned area.

To investigate whether the QDs were optically active a sample was grown under the same conditions as SF1457 and then capped with GaAs. A low temperature (LT) PL measurement is shown for sample SF1475 in Figure 5-21. Areas on the nanohole pattern and off the nanohole pattern were measured. The GaAs peak, wetting layer peak, and QD ensemble were visible both on and off pattern. The observed fringes were caused by optical etaloning, which is associated with charge coupled device (CCD) detectors [200]. The broad QD peak, visible from around 900 nm to 1100 nm, was around two and a half times brighter on pattern. Additionally, there appeared to be a bimodal distribution on pattern centering at around 920 nm and 980 nm. These observations suggests that there is a higher density of QDs on pattern and that more of those QDs are at longer wavelength. This observation is supported by the large variability in size between the SCQDs and the large numbers of smaller QDs which were seen off pattern in AFM for sample SF1457.

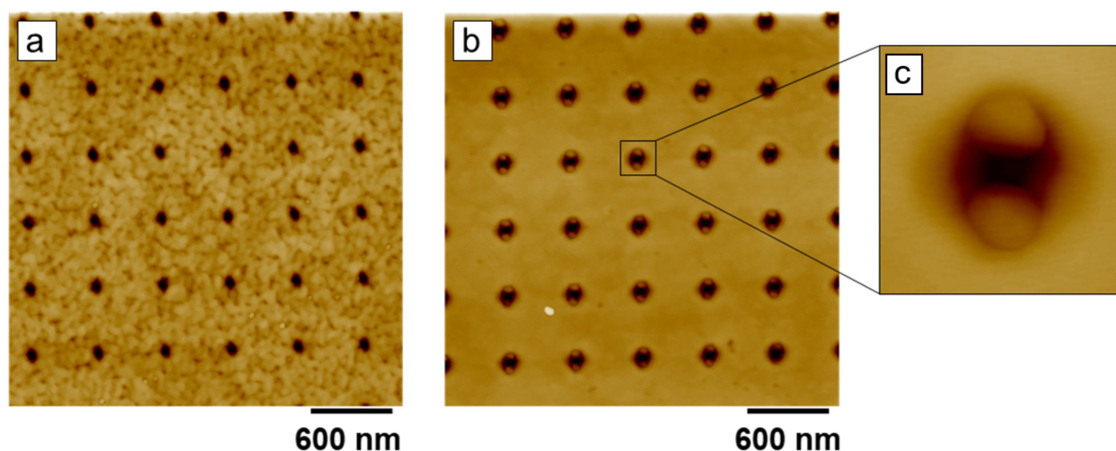

Figure 5-22. AFM images of samples (a) SF1539 (b) SF1538, with (c) a zoom in on a typical nanohole with two SCQDs nucleated along the [110] axis.

Due to the large size of the SCQDs and preference of off pattern QD nucleation the coverage was reduced in the next series of growths. A 20 nm re-growth buffer with 88 % and 83 % of the 2D to 3D time were used for samples SF1558 and SF1559 respectively. AFM images of samples SF1559 (a) and SF1558 (b) are shown in Figure 5-22. There was a significant difference in the RMS for the two samples. Values were 1.53 nm and 0.421 for SF1559 abd SF1558 respectively. Reports have shown that thermal desorption can cause surface roughening when removing oxides for GaAs surfaces [153]. A model, reported in the literature, explains this roughening through evaporation of the oxide occurring inhomogeneously [159]. Additionally, it was shown that the temperature required to remove an oxide increases in a linear manner with oxide thickness. This roughening was observed for several subsequent samples, not discussed here in detail. Therefore, it is thought that very small differences in temperature between samples were leading to roughening intermittently occurring. A reproducible thermal desorption process was not established, and instead the development of an atomic hydrogen cleaning (AHC) method on the DCA MBE will be discussed.

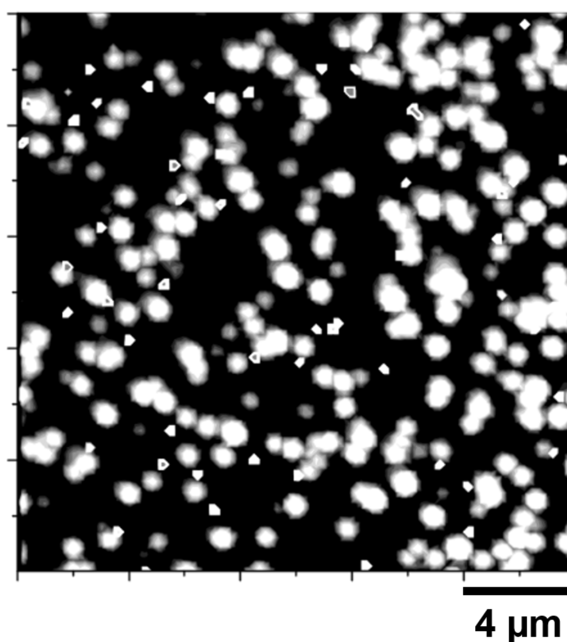

Figure 5-23. A μPL map of sample SF1535 (indium coverage 90 % of the 2D to 3D time), obtained using a solid immersion lens by Dr. Maxim Makhonin.

A μPL map for sample SF1535 is shown in Figure 5-23. The image was constructed from 10000 spectra, where the artefacts were caused by cosmic rays. Emission from regular arrays of nanoholes was not observed and instead the map demonstrated random nucleation of QDs. This is likely to be due to roughness, as was observed for sample SF1559 in AFM, which caused QDs to nucleate across the surface rather than only at the nanohole sites. Attempts to filter the image either by single QD linewidth or emission wavelength did not uncover any underlying pattern.

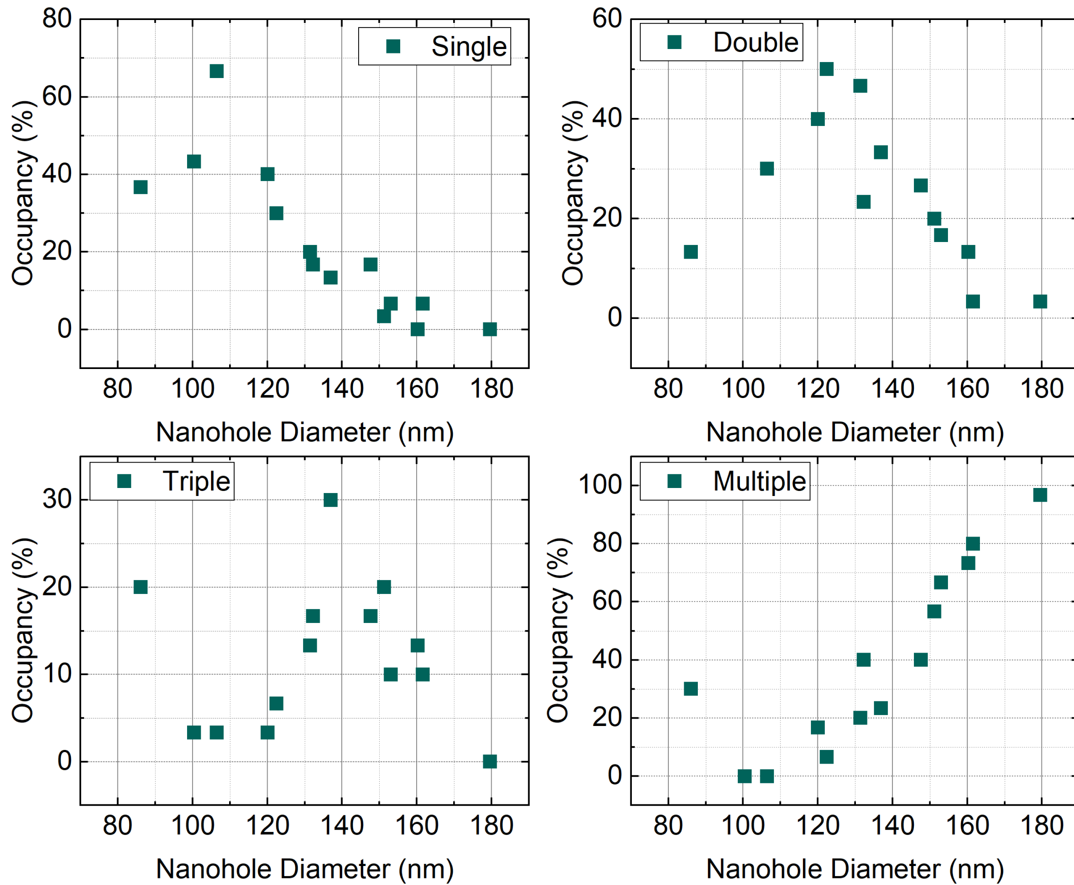

Figure 5-24. Sample SF1558, where the percentage of nanoholes occupied by one, two, three, or more than three QDs is shown as a function of nanohole diameter.

The effect of nanohole diameter on QD occupancy was investigated for sample SF1558. Figure 5-24 shows the percentage of nanoholes occupied by one, two, three, or more than three QDs for a range of nanohole diameters. For smaller nanoholes, the majority of sites (68 %) were occupied by a single QD. As nanohole diameter increased the occupancy increased, until for the largest nanoholes almost all sites were occupied by four or more QDs. This demonstrates that nanoholes of small diameter are required for single occupancy and that nanohole diameter can be used to tune SCQD occupancy. For this reason, the EBL pattern was modified to include smaller size nanoholes.

5.6 Summary

This chapter presented the development of a controllable and reproducible nanohole fabrication process using EBL and ICP-RIE. Etch recipes were developed on two ICP-RIE machines due to machine downtime, which give similar nanohole dimensions. The depth of nanoholes was controlled using etch time, whilst the EBL parameters of dose and drawn size determined nanohole diameter. Very small deviations in nanohole size were seen across the arrays. The EBL pattern went through a number of refinements as the project developed, with the final refinement incorporating alignment marks that allowed individual nanoholes or QDs to be returned to repeatably. To ensure a clean, high quality surface post fabrication a robust and reproducible ex-situ clean was developed. Nanohole positioning accuracy was assessed against devices simulated using 3D FDTD and shown to be well above acceptable levels, with the Purcell Factor of an H1 cavity remaining above 95 % of maximum for the measured deviation values. Finally, initial SCQD growth experiments were undertaken using the V-90 MBE. For uncapped samples, site-control of QDs was demonstrated, however a reproducible oxide desorption method could not be established. This meant that a high proportion of samples were very rough and meaningful data could not be gathered. Additionally, μPL results were affected and emission from regular arrays of nanoholes was not detected.

This page intentionally left blank

6 | Atomic Hydrogen Cleaning

Prior to commencing growth on epiready or buffer GaAs substrates, it is necessary to remove the protective or native oxide from the surface. When growing the planar buffer structures used in this work, a sample is heated to a temperature that induces thermal desorption of the native oxide species [201]. During thermal desorption arsenic oxides and Ga_2O oxides desorb from the suface at relatively low temperatures, however the removal of the more stable gallium oxide (Ga_2O_3) requires the use of high temperatures. At the high temperatures required to remove the thermally stable Ga_2O_3 oxides, reactions between bulk GaAs and Ga_2O_3 take place and cause surface roughening [202,203]. This roughening is reduced by holding the substrate at a high temperature for long enough that the oxides fully desorb and then allowing surface GaAs to form a stable reconstruction [204]. Use of a thick buffer can then fully smooth the surface. However, when re-growth on patterned samples is being undertaken this approach does not work well, as seen in Chapter 7. A high temperature cannot be maintained to allow smoothing, as this would degrade the nanohole pattern. Additionally, a thin re-growth buffer is grown meaning that any roughening at the fabrication interface is transferred to the surface on which QDs are grown.

Surface roughening has been reported to be significantly reduced by supplying gallium to the sample while desorption is occuring, which is known as gallium assisted deoxidation [205]. The gallium reacts with the stable Ga_2O_3 oxides to form volitile Ga_2O and water, which can be removed at lower temperatures. However, oversupply of the metal can lead to the formation of metallic droplets, which are also undesirable. A similar mechanism occurs for indium assisted deoxidation, where a reaction occurs between indium and Ga_2O_3 to form volatile by-products [206–208]. An alternative in-situ surface cleaning

technique is atomic hydrogen cleaning (AHC), which facilitates the removal of oxides at lower temperatures.

This chapter focuses on the development of an effective AHC method, including optimisation of secondary ion mass spectrometry (SIMS) analysis. The main criteria that the method will be assessed against are the level of contaminations that remain after cleaning, surface roughness and quality, and preservation of the nanohole pattern. The AHC development was analysed using SIMS, AFM, RHEED and μPL. SIMS is a highly sensitive surface analysis technique that allows quantification of compounds based on their mass to charge ratio. Planar samples were first investigated, to benchmark initial AHC parameters and investigate the impact of native oxide thickness on cleaning efficacy. Next, substrate temperature effect will be discussed for planar, epiready samples and planar buffers. Finally, fine tuning of parameters was performed on patterned substrates and an optimised AHC method established. The optimised method is shown to produce contamination free surfaces, without introducing surface roughening. Elongation of the nanohole in the [110] direction was observed, as is consistent with the literature.

6.1 Secondary ion mass spectrometry set-up

In order to verify the effectivness of the AHC process, a SIMS system was installed in the analysis chamber of the DCA MBE. The manipulator allows a sample to be rotated through 360 deg and be raised or lowered. Rotation of the sample allows multiple spots on the surface to be hit. This is an important feature as contamination from the fabrication process will be surface level only and SIMS is a destructive analysis process. Therefore, as multiple measurements of surface composition are required (pre- and post-AHC) the sample must be rotated so that a new area is hit. The rate at which surface chemicals are removed depends on the ion beam current. When performing surface analysis, it is therefore preferable to have a low ion beam current and a beam profile with a wide diameter. This allows a large area to be sampled and gives better statistical results.

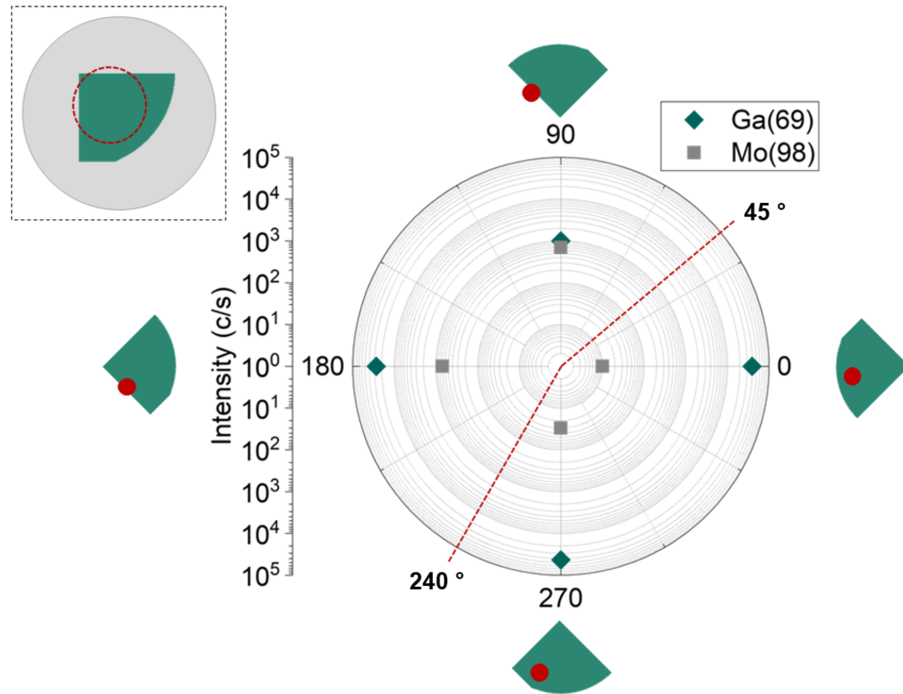

Figure 6-1. Ga and Mo intensity as a function of sample holder rotation in ANA. The insert indicates, with a red circle, the positions that the SIMS analysis beam hit as the sample was rotated.

The site-controlled GaAs growth experiments were all performed on quarter 3 inch wafers, which are not rotationally symmetric. Therefore, it was necessary to determine where the analysis beam hit in relation to the rotation angle of the sample holder. Figure 6-1 shows the intensities of the Ga and Mo peaks, which arise from the GaAs substrate and the Mo sample holder. A visual inspection of the wafer was performed after removing it from the system and along with SIMS data allowed the manipulator angle to be mapped onto the analysis beam impact position. Over an angular range of 45 deg to 240 deg the analysis beam only hit areas on the sample and not on the Mo holder, therefore all furture experiments were performed in this range.

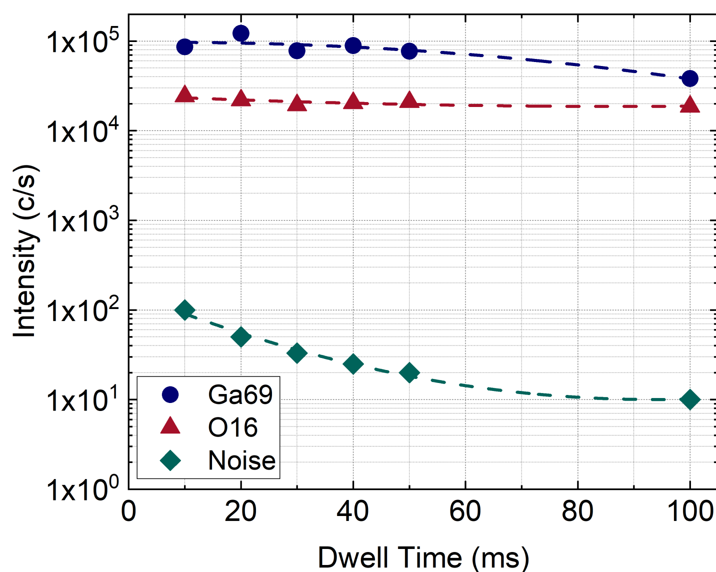

Figure 6-2. Intensity of Ga-69, O-16, and background noise as a function of dwell time.

The next parameter investigated was the dwell time, which controls the analysis time at each mass in the set range. Because the SIMS process is destructive, it is possible for heavier masses of interest to be completely removed during the scan before analysis has occurred if the dwell time at each mass is very long. However, a short dwell time will lead to increased background noise. Figure 6-2 demonstrated that increasing dwell time reduced noise significantly over the 10 ms to 50 ms range, while Ga and O counts were relatively constant. When the dwell time was increased from 50 ms to 100 ms, there was a drop in GaAs counts but very little improvement in the noise. Therefore, a dwell time of 50 ms was chosen as a good compromise.

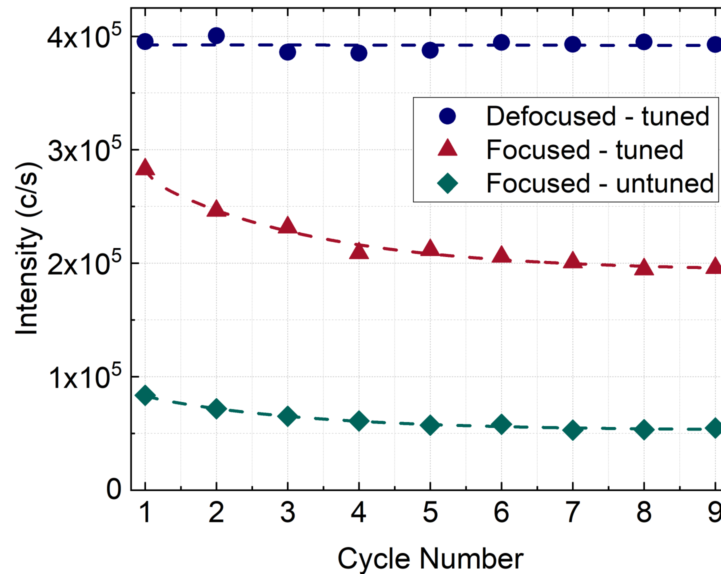

Figure 6-3. Variation in the Ga-69 peak intensity as a function of SIMS cycle number for focused beam parameters before and after tuning, and for tuned, de-focused beam parameters.

The SIMS system must be regularly tuned as the system will change over time, but also when any parameters are altered. The process optimises the mass spectrometer parameters to maximise the number of counts measured per second. Figure 6-3 shows the intensity of the Ga-69 peak for a tuned and untuned focused beam and for a tuned defocused beam. In each case the system was run for 9 cycles (9 positive mode and 9 negative mode). The focused setting had a beam current of 2 nA and beam diameter of around 500 μm. It can be seen that by running a tune the counts were significantly improved. However, the beam current was relatively high meaning over this period the beam 'drilled' into the sample. This changed the sample profile exposed to the beam and caused a slight drop in counts over the cycles. To produce a more defocused beam, which samples a larger area with less damage, ion beam settings were altered to give a beam current of 1 nA and diameter of around 1000 μm. The defocused settings gave higher and more consistent Ga-69 counts over the 9 cycles. The two set-ups can be used for different purposes depending on the sample analysis required. A low current, defocused beam gives surface information while a higher current, focused beam can be used for depth profiling. Figure 6-4 compares the effect on Ga-69 counts when beam currents were 2 nA, 1 nA and 0.5 nA. The beam diameter of the 500 pA beam was around 2000 μm and gave significantly higher

counts. For analysis of site-controlled growth samples, the defocused 500 pA beam current was chosen to optimise counts while sampling a larger area and minimising sample damage.

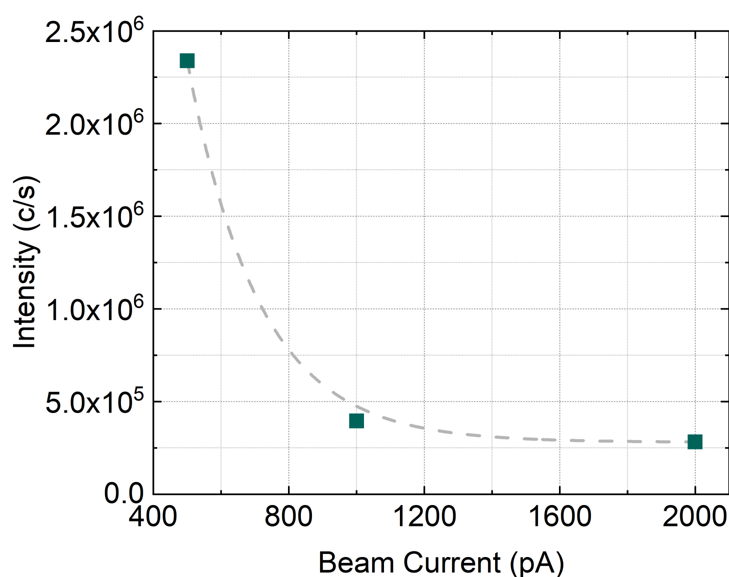

Figure 6-4. Ga-69 intensity as a function of beam current.

When a semi-insulating sample is measured, ion bombardment during SIMS analysis can lead to charging. The SCQD experiments were performed on insulating samples, which left them susceptible to charging, where the signal was lost. To mitigate this behaviour, the sample can be heated. Ga-69 counts were recorded while temperature, measured using the thermocouple, was varied. Figure 6-5 shows that in addition to its ability to overcome charging issues, counts were increased at higher temperatures. Semi-insulating GaAs samples that previously demonstrated charging, were found to not charge at 150 °C. Therefore, a temperature of 150 °C was chosen for future site-controlled sample analysis.

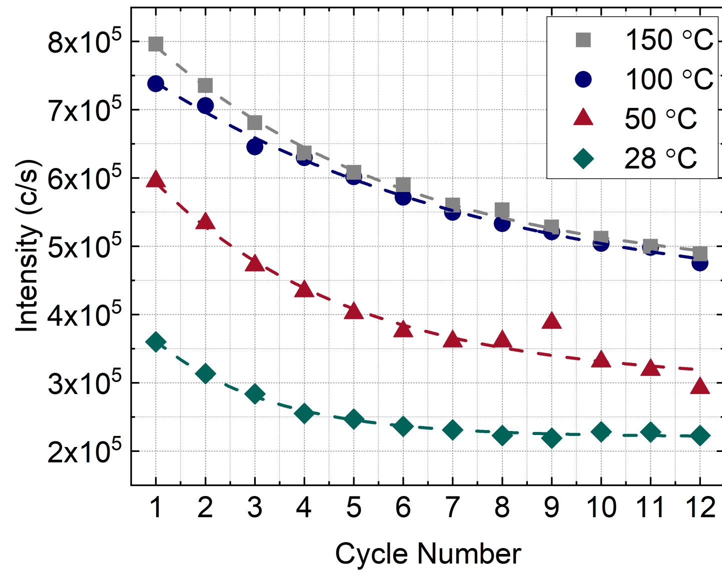

Figure 6-5. Ga-69 intensity as a function of cycle number at thermocouple measured temperatures, 28 °C (no heating applied), 50 °C, 100 °C, and 150 °C.

To benchmark the optimised 500 pA beam parameters at a sample temperature of 150 °C, a semi-insulating epiready GaAs sample was measured in negative and positive modes. Typical sample spectra are shown in Figure 6-6, a full list of commonly identified masses is listed in Table A.1. Oxide species were most commonly seen in negative mode, while Ga, As and ionic salts were seen in positive mode.

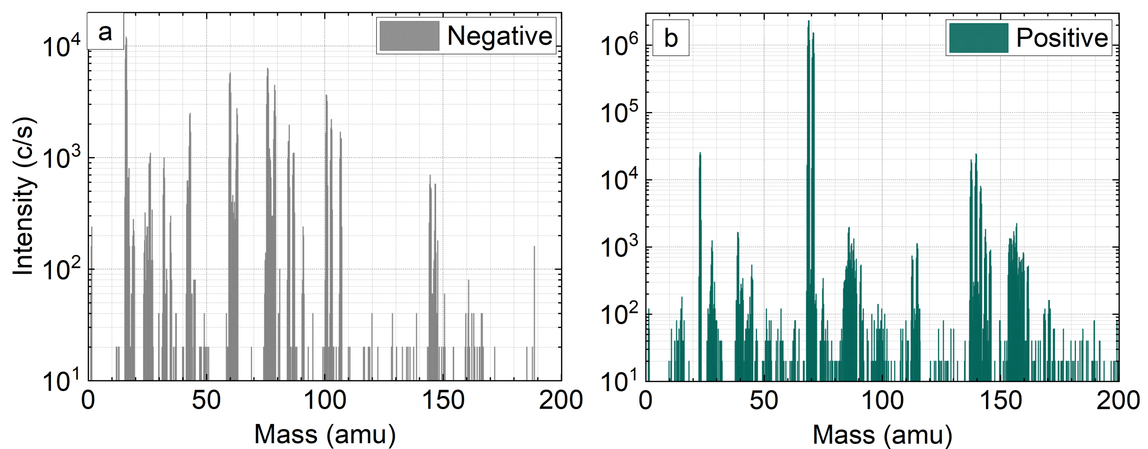

Figure 6-6. Initial SIMS spectra in positive and negative modes for an undoped, epiready GaAs sample, using a 500 pA, defocused and tuned beam set-up.

6.2 Atomic hydrogen cleaning

6.2.1 Hydrogen cleaning planar surfaces

Initial AHC parameters were investigated, using two epiready GaAs samples. Sample A was dipped in a 1:1 HCl/ H_2O solution for 1 minute prior to being loading into the system for de-gas. Sample B underwent no ex-situ preparation and was loaded straight into the system and de-gassed with sample A. To benchmark an initial substrate temperature for cleaning, a value of 400 °C, measured on the thermocouple, was chosen. The highest available HABS current of 14 A was applied and a long cleaning time of 1 hr was chosen, to ensure that oxide removal would not be limited by these parameters.

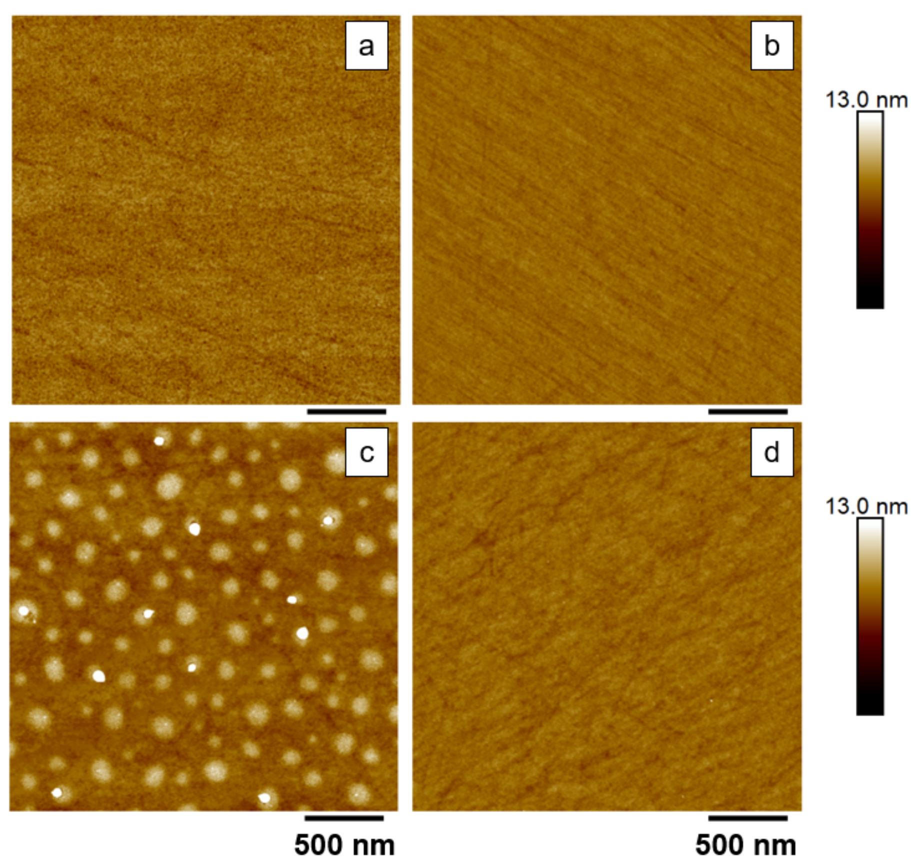

Figure 6-7. AFM images for (a) an un-processed epiready sample, (b) sample A (acid dipped) post-AHC, (c) sample B (not acid dipped) post-AHC and, (d) sample B post-AHC and a post-acid dip. The scale bar for all images is between 0 nm and 13 nm, however the very highest regions for (d) are saturated on this scale and are between 15 nm and 20 nm.

To assess the effectiveness of the clean, the samples were measured via SIMS and AFM. Figure 6-7 (a) shows an AFM image of the fresh epiready wafer, with a measured RMS of 0.288 nm. In (b) the AFM of sample A post AHC is shown, the RMS was very similar to the fresh wafer at 0.313 nm. For the undipped sample B shown in (c), oxide removal appeared to be incomplete as raised areas were visible across the surface, and the RMS was elevated at 1.40 nm. To investigate whether the roughness was due to surface GaAs roughening or residue oxides, the sample was dipped in the HCl/H_2O solution (as per sample A). Image (d), post-acid dip, demonstrated removal of the residue. This means that the roughness was caused by oxides remaining on the surface, as the etch would not have affected roughened GaAs. The RMS post AHC and acid dip, was slightly higher than that of the fresh sample.

Figure 6-8 shows SIMS spectra for masses of interest in negative and positive mode. Data for sample A (dipped) and B (undipped) are compared pre-AHC and post-AHC. It can be seen that in general AHC reduced the quantity of negative oxide species present on the surface for both samples. There was some variation in cleaning efficiency for different oxide species between the samples. The oxygen and hydroxide species were removed to a similar degree, however quantities of GaO_2^- remaining on the surface were significantly higher for the undipped sample compared to the dipped sample. Quantities of AsO_2^- were similar for the two samples post AHC. Additionally, the acid dip removed much or the AsO_2^- species pre-AHC. This shows that an acid dip or AHC process can effectively remove arsenic oxides at this substrate temperature. However, oxygen, hydroxy and GaO species were more effectively removed via AHC. Finally at this substrate temperature, both an acid dip and AHC were needed to minimise GaO_2^- levels. This result demonstrates that GaO_2^- species are more difficult to remove that AsO_2^- species, which agrees with the observed high thermal stability of GaO_2 [209]. Therefore, it is likely that the oxide residues observed in AFM were predominantly comprised of Ga_2O. Ionic salt levels were measured pre- and post-AHC for the dipped and undipped samples. An increase in sodium and calcium was seen for the dipped samples, indicating that some contamination could be present in the HCl/H_2O solution. Under these conditions, the AHC process did not remove the salts, meaning samples should be exposed to these contaminants as little

as possible.

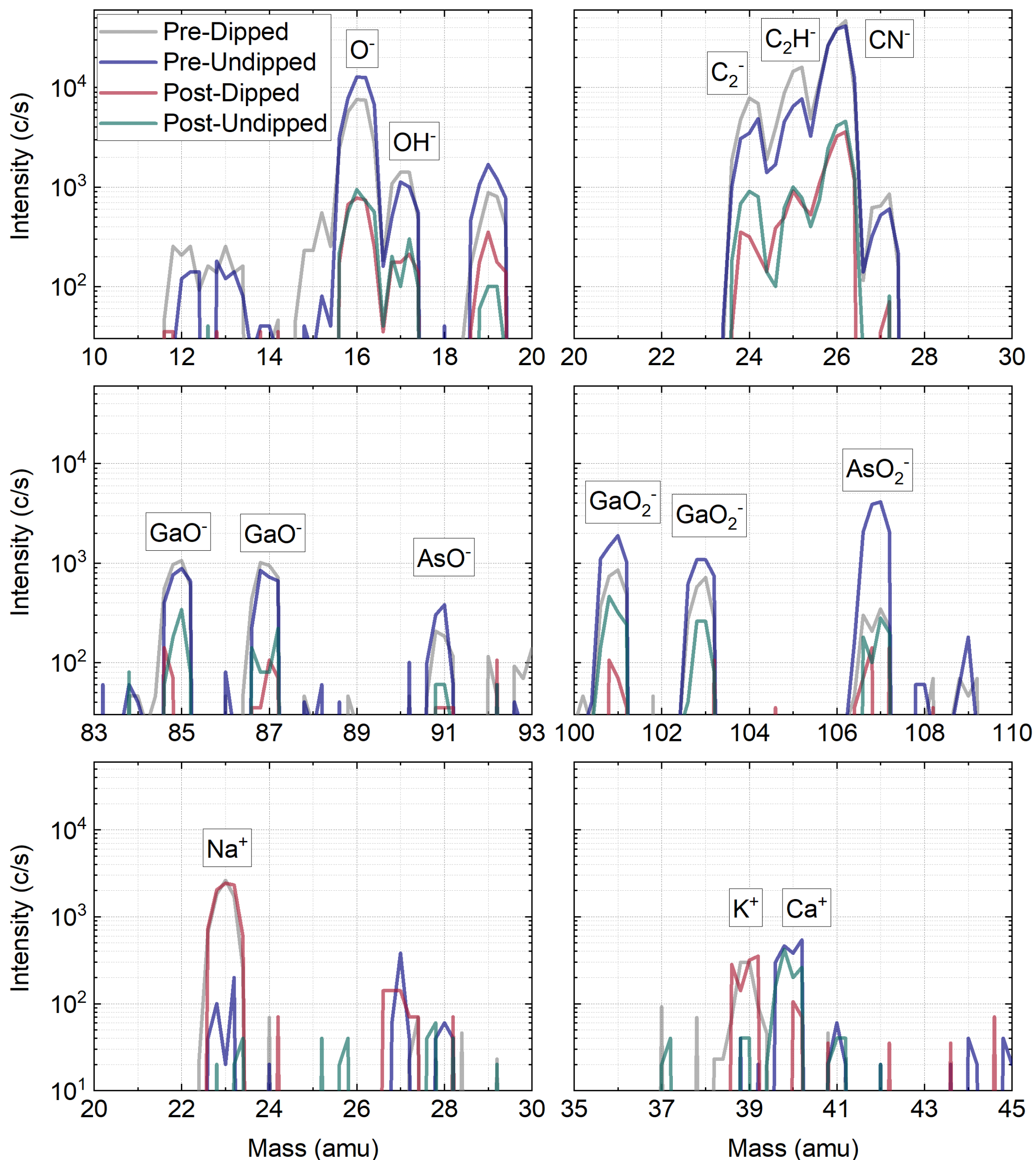

Figure 6-8. SIMS spectra for selected masses for sample A (dipped) pre- and post-AHC and sample B (undipped) pre- and post-AHC.

6.2.1.1 Cleaning epiready wafers

To improve the AHC oxide removal, a series of 5 epiready wafers (not acid dipped) were cleaned while varying substrate temperature and HABS current. Running the HABS at maximum current (14 A) shortens the lifetime of the filament, therefore minimising the

current while maintaining effective cleaning is preferable. Additionally, harsh conditions can cause surface damage and increase roughness. Therefore, parameters were chosen that optimised cleaning and HABS lifetime, while maintaining a smooth surface. The sample smoothness was examined using in-situ RHEED and the oxide levels were measured using SIMS. The sample parameters with the corresponding surface reconstructions are shown in table 6.1.

Table 6.1. Cleaning parameters and the observed surface reconstructions for epiready samples A to E. All samples were cleaned for 1 hour.

Sample	Substrate temperature (°C)		HABS current (A)	RHEED reconstruction ([110] x [1-10])
	Thermocouple	BandiT (estimate)		
A	625	500	14	3 x 6
B	575	450	14	2 x 4
C	575	450	13	3 x 6
D	525	400	13	3 x 6
E	475	310	13	3 x ?

The RHEED patterns in the [110] and [1-10] directions were measured, and the surface reconstruction pattern and clarity was assessed. Figure 6-9 shows the images for samples A to E. In general, as the substrate temperature and HABS current were reduced, the pattern became less clear. This behaviour was associated with increased roughness and the presence of oxides on the surface. The reconstruction could be discerned for all samples except E, suggesting poor oxide removal at a temperature of 310 °C. Clear and bright RHEED patterns were observed for samples A and B, which were cleaned at the hottest substrate temperature of 500 °C and 450 °C at 14 A and 13 A respectively. Sample B was the only sample to demonstrate a 2×4 reconstruction, which is commonly observed when a smooth, planar GaAs buffer has been grown.

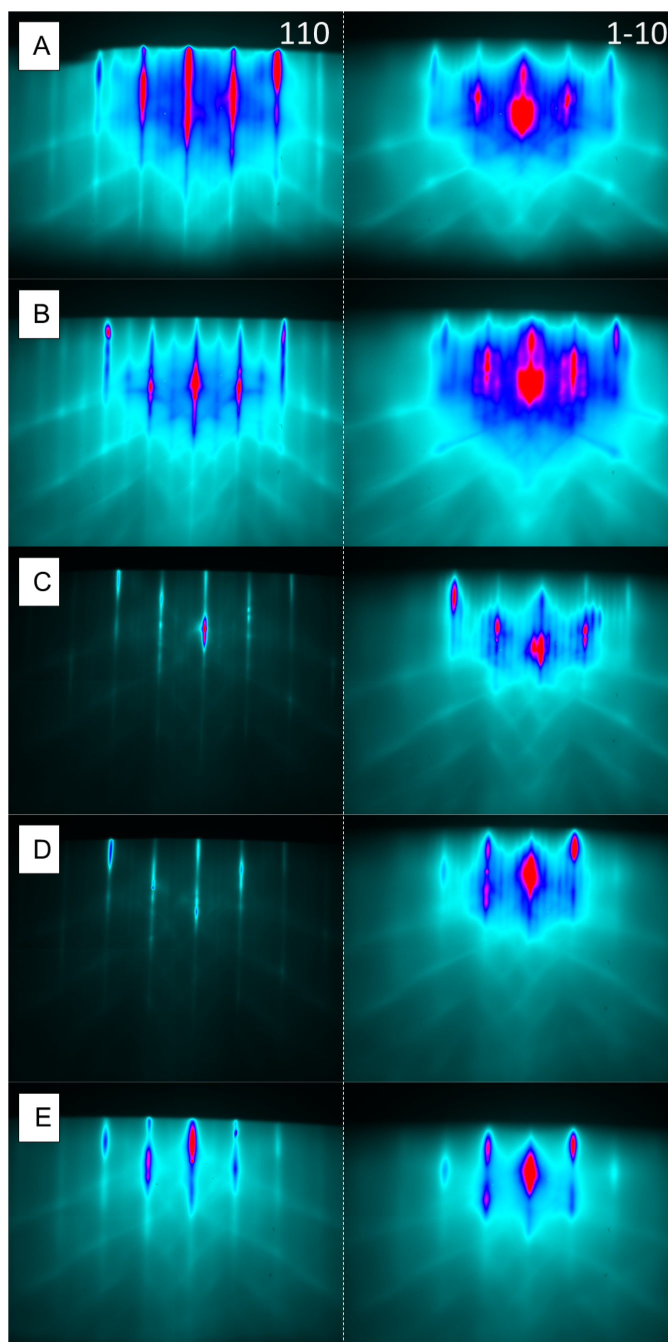

Figure 6-9. RHEED surface reconstructions for samples A to E measured in the [110] and [1-10] crystal directions at a temperature of 500 °C (BandiT).

To further investigate the oxide removal on theses samples, SIMS measurements were taken of the samples before and after AHC. To quantify the effect of cleaning on the levels of contaminants, the percentage remaining after AHC was calculated for each sample, i.e. if mass X had 100 c/s pre-AHC and 20 c/s post-AHC, there would be 20 % remaining. Figure 6-10 shows this data for the 5 samples, for negative and positive masses of interest.

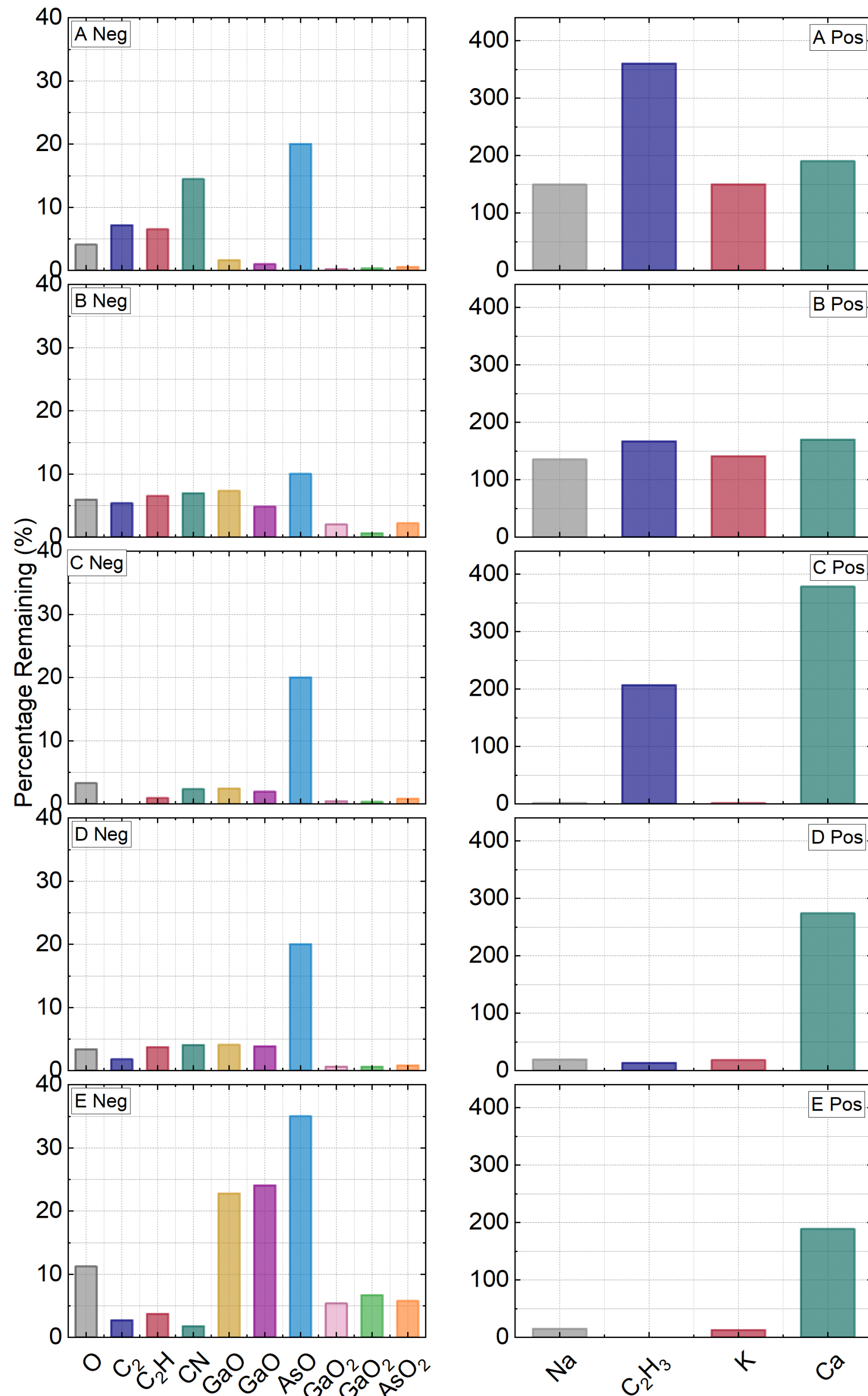

Figure 6-10. SIMS masses of interest for samples A to E remaining post-AHC.

In general, as the substrate temperature and HABS current were increased there was a reduction in the negative mass species on the sample surface. Most notably, GaO was present in much higher levels for sample E when compared to samples A to D. Additionally, the thermally stable GaO_2^- was reduced to very minimal levels for samples A to D,

while $\sim$ 5 % remained for sample E. This is a much larger percentage reduction than was observed at 400 °C at 14 A for 1 hour in Figure 6-8, which was around 25 %. The higher level of contamination remaining on the surface of sample E correlates with the increased surface roughness observed in RHEED. This shows the significant effect of substrate temperature on oxide removal. However, the AHC process did not remove positive organic and salt species, and in fact an increase in counts was observed as the temperature and current increased. As these samples were not processed in any way pre-AHC this observation could be explained in two ways. Firstly, as the sample was more effectively cleaned, contaminants which were already present under the oxide were exposed or moved to the surface. Or secondly, the HABS introduced contaminants onto the sample. The conclusion from the SIMS data was that the parameters used to clean samples A to D were sufficinet to remove oxide species to an acceptable level for QD growth, while the parameters used to clean sample E were not. This conclusion was supported by the RHEED data, where a smooth surface was not observed for sample E.

6.2.1.2 Planar buffers

The next sample type to undergo AHC tests were planar quarter 3 inch GaAs buffers grown via MBE. Buffer substrates differ from epiready substrates in that their native oxide is thinner. When cleaning nanohole patterned buffers, a gentle, cool clean is preferred that will not cause pattern degradation. For these reasons it was decided to test shorter, cooler cleans. Four samples were tested

for this purpose. QDs were deposited on the re-growth buffer and were capped with 200 nm of GaAs before finally surface QDs were deposited. This growth structure was chosen to allow the PL quality of the QDs to be benchmarked, and the RMS and surface QDs to measured using AFM. SIMS measurements were performed pre- and post-AHC. Theses parameters and a summary of the SIMS, AFM, and μPL results are shown in table 6.2. The sample reference associated with the samples post growth was as follows PR0027, PR0029, PR0026 and PR0028.

Table 6.2. Cleaning parameters and a summary of results for planar buffer samples A to D, all cleaned for 20 minutes at a flow rate of 0.5 sccm and HABS current of 13 A.

Sample	Substrate temperature (°C)	Re-growth buffer (nm)	SIMS (contamination levels post AHC)	RMS (nm)	PL (c/s)	Mean single QD linewidth (μeV)
PR0027	350	30	High	5.3	15	75
PR0029	350	20	High	3.1	0	NA
PR0026	350	200	Lower	0.209	200	72
PR0028	400	20	Lower	0.205	65	95

SIMS analysis showing the percentage of each mass remaining after AHC is shown in Figure 6-11. The lower cleaning temperature of 350 °C did not remove oxides or contaminents effectively for samples PR0027 and PR0029. In particular species CN^- and GaO^- were virtually unaffected by the clean. Oxides and contaminants were removed much more successfully for sample C, despite it being cleaned with the same parameters used for A and B. This variation suggests that 350 °C was close to the lowest temperature required for effective cleaning. Sample D showed a very similar reduction for surface species post-AHC as was seen for sample PR0026. More positive species were detected post-cleaning than pre-cleaning for all samples, with the largest increase being observed for the samples that had the most negative oxide species removed.

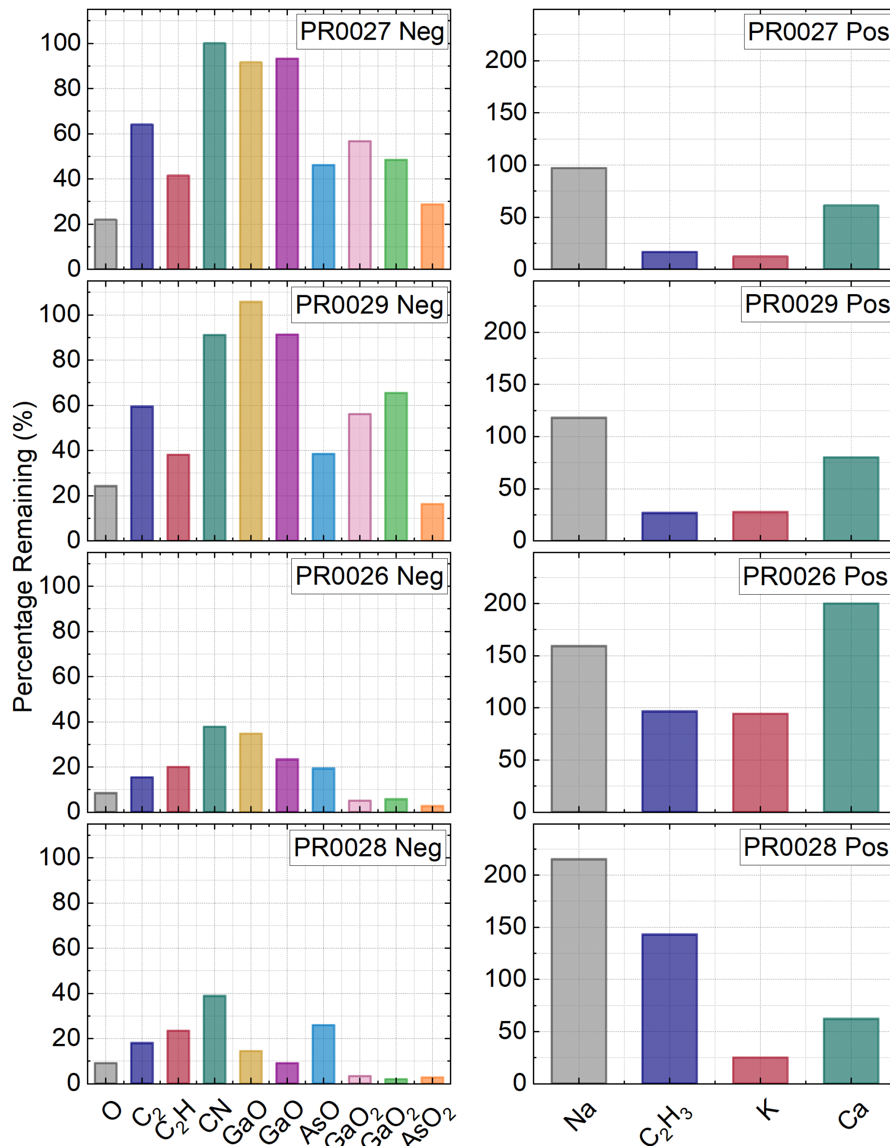

Figure 6-11. SIMS masses of interest for samples PR0027, PR0029, PR0026, and PR0028 remaining post-AHC.

Figure 6-12 shows AFM images for the four samples. First, PR0027 (30 nm re-growth buffer) and PR0029 (20 nm re-growth buffer) will be compared. Both samples showed high roughness, sample PR0027 had an RMS of 5.3 nm and sample PR0029 had a RMS of 3.1 nm. Surface QDs were visible for both samples; however, they were larger for sample PR0029. Sample PR0026 (200 nm buffer) and sample PR0028 (20 nm buffer) showed a smoothness consistent with a good quality GaAs surface, with a RMS of 0.209 nm for sample PR0026 and 0.205 nm for sample PR0028. There was a slight difference in QD density for the samples, the density was 5.8 x10^9 cm^{-2} and 6.9 x10^9 cm^{-2} for samples PR0026

and PR0028 respectively. This clearly demonstrates the impact of the AHC procedure on the surface quality and that incomplete oxide removal causes significant and detrimental roughening.

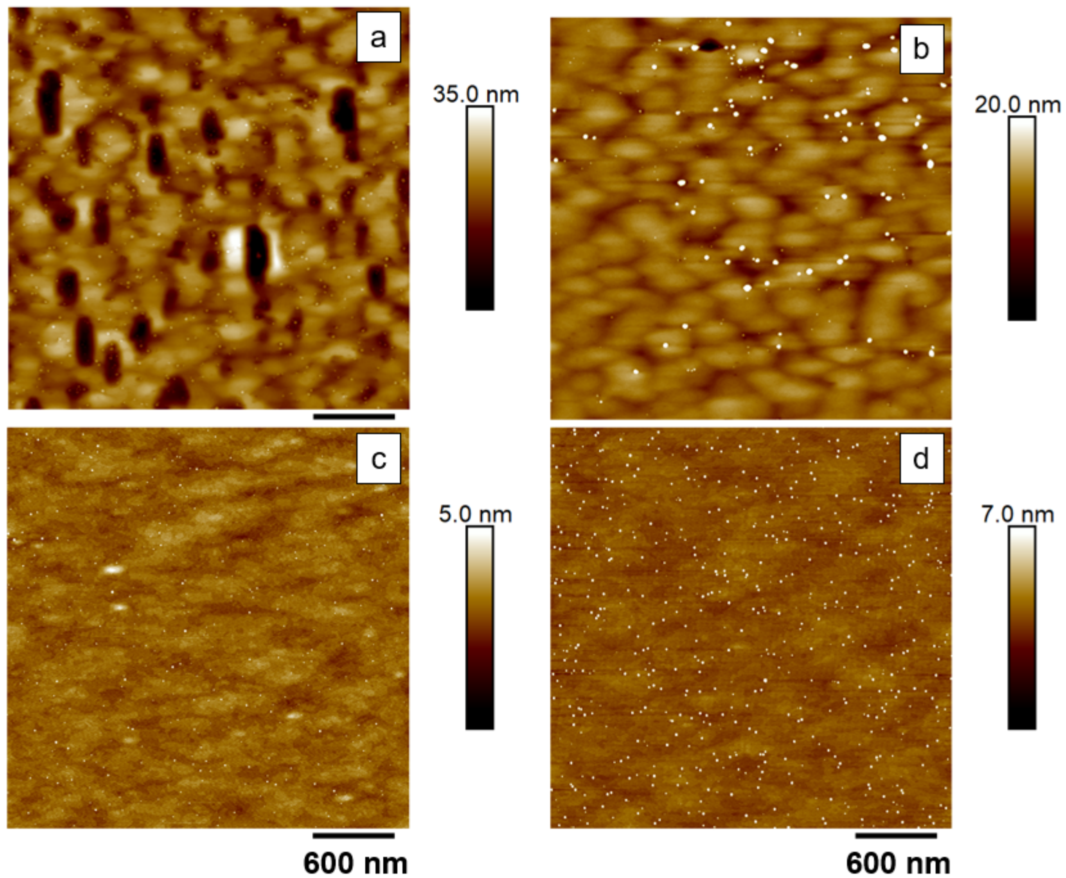

Figure 6-12. AFM images of planar buffer samples post-AHC, buffer, and QD growth for samples (a) PR0027, (b) PR0029, (c) PR0026, and (d) PR0028.

Figure 6-13 shows μPL data for single QDs measured for samples PR0027, PR0026, and PR0028. No emission was observed for sample PR0029, despite exciting with a high power. Weak QD emission was observed for sample PR0027 and the brightest emission was observed for sample PR0026. Both samples PR0027 and PR0029 showed very similar SIMS and AFM, therefore the difference in emission can be attributed to the differing re-growth buffer thicknesses. Although the emission intensity for sample PR0027 was still weak, moving the QDs further from the rough interface allowed some emission to be observed. This behaviour was paralleled for samples PR0026 and PR0028, as although they were both shown to be clean in SIMS and gave low RMS values in AFM, the QDs grown on sample

PR0026 were brighter and demonstrated a lower linewidth than those grown on sample PR0028. Samples PR0027 and PR0026 showed very similar modal linewidths, whereas sample PR0028 showed a broadening in the modal single QD linewidth. Re-growth buffers of 20 nm were used for both samples PR0029 and PR0028, showing again that growing QDs near a poor quality interface negatively impacts on their brightness and single QD linewidth. In general, the QD brightness was lower than desired, suggesting that further optimisation of the AHC parameters was required.

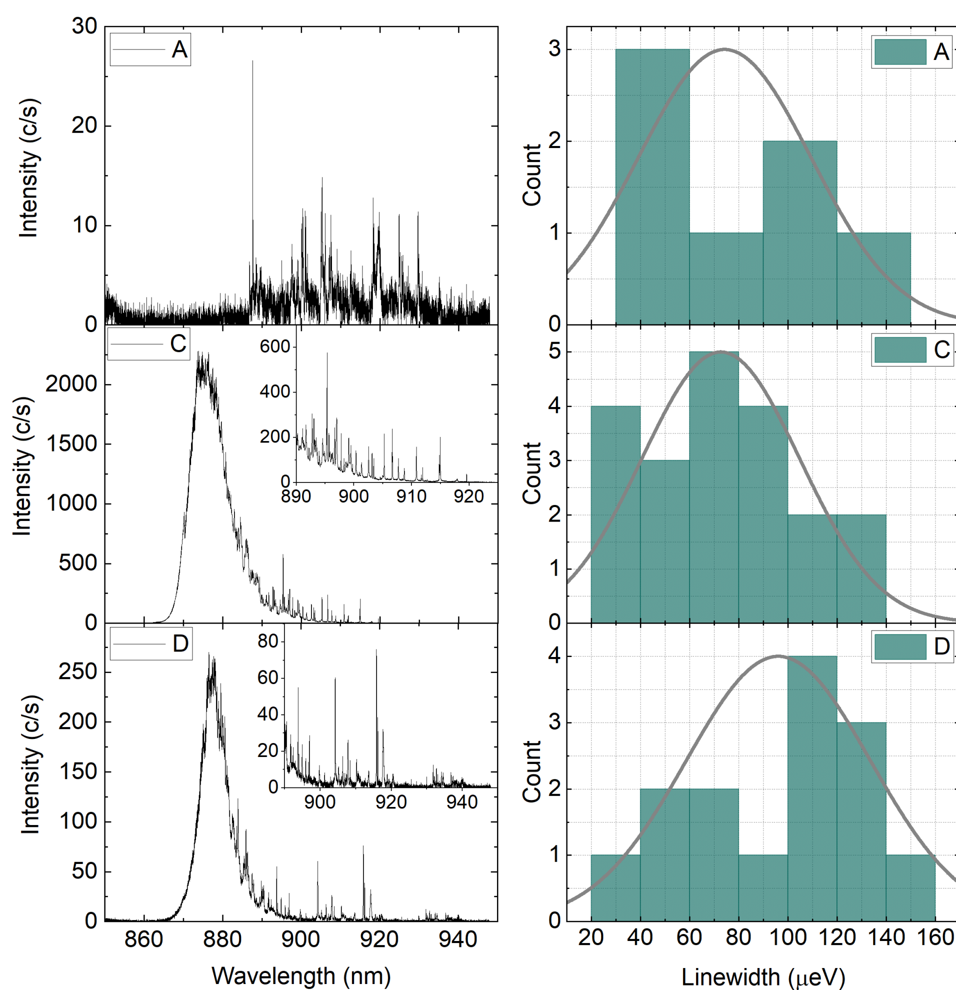

Figure 6-13. Spectra for single QDs measured using μPL at a laser power of 1.5 μW, with an integration time of 20 s for samples PR0027, PR0026, and PR0028 with corresponding single QD linewidth distributions. The inserts show a close-up of the QD lines for samples PR0026 and PR0028.

6.2.1.3 Buffers patterned with nanoholes

The final sample type to be investigated was nanohole patterned buffers, where nanohole arrays were fabricated on four samples and the HABS current was varied. SIMS analysis was used to measure the contamination levels remaining post-AHC, and AFM analysis to check the surface roughness and visualise the effect of hydrogen cleaning on the nanohole pattern. Because these samples underwent the fabrication process and so were exposed to a number of extra contaminants compared to an unpatterned buffer a longer cleaning time of 1 hour was chosen. Additionally, the substrate temperature was slightly raised to 450 °C (BandiT). Four samples were cleaned for 1 hour at a flow rate of 0.5 sccm with a substrate temperature of 450 °C. The currents applied to the HABS were 12 A, 13 A, 13.5 A, and 14 A for samples TS2776-3 A, PR0074, PR0075, and PR0076 respectively and the reduction in contamination and oxide levels were assessed using SIMS by measuring pre- and post-AHC. A short thermal desorption was undertaken in D1 (5 mins, 580 °C) before a re-growth buffer, 30 nm in thickness, was deposited on samples PR0074 to PR0076. The sample identities post-growth were PR0074 (13 A), PR0075 (13.5 A), and PR0076 (14 A). As sample TS2776-3 A underwent SIMS and AHC but was not grown on, no post-growth identifier was asigned to it.

SIMS spectra for the planar unpatterned buffer sample PR0028 was compared to the nanohole patterned sample PR0074, pre- and post-AHC. Figure 6-14 shows the SIMS spectra for these samples. The oxide intensities for the patterned and unpatterned samples pre-AHC were very similar, however the patterned sample had considerably more carbon compounds present on the surface (C_2^-, C_2H^-, and CN^-). This was caused by small amounts of organic resist remaining on the sample after ex-situ cleaning. Additionally, higher levels of salt ions were measured for the patterned sample, in particular Na^+ and Ca^+. Again they were possibly introduced during the fabrication process. AHC cannot remove ionic salts of this type, therefore investigation of alternative ex-situ removal techniques are required. For instance, a de-ionised (DI) water weir with resistivity monitoring could be used to flush water over the sample post fabrication. This mechanism could be used to quantitively analyse the point at which the ion concentration in the water is low enough

for cleaning requirements.

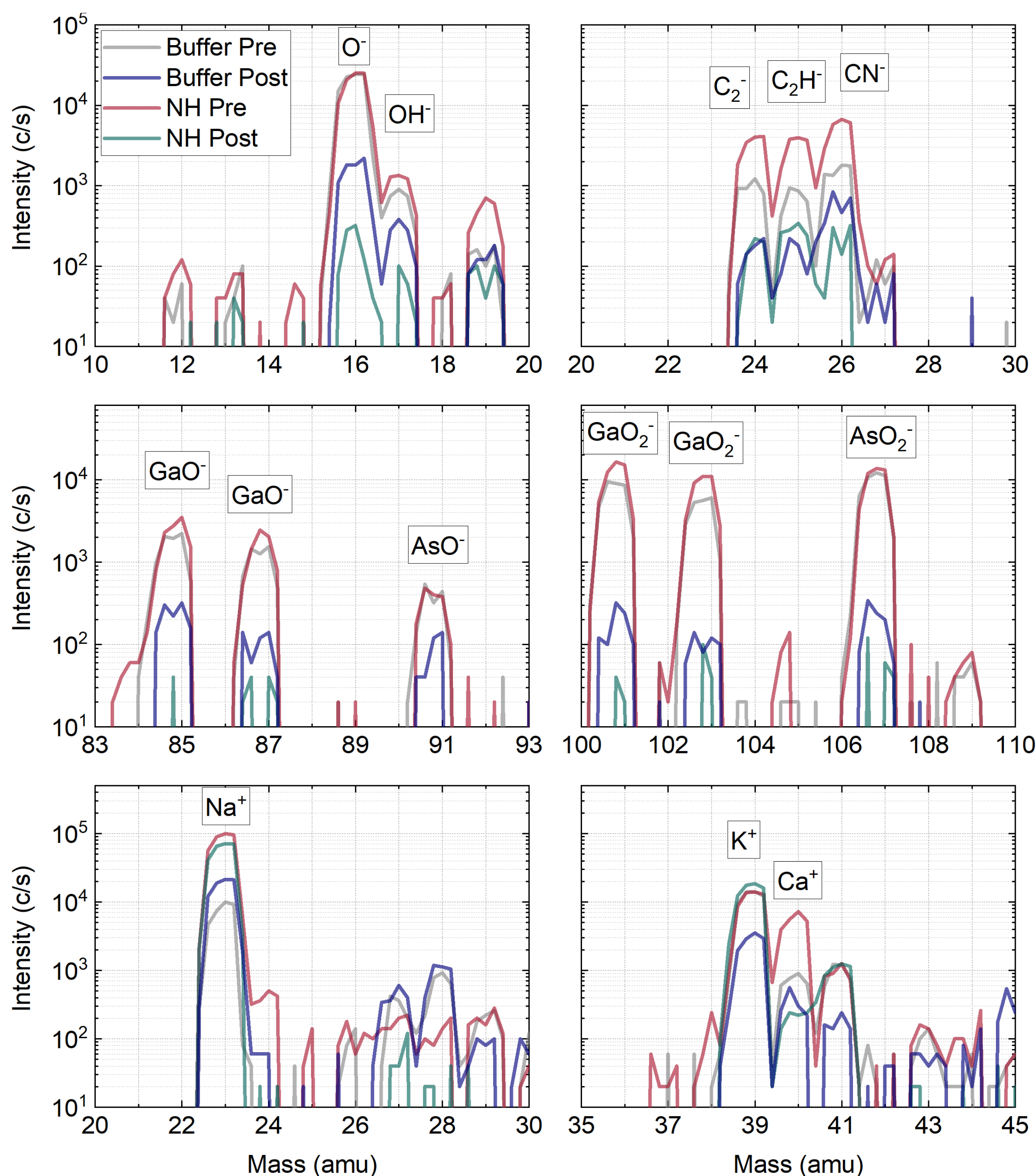

Figure 6-14. SIMS spectra for selected masses comparing planar sample PR0028 (discussed in section 6.2.1.2 labelled 'Buffer' pre- and post-AHC to nanohole patterned sample PR0074 labelled 'NH' pre- and post-AHC.

The reduction in the measured quantities of each of these masses of interest post-AHC is shown in Figure 6-15. Oxides and negative species contaminants were removed effectively for all samples, in all cases the percentage remaining after AHC cleaning was below 10 % of the starting quantity. The higher substrate temperature and longer cleaning time

compared favourably to the previous conditions used to clean the planar buffer, as between a 60 % and over 95 % reduction for negative species of interest was observed for planar sample PR0076. There was very little difference in the SIMS results for the four currents supplied to the HABS.

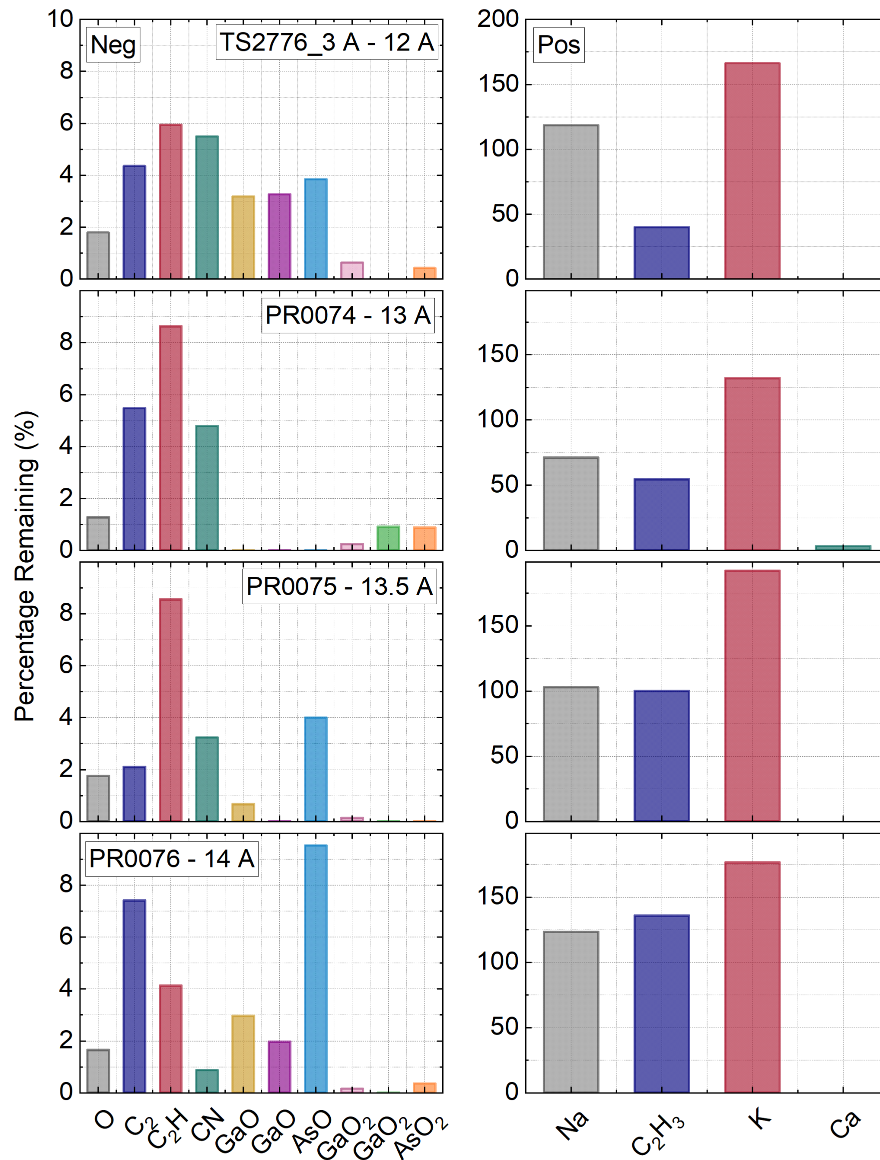

Figure 6-15. SIMS masses of interest for nanohole patterned GaAs samples TS2776-3 A and PR0074 to PR0076 remaining post-AHC.

The effect of the hotter, longer clean on sample smoothness and nanohole shape was next investigated. Figure 6-16 shows AFM images for sample PR0074 (a) nanoholes post ex-situ cleaning and (b) post-AHC and growth. A clear change in the nanohole shape and size was seen for all samples. The nanoholes became generally wider, in particular

anisotropic elongation in the [110] direction was observed. This is commonly reported in the literature [66]. Additionally, the initially round nanoholes became faceted and could be described as hexagonal in shape. The RMS for the samples did not change significantly post-growth, where the RMS values were collected from a single area for each scan, discluding the nanoholes.

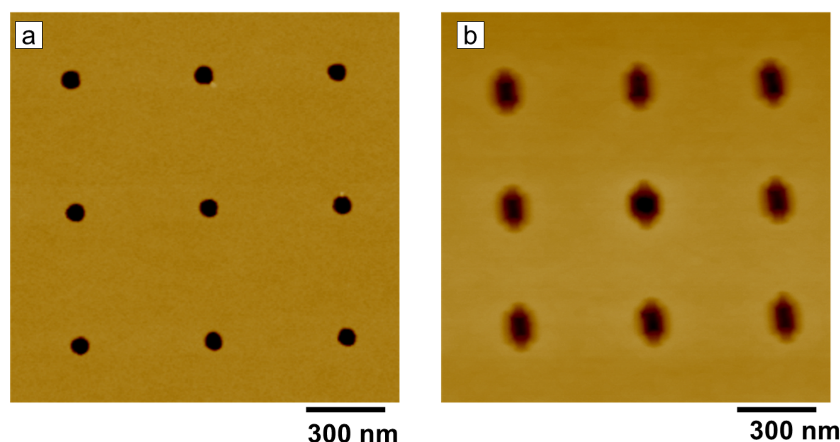

Figure 6-16. AFM images for sample PR0074 (a) directly after patterning and ex-situ cleaning and (b) post-AHC and growth of 30 nm GaAs buffer.

The next parameter to be investigated was nanohole in-filling. This describes the amount of material that has grown in the nanohole compared to the planar surface and determines the nanohole depth after growth. If no in-filling occurs then the nanohole will be its starting depth plus the amount of buffer deposited, if material grow equally in the nanohole and on the planar surface the nanohole will remain at the same (pre-growth) depth, and if material grows preferentially in the nanohole then it will become shallower post-growth. Ideally conditions should be such that nanoholes partially in-fill and therefore have a smaller depth after growth than before growth. This shows that the nanohole is an area of preferential nucleation for material, be that InAs QDs or GaAs buffer material. Additionally, if the nanohole in-fills enough the QD will be further from the fabrication interface and any sources of charge noise. Optimised in-filling can therefore assist in reducing single QD emission linewidths.

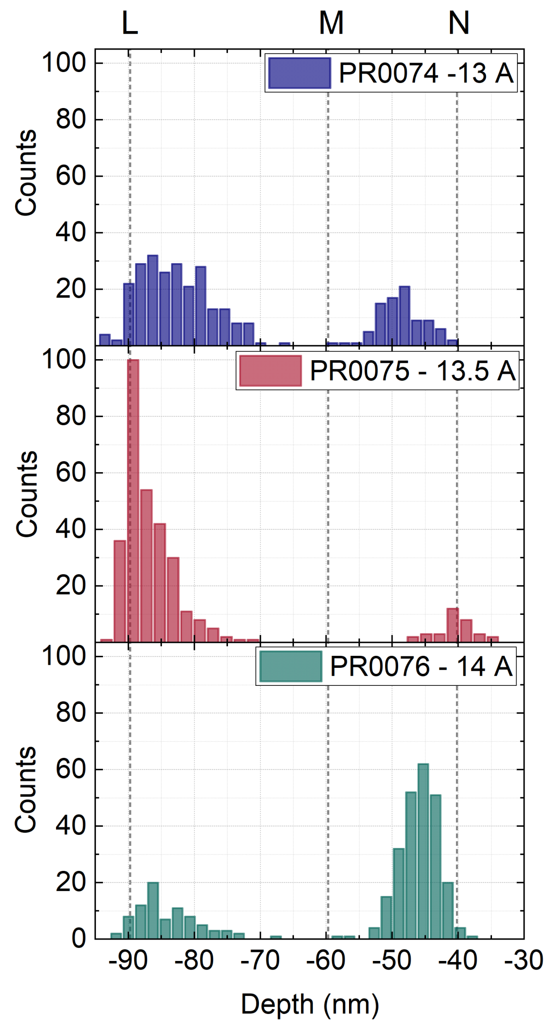

Figure 6-17. Distributions in nanohole depths post-AHC and growth for samples PR0074 (13 A), PR0075 (13.5 A) and PR0076 (14 A). Marked points L, M, and N correspond respectively to: no nanohole in-filling; the mean nanohole depth pre-AHC; and an arbitrary amount of partial nanohole in-filling, where nanoholes become 20 nm shallower.

Histograms of nanohole depth post growth for array 60 nm D4 are shown in Figure 6-17 for samples PR0074 (13 A), PR0075 (13.5 A), and PR0076 (14 A), where the data was gathered from 10 $\times$ 10 μm AFM images (18 $\times$ 18 nanohole grids). Three depths are marked, depth M is the mean depth of the nanoholes post ex-situ clean, which was 59.6 nm $\pm$ 1.7 nm, L corresponds to a nanohole depth where no in-filling occured and nanoholes were the original depth plus the buffer thickness (30 nm), N corresponds to a nanohole depth where partial in-filling occurred, and material grew preferentially in the nanohole. For case N 50 nm of material grew in the nanohole, whilst 30 nm grew on the planar surface. For all three

samples there was a bimodal distribution in the nanohole depth. For some percentage of nanoholes no in-filling was observed and for the remainder some preferential in-filling occurred. No trend in the data was observed as HABS current was increased. It was believed that the variability on nanohole depths was not caused by lack of AHC parameter optimisation, as 14 A was the highest current that could be supplied to the HABS and due to the very long cleaning time and excellent oxide removal. Therefore, buffer growth parameters were also be investigated and will be discussed in Chapter 7.

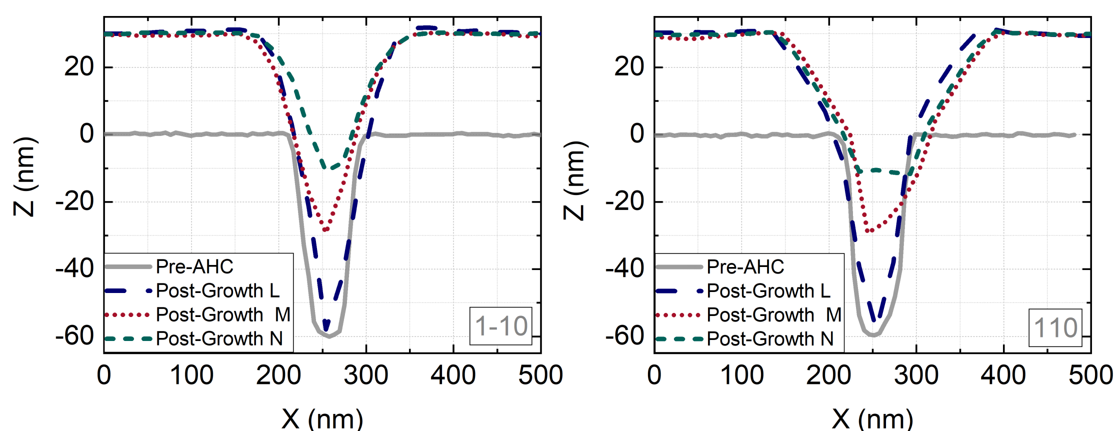

Figure 6-18. Sections through nanoholes for sample PR0074 (13 A HABS current) in the [110] and [1-10] directions pre-AHC and post-AHC and growth for nanoholes that are representative of criteria L, M, and N.

The change in nanohole depth and shape is shown for sample B. Sections were taken through AFM images of nanoholes of depth L, M, and N. The nanohole depth pre-AHC is shown in grey, the post-growth profiles are shown shifted up 30 nm to indicate the growth of 30 nm of buffer. Sections were taken in the [1-10] and [110] directions. The nanoholes show anisotropic widening in the [110] direction, as has been reported in the literature [210]. Additionally, for nanoholes where preferential in-filling occurred e.g. depth N, the bottom of the nanohole flattened, leaving two corner points in the [110] direction. These points could act as enhanced nucleation points for QDs.

6.3 Summary

A method for removing oxides and carbon contamination from a nanohole patterned GaAs surface has been developed. The process ensures surface smoothness is maintained, whilst preserving the nanohole array, demonstrated via RHEED and AFM. Production of a smooth surface was reproducibly achieved for all samples cleaned using the optimised method. Therefore, it can be seen that AHC offers a higher quality and more reproducible method for removing oxides when compared to a thermal oxide desorption process, where surface roughness was introduced, as seen in Figure 5-22. Furthermore, it was reported in the literature that after AHC surfaces at 490 °C could be pitted with a high density of small holes of 1 nm to 3 nm in depth [211]. Very low levels of contamination were shown to remain after AHC, which were measured using the optimised SIMS set-up. Production Therefore, this work shows that oxide free, smooth and pit free nanohole patterned samples can be produced by cleaning at 450 °C. The process was first investigated using epiready GaAs samples and optimised for planar buffer samples, then finally nanohole samples. The parameters assessed were substrate temperature, HABS current, and buffer thickness. Additionally, the effect of oxide thickness was investigated by AHC acid-dipped and un-processed samples, where the acid-dip was shown to assist the cleaning process. Single QD emission was demonstrated to occur from planar buffer samples and high levels of contamination in conjunction with a thin re-growth buffer was shown to cause optical inactivity in QDs. This observation clearly demonstrates the requirement for a thorough in-situ cleaning process.

This page intentionally left blank

7 | QD Growth and Characterisation

A scalable and high yield quantum information system, that uses SCQDs integrated within photonic devices as qubits, would consist of perfectly regular arrays of homogenous, low linewidth QDs that emit at the designed wavelength. Therefore, the parameters the SCQD growths will be assessed against are as follows: the mean emission wavelength of the ensemble; the size and wavelength distribution of QDs; the positioning accuracy with which QDs nucleate within nanoholes; the number of sites occupied by a QD and the occupation number of each site; and the single QDs emission linewidths. Site-controlled QDs have been shown to function properly in devices [15–17,212], however truly scalable systems have yet to be demonstrated. For integrated arrays that contain small numbers of QDs, then QDs in near neighbour sites must be similar enough to one another to allow demonstration of desired effects, such as entanglement.

7.1 SCQD sample growth overview

The growth process flow for samples discussed in this chapter is shown in Figure 7-1, where all samples were grown using the DCA MBE system. The analysis of QDs nucleated on nanoholes fabricated using EBL/ICP-RIE (EBL QDs), and LAO (LAO QDs) and measured using AFM and μPL will be discussed in this chapter. Nanohole diameter was used as a control parameter to investigate occupancy, emission wavelength, and QD size. Additionally, QD positioning accuracy was measured, and the effect of nanohole pitch on QD emission wavelength will be discussed. More detailed analysis, using site specific μPL data will be presented, where single QD linewidths and electronic properties are shown. The behaviour of EBL QDs and LAO QDs will then compared and discussed. The EBL QD

arrays will be identified by their drawn size and dose e.g. array 40 nm dose 5, would be referred to throughout this chapter as 40D5. Where nanohole parameters are described as 'pre-growth', AFM data was collected directly after ex-situ cleaning.

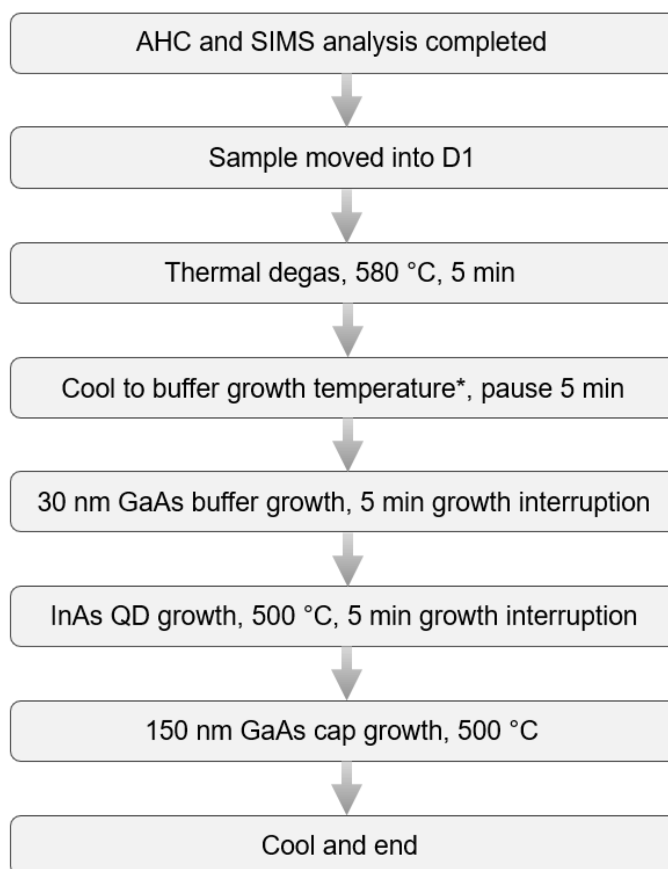

Figure 7-1. Process flow for growth of all SCQD samples from entering the growth chamber (D1) to exiting. The growth temperature was investigated, therefore a range of temperatures were used. A 30 nm re-growth buffer was used for all samples except PR0063 and PR0066, which had 15 nm of GaAs buffer deposited on them.

The thermal degas at 580 °C ensured complete removal of any oxide. Optimisation of the buffer growth temperature will be discussed in section 7.3 then the rest of the chapter will focus on the characterisation of SCQD arrays from two samples, PR0097, a capped sample suitable for PL analysis and PR0100, an un-capped sample for AFM analysis.

7.2 Initial site-controlled QD growths

To assess initial parameters selected for site-controlled growth of QDs using the DCA MBE samples PR0063 and PR0066 were grown. A 15 nm buffer and QD growth temperature of 500 °C were used and indium was deposited for 93.5 % of the 2D to 3D time at a rate of 0.01 ML/s. A temperature of 500 °C was chosen as it has been demonstrated to be a suitable growth temperature by other groups and it produced randomly grown QDs that emitted between 890 nm and 920 nm [106]. PR0063 was left un-capped for AFM analysis and PR0066 was capped for PL analysis.

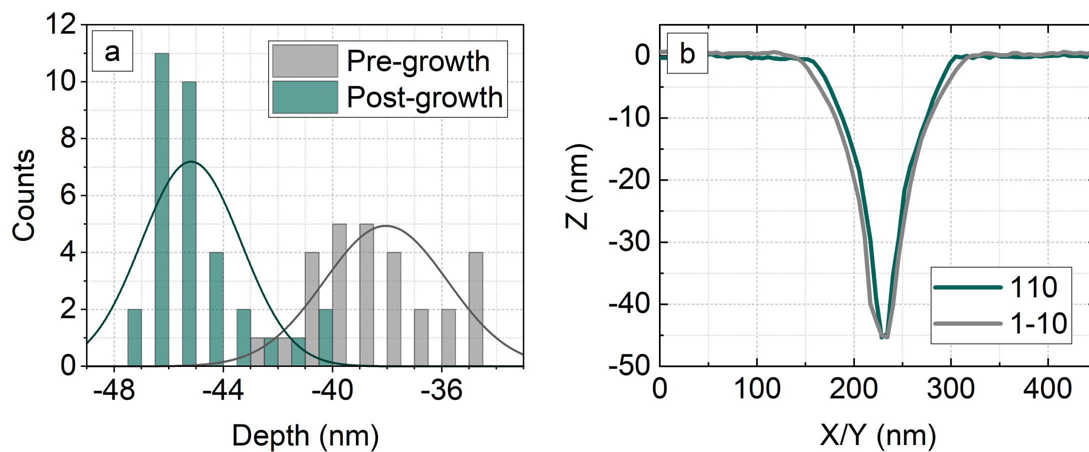

Figure 7-2. Sample PR0063 (a) distributions in nanohole depths pre-growth and post-growth, where 15 nm of GaAs buffer and QDs were deposited at 500 °C (mean pre-growth -38.0 nm ± 2.3 nm and post-growth was -45.2 ± 1.8 nm) and (b) a section through a nanohole in the [110] and [1-10] directions post-growth.

Nanohole in-filling was investigated via AFM. An area of the sample where no QD nucleation in nanoholes occurred was chosen. The same nanoholes were measured pre- and post-growth and the depth distributions are shown in Figure 7-2 (a). The mean nanohole depth increased from 38.0 nm ± 2.3 nm to 45.2 nm ± 1.8 nm post-growth. Therefore, an increase of 7.2 nm was associated with 15 nm of buffer deposition and 1.59 ML of InAs deposition, meaning that the growth rate in the nanoholes was slower than for the planar surface. The shape change of the nanohole was also assessed in (b) by taking a section through an AFM image from Figure 7-3 (a), where it can be seen that the nanoholes were close to being circular and no elongation in the [110] direction was observed. This is un-

like the observed behaviour for samples that had only undergone AHC and buffer growth or InAs deposition, as seen in Chapter 6.

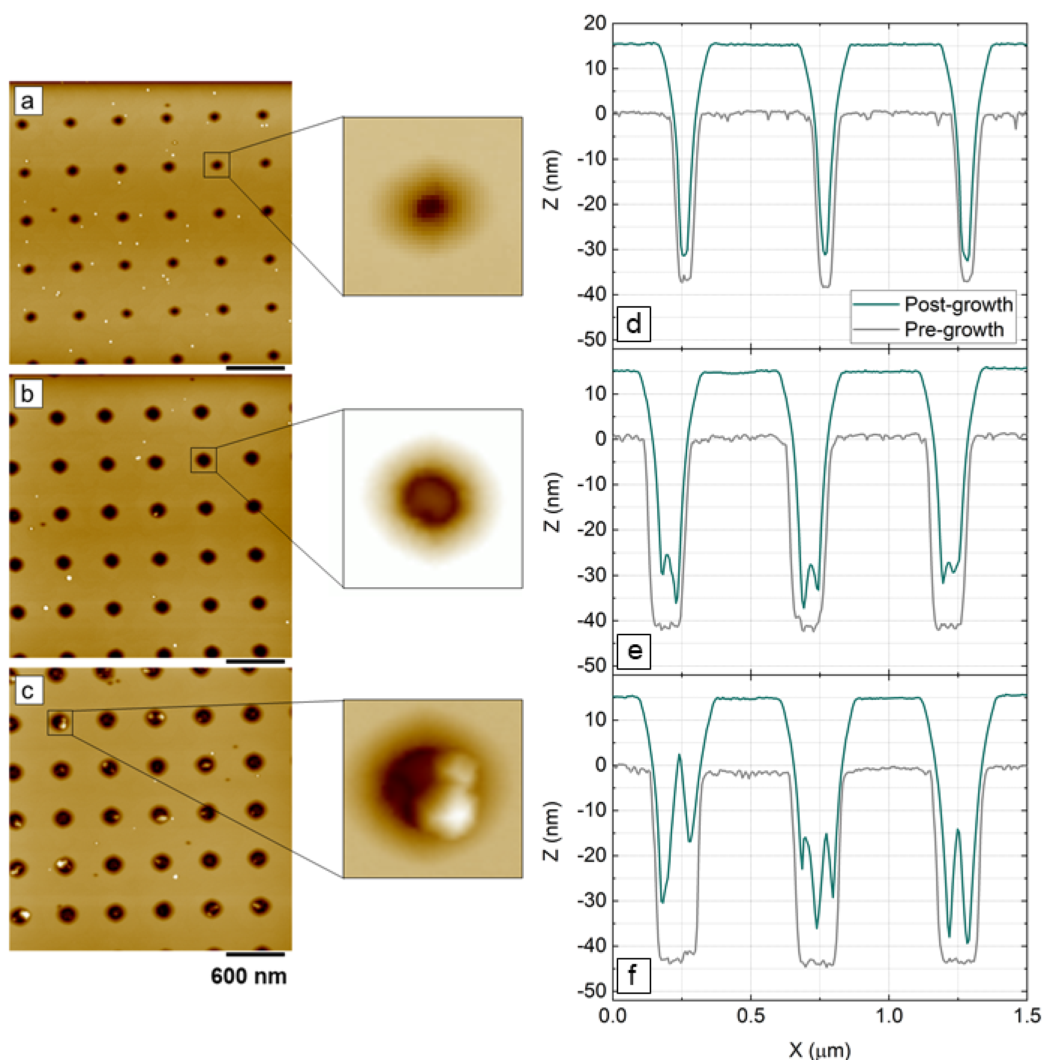

Figure 7-3. Sample PR0063, AFM images of QD growth on patterned surfaces/corresponding sections (a)/(d) for area 50D4, mean nanohole diameter 144.2 $\pm$ 6.3 nm, (b)/(e) area 60D5, mean nanohole diameter 184.7 nm $\pm$ 6.6 nm and (c)/(f) area 50D6, mean nanohole diameter 224.6 nm $\pm$ 19.1 nm.

EBL arrays of 0.5 μm pitch for sample PR0063 were measured via AFM for areas where QDs nucleated in nanoholes. Figure 7-3 shows AFM images for small, medium and large nanoholes and corresponding sections through representative nanoholes. In array (a) nanoholes were narrower in diameter than the other arrays and no site-controlled QD growth was observed. Additionally, many QDs nucleated between nanoholes; 39 non-site controlled QDs grew in an area containing 30 nanoholes. For area (b) nanoholes were

wider and 100 % of nanoholes were occupied by small, single site-controlled QDs, as can be seen in the section in (e). Fewer QDs nucleated between nanoholes; 12 non-site controlled to 30 site-controlled. Finally, (c) demonstrated the largest nanoholes for the shown arrays, which nucleated multiple QDs per site.

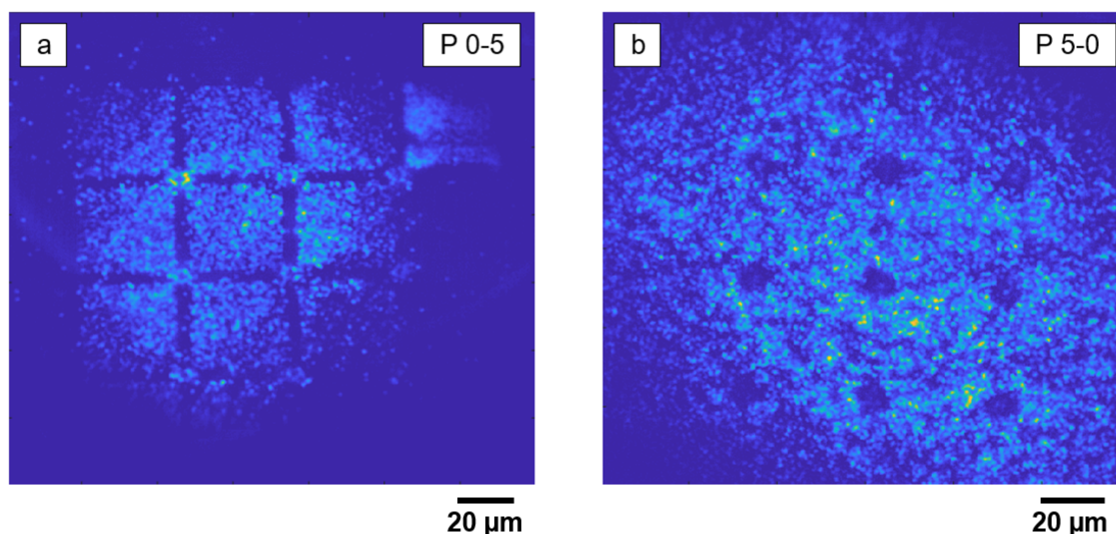

Figure 7-4. PR0066, PL images, with the same field of view, showing emission from patterned areas with a pitch of (a) 0.5 μm and (b) 5 μm with a 890 nm long pass filter in place.

The capped sample, PR0066 was measured in PL, using the PL imaging set-up described in Chapter 3. Figure 7-4 shows images for (a) 0.5 μm and (b) 5 μm pitches. The 0.5 μm pitch was below the imaging resolution limit of the set-up, so it would not be possible to resolve an array of single QDs. However, it can be seen that the pattern had an effect on QD nucleation, as there were square arrays, separated by regions without emission. However, at the 5 μm pitch, which was over double the imaging resolution distance, there was some change in nucleation around the alignment mark region but still no clear array of QDs could be seen. It is likely that due to the large numbers of QDs nucleated between nanoholes, any regular pattern was masked. It was concluded from this experiment that further optimisation of growth conditions was necessary to prevent QDs nucleating between nanoholes.

7.3 Optimising nanohole and growth parameters

To suppress QD nucleation between nanohole sites nanohole depth and buffer growth temperature were varied. The aim was for material to preferentially nucleate within the nanoholes, so that a subsequently nucleated QD would be further from the fabrication interface without causing complete planarisation of any nanoholes.

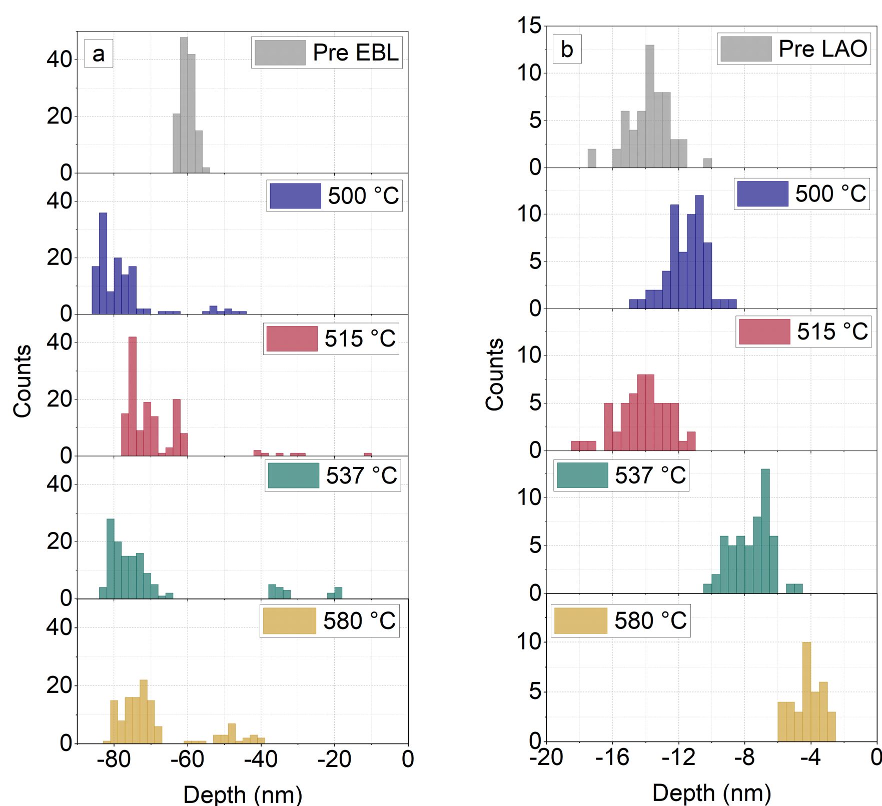

Figure 7-5. Samples, PR0082, 83, 84, 85, nanohole depths pre-growth and post-growth of 30 nm of GaAs buffer growth at a range of temperatures 500 °C (PR0082), 515 °C (PR0085), 537 °C (PR0084), and 580 °C (PR0083), for (a) EBL fabricated nanoholes and (b) LAO fabricated nanoholes, pre-growth and post-growth while varying buffer temperature. Note that the x-axis on (a) and (b) are different to one another

.

Figure 7-5 shows distributions in nanohole depth for nanoholes fabricated via EBL (a) and LAO (b) pre-growth and post-growth. Four samples were grown using 30 nm of GaAs buffer whilst varying the growth temperature. The EBL nanoholes were $\sim$ 60 nm deep

pre-growth and the LAO nanoholes ∼ 14 nm. In general, the EBL nanoholes did not become shallower and there was no trend associated with the increase in temperature. Conversely, LAO nanoholes became shallower at a temperature of 537 °C, and 580 °C. After this point a trend was observed with increased temperature. However, almost 20 % of LAO sites were completely planarised at 580 °C. As the aim was to use a growth temperature that allows some in-filling without planarisation or loss of nanoholes within the array, a growth temperature of 537 °C was the most favourable of the temperatures studied.

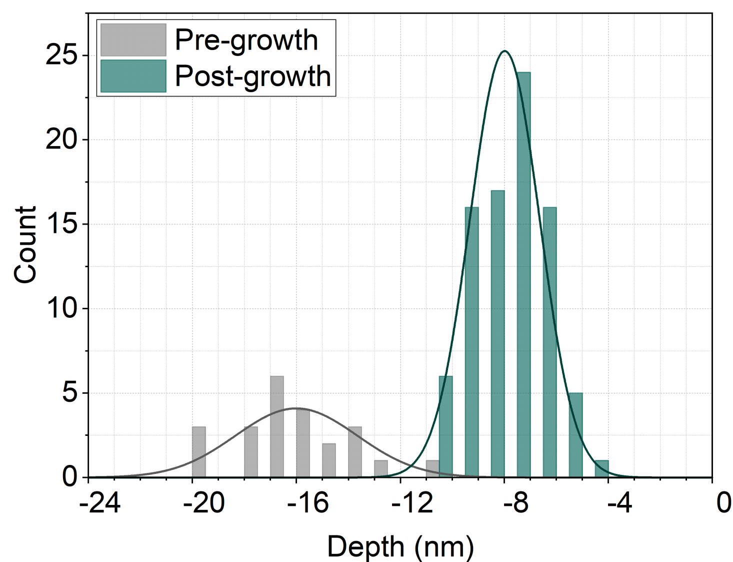

Figure 7-6. Sample PR0093 nanohole depth pre-growth and post-growth of 30 nm of GaAs buffer growth at a temperature of 537 °C and InAs QD deposition at 500 °C.

The observed difference in nanohole depth change for LAO and EBL fabricated nanoholes was assessed to see whether the fabrication method or the difference in nanohole depth pre-growth was the cause. This was done by fabricating a new EBL nanohole array sample, PR0093, with shallower nanoholes that matched LAO depths. Again, 30 nm of GaAs buffer was grown on them at a temperature of 537 °C and InAs QDs were deposited at 500 °C. The depth distributions pre- and post-growth are shown in Figure 7-6. The same behaviour that was observed for LAO nanoholes with a pre-growth depth of ∼ 14 nm was observed for EBL nanoholes with a pre-growth depth of ∼ 16 nm. None of the nanoholes within the array fully planarised.

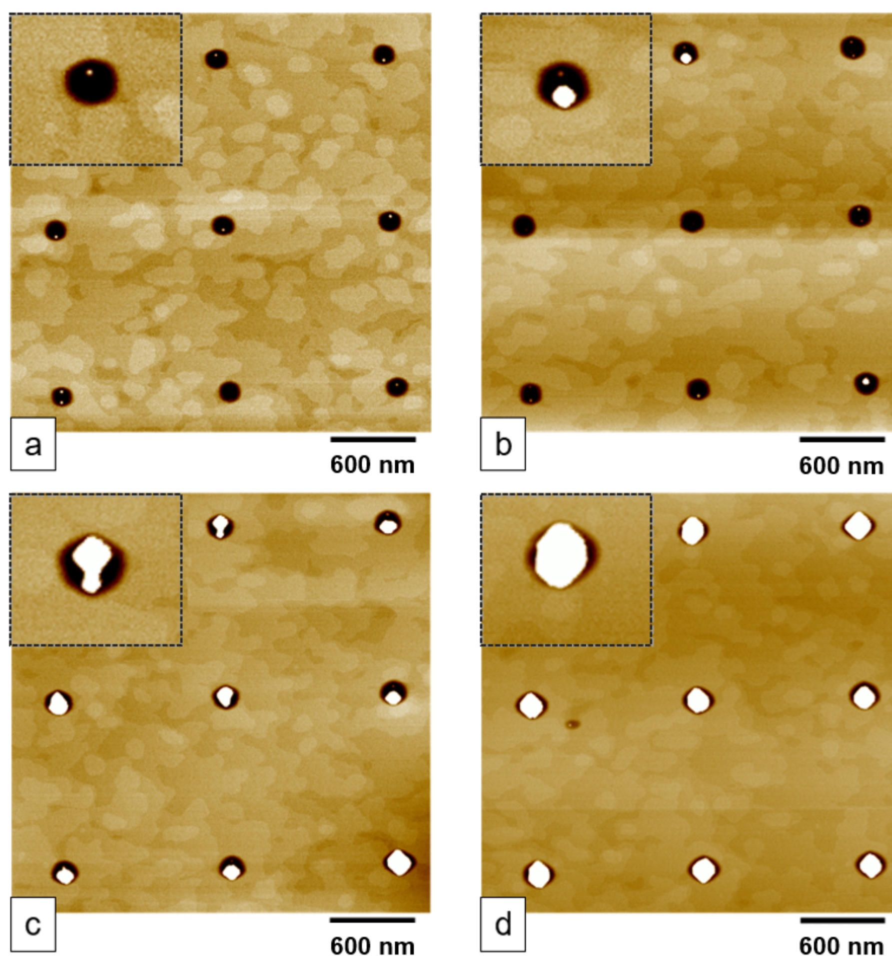

Figure 7-7. Sample PR0093, AFM images cropped from areas (a) 40D3 (b) 40D4 (c) 40D5 and (d) 60D5 showing QD or large 3D island size and occupancy varying with nanohole size. The inserts show a zoomed in crop out of a representative QD/3D island from each image.

Areas where QD nucleation occurred in nanoholes were measured for sample PR0093. AFM images in Figure 7-7 are shown for nanohole arrays of various sizes. Firstly, it can be seen that QD growth between nanoholes was eliminated by using a buffer growth temperature of 537 °C. Additionally, there was a clear relationship between nanohole size and QD size. In (a) 69 % of the nanoholes were occupied by small QDs, (b) there was a bimodal distribution in sizes, (c) 62.5 % of nanoholes were occupied by large QDs, with the remainder of the sites being occupied by a large and a small QD, and (d) 100 % of sites were occupied by single, 3D islands that are most likely optically inactive due to their large size. A 3D AFM image of a larger portion of the array for array (d) is shown in Figure 7-8 (a) and a section through a large and small QD is shown in (b). The next section will discuss

the impact of nanohole size on QD size and emission wavelength in detail. The effect of indium coverage amount was compared for samples where indium was deposited for 93 % (PR0093), 92.5 % (PR0095), 92 % (PR0092), and 91 % (PR0094) of the 2D to 3D time. No trend in QD height was observed when changing this parameter over this range.

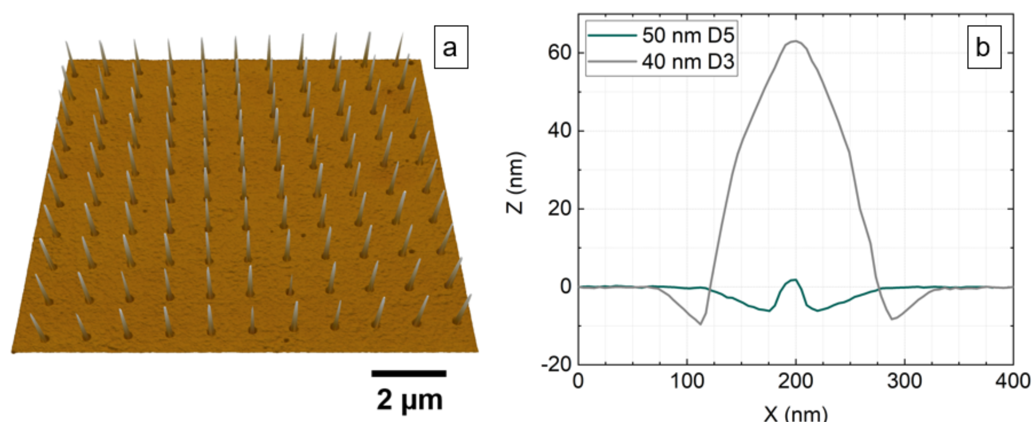

Figure 7-8. Sample PR0093, (a) a 3D AFM image of large, single 3D islands from array 60D5 and (b) a section through large 3D islands (60D5) and small (40D3) QDs showing the difference in size.

7.4 Characterisation of site-controlled QD arrays

The remainder of this chapter will focus on the comparison between two samples, PR0097 a sample capped for PL analysis and PR0100, a sample left uncapped for AFM analysis. Nanohole arrays were fabricated using EBL/ICP-RIE and LAO for direct comparison in the same growth, which as yet has not been reported on in the literature. All nanohole diameters will be expressed in pre-growth dimensions as this was the control parameter used to investigate the effect on QD properties. Nanohole diameter is an important parameter for controlling SCQD properties. The dependence of nanohole depth on diameter is shown in Figure 7-9 (a). In subsequent analysis, parameters such as QD height, were found to have the same dependence on nanohole depth as diameter due to the linear coupling of the two parameters. In (b) a histogram of nanohole diameter before and after growth is shown. The mean diameter before growth for these nanoholes was 81.2 nm ± 2.7 nm and after growth was 183.2 nm ± 12.1 nm. It was not possible to obtain completely accurate results for post-growth nanoholes, due to the presence of the QDs, however in general

nanoholes increase in diameter by around 100 nm.

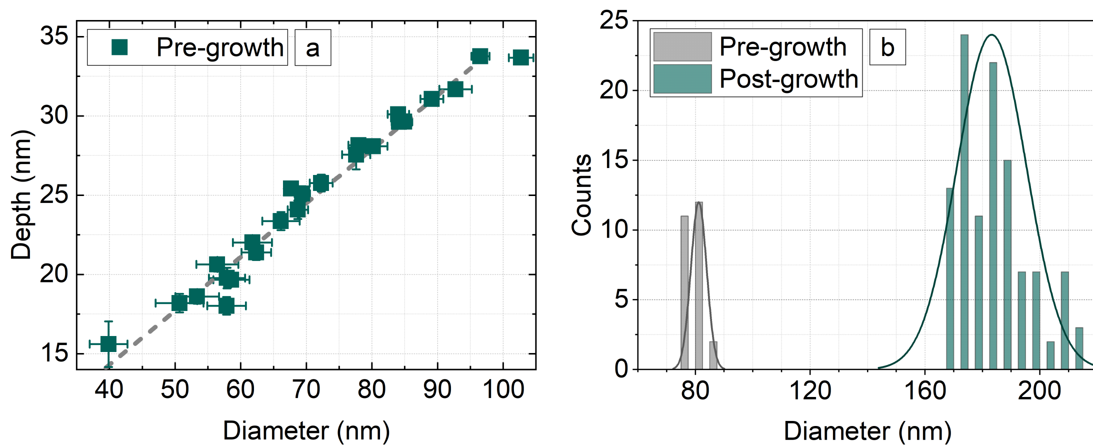

Figure 7-9. Sample PR0100, (a) the relationship between nanohole diameter and nanohole depth pre-growth, a linear fit is added as a guide to the eye and (b) histograms showing a typical increase in nanohole diameter pre- to post-growth.

A reminder of the EBL pattern used is shown in Figure 7-10 (a). Image (b) shows an example of a PL image of SCQD emission in regular arrays. The corresponding arrays are marked with the dotted red square (32D7, 32D8, 40D7, and 40D8). The alignment crosses appeared as lines that are orientated in the [110] direction. At the end of the [1-10] arm of each cross, a point of emission can also be seen. An example AFM image of a SCQD array is shown in (c), for array 40D8, for a pitch of 0.6 μm.

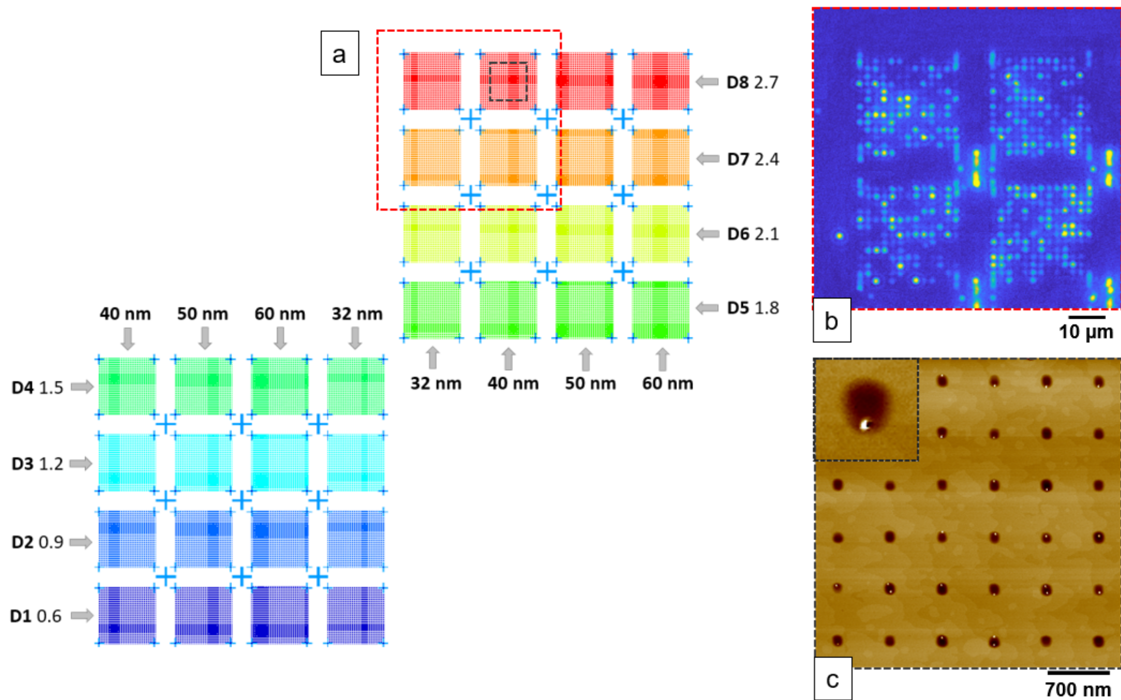

Figure 7-10. (a) EBL pattern for nanohole arrays with drawn sizes 32 nm to 60 nm and doses 1 to 8, (b) a PL image of SCQDs from the indicated area (red box) of the pattern and, (c) an AFM image from the indicated area (black box) of the pattern where the insert shows a zoom in of a typical QD.

An AFM image of an alignment cross is shown in Figure 7-11. QDs aligned themselves in the [110] direction, and did not favour growth in the [1-10] direction, which matches the observation seen in PL imaging.

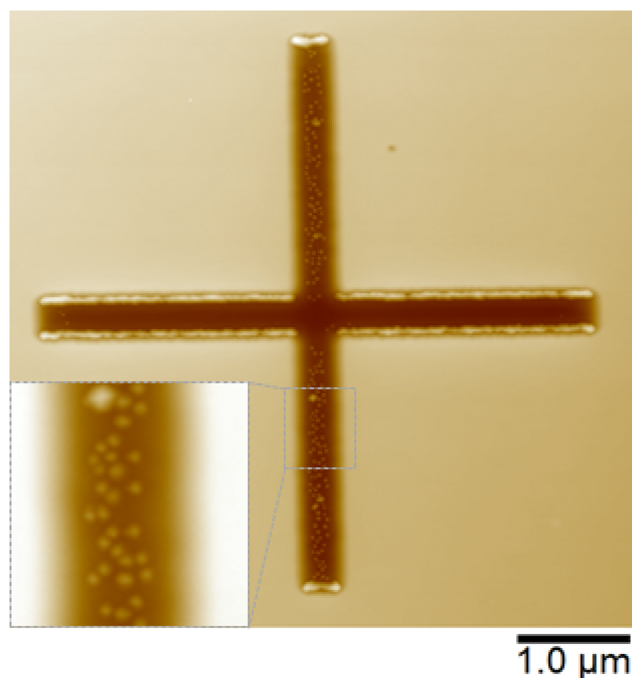

Figure 7-11. Sample PR0100, AFM image of an alignment cross, showing QDs predominently growing down the y arm of the cross.

To gather site-specific data such as emission wavelength and single QD linewidths, μPL spectroscopy was used. An example spectrum is shown in Figure 7-12. The single QDs showed bright and clear lines. Spectra covering the range 900 nm to 1000 nm were acquired for each array, with the grating selected depending upon the required integration time and spectral resolution. Neutral exciton, charged exciton, and biexciton lines were identified using power dependence and FSS measurements, which will be discussed further in section 7.4.4.

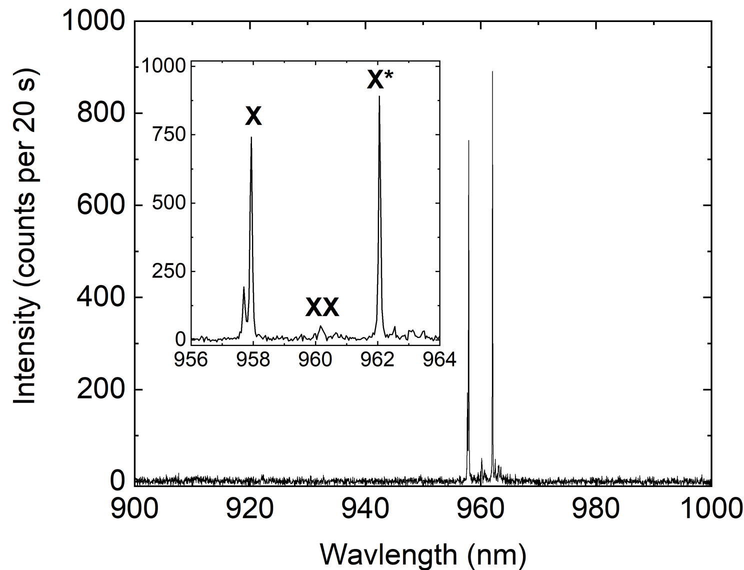

Figure 7-12. A μPL spectrum of a single SCQD excited at an LED voltage of power 0.495 mW and the insert showing a zoom in of the neutral, charged and biexciton lines, which are identified later in the chapter.

Results from samples PR0097 and PR0100 will now be discussed, predominantly focusing on 2.4 μm pitch. The pitch was chosen with device integration in mind, where the lattice period of a W1 waveguide optimised for 920 nm is 240 nm. Using a pitch that is a multiple of this value allows a number of QDs to be deterministically placed along the waveguide at equivalent points (e.g. in positions where chiral behaviour is supported). Additionally, QDs grown at this pitch are spaced far enough apart to allow arrays of devices to be fabricated around them, without the risk of multiple QDs being present within a device. Finally, this pitch allows for easy characterisation of the QDs, due to the resolution of the imaging set-up being around 2 μm.

7.4.1 PL imaging analysis

Figure 7-13 shows PL imaging from array 40D7 using a range of long pass (LP) filter settings, note the roll off of the filter was $\sim$ 20 nm. Values between 900 nm and 1000 nm in steps of 25 nm were recorded. For 900LP, a regular array of QDs of varying brightness was observed. As the wavelength cut-off shifted towards longer wavelengths some of the bright QDs were seen to disappear. At 1000LP a clear array of emitting QDs was still seen.

This observation indicates that there were many QDs within the array that emitted at a wavelength near to or longer than 1000 nm, where the detector loses sensitivity. However, the filter roll-off must also be considered, which was around 30 nm. Therefore, accurate wavelength information cannot be obtained by using the imaging camera alone and instead μPL spectroscopy was required to gather precise wavelength information, which will be shown in Figure 7-18. A small number of QDs were observed to disappear (60 dropped to 55), suggesting that a small number of shorter wavelength QDs were present within the array. This observation was supported when measuring the array using the spectrometer and will be discussed in more detail subsequently.

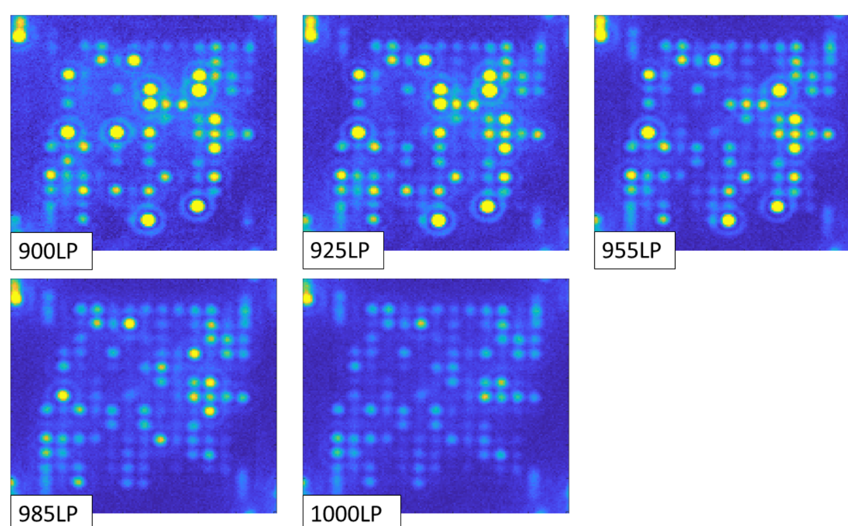

Figure 7-13. PL images of array 40D7 using an excitation power of 3.1 V (5.21 mW) and a long pass (LP) filter at 900 nm, 925 nm, 955 nm, 985 nm and 1000 nm.

Using images taken with a 900 nm LP filter in place, the percentage of sites that demonstrated emission was found for all arrays. Figure 7-14 shows the percentage occupancy for each array, where EBL parameters drawn size and dose are marked. The dark regions correspond to arrays where no emission was observed. It can be seen that the highest occupancy areas were 50D3, 40D7 and the cluster in the top left of the pattern (32D7, 40D7, 32D8 and 40D8).

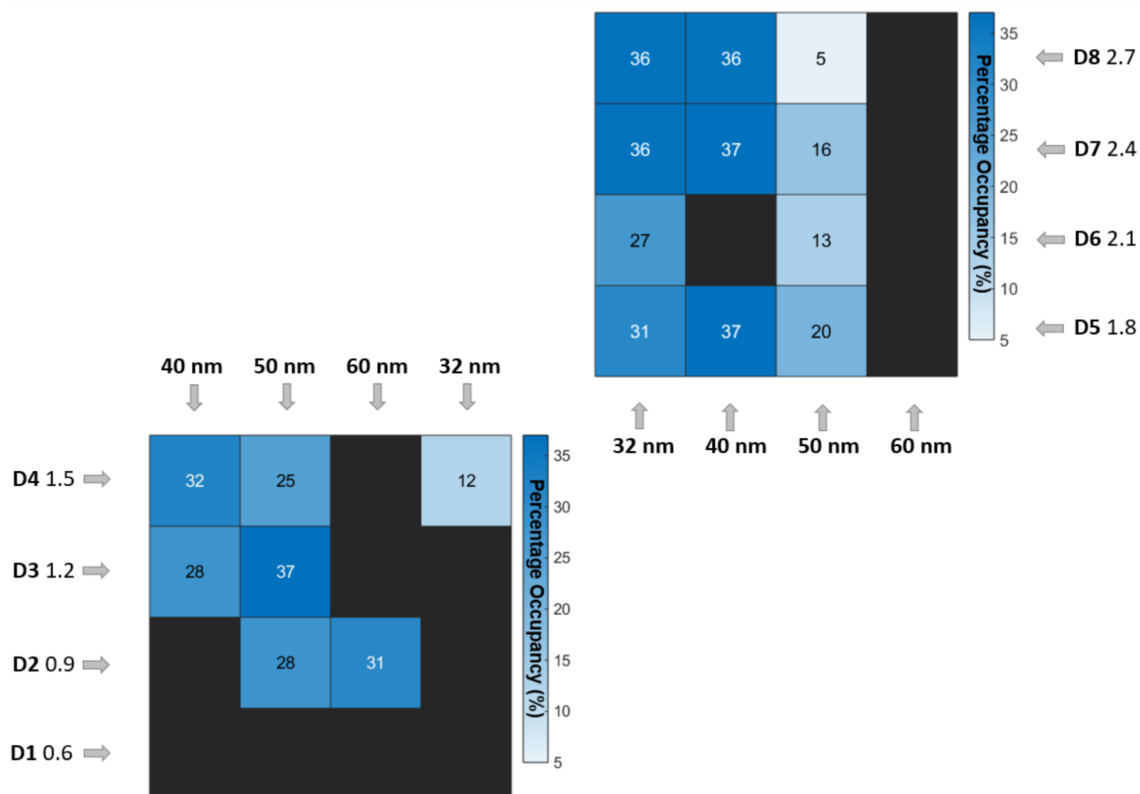

Figure 7-14. An occupancy map for all arrays of sample PR0097. The percentage of sites in each array that showed emission in PL imaging is indicated. Arrays where no emission was observed are dark areas.

7.4.2 PL spectroscopy and AFM analysis

Detailed analysis, using μPL and AFM techniques, will now be discussed for areas 50D2, 60D2, 40D3, 50D3, 40D4, 50D4, 40D5, and 40D7, which provide a range a nanohole sizes for comparison. The areas were chosen to allow investigation into how QD emission parameters, within the wavelength region of interest, were affected by changes in nanohole size.

7.4.2.1 Occupancy

It is desirable for each nanohole site in an array to be occupied by a single QD so that device yield is maximised. Figure 7-15 shows the percentage of sites in an array that contained an optically active QD (PL) and the percentage of sites that were occupied by one or more QDs (AFM) as a function of nanohole diameter. For μPL spectra single QD

lines were observed. A nanohole diameter of 66 nm produced the highest percentage of occupied sites in PL of 24 %. For AFM, 100 % of sites were occupied for nanohole diameters over 77 nm.

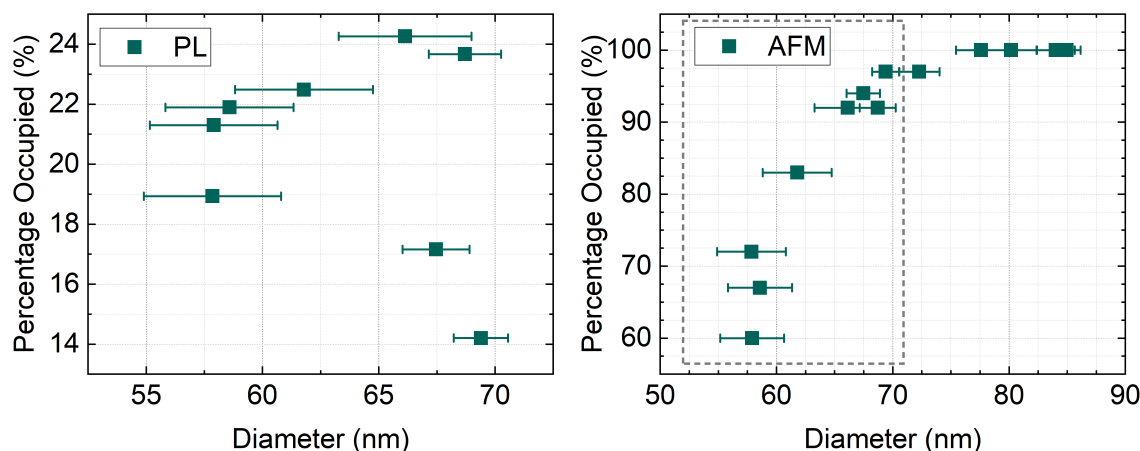

Figure 7-15. Percentage of occupied sites measured using muPL spectroscopy and AFM as a function of nanohole diameter. The box on the AFM graph indicates the nanohole diameter over which emission was observed in PL.

To understand this observation further, the single and double occupancy percentages were extracted for the AFM sample. The remainder of nanoholes were either unoccupied, or in a small number of cases were triple occupied. Figure 7-16 shows that in small nanoholes, single occupancy was most prevalent, highest single occupancy was 53 %. For medium nanohole diameters, single occupancy dropped and more sites were doubly occupied. As nanoholes and QDs became larger this behaviour reversed and the majority of nanoholes were occupied by large single QDs.

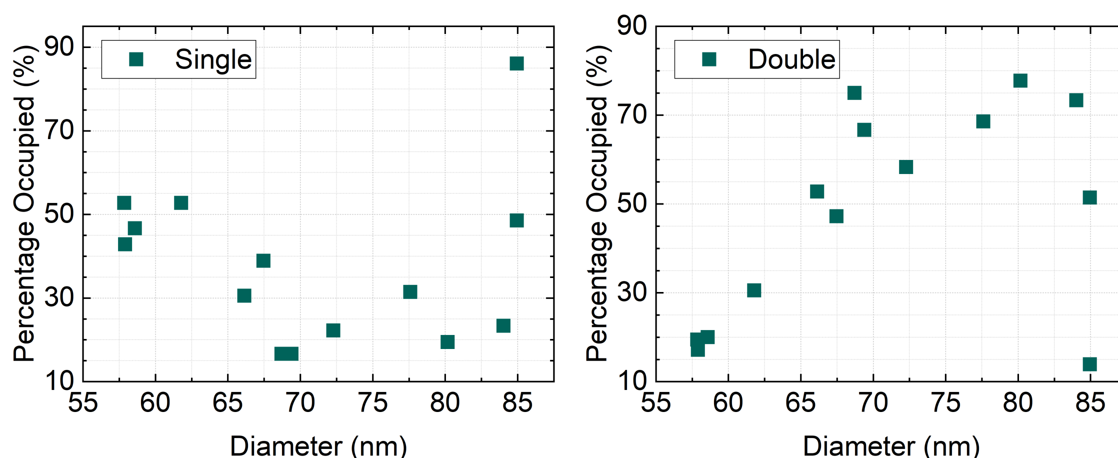

Figure 7-16. AFM occupancy data showing the percentage of single or double occupied sites as a function of nanohole diameter.

These observations show that there was a difference between the percentage of sites containing an optically active QD emitting between 900 nm and 1000 nm, and the percentage of sites containing a single QD. Figure 7-17 compares the percentage of sites occupied by single QDs measured via AFM and measured using the PL imaging camera. For the two samples the behaviour was reasonably similar for nanoholes above 65 nm in diameter, however below 65 nm more sites were observed to be occupied by single QDs for the AFM sample. There are a number of possible reasons for this observation. Firstly, the capping process could dissolve the smallest QDs, meaning that they would be seen in AFM but would no longer be present for the PL sample. Alternatively, the QDs could be optically inactive. Additionally, there is evidence for some emission outside the detection range of the spectrometer in smaller nanoholes as emission was still detected using the 1000 nm LP filter. Future studies should involve measuring the ensemble emission from the arrays using an InGaAs camera. Transmission electron microscopy (TEM) could be used to ascertain whether small QDs are dissolved in the capping process or present and optically inactive. It should also be noted that for the larger diameter nanoholes, the single QDs measured via AFM were also large. Therefore, PL emission was likely being observed from a site containing a small, multiple occupancy QD.

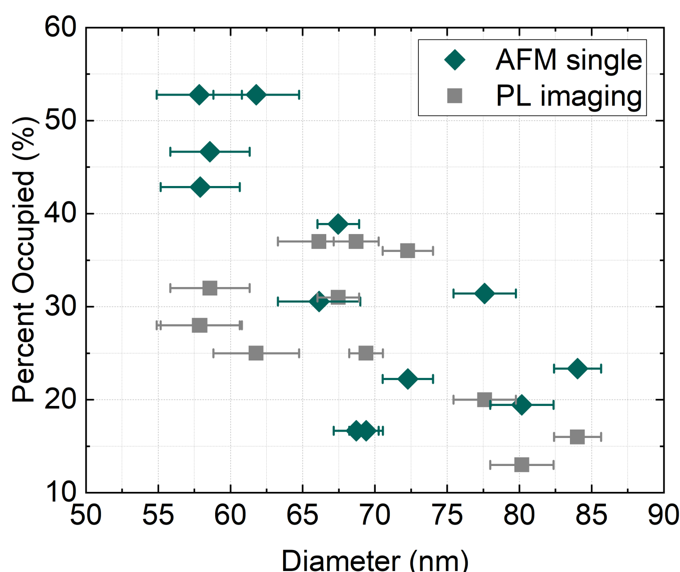

Figure 7-17. Percentage of sites from which emission was observed in imaging PL and that were occupied by a single QD in AFM as a function of the mean nanohole diameter. Note that the largest nanohole diameters (< 85 nm) are not included as little or no emission was observed from these areas.

7.4.2.2 QD emission wavelength and size

The mean emission wavelength as a function of nanohole diameter is shown in Figure 7-18 (PL) and the mean QD height as a function of nanohole diameter (AFM). For the PL measurements the mean was taken from all optically active QDs in the array, which consisted of 165 nanoholes. For the AFM measurements a representitive scan size of 15 x 15 μm, which consisted of 36 nanoholes. A smaller range of nanohole diameters are shown in PL as no emission was visible from the larger diameter arrays. Over the range shown, there was very little change in mean emission wavelength. The corresponding region is marked on the AFM graph by the grey dotted box. In AFM there was no significant increase in height over the range of 55 nm to 65 nm and a small increase in mean QD height from 65 nm to 70 nm, however beyond this range there was a significant increase. The smallest QDs showed small height deviations and appeared to be homogenous in size. The wider distribution in QD heights for nanoholes from around 72.5 nm to 84 nm were associated with a bimodal distribution in QD sizes. It is proposed that the lack of observable emission in PL from arrays with larger nanoholes sizes was due to an increase in QD size, and therefore emission from QDs in these areas was either outside the detection range of the set-up or the QDs/3D islands were optically inactive. Nanoholes below 70 nm in diameter are therefore of particular interest as this range seems to produce emission in the desired wavelength range.

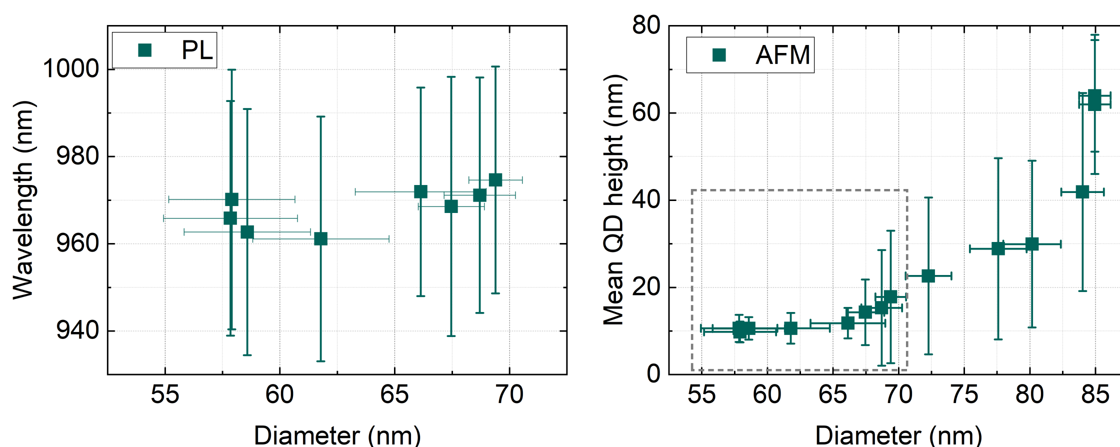

Figure 7-18. Mean QD wavelength (PL) and mean QD height (AFM) as a function of nanohole diameter, where the grey box indicates the nanohole diameters over which PL emission was observed.

Example AFM images of various QD sizes that change from single to double to single occupancy as nanohole diameter increased is shown in Figure 7-19. When assessed against the growth aims, it can be concluded that small nanoholes provide the best environment for nucleation of QDs that are small, have narrow size distributions, and show single occupancy. Very large nanoholes also lead to single, size homogenous QDs. Depending on nanohole diameter, the minimum energy configuration transitions between smaller, double occupancy QDs and single, large QDs.

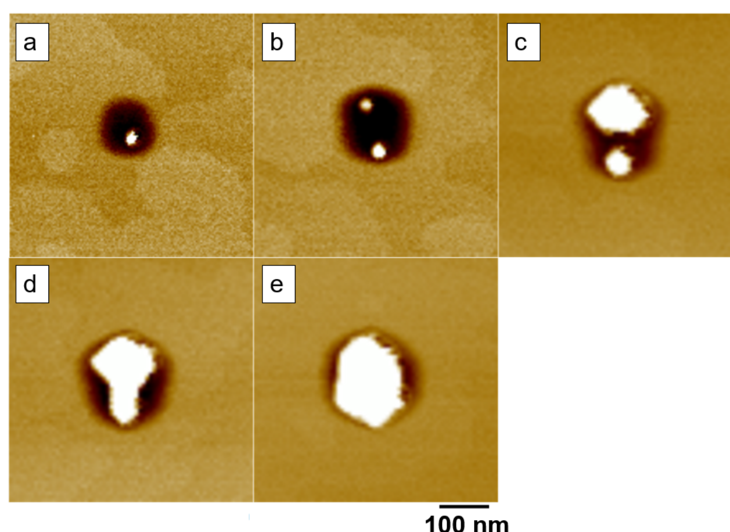

Figure 7-19. AFM images showing examples of (a) single, small QDs (b) double, small QDs (c) double, bimodal sized QDs (d) a single, large QD which appears to have formed after two different sized QDs coalesced and (e) single, large QDs. The nanohole crystals (d) and (e) will be referred to as QDs, however this is not necessarily an accurate description due to their size and lack of confirmation of optical activity.

7.4.2.3 QD positioning accuracy

As discussed, the positioning accuracy of a QD (deviation from its designated position in the regular array) has a significant impact on how well light from the QD couples to a cavity mode or how well chiral behaviour is expressed. Figure 7-20 shows example AFM images for the position of nucleation of QDs in (a) small and (b) large nanoholes. It can be seen that in the small nanoholes QD nucleation occurred along the [110] axis for single or double QDs. For large nanoholes, the QDs were large enough to fill the nanohole with their apex being at the centre, meaning there was excellent positioning accuracy.

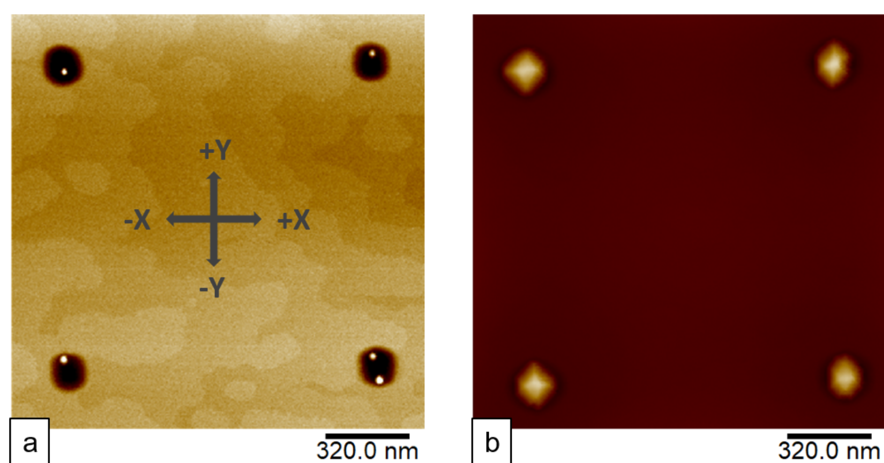

Figure 7-20. Example AFM images for (a) small nanoholes containing small QDs, aligned in the [110] direction and (b) large nanoholes containing single, large QDs nucleated at the center of the nanoholes. The $\pm$ X/Y directions in relation to Figures 7-21, 7-22 and for subsequent analysis of LAO QDs are indicated.

Figure 7-21 shows the distribution of deviations in QD nucleation position, for small nanoholes (50D2). In the X axis deviations were distributed between -18 nm and +15 nm, for single QDs. In Y, the deviation was much larger and there was a bimodal split between positive and negative deviations, which corresponded to the two ends of the nanoholes. For single QDs, the largest deviations were − 54 nm and + 44 nm, with the mean being -39 nm and +26 nm. This behaviour could be explained through the preferential migration of material in the [110] direction, which also caused QD growth along one arm of an alignment cross. The double QDs behaved in the same manner. This deviation compares favourably to figures seen in the literature, for SCQD and registration techniques. A deviation of this magnitude would cause a drop in the Purcell enhancement by between 30 % and 70 % depending on the orientation.

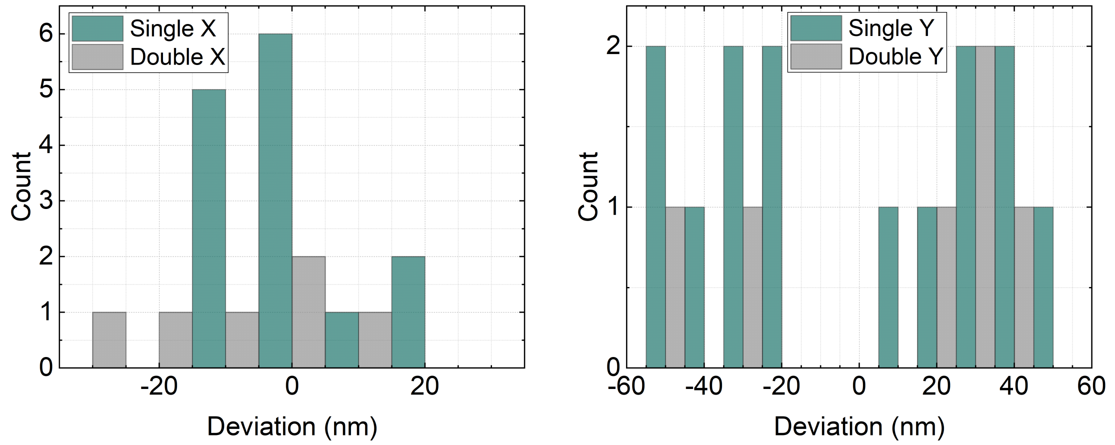

Figure 7-21. QD positioning deviation with respect to nanohole centre in X [1-10] and Y [110] for small nanoholes (50D2) at pitch of 2.4 μm for single or double QDs.

Figure 7-22 shows deviations for QDs nucleated in large nanoholes (50D8). As seen in the AFM image, large single QDs nucleated at the centre of the nanohole and so were very well positioned. Double QDs nucleated at the opposite ends of the nanoholes in the Y direction, as seen for smaller nanoholes. As seen previously, the large QDs although homogenous and well positioned, did not emit within the wavelength region of interest.

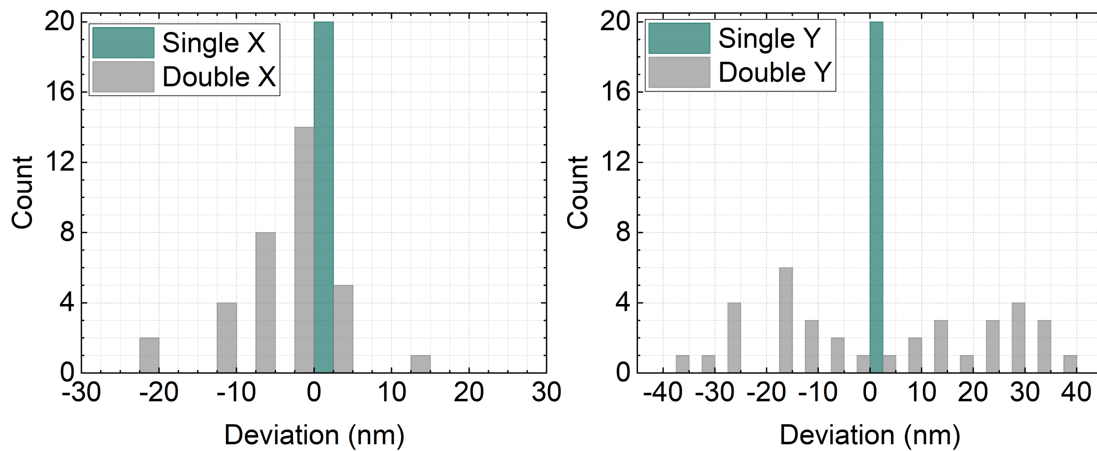

Figure 7-22. QD positioning deviation in respect to nanohole centre in X [1-10] and Y [110] for large nanoholes (50D8) at pitch of 2.4 μm single or double QDs.

7.4.2.4 Single QD linewidths

Single QD linewidths for an unpatterned, planar InAs/ GaAs sample were measured using a different PL system to the rest of this work. The spectrum and linewidth distributions are

shown in Figure 7-23 (a). A significant proportion of the lines approach the resolution limit of the grating, which was $\sim 20\ \mu$eV, and the mode was 27 μeV $\pm$ 3 μeV. The corresponding spectrum (b) shows bright, narrow lines between 890 nm and 900 nm. This result allowed SCQD results to be benchmarked against results for random QDs grown using the DCA MBE on planar surfaces.

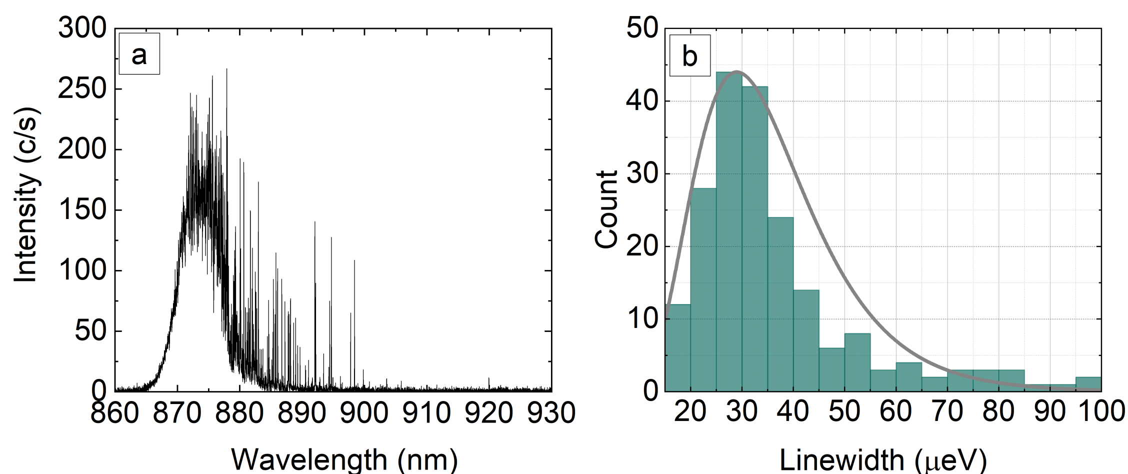

Figure 7-23. Sample PR0080, a planar non-site controlled QD sample grown and measured by Dr. Aristotelis Trapalis using a double 1200 lines/mm grating with a 20 μeV resolution, using 100 nW laser power and a 10 s integration time. In (a) the spectrum is shown and in (b) the single QD linewidth distribution.

Single QD linewidth data for the SCQDs is shown in Figure 7-24. The resolution limit of the grating was 25 μeV. The mode of the linewidths was 44 μeV with a lognormal distribution (the mean was 54.9 μeV $\pm$ 25.1 μeV). The lowest measured linewidth was 26.3 μeV. The low number of lines was due to the grating having poor efficiency at longer wavelengths, 118 lines were observed when measuring the same area using the 600 lines/mm grating.

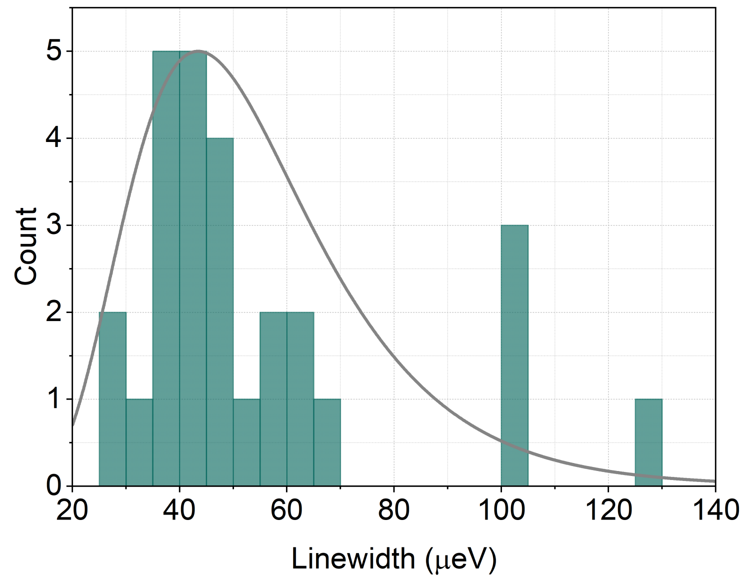

Figure 7-24. Sample PR0097, the distribution in single QD linewidths obtained via μPL using a 1800 lines/mm grating for a 10 $\times 10\mu$m area of array 40D5 for 0.6 μm pitch. An LED voltage of 0.495 mW, with a 20 s integration time was used.

The single QD linewidth result achieved in this work compares very favourably with reports in the literature, particularly for thin buffer, single layer growth systems. However, it can be seen that there is some broadening when compared to planar QDs. Therefore, this suggests that the proximity to the fabrication interface could be having a detrimental effect on the QDs, as previously discussed. This broadening could be reduced by using a stacked growth system. Additionally, broadening that is brought about by charge noise can be mitigated to some extent by increasing the Fourier transform limited linewidth. This can be achieved by incorporating QDs into W1 PC waveguides, where the QD emits near the photonic band edge. This ensures the QD is in the slow light regime, where there is an increased density of states into which the QD can emit. This increases the spontaneous emission rate of the QD, which leads to an increased transform linewidth.

7.4.2.5 Pitch

Being able to successfully grow SCQDs at a variety of pitches is important as different photonic devices could have different QD spacing requirements. As discussed, pitches of 1.2 μm, 2.4 μm, and 4.8 μm are multiples of the distance between chiral points in a W1 waveguide (240 nm), optimised for a wavelength of 920 nm. The addition of the high

denisty 0.6 μm pitch was useful for AFM characterisation, where better statistics could be gathered while scanning a small area. Included in the EBL pattern design was the capacity to investigate the effect of pitch on site-controlled QD properties. Using PL spectroscopy and AFM imaging the mean wavelengths and QD heights were found for a small nanohole diameter array and are shown in Figure 7-25. In AFM, SCQD growth was observed for all pitches, with no nucleation of QDs between nanoholes at any pitch. In PL, emission was observed from all pitches. In general, an increase in emission wavelength was observed as pitch increased from 948 nm (P0.6) to 972 nm (P2.4). However, no significant increase in mean QD height was seen. There is was no trend in single occupancy in AFM for the four pitches at this nanohole size (0.6 μm 43 %, 1.2 μm 38 %, 2.4 μm 53 %, and 4.8 μm 43 %). The percentage of sites with observable emission could not be calculated for pitches 0.6 μm and 1.2 μm, as they are below the resolution limit of the setup. For 2.4 μm 22 % of sites showed emission, and for 4.8 μm it was 28 % of sites.

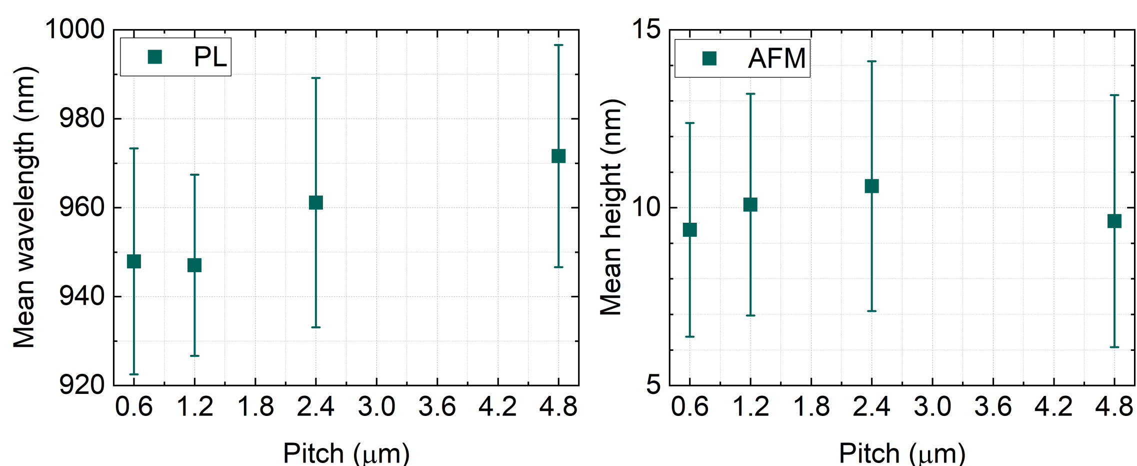

Figure 7-25. Mean QD wavelength (PL) and mean QD height (AFM) extracted from array 40D5 while pitch was varied.

In the nanohole diameter region where PL emission is not detected (above 70 nm), a pitch dependency was observed for mean QD height, Figure 7-26 (a). Pitches 1.2, 2.4, and 4.8 μm showed an increase in QD height as nanohole diameter increased. However, there was very little change in QD height over the nanohole diameter range for pitch 0.6 μm, shown in Figure 7-26 (a). AFM images of (b) 2.4 μm pitch and (c) 0.6 μm pitch are also shown. As discussed, large nanoholes patterned at a pitch of 2.4 μm demonstrated growth of large, single occupancy SCQDs. For pitch 0.6 μm, larger diameter nanoholes led to multiple

QD occupancy, up to as many as five QDs per site. Additionally, enhanced nanohole asymmetry in the [110] and [1-10] directions was observed. This behaviour shows that SCQD growth can be pitch dependent, therefore growth parameter tuning is required when varying pitch.

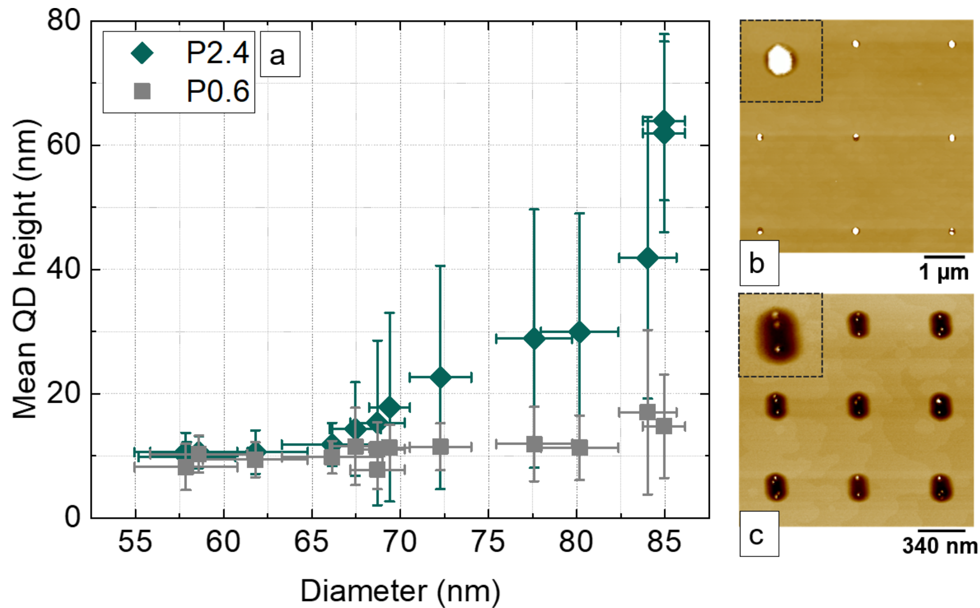

Figure 7-26. (a) Mean QD height as a function of nanohole diameter for 0.6 μm pitch and 2.4 μm pitch (b) an AFM image (with an insert showing a zoom in of a QD) for 2.4 μm pitch and (c) an AFM image for 0.6 μm pitch.

7.4.3 Site-to-site QD characteristics

For initial integration of the grown QDs into devices a small number (two to four) QDs can be selected. It is important that the chosen QDs are close in emission wavelength to each other and have low single QD linewidths. A representative array (50D2) was fully characterised and then specific QDs within the array were investigated further. The criteria for selection was based on QDs being spatially near, close in wavelength, and bright.

7.4.3.1 Emission wavelength

Figure 7-27 (a) shows a site-specific wavelength map of all areas from which emission was detected using μPL spectroscopy with a 600 lines/mm grating. Of the 169 site array,

34 nanoholes (20.5 %) contained single, site-controlled QDs that emitted in the 900 nm to 1000 nm range. There were some areas of the array with very few emitting sites and some clusters of QDs that were close in wavelength. The wavelength distribution of these sites is shown in (b), where the mean was 970.2 nm ± 28.8 nm. This standard deviation is equivalent to a FWHM linewidth of 75 meV. The majority of lines were between 960 nm and 1000 nm and the distribution was against the long wavelength end of the detection range. The ensemble linewidth for the long wavelength cluster was 32 meV. This result shows that an array of QDs that has a narrow ensemble linewidth has not been produced, meaning that identical devices could not be fabricated around the entire array of QD and function efficiently.

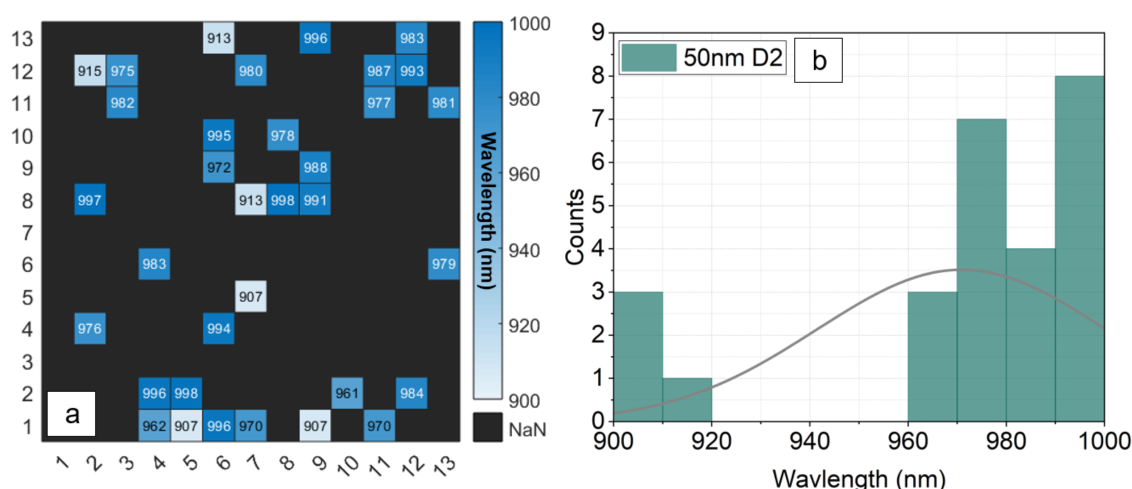

Figure 7-27. (a) Site-specific μPL wavelength map for area 50D2, measured using a 600 lines/mm grating and (b) the corresponding distribution of the wavelengths, with a mean of 970.2 nm ± 29.8 nm.

7.4.3.2 Single QD linewidth

Sites close in wavelength were measured using the 1800 lines/mm grating to give accurate linewidth information. A site-specific single QD linewidth map is shown in Figure 7-28 (a) and a wavelength map for those measured areas is shown in (b) for reference. The mean linewidth was 65.7 μeV with a standard deviation of 21.9 μeV. Two areas (4-1 and 7-8) showed very narrow linewidths of 26 μeV that were just above the resolution of the spectrometer. However, the sites were not close in position or wavelength. A cluster of QDs with similar wavelengths can be seen the top right corner of the array. Four QDs

all within a 10 nm range were measured and had linewidths between 66 μeV and 80 μeV. These QDs are suitable for incorporation into waveguide devices or cavities for testing and will be discussed further in Chapter 8. There was no apparent dependence between linewidth and wavelength.

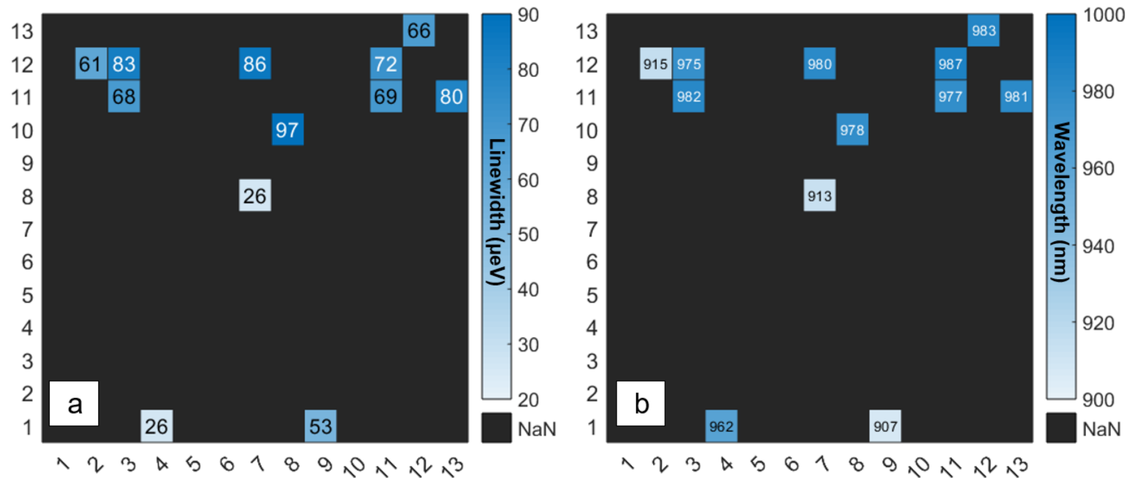

Figure 7-28. Maps of (a) site-specific single QD linewidths of selected lines, measured using the 1800 lines/mm grating from array 50D2 and (b) the corresponding site-specific wavelengths plotted as a map.

7.4.4 Single QD properties

The final analyses to be discussed for SCQDs grown on nanoholes fabricated using EBL, focuses on single QD properties. The aim of this section of work was to identify individual lines in a QD spectrum and comment on the single QD quality. The QD nucleated in site 4-1 was selected due to its brightness. Additionally, its emission wavelength being below 970 nm produced better counts when using the 1800 lines/ mm grating.

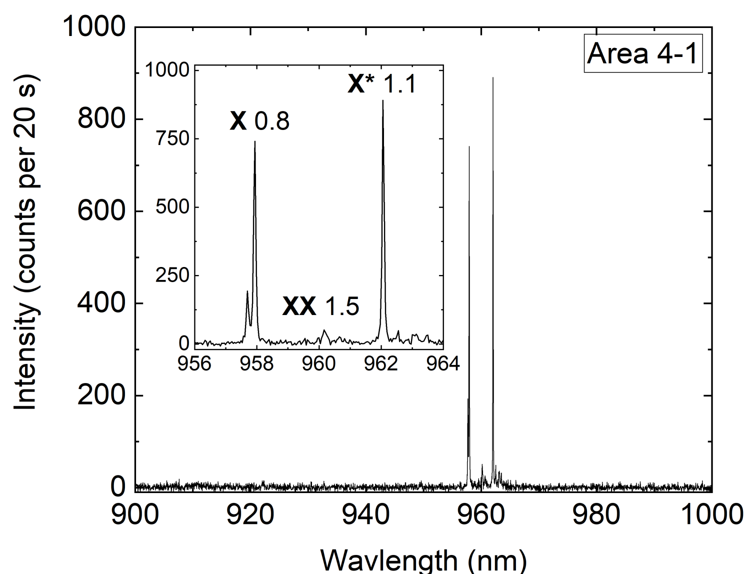

Figure 7-29. A μPL spectrum taken using the 1800 lines/mm grating from area 4-1, showing the exciton, charged exciton and biexciton lines. The lines were identified using power dependence and fine structure splitting measurements.

Figure 7-29 shows the spectrum of the QD. The neutral and charged exciton were identified using a fine structure splitting (FSS) measurement. At this low power, the biexciton line was not bright in comparison to the neutral exciton and charged exciton lines. It can be seen that the lines were narrow and well defined. A power dependence measurement of the line was taken from 0.02 mW to 10.68 mW (19 points total). Figure 7-30 (a) shows a selection of these measurements. The first line to appear was the neutral exciton, followed by the charged exciton, and finally the biexciton. It is common for biexciton emission to be at lower energy than the exciton emission, as observed here. At higher powers, the initial s-state line saturated and a p-state was seen to appear at around 925 nm. An energy gap of around 40 nm between the s- and p-states was commonly seen. The integrated intensities of the exciton, charged exciton, and biexciton lines as a function of measured LED power for each voltage are shown in (b) to (d). All transitions were observed to saturate over the power range used. The similar slope values for the neutral and charged excitons are due to carrier capture statistics, where both show linear dependence [213]. The biexciton line had a quadratic dependence and a value roughly double that of the neutral exciton [214]. Biexciton transitions slopes with a value below 2 have been reported for SCQDs, where the importance of describing excited state properties was shown for quantum information

technology [215].

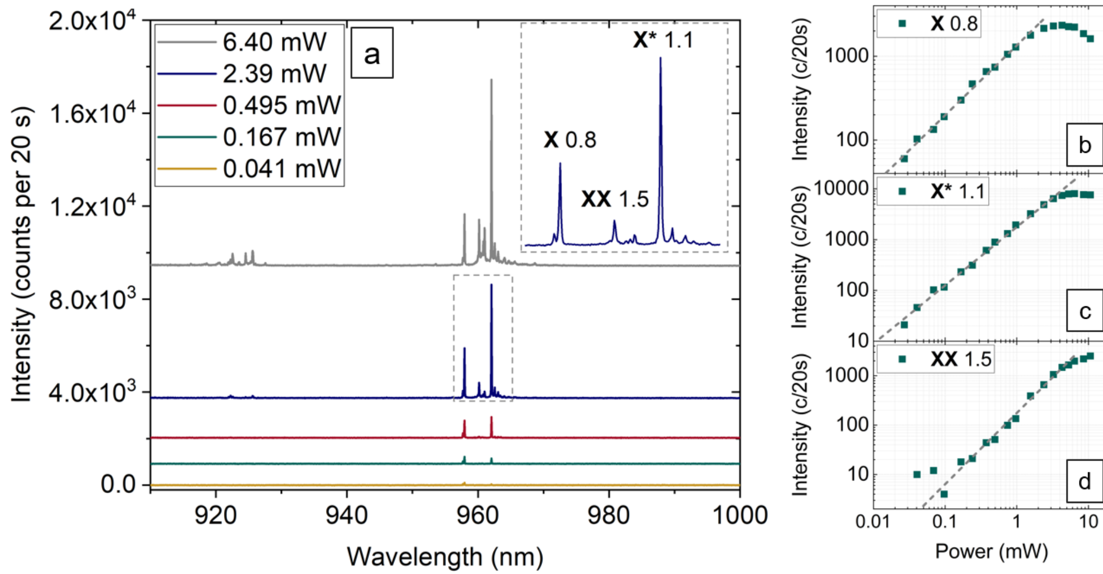

Figure 7-30. For line 4-1 (a) a selection of spectra from a power dependence measurement, where the insert shows a zoom in of the 2.39 mW lines. The neutral exciton line appeared first, followed by the charged state, and finally the biexciton line was observed. At higher power the p-shell state was seen at ~ 935 nm. The integrated intensity of the (b) neutral exciton line, (c) the charged exciton line, and (d) the biexciton line were 0.8, 1.1, and 1.5 respectively.

The neutral and charged exciton transitions were identified via a FSS measurement. No fine structure was observed for the 961 nm line, therefore assigning it as a transition from a charged exciton [216]. The FSS for the neutral transition was measured to be 16.2 μeV and is shown in Figure 7-31. A further FSS was measured for area 9-12 (emission wavelength 933 nm) and found to be close to this value at 25.7 μeV. For comparison, a measurement of a non site-controlled QD which emitted at 955 nm, was bright, and demonstrated a low linewidth of 49 μeV was taken and found to have a FSS of 54.0 μeV. The results associated with the SCQD compare favourably with the literature and demonstrate that the nanohole is having a positive effect on the symmetry of this QD [217].

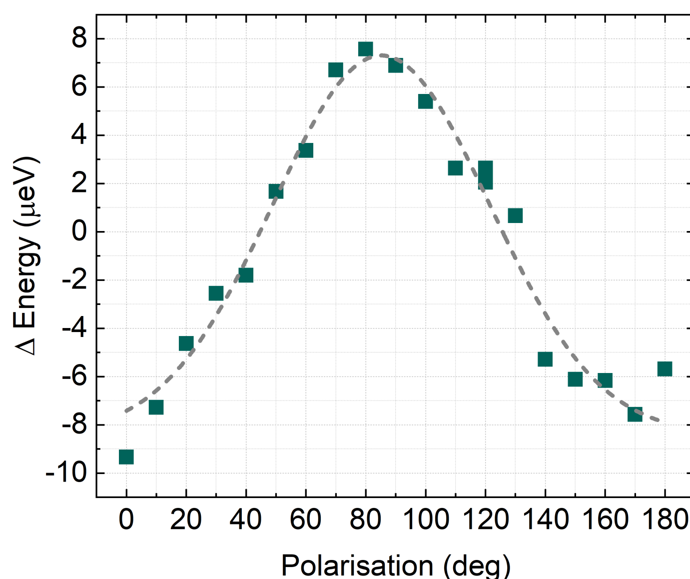

Figure 7-31. A FSS measurment for line 4-1 at 957.9 nm, showing an energy splitting of 16.2 μeV.

7.4.5 SCQD growth on LAO fabricated nanohole arrays

While LAO does not involve the use of organic resists, broad linewidths have been reported by a number of groups using this technique. To directly compare the methods, EBL and LAO nanoholes were fabricated on the same samples, PR0097 and PR0100. However, this means that the LAO process occurred on a sample that had been covered in EBL resist and that the results may not be a true reflection of the potential of the LAO process. The 8 by 8 grid of nanoholes fabricated via LAO had a mean diameter of 359.4 nm $\pm$ 16.4 nm, and mean depth of 11.0 nm $\pm$ 0.9 nm. Post-growth they had a mean diameter of 255.4 nm $\pm$ 21.529 nm, and mean depth of 6.7 nm $\pm$ 0.7 nm.

7.4.5.1 Occupancy

Figure 7-32 (a) shows a portion of the array. Small, well positioned QDs were nucleated in the nanoholes and there was no nucleation of QDs in the planar areas between nanoholes. The QDs were measured to be 7.9 nm in height with a standard deviation of 2.1 nm. Of the 64 sites, 14 sites had at least one QD present (22 %). In (b) a PL image of the entire array is shown. Emission, of variable intensity, was seen from 16 (25 %) of sites. Therefore,

growth of optically active SCQDs has been successfully demonstrated using nanoholes fabricated via LAO. This occupancy percentage is very similar to that observed for the EBL arrays.

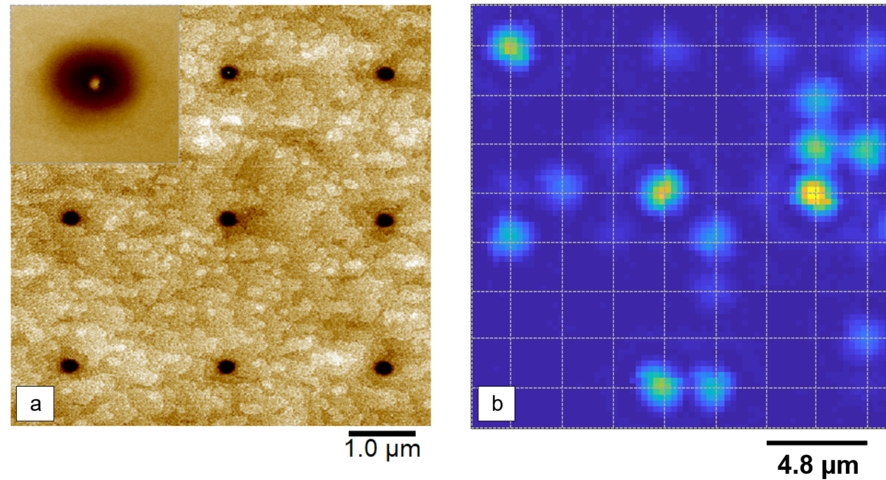

Figure 7-32. Images showning (a) an AFM, which was cropped from 64 nanoholes and (b) a PL map of SCQDs grown in nanoholes fabricated via LAO. The grey lines are a guide to the eye and a crossing point indicated the position at which a nanohole was fabricated.

The occupancy statistics of the number of QDs nucleated in nanoholes is shown in Figure 7-33. The majority of sites that were occupied contained one QD (13 out of 14 sites) and one nanohole contained three QDs. However, for device integration it would be beneficial for a larger percentage of nanoholes to be occupied by a single QD. The low occupancy and lack of QDs nucleated between nanoholes suggests that an experiment investigating material coverage should be an initial step in optimising occupancy statistics.

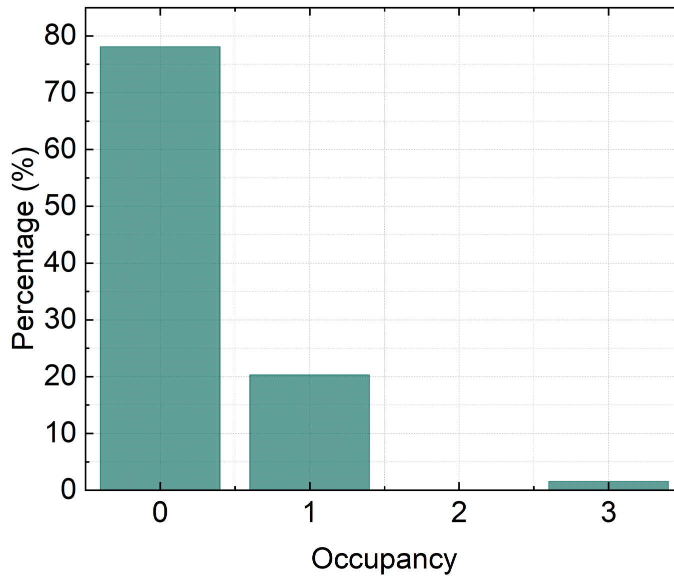

Figure 7-33. The occupancy distribution extracted from an AFM image of the entire LAO array showing 20 % single occupancy and 1.6 % triple occupancy. All other sites were un-occupied.

7.4.5.2 QD emission wavlength

Figure 7-34 (a) shows a site-specific wavelength map for the LAO fabricated array. There was a small cluster of QDs that emitted between 980 nm and 1000 nm in the top right of the array. In (b) the distributions of the wavelengths are shown, the mean was 967.8 nm $\pm$ 33.5 nm. This is a broad distribution in wavelengths, however the majority of QDs (12 from 16) emitted between 970 nm and 1000 nm.

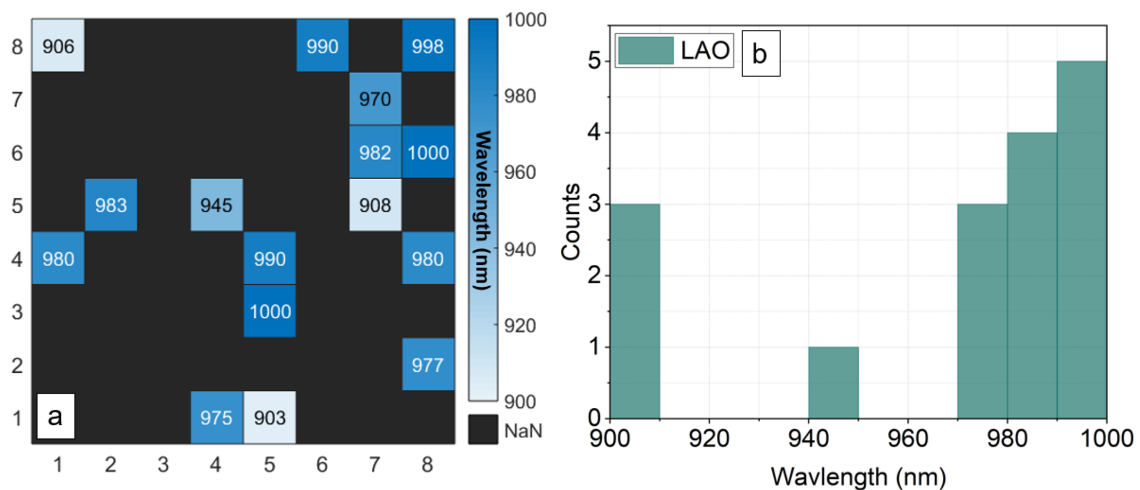

Figure 7-34. (a) Site-specific wavelength map, measured using a 600 lines/mm grating and spectrometer, showing emission from 25 % of sites using the spectrometer and (b) the distribution of the QD wavelengths.

7.4.5.3 QD positioning accuracy

The positioning deviation for LAO QDs was measured in the X [1-10] and Y [110] directions, in the same manner shown for EBL QDs, and is shown in Figure 7-35. In X, the majority of QDs had a deviation between 0 nm and +30 nm, with the remainder all falling within ± 38 nm. In Y, there was a clear mode between +20 nm and +30 nm deviation, with the positioning deviation falling between ± 55 nm. These results show good positioning accuracy, despite nanoholes being large in diameter (255 nm post-growth). This indicates that the QDs tend to nucleate near the centre of the nanohole rather than near the edges. The QD closest to perfect positioning was − 12 nm in X and − 1 nm in Y from centre. As previously outlined, InAs nucleation depends on the curvature of the nanohole and the number of step edges. This result suggests that LAO nanoholes promote nucleation near the centre of the nanohole due to one of these reasons.

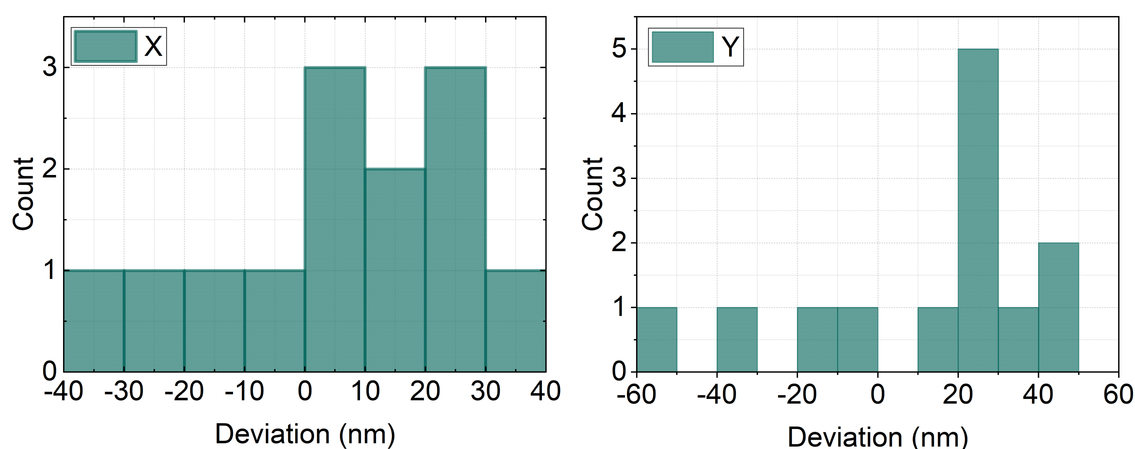

Figure 7-35. Positioning deviation in the X and Y directions. The mode was between 0 and 30 nm in X and 20 to 30 nm in Y.

7.4.5.4 Single QD linewidths

Finally, single QD linewidths were measured for the array using the 1800 lines/mm grating. As previously noted, the grating sensitivity drops off after 970 nm, therefore an integration time of 30 s was used at a power of 1.56 mW to increase counts. An example spectrum for site 5-1 is shown in Figure 7-36, which was the only line present at this site at this power.

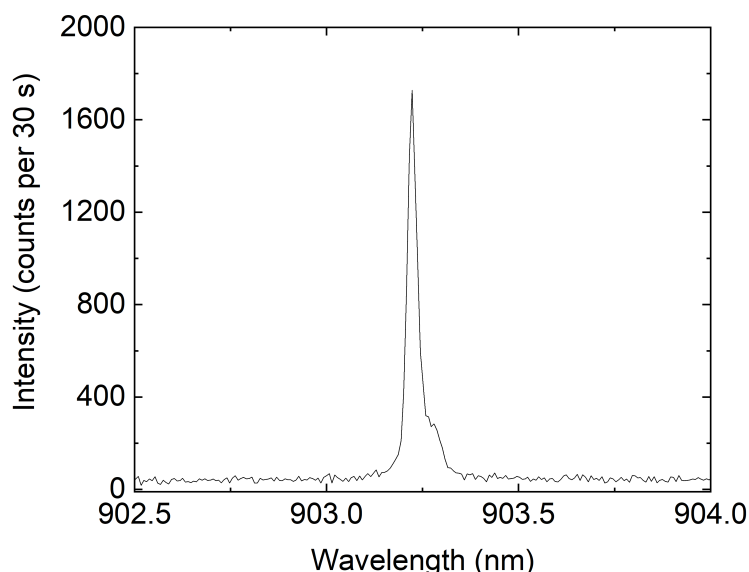

Figure 7-36. An example μPL spectrum measured at a power of 1.56 mW for 30 s using the 1800 lines/mm grating. The measured linewidth was 33 μeV.

Linewidths were measured for the 13 QDs that were bright enough to measure using the 1800 lines/mm grating, and are shown as a site-specific linewidth map in Figure 7-37 (a) and the histogram of distributions is shown in (b). The minimum measured linewidth was 33 μeV, with a mode of 62 μeV and mean of 83 μeV $\pm$ 35.8 μeV. Note, the linewidths were measured at a low excitation power as power broadening was observed, as is regularly reported in the literature [218]. As described, the sample first underwent the EBL process and has been exposed to contaminants such as organic resist. Therefore, this experiment does not show the result of a sample only undergoing LAO fabrication. However, because the linewidths are not narrower than for QDs grown on EBL nanoholes, it could be suggested the LAO process produces slightly broader linewidths. These linewidth measurements compare favourably to results reported in the literature for similar systems.

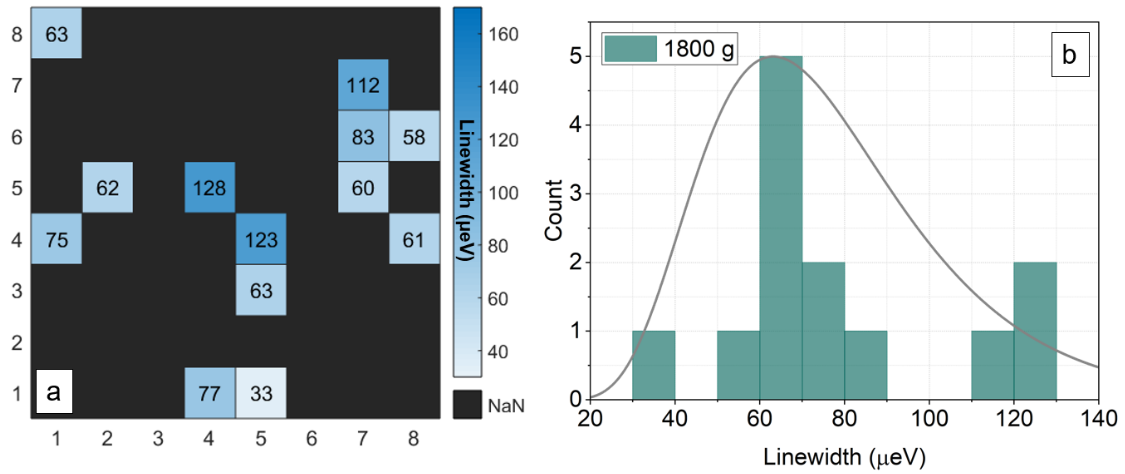

Figure 7-37. (a) Site-specific single QD linewidth map and (b) the corresponding distribution in the QD linewidths.

7.4.6 Comparison between EBL and LAO fabricated nanoholes

QDs from array 50D2 (EBL) will be compared to QDs from the LAO array. Table 7.1 summarises some of the key parameters that were measured. Despite the QDs being very similar in size and emission wavelength, the LAO nanoholes were measured to be almost double the diameter of the EBL nanoholes for this array.

Table 7.1. A comparison of the properties of QDs grown on nanoholes fabricated using EBL and ICP-RIE (array 50D2) and using LAO.

Parameter	EBL (50D2)	LAO
Linewidth (mean)	55 ± 25 μeV	83 ± 36 μeV
Linewidth (mode)	44 μeV	62 μeV
Linewidth (minimum)	26 μeV	33 μeV
Mean wavelength	970 ± 30 nm	968 ± 34 nm
QD height	9.8 ± 2.4 nm	7.9 ± 2.1 nm
PL occupancy (imaging)	28%	25%
PL occupancy (spectrometer)	21%	25%
AFM single occupancy	43%	20%
Positioning deviation [110]	± 55 nm	± 56 nm
Positioning deviation [1-10]	± 18 nm	± 38 nm
Nanohole diameter (before)	57.9 ± 2.7 nm	359.4 ± 16.4 nm
Nanohole depth (before)	19.8 ± 0.6 nm	11.0 ± 0.9 nm

The measured single QD linewidths were similar for both arrays, with slightly broader results being seen for LAO QDs. For QDs grown on EBL nanoholes, contamination is a significant cause of charge noise, whilst defects introduced during the oxidation process are more likely to cause linewidth broadening in LAO QDs. However, a highly rigorous ex-situ cleaning protocol was developed to mitigate linewidth broadening for QDs grown on EBL nanoholes. The difference in single QD linewidths for the two types of QDs indicates that the cleaning method removed any residue from nanoholes successfully. However, some defects could be causing broadening for LAO QDs. It is suggested that a further experiment, where QDs grown on a wafer where only LAO processes are used, would allow better measurement of the linewidths associated with the LAO method.

The number of sites that demonstrated single QD emission for LAO and EBL arrays was very similar, using both the imaging camera and spectrometer (between 20 % and 30 % in all cases). However, the occupancy in AFM was significantly different, with almost double the number of single QDs being measured in EBL nanohole arrays than LAO nanohole arrays. Additionally, 17 % of sites were occupied by multiple QDs for EBL nanoholes, whilst only 1.6 % of sites were for LAO nanoholes. As discussed, for the EBL QDs some emission could be beyond the detection range of the set-up, which would affect large QDs, or QDs could be dissolving during the capping process, which would reduce the number of small QDs.

Finally, the position deviation for LAO and EBL QDs had a similar maximum value for the Y direction. However, the X value for LAO QDs was almost twice as large, which could be due to the diameter of LAO nanoholes being almost twice as large. However, the LAO QDs did not display the same tendency to nucleate at an extreme end of a nanohole as seen with EBL QDs, even though neither type of nanohole elongated in the [110] direction. This suggests that preferential indium migration in the [110] direction was less significant in the LAO nanoholes. Therefore, the mode deviation for LAO QDs was lower than EBL nanoholes, as seen in Figures 7-35 and 7-21.

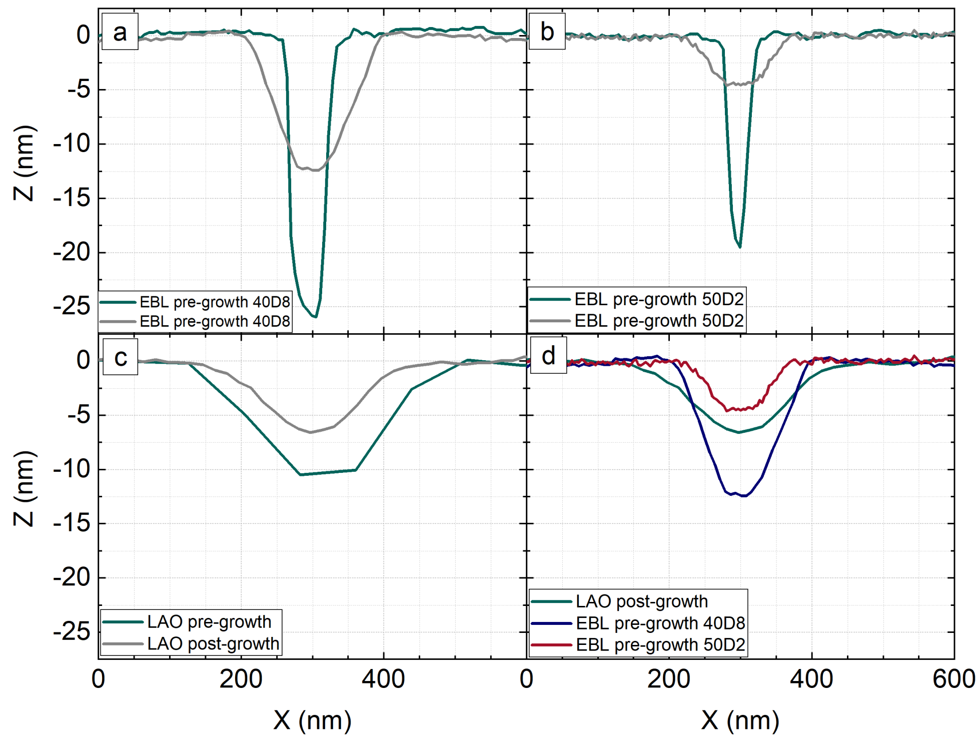

Figure 7-38. Sections through nanoholes pre- and post-growth to indicate the change in size and shape of nanoholes for (a) large EBL nanoholes (40D8), (b) small EBL nanoholes (50D2), (c) LAO nanoholes and, (d) a comparison of LAO, large EBL, and small EBL nanoholes after growth.

Figure 7-38 shows the changes in nanohole size and shape before and after growth. Measurements for large and small EBL nanoholes are shown and compared to LAO nanohole results. EBL nanoholes were wider and significantly shallower after growth, whilst LAO nanoholes became slightly shallower and narrower. After growth small EBL nanoholes and LAO nanoholes were of similar depths, however the aspect ratios were 38:1 and 27:1 for LAO and EBL nanoholes respectively. This did not seem to affect QD heights, however occupancy did differ as discussed. The large EBL nanoholes were deeper, however it was not possible to measure this accurately for all nanoholes after growth, as most were filled with large QDs. The nanohole shown was measured around 12.5 nm deep after growth and has an aspect ratio of 16:1. The difference in QD size is shown in Figure 7-8 (b), where it can be seen that QDs nucleated in this type of nanohole were significantly larger than those seen in small EBL or LAO nanoholes. It would be interesting to investigate aspect ratio, as it is known that nanohole curvature affects InAs nucleation, and there is a clear difference in this property when EBL and LAO nanoholes are compared.

7.5 Summary

A site-controlled QD growth process has been successfully developed, using nanoholes fabricated using EBL and ICP-RIE and LAO. The lowest single QD linewidths measured were 26 μeV. This was produced using just 30 nm of re-growth buffer on EBL and ICP-RIE fabricated nanoholes, demonstrates the very high quality of the fabrication interface post ex-situ and in-situ cleaning. By optimising the re-growth buffer temperature, the nanohole sites became areas of preferential nucleation, meaning that no QD growth occurred on planar surfaces between nanoholes. Using μPL and AFM, nanohole diameter was explored as a control parameter for nanoholes fabricated using EBL/ICP-RIE. In AFM, nanohole diameter was shown to affect QD size and occupancy. Small QDs nucleated in small nanoholes. The best single occupancy was achieved using both small and large nanoholes, and an intermediate size led to double occupancy, as has been observed in the literature [219]. In μPL and PL imaging, emission was only observed from smaller nanohole arrays, which was explained by QDs in larger nanohole arrays not emitting within the detection range of the Si CCD used in the PL set-up. Over the range of nanohole sizes where PL could be detected (55 nm to 70 nm), there was little change in the mean PL emission wavelength. Single QD properties, such as FSS, were also favourable in comparison to the literature. Finally, QDs grown on nanoholes fabricated via EBL/ICP-RIE and LAO were compared. The properties of the LAO QDs were similar to those of the EBL QDs, despite a significant difference in the nanohole diameters for the two processes. The effect of the aspect ratio, diameter, and depth of nanohole nucleation sites on QD properties, such as occupancy and size, could therefore be explored further.

8 Conclusions and Outlook

8.1 Conclusions

The goal of this project was to develop methods for deterministically positioning InAs QDs in regular arrays using ex-situ fabricated nanoholes as nucleation sites. The fabrication, surface preparation and growth processes were designed with the aim of providing SCQDs suitable for incorporation into single mode nanophotonic devices and provide the building blocks for the engineering of scalable qubit systems. A set of goals were set up to this end. Firstly, design and use of a complete structure that had a thickness matching the single mode device height was required. A number of requirements were also needed of the SCQDs, these being, narrow single QD linewidths, narrow ensemble wavelength distributions, a high percentage of single occupancy sites and regular positioning within the array. Additionally, a fast, robust, and scalable nanohole and alignment mark fabrication process was required. A summary of the steps taken to fulfil these goals will now be presented and conclusions will be drawn as to the successes of the project and the next steps that could be taken to improve on areas where goals have not been fully met.

Chapter 4 focused on the development and characterisation of the kinetics of LAO of InP. A process for fabricating high quality nanoholes where the radius and depth could be controlled using humidity and applied AFM tip bias was developed. The positioning accuracy of nanoholes with an array was assessed and found to have a very low deviation of 3.8 nm. An initial site-controlled indium droplet epitaxy growth demonstrated that the nanoholes could successfully control the nucleation position of the droplets. Although no droplets nucleated between nanohole sites, a very low percentage of sites were occupied. Therefore, further optimisation of growth conditions would be required to increase

droplet density and occupancy statistics. At this point, the metallic droplets could be crystallised under a supply of arsenic. This would facilitate the formation of QDs and would allow optical characterisation and benchmarking against the project goals to take place. Additionally, the activation energy for LAO on InP was reported and the effect of doping type on growth kinetics were presented. Finally, it was shown using FDTD simulations that the resonant frequency of an InP H1 PCC could be tuned using LAO fabricated oxides. A logical next step would be to test the process experimentally by fabricating the H1 PCC using the designed parameters and subsequently measuring the range of tuning by LAO.

Chapters 5, 6, and 7 presented an alternative nanohole fabrication and ex-situ cleaning method for a GaAs substrate, where EBL with ICP-RIE was used. Initial SCQD growth experiments highlighted issues with using a thermal oxide desorption process. An in-situ AHC method was developed so that contamination and oxide free surfaces could be produced, while maintaining low surface RMS and preserving the nanohole pattern. Using these developed methods, buffer and QD growth were optimised and arrays of emitting SCQDs were produced and characterised. SCQDs grown on LAO and EBL/ ICP-RIE fabricated nanoholes were compared.

Using EBL with ICP-RIE allowed very high quality and well positioned nanoholes to be fabricated. The positioning deviation was tested against simulated devices and shown to have little impact on position dependent device properties, such as the Purcell factor or chiral behaviour. The nanohole dimensions were easily controllable using EBL and ICP-RIE parameters and alignment marks were fabricated simultaneously with the nanoholes. This method provided a fast, reliable, and highly scalable fabrication method. The established AHC method and thorough and robust ex-situ cleaning process were shown to effectively reduce contamination levels to a minimum.

The SCQD arrays were characterised in detail using AFM and μPL. When assessed against the project aims it can be seen that there was some success and some further work required. Firstly, the growth structure design was suitable for incorporation into single mode devices. And as explained, single QD linewidths were narrow. However, only

around 20 to 25 % of sites were occupied by a single QD that emitted in the wavelength region of interest. Additionally, the spread in the wavelength distribution was broad. The literature indicates a number of possible routes towards improvement of these properties. In short, these include, using deeper etched nanoholes, using a stacked system, and optimising growth parameters further. This will be discussed in detail in the following section. It should be noted that a small number of QDs close in wavelength and with narrow single linewidths were found, therefore a small number of devices could be fabricated around these QDs for characterisation. Minimal differences in emission wavelength could be overcome using tuning techniques.

The outcome of growing SCQDs on LAO and EBL/ICP-RIE fabricated nanoholes for direct comparison highlighted some differences in behaviour between the two techniques. Namely, the small size of QDs nucleated in very wide LAO nanoholes and the observation that almost all occupied sites contained a single QD for LAO nanoholes, whilst there was a much higher percentage of double, or triple occupied nanoholes for EBL/ICP-RIE nanoholes. The origin of these differences should therefore be investigated. In terms of fabrication ease, LAO allowed fabrication of small numbers of high quality nanoholes. However, EBL and ICP-RIE fabrication was a more scalable and controllable method.

Finally, the results will now be compared to the thesis aims and previous literature. Table 8.1 shows a summary of the results for EBl and LAO SCQDs. The aims were achieved for single QD linewidths and positioning accuracy. However, the desired single QD occupancy and wavelength distributions were not achieved. The impact of not achieving these aims is that when integrating the QDs into photonic devices there would be a low yield of working devices. Additionally, it wouldn't be possible to create entanglement between multiple single photon sources. Furthermore, if an array of identical H1 PCC were fabricated around the array of SCQD a high percentage of the QDs would not be in resonance with the PCCs.

Table 8.1. A summary of the results for the parameters of interest for the nanohole fabrication methods involving EBL and LAO, and the parameter aims.

Fab. method	Maximum single occupancy (%)		Minimum linewidth (μeV)	Center wavelength (nm)	Wavelength distribution (meV)	Positioning accuracy (nm)	
	AFM	PL				[110]	[1-10]
EBL	43	28	26	970	79	55	18
LAO	25	25	33	968	90	56	38
Aim	40	40	~25	950	25	50	50

The results should also be compared to literature results where comparable fabrication and growth methods have been used. A reprint of Table 2.1 is shown below. For an EBL fabrication method reference A from Table 8.2 and for LAO reference I are comparable to this work. In both cases the minimum single QD linewidths reported in this work are significantly narrower than those reported in the literature. However, again the wavelength distribution in this work is significantly broader than the literature result. In conclusion, this work has developed a method for the growth of narrow linewidth SCQDs. Further work is needed to increase single occupancy of sites and decrease the distribution in wavelength of the QDs across an array, which will now be discussed.

Table 8.2. A summary of some of the key literature results using electron beam lithography with dry or wet etching and local anodic oxidation nanohole fabrication methods, where temp. is temperature, min. LW is the minimum measured single QD linewidth, and WL is the mean ensemble emission wavelength A [115] B [114] C [106] D [16] E [128] F [111] G [113] H [36] I [119] J [134] K [117].

	Fab. method	QD growth		Buffer growth		Stack	Control parameter	Occupancy		Min. LW	WL (nm)	QD height/ Wavelength distribution
		Rate	Temp. (°C)	Thickness (nm)	Temp. (°C)			AFM	PL			
A	EBL, dry etch	0.031 µm/hr	470	15		N	Buffer thickness			80 µeV		
							Nanohole diameter: 32 nm				1020	
B			500	12	500	N	Nanohole diameter	Best single occupancy 50 % for narrow nanoholes				
							Nanohole depth	Best single occupancy 65 % for narrow, deep nanoholes				
C		0.01 ML/s	470, 500	18 ML	500	Y	Indium coverage: 1.2 ML, 1.7 ML, 2.0 ML	1.2 ML, small double QDs. 1.7 ML, single QDs. 2.0 ML, large single QDs and QDs between nanoholes.				
							1st layer (210 nm/ 160 nm pitch)					210 nm = 19.37, 160 nm = 17.8 and 13.73
							6th layer (210 nm/ 160 nm pitch)					210 nm = 5.58, 160 nm = 5.29
D	EBL, wet	0.005 to 0.010 nm/s	530	20 nm		Y	Buffer thickness			0.66 meV		
	EBL, dry			34 nm			Buffer thickness			0.6 meV		
E	EBL, wet etch	0.006 nm/s	545	20		Y	Nanohole diameter: 60 nm to 65 nm	77 % single occupancy for 60 nm, 49 % single occupancy for 65 nm	90%	25 µeV	925 (300 nm pitch)	15.9 meV
							Pitch: 200 nm to 350 nm				922 to 927	
F			520	90	550C	N	Buffer thickness, anisotropy			6 µeV	950	
G						Y				43 µeV	925	14.4 meV
H		0.01 ML/s	510	22	510	Y	Stacked system	40 % single occupancy	60%	7 µeV	950	
I	LAO	0.01 ML/s	510	30	450	N	30 nm buffer compared to no buffer	30 nm buffer = multiple/ no occupancy, 0 nm buffer = single occupancy		304 µeV		
				15		Y	15 nm spacer	Single occupancy, 89 %	85%	64 µeV	994	23 meV
				20			20 nm spacer	Unoccupied sites, 75 %				
J				7	480	N	QD growth temperature: 460, 480, 520 °C					520 °C = 3, 480 °C = 15, 460 °C = 55
K		Varied	510	0		Y	QD growth rate: 0.5, 2 and 3.5 ML/s	90 % single occupancy for 0.5 ML/s and 50 % double occupancy for 3.5 Ml/s	88%	81 µeV	1004	7 nm

8.2 Outlook

Possible directions for future work will now be summarised. The routes of investigation will be divided into two main areas. Firstly, the improvement of SCQD array properties such as occupancy, and emission wavelength distribution, so that the project aims can be further met. This section includes the comparison between LAO and EBL/ICP-RIE nanohole fabrication methods and the effect on nucleated QDs. Secondly, experiments where SCQDs are integrated into photonic devices will be discussed.

8.2.1 Improving SCQD properties

In Chapter 7 it was shown that very narrow single QD linewidths could be produced using the developed fabrication and cleaning methods. However, if occupancy and emission wavelength distributions were improved the system would give a higher yield of devices. In the literature, the positive impact of growing a stacked system, where a seed QD controls the nucleation position of a vertically coupled and optically active QD, has been widely demonstrated [106, 113, 117, 128]. The potential well introduced by the strain environment directly above the seed QD provides a more homogenous environment than the nanohole. Therefore, QDs tend to be brighter and ensemble linewidths are narrower [140]. Additionally, the use of a stacked system has been shown to reduce the number of SCQDs nucleated at a site [208]. Finally, it has been demonstrated that improvements to single QD linewidths can be made when using a stacked growth system [16, 119].

These observations strongly suggest that development of a stacked QD growth system would be widely beneficial to SCQD properties. A number of optimisations would be required to achieve this goal. Firstly, it would be preferable for 100 % of nanoholes to be occupied by a single seed QD. This could be achieved through optimising growth conditions or possibly by using slightly deeper nanoholes. The literature shows that for SCQD higher QD growth temperatures and lower growth rates are often used. The growth rates used in this work are very similar to literature values, however this parameter in addition

to QD growth temperature could be investigated further. Additionally, indium coverage and methods such as growth interrupts can be used to improve SCQD properties. These parameters could be systematically investigated to find a window where QD size and occupancy statistics are improved. Next, an appropriate growth temperature for the spacer buffer layer would need to be chosen. Finally, the conditions used to grow the active layer of QDs would have to be optimised, as the critical thickness for nucleation would be changed by the strain field. A partial cap and anneal process could be developed to reduce the emission wavelength of the active QDs. The nucleation position of the QDs and therefore the regularity of the array should also be investigated using the optimised method.

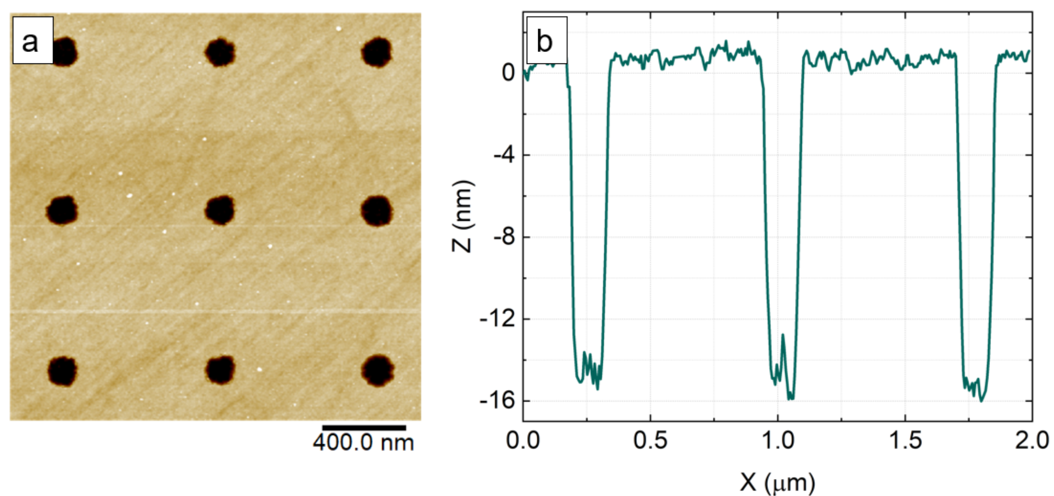

Figure 8-1. (a) An AFM image of a nanohole array produced using EBL and a wet chemical etch and (b) a section through the top three nanoholes.

The properties of nanoholes used as nucleation sites have been shown to strongly influence QD properties. This is an area of focus for future work. The narrowest single QD linewidths have been produced using an EBL and wet chemical etch nanohole fabrication method. However, when directly comparing wet and dry etching techniques, narrower linewidths were observed for wet etched nanoholes. Therefore, use of a wet etch in place of a dry etch should be investigated. To this end a wet chemical etch using 1:8:800 of $H_2SO_4/H_2O_2/H_2O$ was tested, and found to give an etch rate of 0.8 nm/s. Figure 8-1 shows some early results from this approach, an AFM image and a section through the nanoholes. No nanohole feature size and etch depth dependence was observed, as seen with dry etch-

ing, so nanoholes and alignment marks were the same depth. The wet etch produced a straighter side wall to that observed for dry etching. Additionally, the nanoholes produced by wet etching were wider than the corresponding nanoholes produced using a dry etch. The nanohole diameter was controlled using EBL dose and drawn size and the depth with the etch time. The smallest nanoholes produced in this early experiment were $\sim$ 100 nm in diameter and 16 nm in depth, which are of a suitable size for SCQD growth.

It would be interesting to further study the effect of nanohole depth, diameter and aspect ratio on SCQD properties. To this end a set of samples could be fabricated using EBL and ICP-RIE, where the nanohole diameter is varied, as seen in Chapter 7, but additionally nanohole depth is varied by etching the nanoholes for different lengths of time. Additionally, a range of LAO nanohole sizes could be fabricated by varying humidity and applied tip bias. The SCQD properties could then be compared and an optimum nanohole size and aspect ratio found. In the literature it has been noted that deep nanoholes produced better single occupancy statistics [114].

8.2.2 Incorporating SCQDs into nanophotonic devices

An important direction for further investigation would be integration of SCQDs into devices. Initially, small numbers of QDs could be integrated into a small number of coupled devices such as L3 PCC, such as demonstrated by Rigal *et al.* [17]. A SCQD with a FSS of 32 μeV and linewidth of 38 μeV has been successfully integrated into an optical resonator [212]. Therefore, the best results obtained in this work (26 μeV single QD linewidth and 16 μeV FSS) are of high enough quality for use in nanophotonic devices of this type.

Looking further ahead, a larger scale array of devices with integrated SCQDs should be produced by using samples that demonstrate the optimised properties (single QD linewidth, ensemble linewidth, emission wavelength, positioning accuracy). The ultimate goal would be for QDs to be of such high quality that entanglement between scalable systems could be acheived. However, a shorter term goal could be the demonstration of chiral behaviour

across an array of nanobeam waveguides. Because the chiral behaviour in this device is strongly position dependent it would effectively demonstrate the enhaced scalibility of well positioned, well coupled SCQDs in devices.

This page intentionally left blank

Bibliography

[1] G. E. Moore, *Cramming more components onto integrated circuits*, Reprinted: IEEE Solid-State Circuits Society Newsletter, 11 (2006), pp. 33–35. 1

[2] F.-Q. Xie, L. Nittler, C. Obermair, and T. Schimmel, *Gate-Controlled Atomic Quantum Switch*, Physical Review Letters, 93 (2004), p. 128303. 1

[3] R. P. Feynman, *Simulating physics with computers*, International Journal of Theoretical Physics, 21 (1982), pp. 467–488. 1

[4] D. P. DiVincenzo, *The Physical Implementation of Quantum Computation*, Fortschritte der Physik, 48 (2000), pp. 771–783. 1

[5] D. Loss and D. P. DiVincenzo, *Quantum computation with quantum dots*, Physical Review A, 57 (1998), pp. 120–126. 1

[6] R. Young, R. M. Stevenson, P. Atkinson, K. Cooper, D. Ritchie, and A. Shields, *Improved fidelity of triggered entangled photons from single quantum dots*, New Journal of Physics, 8 (2006), p. 29. 1

[7] A. V. Kuhlmann, J. H. Prechtel, J. Houel, A. Ludwig, D. Reuter, A. D. Wieck, and R. J. Warburton, *Transform-limited single photons from a single quantum dot*, Nature Communications, 6 (2015), p. 8204. 2

[8] A. Musiał, P. Holewa, P. Wyborski, M. Syperek, A. Kors, J. P. Reithmaier, G. Sęk, and M. Benyoucef, *High-Purity Triggered Single-Photon Emission from Symmetric Single InAs/InP Quantum Dots around the Telecom C-Band Window*, Advanced Quantum Technologies, 3 (2019), p. 1900082. 2

[9] L. Hanschke, K. A. Fischer, S. Appel, D. Lukin, J. Wierzbowski, S. Sun, R. Trivedi, J. Vučković, J. J. Finley, and K. Müller, *Quantum dot single-photon sources with ultra-low multi-photon probability*, NPJ Quantum Information, 4 (2018), p. 43. 2

[10] F. Liu, A. J. Brash, J. O'Hara, L. M. P. P. Martins, C. L. Phillips, R. J. Coles, B. Royall, E. Clarke, C. Bentham, N. Prtljaga, I. E. Itskevich, L. R. Wilson, M. S. Skolnick, and A. M. Fox, *High Purcell factor generation of indistinguishable on-chip single photons*, Nature Nanotechnology, 13 (2018), pp. 835–840. 2, 104

[11] M. Müller, H. Vural, C. Schneider, A. Rastelli, O. G. Schmidt, S. Höfling, and P. Michler, *Quantum-Dot Single-Photon Sources for Entanglement Enhanced Interferometry*, Physical Review Letters, 118 (2017), p. 257402. 2

[12] A. Faraon, I. Fushman, D. Englund, N. Stoltz, P. Petroff, and J. Vuckovic, *Coherent generation of non-classical light on a chip via photon-induced tunnelling and blockade*, Nature Physics, 4 (2008), p. 859. 2

[13] A. P. Foster, D. Hallett, I. V. Iorsh, S. J. Sheldon, M. R. Godsland, B. Royall, E. Clarke, I. A. Shelykh, A. M. Fox, M. S. Skolnick, I. E. Itskevich, and L. R. Wilson, *Tunable Photon Statistics Exploiting the Fano Effect in a Waveguide*, Physical Review Letters, 122 (2019), p. 173603. 2

[14] D. L. Hurst, D. M. Price, C. Bentham, M. N. Makhonin, B. Royall, E. Clarke, P. Kok, L. R. Wilson, M. S. Skolnick, and A. M. Fox, *Nonreciprocal Transmission and Reflection of a Chirally Coupled Quantum Dot*, Nano Letters, 18 (2018), pp. 5475–5481. 2

[15] C. Schneider, T. Heindel, A. Huggenberger, P. Weinmann, C. Kistner, M. Kamp, S. Reitzenstein, S. Höfling, and A. Forchel, *Single photon emission from a site-controlled quantum dot-micropillar cavity system*, Applied Physics Letters, 94 (2009), p. 111111. 2, 143

[16] C. Schneider, A. Huggenberger, Sünner, T. Heindel, M. Strauss, S. Göpfert, P. Weinmann, S. Reitzenstein, L. Worschech, M. Kamp, S. Höfling, and A. Forchel, *Single site-controlled In(Ga)As/GaAs quantum dots: growth, properties and device integration*, Nanotechnology, 20 (2009), p. 434012. 2, 21, 23, 26, 143, 185, 186

[17] B. Rigal, C. Jarlov, P. Gallo, B. Dwir, A. Rudra, M. Calic, and E. Kapon, *Site-controlled quantum dots coupled to a photonic crystal molecule*, Applied Physics Letters, 107 (2015), p. 141103. 2, 143, 188

[18] C. B. Duke, *Semiconductor Surface Reconstruction: The Structural Chemistry of Two-Dimensional Surface Compounds*, Chemical Reviews, 96 (1996), pp. 1237–1259. 5

[19] A. Ohtake, *Surface reconstructions on GaAs(001)*, Surface Science Reports, 63 (2008), pp. 295–327. 5

[20] R. C. C. Leon, C. H. Yang, J. C. C. Hwang, J. C. Lemyre, T. Tanttu, W. Huang, K. W. Chan, K. Y. Tan, F. E. Hudson, K. M. Itoh, A. Morello, A. Laucht, M. Pioro-Ladrière, A. Saraiva, and A. S. Dzurak, *Coherent spin control of s-, p-, d- and f-electrons in a silicon quantum dot*, Nature Communications, 11 (2020), p. 797. 6

[21] M. C. Löbl, S. Scholz, I. Söllner, J. Ritzmann, T. Denneulin, A. Kovács, B. E. Kardynał, A. Wieck, A. Ludwig, and R. J. Warburton, *Excitons in InGaAs quantum dots without electron wetting layer states*, Communications Physics, 2 (2019), pp. 1–7. 6

[22] Y.-L. L. Fang, H. Zheng, and H. U. Baranger, *One-dimensional waveguide coupled to multiple qubits: photon-photon correlations*, EPJ Quantum Technology, 1 (2014), pp. 1–13. 7

[23] N. P. Brawand, M. B. Goldey, M. Vörös, and G. Galli, *Defect States and Charge Transport in Quantum Dot Solids*, Chemistry of Materials, 29 (2017), pp. 1255–1262. 7

[24] M. Zieliński, *Vanishing fine structure splitting in highly asymmetric InAs/InP quantum dots without wetting layer*, Scientific Reports, 10 (2020), p. 13542. 8

[25] J. D. Plumhof, V. Křápek, F. Ding, K. D. Jöns, R. Hafenbrak, P. Klenovský, A. Herklotz, K. Dörr, P. Michler, A. Rastelli, and O. G. Schmidt, *Strain-induced anticrossing of bright exciton levels in single self-assembled GaAs/$Al_xGa_{1-x}As$ and $In_xGa_{1-x}As$/GaAs quantum dots*, Physical Review B, 83 (2011), p. 121302. 8

[26] P. Lodahl, S. Mahmoodian, and S. Stobbe, *Interfacing single photons and single quantum dots with photonic nanostructures*, Reviews of Modern Physics, 87 (2015), pp. 347–400. 8

[27] H. Dartsch, C. Tessarek, T. Aschenbrenner, S. Figge, C. Kruse, M. Schowalter, A. Rosenauer, and D. Hommel, *Electroluminescence from InGaN quantum dots in a fully monolithic GaN/AlInN cavity*, Journal of Crystal Growth, 320 (2011), pp. 28–31. 9

[28] C. Bentham, D. Hallett, N. Prtljaga, B. Royall, D. Vaitiekus, R. J. Coles, E. Clarke, A. M. Fox, M. S. Skolnick, I. E. Itskevich, and L. R. Wilson, *Single-photon electroluminescence for on-chip quantum networks*, Applied Physics Letters, 109 (2016), p. 161101. 9

[29] A. J. Bennett, R. B. Patel, J. Skiba-Szymanska, C. A. Nicoll, I. Farrer, D. A. Ritchie, and A. J. Shields, *Giant Stark effect in the emission of single semiconductor quantum dots*, Applied Physics Letters, 97 (2010), p. 031104. 9

[30] R. Bose, T. Cai, G. S. Solomon, and E. Waks, *All-optical tuning of a quantum dot in a coupled cavity system*, Applied Physics Letters, 100 (2012), p. 231107. 9, 80

[31] J. D. Ryckman and S. M. Weiss, *Low mode volume slotted photonic crystal single nanobeam cavity*, Applied Physics Letters, 101 (2012), p. 071104. 11

[32] E. M. Purcell, H. C. Torrey, and R. V. Pound, *Resonance Absorption by Nuclear Magnetic Moments in a Solid*, Physical Review Journals. 12

[33] T. Pregnolato, X. Chu, T. Schröder, R. Schott, A. D. Wieck, A. Ludwig, P. Lodahl, and N. Rotenberg, *Deterministic positioning of nanophotonic waveguides around single self-assembled quantum dots*, APL Photonics, 5 (2020), p. 086101. 12

[34] L. Sapienza, M. Davanc, A. Badolato, and K. Srinivasan, *Nanoscale optical positioning of single quantumdots for bright and pure single-photon emission*, Nature Communications, 6 (2015), p. 7833. 12, 33

[35] M. Gschrey, R. Schmidt, J. Schulze, A. Strittmatter, S. Rodt, and S. Reitzenstein, *Resolution and alignment accuracy of low-temperature in situ electron beam lithography for nanophotonic device fabrication*, Journal of Vacuum Science & Technology B, 33 (2015), p. 021603. 12

[36] K. D. Jöns, P. Atkinson, M. Müller, M. Heldmaier, S. M. Ulrich, O. G. Schmidt, and P. Michler, *Triggered Indistinguishable Single Photons with Narrow Line Widths from Site-Controlled Quantum Dots*, Nano Letters, 13 (2013), pp. 126–130. 12, 23, 27, 33, 185

[37] P. Gallo, M. Felici, B. Dwir, K. A. Atlasov, K. F. Karlsson, A. Rudra, A. Mohan, G. Biasiol, L. Sorba, and E. Kapon, *Integration of site-controlled pyramidal quantum dots and photonic crystal membrane cavities*, Applied Physics Letters, 92 (2008), p. 263101. 12

[38] D. L. Hurst, D. M. Price, C. Bentham, M. N. Makhonin, B. Royall, E. Clarke, P. Kok, L. R. Wilson, M. S. Skolnick, and A. M. Fox, *Nonreciprocal Transmission and Reflection of a Chirally Coupled Quantum Dot*, Nano Letters, 18 (2018), pp. 5475–5481. 13

[39] R. J. Coles, D. M. Price, J. E. Dixon, B. Royall, E. Clarke, P. Kok, M. S. Skolnick, A. M. Fox, and M. N. Makhonin, *Chirality of nanophotonic waveguide with embedded quantum emitter for unidirectional spin transfer*, Nature Communications, 7 (2016), p. 11183. 13

[40] H. Pichler, T. Ramos, A. J. Daley, and P. Zoller, *Quantum optics of chiral spin networks*, Physical Review A, 91 (2015), p. 042116. 13

[41] R. J. Coles, D. M. Price, B. Royall, E. Clarke, M. S. Skolnick, A. M. Fox, and M. N. Makhonin, *Path-dependent initialization of a single quantum dot exciton spin in a nanophotonic waveguide*, Physical Review B, 95 (2017), p. 121401. 13

[42] C. Sayrin, C. Junge, R. Mitsch, B. Albrecht, D. O'Shea, P. Schneeweiss, J. Volz, and A. Rauschenbeutel, *Nanophotonic Optical Isolator Controlled by the Internal State of Cold Atoms*, Physical Review X, 5 (2015), p. 041036. 13

[43] K. Xia, F. Nori, and M. Xiao, *Cavity-Free Optical Isolators and Circulators Using a Chiral Cross-Kerr Nonlinearity*, Physical Review Letters, 121 (2018), p. 203602. 13

[44] L. N. McCabe and J. M. O. Zide, *Techniques for epitaxial site-selective growth of quantum dots*, Journal of Vacuum Science & Technology A, 39 (2021), p. 010802. 14

[45] J. H. Neave and B. A. Joyce, *Temperature range for growth of autoepitaxial GaAs films by MBE*, Journal of Crystal Growth, 43 (1978), pp. 204–208. 14

[46] J. Wu and P. Jin, *Self-assembly of InAs quantum dots on GaAs(001) by molecular beam epitaxy*, Frontiers of Physics, 10 (2015), pp. 7–58. 15, 20

[47] F. C. Frank and J. H. van der Merwe, *One-dimensional dislocations*, Proceedings of the Royal Society A, 198 (1949), pp. 205–216. 15

[48] M. Volmer and A. Weber, *Keimbildung in übersättigten Gebilden.*, Zeitschrift für Physikalische Chemie, 119 (1926), p. 277. 15

[49] I. N. Stranski and L. Krastanow, *Zur Theorie der orientierten Ausscheidung von Ionenkristallen aufeinander.*, Monatshefte für Chemie, 71 (1938), pp. 351–364. 15

[50] J.-I. Jun-ichi Nishizawa, T. Toru Kurabayashi, H. Abe, and N. Sakurai, *Deposition Mechanism of GaAs Epitaxy*, Journal of The Electrochemical Society, 134 (1987), pp. 945–951. 15

[51] P. D. Wang, N. N. Ledentsov, C. M. Sotomayor Torres, P. S. Kop'ev, and V. M. Ustinov, *Optical characterization of submonolayer and monolayer InAs structures grown in a GaAs matrix on (100) and high-index surfaces*, Applied Physics Letters, 64 (1994), pp. 1526–1528. 15

[52] N. Koguchi, S. Takahashi, and T. Chikyow, *New MBE growth method for InSb quantum well boxes*, Journal of Crystal Growth, 111 (1991), pp. 688–692. 16

[53] J. H. Lee, Z. M. Wang, K. Sablon, and G. J. Salamo, *Formation of Hybrid Molecules Composed of Ga Metal Particle in Direct Contact with InGaAs Semiconductor Quantum Ring*, Crystal Growth & Design, 8 (2008), pp. 690–694. 16

[54] J. H. Lee, Z. M. Wang, Z. Y. AbuWaar, and G. J. Salamo, *Design of Nanostructure Complexes by Droplet Epitaxy*, Crystal Growth & Design, 9 (2009), pp. 715–721. 16

[55] N. Pankaow, S. Panyakeow, and S. Ratanathammaphan, *Formation of In0.5Ga0.5As ring-and-hole structure by droplet molecular beam epitaxy*, Journal of Crystal Growth, 311 (2009), pp. 1832–1835. 16

[56] J. H. Lee, Z. M. Wang, and G. J. Salamo, *The Control on Size and Density of InAs QDs by Droplet Epitaxy*, IEEE Transactions on Nanotechnology, 8 (2009), pp. 431–436. 16

[57] C. Heyn, A. Stemmann, A. Schramm, H. Welsch, W. Hansen, and A. Nemcsics, *Regimes of GaAs quantum dot self-assembly by droplet epitaxy*, Physical Review B, 76 (2007), p. 075317. 16

[58] V. Cambel and J. Šoltýs, *The influence of sample conductivity on local anodic oxidation by the tip of atomic force microscope*, Journal of Applied Physics, 102 (2007), p. 074315. 16

[59] R. Garcia, A. W. Knoll, and E. Riedo, *Advanced scanning probe lithography*, Nature Nanotechnology, 9 (2014), p. 577–587. 16

[60] K. M. Cha, K. Shibata, M. Kamiko, R. Yamamoto, and K. Hirakawa, *Chemical Composition and Thermal Stability of Atomic Force Microscope-Assisted Anodic Ox-*

ides as Nanomasks for Molecular Beam Epitaxy, Japanese Journal of Applied Physics, 50 (2011), p. 120205. 17, 18, 67, 70

[61] X. Wang, B. Theogene, H. Mei, J. Zhang, C. Huang, X. Ren, and M. Xu, *Impact of various parameters on nanostructures fabrication mechanism on silicon surface with AFM tip induced local anodic oxidation*, Ferroelectrics, 549 (2019), pp. 70–77. 17, 67

[62] G. Rius, M. Lorenzoni, S. Matsui, M. Tanemura, and F. Perez-Murano, *Boosting the local anodic oxidation of silicon through carbon nanofiber atomic force microscopy probes*, Beilstein Journal of Nanotechnology, 6 (2015), pp. 215–222. 17

[63] A. S. Kozhukhov, D. V. Scheglov, L. I. Fedina, and A. V. Latyshev, *The initial stages of atomic force microscope based local anodic oxidation of silicon*, AIP Advances, 8 (2018), p. 025113. 17

[64] Y. Okada, S. Amano, M. Kawabe, and J. S. Harris, *Basic mechanisms of an atomic force microscope tip-induced nano-oxidation process of GaAs*, Journal of Applied Physics, 83 (1998), pp. 7998–8001. 17

[65] J. Martín-Sánchez, Y. González, L. González, M. Tello, R. García, D. Granados, J. García, and F. Briones, *Ordered InAs quantum dots on pre-patterned GaAs (001) by local oxidation nanolithography*, Journal of Crystal Growth, 284 (2005), pp. 313–318. 17

[66] J. Martín-Sánchez, G. Muñoz-Matutano, J. Herranz, J. Canet-Ferrer, B. Alén, Y. González, P. Alonso-González, D. Fuster, L. González, J. Martínez-Pastor, and F. Briones, *Single Photon Emission from Site-Controlled InAs Quantum Dots Grown on GaAs(001) Patterned Substrates*, ACS Nano, 3 (2009), pp. 1513–1517. 17, 138

[67] E. Tranvouez, M. Gendry, P. Regreny, and G. Bremond, *InP patterning using contact mode and non-contact AFM lithography for quantum dot localization*, Superlattices and Microstructures, 36 (2004), pp. 325–333. 17, 69

[68] H. Z. Song, T. Usuki, S. Hirose, K. Takemoto, Y. Nakata, N. Yokoyama, and Y. Sakuma, *Site-controlled photoluminescence at telecommunication wavelength from InAsInP quantum dots*, Applied Physics Letters, 86 (2005), p. 113118. 17, 18, 64

[69] J. A. Dagata, J. Schneir, H. H. Harary, C. J. Evans, M. T. Postek, and J. Bennett, *Modification of hydrogen-passivated silicon by a scanning tunneling microscope operating in air*, Applied Physics Letters, 56 (1990), pp. 2001–2003. 17

[70] V. I. Avilov, O. A. Ageev, Y. F. Blinov, B. G. Konoplev, V. V. Polyakov, V. A. Smirnov, and O. G. Tsukanova, *Simulation of the formation of nanosize oxide structures by local anode oxidation of the metal surface*, Technical Physics, 60 (2015), pp. 717–723. 17

[71] P. Avouris, T. Hertel, and R. Martel, *Atomic force microscope tip-induced local oxidation of silicon: kinetics, mechanism, and nanofabrication*, Applied Physics Letters, 71 (1997), pp. 285–287. 17, 73

[72] P. Avouris, R. Martel, T. Hertel, and R. Sandstrom, *AFM-tip-induced and current-induced local oxidation of silicon and metals*, Applied Physics A, 66 (1998), p. S659–S667. 17

[73] R. V. Martinez, N. S. Losilla, J. Martinez, M. Tello, and R. Garcia, *Sequential and parallel patterning by local chemical nanolithography*, Nanotechnology, 18 (2007), p. 084021. 17

[74] V. I. Avilov, O. A. Ageev, V. A. Smirnov, M. S. Solodovnik, and O. G. Tsukanova, *Studying the modes of nanodimensional surface profiling of Gallium Arsenide epitaxial structures by local anodic oxidation*, Nanotechnologies in Russia, 10 (2015), pp. 214–219. 17

[75] N. Cabrera and N. F. Mott, *Theory of the oxidation of metals*, Reports on Progress in Physics, 12 (1949), pp. 163–184. 17, 73

[76] D. Stiévenard, P. A. Fontaine, and E. Dubois, *Nanooxidation using a scanning probe microscope: An analytical model based on field induced oxidation*, Applied Physics Letters, 70 (1997), pp. 3272–3274. 17, 74

[77] J. Červenka, R. Kalousek, M. Bartošík, D. Škoda, O. Tomanec, and T. Šikola, *Fabrication of nanostructures on Si(100) and GaAs(100) by local anodic oxidation*, Applied Surface Science, 253 (2006), pp. 2373–2378. 17, 76

[78] J. J. Ahn, K. S. Moon, and S. M. Koo, *Nano-structure fabrication of GaAs using AFM tip-induced local oxidation method: different doping types and plane orientations*, Applied Physics Letters, 6 (2011), p. 550. 17, 73

[79] E. M. Sala, M. Bollani, S. Bietti, A. Fedorov, L. Esposito, and S. Sanguinetti, *Ordered array of Ga droplets on GaAs(001) by local anodic oxidation*, Journal of Vacuum Science & Technology B, 32 (2014), p. 061206. 18

[80] N. Ozaki, K. Takeuchi, Y. Hino, Y. Nakatani, T. Yasuda, S. Ohkouchi, E. Watanabe, H. Ohsato, N. Ikeda, Y. Sugimoto, E. Clarke, and R. Hogg, *Integration of Emission-Wavelength-Controlled InAs Quantum Dots for Ultra-Broadband Near-Infrared Light Source*, Nanomaterials and Nanotechnology, 4. 18

[81] H. Liu, W-S.and Chang and J.-I. Jen-Inn Chyi, *Effects of dot height uniformity on the performance of 1.3 μm InAs quantum dot lasers*, 5th IEEE Conference on Nanotechnology, 2005., 2 (2005), pp. 784–787. 18

[82] P. B. Joyce, T. J. Krzyzewski, G. R. Bell, T. S. Jones, S. Malik, D. Childs, and R. Murray, *Effect of growth rate on the size, composition, and optical properties of InAs/GaAs quantum dots grown by molecular-beam epitaxy*, Physical Reviews B, 62 (2000), pp. 10891–10895. 18

[83] P. Joyce, T. Krzyzewski, G. Bell, T. Jones, S. Malik, D. Childs, and R. Murray, *Growth rate effects on the size, composition and optical properties of InAs/GaAs quantum dots grown by molecular beam epitaxy*, Journal of Crystal Growth, 227-228 (2001), pp. 1000–1004. 18

[84] L. Chu, M. Arzberger, G. Böhm, and G. Abstreiter, *Influence of growth conditions on the photoluminescence of self-assembled InAs/GaAs quantum dots*, Journal of Applied Physics, 85 (1999), pp. 2355–2362. 18

[85] B. Zhang, G. S. Solomon, M. Pelton, J. Plant, C. Santori, J. Vučković, and Y. Yamamoto, *Fabrication of InAs quantum dots in AlAsGaAs DBR pillar microcavities for single photon sources*, Journal of Applied Physics, 97 (2005), p. 073507. 18

[86] F. Ferdos, M. Sadeghi, Q. X. Zhao, S. M. Wang, and A. Larsson, *Optimisation of MBE growth conditions for InAs quantum dots on (001) GaAs for 1.3μm luminescence*, Journal of Crystal Growth, 227-228 (2001), pp. 1140–1145. 18

[87] G. Trevisi, L. Seravalli, P. Frigeri, and S. Franchi, *Low density InAs/(In)GaAs quantum dots emitting at long wavelengths*, Nanotechnology, 20 (2009), p. 415607. 18

[88] K. Mukai, Y. Nakata, K. Otsubo, M. Sugawara, N. Yokoyama, and H. Ishikawa, *1.3 μm CW lasing characteristics of self-assembled InGaAs-GaAs quantum dots*, IEEE Journal of Quantum Electronics, 36 (2000), pp. 472–478. 18

[89] K. Yamaguchi, K. Yujobo, and T. Kaizu, *Stranski-Krastanov Growth of InAs Quantum Dots with Narrow Size Distribution*, Japanese Journal of Applied Physics, 39 (2000), pp. L1245–L1248. 18

[90] L. Wang, M.-C. Li, W.-X. Wang, H.-C. Gao, H.-T. Tian, M. Xiong, and L.-C. Zhao, *Suppressing the multimodal size distribution of InAs/GaAs quantum dots through flattening the surface fluctuation*, Science China Physics, Mechanics & Astronomy, 53 (2010), pp. 788–792. 18

[91] T. Sugaya, T. Amano, and K. Komori, *Suppressed bimodal size distribution of InAs quantum dots grown with an As2 source using molecular beam epitaxy*, Journal of Applied Physics, 104 (2008), p. 083106. 18

[92] I. Han, R. P. Smith, J. S. Kim, S. K. Noh, S. J. Lee, C.-L. Lee, and J.-Y. Leem, *Efficiency limit of InAs/GaAs quantum dot solar cells attributed to quantum dot size effects*, Solar Energy Materials and Solar Cells, 155 (2016), pp. 70–78. 19

[93] R. Heitz, A. Kalburge, Q. Xie, M. Grundmann, P. Chen, A. Hoffmann, A. Madhukar, and D. Bimberg, *Excited states and energy relaxation in stacked InAs/GaAs quantum dots*, Physical Review B, 57 (1998), pp. 9050–9060. 19

[94] S. Sengupta, S. Y. Shah, N. Halder, and S. Chakrabarti, *Comparison of single-layer and bilayer InAs/GaAs quantum dots with a higher InAs coverage*, Opto-Electronics Review, 18 (2010), pp. 295–299. 19, 63

[95] G. S. Solomon, J. A. Trezza, A. F. Marshall, and J. S. Harris Jr., *Vertically aligned and electronically coupled growth induced InAs islands in GaAs*, Physical Review Letters, 5 (1996), pp. 952–955. 19

[96] J. Tersoff, C. Teichert, and M. G. Lagally, *Self-Organization in Growth of Quantum Dot Superlattices*, Physical Review Letters, 76 (1996), pp. 1675–1678. 19

[97] A. Patel, D. Panda, S. Dongre, S. Alam Gazi, D. Das, and S. Chakrabarti, *A detailed investigation on the impact of variation in monolayer coverage on optical properties of InAs/GaAs multilayer quantum dot heterostructure*, vol. 11085, SPIE, 2019. 19

[98] P. Howe, E. C. Le Ru, E. Clarke, B. Abbey, R. Murray, and T. S. Jones, *Competition between strain-induced and temperature-controlled nucleation of InAs/GaAs quantum dots*, Journal of Applied Physics, 95 (2004), pp. 2998–3004. 19

[99] P. Joyce, T. Krzyzewski, P. Steans, G. Bell, J. Neave, and T. Jones, *Variations in critical coverage for InAs/GaAs quantum dot formation in bilayer structures*, Journal of Crystal Growth, 244 (2002), pp. 39–48. 19

[100] C. H. Chan, C. H. Lee, Y. S. Huang, J. S. Wang, and H. H. Lin, *Characterization of excitonic features in self-assembled InAs/GaAs quantum dot superlattice structures via*

surface photovoltage spectroscopy, Journal of Applied Physics, 101 (2007), p. 103102. 19

[101] D. Srolovitz, *On the stability of surfaces of stressed solids*, Acta Metallurgica, 37 (1989), pp. 621–625. 20

[102] S. Kiravittaya, M. Benyoucef, R. Zapf-Gottwick, A. Rastelli, and O. G. Schmidt, *Ordered GaAs quantum dot arrays on GaAs(001): Single photon emission and fine structure splitting*, Applied Physics Letters, 89 (2006), p. 233102. 20

[103] X. Mei, M. Blumin, M. Sun, D. Kim, Z. H. Wu, H. E. Ruda, and Q. X. Guo, *Highly-ordered GaAs/AlGaAs quantum-dot arrays on GaAs (001) substrates grown by molecular-beam epitaxy using nanochannel alumina masks*, Applied Physics Letters, 82 (2003), pp. 967–969. 20

[104] B. Yang, F. Liu, and M. G. Lagally, *Local Strain-Mediated Chemical Potential Control of Quantum Dot Self-Organization in Heteroepitaxy*, Physical Review Letters, 92 (2004), p. 025502. 20

[105] S. Kohmoto, H. Nakamura, T. Ishikawa, S. Nishikawa, T. Nishimura, and K. Asakawa, *Site-controlled self-organization of InAs quantum dots*, Materials Science and Engineering: B, 88 (2002), pp. 292–297. 20

[106] S. Kiravittaya, H. Heidemeyer, and O. Schmidt, *Growth of three-dimensional quantum dot crystals on patterned GaAs (001) substrates*, Physica E: Low-dimensional Systems and Nanostructures, 23 (2004), pp. 253–259. 20, 23, 29, 145, 185, 186

[107] P. Atkinson, S. Kiravittaya, M. Benyoucef, A. Rastelli, and O. G. Schmidt, *Site-controlled growth and luminescence of InAs quantum dots using in situ Ga-assisted deoxidation of patterned substrates*, Applied Physics Letters, 93 (2008), p. 101908. 21

[108] R. Songmuang, S. Kiravittaya, and O. Schmidt, *Formation of lateral quantum dot molecules around self-assembled nanoholes*, Applied Physics Letters, 82 (2003), pp. 2892–2894. 21

[109] B. L. Liang, Z. M. Wang, J. H. Lee, K. Sablon, Y. I. Mazur, and G. J. Salamo, *Low density InAs quantum dots grown on GaAs nanoholes*, Applied Physics Letters, 89 (2006), p. 043113. 21

[110] T. Pfau, A. Gushterov, J. P. Reithmaier, I. Cestier, and G. Eisenstein, *High optical quality site-controlled quantum dots*, Microelectronic Engineering, 87 (2010), pp. 1357–1359. 21

[111] M. K. Yakes, L. Yang, A. S. Bracker, T. M. Sweeney, P. G. Brereton, M. Kim, C.-S. Kim, P. M. Vora, D. Park, S. G. Carter, and D. Gammon, *Leveraging Crystal Anisotropy for Deterministic Growth of InAs Quantum Dots with Narrow Optical Linewidths*, Nano Letters, 13 (2013), pp. 4870–4875. 21, 23, 26, 185

[112] T. J. Pfau, A. Gushterov, J. P. Reithmaier, I. Cestier, G. Eisenstein, E. Linder, and D. Gershoni, *Site-controlled InAs quantum dots grown on a 55 nm thick GaAs buffer layer*, Applied Physics Letters, 95 (2009), p. 243106. 21

[113] A. Huggenberger, S. Heckelmann, C. Schneider, S. Höfling, S. Reitzenstein, L. Worschech, M. Kamp, and A. Forchel, *Narrow spectral linewidth from single site-controlled In(Ga)As quantum dots with high uniformity*, Applied Physics Letters, 98 (2011), p. 131104. 21, 23, 185, 186

[114] C. J. Mayer, M. F. Helfrich, and D. M. Schaadt, *Influence of hole shape/size on the growth of site-selective quantum dots*, Nanoscale Research Letters, 8 (2013), p. 504. 21, 23, 28, 185, 188

[115] J. Skiba-Szymanska, A. Jamil, I. Farrer, M. B. Ward, C. A. Nicoll, D. J. P. Ellis, J. P. Griffiths, D. Anderson, G. A. C. Jones, D. A. Ritchie, and J. A. Shields, *Narrow emission linewidths of positioned InAs quantum dots grown on pre-patterned GaAs(100) substrates*, Nanotechnology, 22 (2011), p. 065302. 21, 23, 25, 27, 91, 185

[116] K. M. Cha, K. Shibata, and K. Hirakawa, *Single electron transport through site-controlled InAs quantum dots*, Applied Physics Letters, 101 (2012), p. 223115. 21

[117] J. Herranz, L. González, L. Wewior, B. Alén, D. Fuster, and Y. González, *Study of Growth Parameters for Single InAs QD Formation on GaAs(001) Patterned Substrates by Local Oxidation Lithography*, Crystal Growth & Design, 15 (2015), pp. 666–672. 21, 23, 31, 32, 64, 185, 186

[118] Y. Ryu and R. Garcia, *Advanced oxidation scanning probe lithography*, Nanotechnology, 28 (2017), p. 142003. 21

[119] J. Herranz, L. Wewior, B. Alén, D. Fuster, L. González, and Y. González, *Role of re-growth interface preparation process for spectral line-width reduction of single InAs site-controlled quantum dots*, Nanotechnology, 26 (2015), p. 195301. 21, 23, 26, 64, 185, 186

[120] J. Tommila, A. Tukiainen, J. Viheriälä, A. Schramm, T. Hakkarainen, A. Aho, P. Stenberg, and M. Dumitrescu, M. andGuina, *Nanoimprint lithography patterned GaAs templates for site-controlled InAs quantum dots*, Journal of Crystal Growth, 323 (2011), pp. 183–186. 21

[121] C.-C. Cheng, K. Meneou, and K. Cheng, *Effects of nano-pattern size on the property of InAs site-controlled quantum dots*, Journal of Crystal Growth, 323 (2011), pp. 180–182. 21

[122] T. Saucer, J.-E. Lee, A. Martin, D. Tien, J. Millunchick, and V. Sih, *Photoluminescence of patterned arrays of vertically stacked InAs/GaAs quantum dots*, Solid State Communications, 151 (2011), pp. 269–271. 21

[123] Y.-R. Wang, I.-S. Han, C.-Y. Jin, and M. Hopkinson, *Formation of laterally ordered quantum dot molecules by in situ nanosecond laser interference*, Applied Physics Letters, 116 (2020), p. 201901. 21

[124] Y.-R. Wang, C.-Y. Han, I-Sand Jin, and M. Hopkinson, *Precise Arrays of Epitaxial Quantum Dots Nucleated by In Situ Laser Interference for Quantum Information Technology Applications*, ACS Applied Nano Materials, 3 (2020), pp. 4739–4746. 21

[125] S. Kohmoto, H. Nakamura, T. Ishikawa, and K. Asakawa, *Site-controlled self-organization of individual InAs quantum dots by scanning tunneling probe-assisted nanolithography*, Applied Physics Letters, 75 (1999), pp. 3488–3490. 21

[126] J. Grosse, M. von Helversen, A. Koulas-Simos, M. Hermann, and S. Reitzenstein, *Development of site-controlled quantum dot arrays acting as scalable sources of indistinguishable photons*, APL Photonics, 5 (2020), p. 096107. 21, 22

[127] N. Kumagai, S. Ohkouchi, M. Shirane, Y. Igarashi, M. Nomura, Y. Ota, S. Yorozu, S. Iwamoto, and Y. Arakawa, *Effects of growth temperature of partial GaAs cap on InAs quantum dots in In-flush process for single dot spectroscopy*, Physica Status Solidi C, 8, pp. 248–250. 21

[128] C. Schneider, A. Huggenberger, M. Gschrey, P. Gold, S. Rodt, A. Forchel, S. Reitzenstein, S. Höfling, and M. Kamp, *In(Ga)As/GaAs site-controlled quantum dots with tailored morphology and high optical quality*, Physica Status Solidi A, 209 (2012), pp. 2379–2386. 22, 23, 28, 31, 185, 186

[129] V. Dimastrodonato, L. O. Mereni, R. J. Young, and E. Pelucchi, *Growth and structural characterization of pyramidal site-controlled quantum dots with high uniformity and spectral purity*, Physica Status Solidi B, 247, pp. 1862–1866. 22

[130] L. O. Mereni, V. Dimastrodonato, R. J. Young, and E. Pelucchi, *A site-controlled quantum dot system offering both high uniformity and spectral purity*, Applied Physics Letters, 94 (2009), p. 223121. 22

[131] M. Felici, P. Gallo, A. Mohan, B. Dwir, A. Rudra, and E. Kapon, *Site-Controlled InGaAs Quantum Dots with Tunable Emission Energy*, Small, 5, pp. 938–943. 22

[132] F.-Y. Tsai and C. P. Lee, *InGaAs/GaAs quantum dots on (111)B GaAs substrates*, Journal of Applied Physics, 84 (1998), pp. 2624–2627. 22

[133] F.-Y. Tsai and C.-P. Lee, *Photoluminescence Study of High-Quality InGaAs/GaAs Quantum Dots on (111)B GaAs Substrates*, Japanese Journal of Applied Physics, 38 (1999), pp. 558–562. 22

[134] K.-M. Cha, I. Horiuchi, K. Shibata, and K. Hirakawa, *Size-Limiting Effect of Site-Controlled InAs Quantum Dots Grown at High Temperatures by Molecular Beam Epitaxy*, Applied Physics Express, 5 (2012), p. 085501. 23, 31, 32, 64, 185

[135] J. Q. Grim, A. S. Bracker, M. Zalalutdinov, S. G. Carter, A. C. Kozen, M. Kim, C.-S. Kim, J. T. Mlack, M. Yakes, B. Lee, and D. Gammon, *Scalable in operando strain tuning in nanophotonic waveguides enabling three-quantum-dot superradiance*, Nature Materials, 18 (2019), pp. 963–969. 24, 80

[136] P. Mrowiński, P. Schnauber, A. Kaganskiy, J. Schall, S. Burger, S. Rodt, and S. Reitzenstein, *Directional single-photon emission from deterministic quantum dot waveguide structures*, Physica Status Solidi, 14 (2020), p. 2000115. 25

[137] Y. Nakamura, O. Schmidt, N. Jin-Phillipp, S. Kiravittaya, C. Müller, K. Eberl, H. Gräbeldinger, and H. Schweizer, *Vertical alignment of laterally ordered InAs and InGaAs quantum dot arrays on patterned (001) GaAs substrates*, Journal of Crystal Growth, 242 (2002), pp. 339–344. 26, 33

[138] P. Atkinson, O. Schmidt, S. Bremner, and D. Ritchie, *Formation and ordering of epitaxial quantum dots*, Comptes Rendus Physique, 9 (2008), pp. 788–803. 28, 32

[139] S. Hussain, A. Pozzato, M. Tormen, V. Zannier, and G. Biasiol, *Site-Control of InAs/GaAs Quantum Dots with Indium-Assisted Deoxidation*, Materials, 9 (2016), p. 208. 29, 30

[140] S. Kiravittaya, A. Rastelli, and O. G. Schmidt, *Photoluminescence from seeded three-dimensional InAsGaAs quantum-dot crystals*, Applied Physics Letters, 88 (2006), p. 043112. 30, 186

[141] L. N. McCabe, Y. Wang, M. F. Doty, and J. M. O. Zide, *Low-density patterned InAs quantum dot arrays*, Journal of Vacuum Science & Technology B, 38 (2020), p. 022803. 31

[142] T. Sünner, C. Schneider, M. Strauss, A. Huggenberger, D. Wiener, S. Höfling, M. Kamp, and A. Forchel, *Scalable fabrication of optical resonators with embedded site-controlled quantum dots*, Optics Letters, 33 (2008), pp. 1759–1761. 33

[143] C. Schneider, M. Strauss, T. Sünner, A. Huggenberger, D. Wiener, S. Reitzenstein, M. Kamp, S. Höfling, and A. Forchel, *Lithographic alignment to site-controlled quantum dots for device integration*, Applied Physics Letters, 92 (2008), p. 183101. 33

[144] S. Thoms and D. S. Macintyre, *Investigation of CSAR 62, a new resist for electron beam lithography*, Journal of Vacuum Science & Technology B, 32 (2014), p. 06FJ01. 39

[145] M. A. Mohammad, M. Muhammad, S. K. Dew, and M. Stepanova, *Fundamentals of Electron Beam Exposure and Development*, Springer, Vienna, 2012, pp. 11–41. 40

[146] A. Raghunathan and J. G. Hartley, *Influence of secondary electrons in high-energy electron beam lithography*, Journal of Vacuum Science & Technology B, 31 (2013), p. 011605. 40

[147] K. Nojiri, *Dry Etching Damage*, Springer International Publishing, Cham, 2015, pp. 73–89. 41

[148] *Jmol: an open-source Java viewer for chemical structures in 3D*. 43

[149] I. Farrer, J. J. Harris, R. Thomson, D. Barlett, C. A. Taylor, and D. A. Ritchie, *Substrate temperature measurement using a commercial band-edge detection system*, Journal of Crystal Growth, 301-302 (2007), pp. 88–92. 45

[150] P. Atkinson, M. Eddrief, V. H. Etgens, H. Khemliche, M. Debiossac, A. Momeni, M. Mulier, B. Lalmi, and P. Roncin, *Dynamic grazing incidence fast atom diffraction during molecular beam epitaxial growth of GaAs*, Applied Physics Letters, 105 (2014), p. 021602. 47

[151] H. H. Farrell and C. J. Palmstrom, *Reflection high energy electron diffraction characteristic absences in GaAs(100) (2×4)–As: A tool for determining the surface stoichiometry*, Journal of Vacuum Science & Technology B: Microelectronics Processing and Phenomena, 8 (1990), pp. 903–907. 47

[152] T. Sugaya and M. Kawabe, *Low-Temperature Cleaning of GaAs Substrate by Atomic Hydrogen Irradiation*, Japanese Journal of Applied Physics, 30 (1991), pp. L402–L404. 50

[153] D. Fuster, L. Ginés, Y. González, J. Herranz, and L. González, *Low temperature oxide desorption in GaAs (111)A substrates*, Thin Solid Films, 537 (2013), pp. 70–75. 50, 112

[154] T. Burke, E. Linfield, D. Ritchie, M. Pepper, and J. Burroughes, *Hydrogen radical surface cleaning of GaAs for MBE regrowth*, Journal of Crystal Growth, 175-176 (1997), pp. 416–421. 50

[155] Y.-X. Pan, D. Mei, C.-J. Liu, and Q. Ge, *Hydrogen Adsorption on Ga2O3 Surface: A Combined Experimental and Computational Study*, The Journal of Physical Chemistry C, 115 (2011), pp. 10140–10146. 50

[156] A. Khatiri, J. Ripalda, T. Krzyzewski, G. Bell, C. McConville, and T. Jones, *Atomic hydrogen cleaning of GaAs(001): a scanning tunnelling microscopy study*, Surface Science, 548 (2004), pp. L1–L6. 50

[157] G. W. Wicks, E. R. Rueckwald, and M. W. Koch, *Analysis of cracking efficiency of an atomic hydrogen source, and its effect on desorption of AlxGa1xAs native oxides*, Journal of Vacuum Science & Technology B: Microelectronics and Nanometer Structures Processing, Measurement, and Phenomena, 14 (1996), pp. 2184–2186. 50, 52

[158] D. Ugur, A. J. Storm, R. Verberk, J. C. Brouwer, and W. G. Sloof, *Quantification of the atomic hydrogen flux as a function of filament temperature and H2 flow rate*, Journal of Vacuum Science & Technology A, 30 (2012), p. 031603. 50

[159] T. Van Buuren, M. K. Weilmeier, I. Athwal, K. M. Colbow, J. A. Mackenzie, T. Tiedje, P. C. Wong, and K. A. R. Mitchell, *Oxide thickness effect and surface roughening in the desorption of the oxide from GaAs*, Applied Physics Letters, 59 (1991), pp. 464–466. 50, 112

[160] H. Shimomura, Y. Okada, and M. Kawabe, *Low Dislocation Density GaAs on Vicinal Si(100) Grown by Molecular Beam Epitaxy with Atomic Hydrogen Irradiation*, Japanese Journal of Applied Physics, 31 (1992), pp. L628–L631. 50

[161] K. G. Tschersich and V. von Bonin, *Formation of an atomic hydrogen beam by a hot capillary*, Journal of Applied Physics, 84 (1998), pp. 4065–4070. 51, 52

[162] K. G. Tschersich, *Intensity of a source of atomic hydrogen based on a hot capillary*, Journal of Applied Physics, 87 (2000), pp. 2565–2573. 51

[163] K. G. Tschersich, J. P. Fleischhauer, and H. Schuler, *Design and characterization of a thermal hydrogen atom source*, Journal of Applied Physics, 104 (2008), p. 034908. 51

[164] K. G. Tschersich, *Intensity of a source of atomic hydrogen based on a hot capillary*, Journal of Applied Physics, 87 (2000), pp. 2565–2573. 52

[165] K. G. Tschersich, J. P. Fleischhauer, and H. Schuler, *Design and characterization of a thermal hydrogen atom source*, Journal of Applied Physics, 104 (2008), p. 034908. 52

[166] D. Nečas and P. Klapetek, *Gwyddion: an open-source software for SPM data analysis*, Central European Journal of Physics, 10 (2012), pp. 181–188. 54

[167] MATLAB, *version 7.10.0 (r2018b)*, (2018). 54

[168] E. Gadelmawla, M. Koura, T. Maksoud, I. Elewa, and H. Soliman, *Roughness parameters*, Journal of Materials Processing Technology, 123 (2002), pp. 133–145. 54

[169] *Lumerical Inc.*, 2020 R2.4. 58

[170] O. Medenbach, T. Siritanon, M. Subramanian, R. Shannon, R. Fische, and G. Rossman, *Refractive index and optical dispersion of In_2O_3, $InBO_3$ and gahnite*, Materials Research Bulletin, 48 (2013), pp. 2240–2243. 59

[171] S. D. Gedney and B. Zhao, *An Auxiliary Differential Equation Formulation for the Complex-Frequency Shifted PML*, IEEE Transactions on Antennas and Propagation, 58 (2010), pp. 838–847. 60

[172] R. J. Coles, *Quantum Optical Circuits using III-V Nanophotonic Structures.*, (2012). 61

[173] A. Wallucks, I. Marinković, B. Hensen, R. Stockill, and S. Gröblacher, *A quantum memory at telecom wavelengths*, Nature Physics, 16 (2020), pp. 772–777. 63

[174] J. Dias, M. Winnel, N. Hosseinidehaj, and T. C. Ralph, *Quantum repeater for continuous-variable entanglement distribution*, Physical Review A, 102 (2020), p. 052425. 63

[175] Y. Jo, K. Bae, and W. Son, *Enhanced Bell state measurement for efficient measurement-device-independent quantum key distribution using 3-dimensional quantum states*, Scientific reports, 9 (2019), p. 687. 63

[176] T. Miya, Y. Terunuma, T. Hosaka, and T. Miyashita, *Ultimate low-loss single-mode fibre at 1.55 μm*, Electronics Letters, 15 (1979), pp. 106–108. 63

[177] S.-K. Liao, H.-L. Yong, C. Liu, G.-L. Shentu, D.-D. Li, J. Lin, H. Dai, S.-Q. Zhao, B. Li, J.-Y. Guan, W. Chen, Y.-H. Gong, Y. Li, Z.-H. Lin, G.-S. Pan, J. S. Pelc, M. M. Fejer, W.-Z. Zhang, W.-Y. Liu, J. Yin, J.-G. Ren, X.-B. Wang, Q. Zhang, C.-Z. Peng, and J.-W. Pan, *Long-distance free-space quantum key distribution in daylight towards inter-satellite communication*, Nature Photonics, 11 (2017), pp. 4509–513. 63

[178] K. Nishi, H. Saito, S. Sugou, and J.-S. Lee, *A narrow photoluminescence linewidth of 21 meV at 1.35 μm from strain-reduced InAs quantum dots covered by In0.2Ga0.8As grown on GaAs substrates*, Applied Physics Letters, 74 (1999), pp. 1111–1113. 63

[179] V. M. Ustinov, N. A. Maleev, A. E. Zhukov, A. R. Kovsh, A. Y. Egorov, A. V. Lunev, B. V. Volovik, I. L. Krestnikov, Y. G. Musikhin, N. A. Bert, P. S. Kop'ev, Z. I. Alferov, N. N. Ledentsov, and D. Bimberg, *InAs/InGaAs quantum dot structures on GaAs substrates emitting at 1.3 μm*, Applied Physics Letters, 74 (1999), pp. 2815–2817. 63

[180] C. Jiang, J. Ning, X. Li, X. Wang, and Z. Zhang, *Development of a 1550-nm InAs/GaAs Quantum Dot Saturable Absorber Mirror with a Short-Period Superlattice Capping Structure Towards Femtosecond Fiber Laser Applications*, Nanoscale Research Letters, 14 (2019), p. 362. 64

[181] M. Gong, K. Duan, C.-F. Li, R. Magri, G. A. Narvaez, and L. He, *Electronic structure of self-assembled* InAsInP *quantum dots: Comparison with self-assembled* InAsGaAs *quantum dots*, Physical Reviews B, 77 (2008), p. 045326. 64

[182] D. Fuster, K. Abderrafi, B. Alén, Y. González, L. Wewior, and L. González, *InAs nanostructures grown by droplet epitaxy directly on InP(001) substrates*, Journal of Crystal Growth, 434 (2016), pp. 81–87. 64

[183] J. Skiba-Szymanska, R. M. Stevenson, C. Varnava, M. Felle, J. Huwer, T. Müller, A. J. Bennett, J. P. Lee, I. Farrer, A. B. Krysa, P. Spencer, L. E. Goff, D. A. Ritchie, J. Heffernan, and A. J. Shields, *Universal Growth Scheme for Quantum Dots with Low Fine-Structure Splitting at Various Emission Wavelengths*, Physical Reviews Applied, 8 (2017), p. 014013. 64

[184] L. He, M. Gong, C.-F. Li, G.-C. Guo, and A. Zunger, *Highly Reduced Fine-Structure Splitting in* InAs/InP *Quantum Dots Offering an Efficient On-Demand Entangled 1.55-*μm *Photon Emitter*, Physical Review Letters, 101 (2008), p. 157405. 64

[185] K. J. Smirnov, V. I. Medzakovskiy, V. V. Davydov, M. G. Vysoczky, and S. F. Glagolev, *High sensitive InP emitter for InP/InGaAs heterostructures*, Journal of Physics: Conference Series, 917 (2017), p. 062019. 65

[186] Y. Sun, Z. Liu, F. Machuca, P. Pianetta, and W. E. Spicer, *Preparation of clean InP(100) surfaces studied by synchrotron radiation photoemission*, Journal of Vacuum Science & Technology A, 21 (2003), pp. 219–225. 65

[187] V. I. Avilov, O. A. Ageev, Y. F. Blinov, B. G. Konoplev, V. V. Polyakov, V. A. Smirnov, and O. G. Tsukanova, *Simulation of the formation of nanosize oxide structures by local anode oxidation of the metal surface*, Technical Physics, 60 (2015), pp. 717–723. 69

[188] S.-R. Jian, T.-H. Fang, and D.-S. Chuu, *Mechanisms ofp-GaAs(100) surface by atomic force microscope nano-oxidation*, Journal of Physics D: Applied Physics, 38 (2005), pp. 2424–2432. 70

[189] Y. Komijani, M. Csontos, T. Ihn, K. Ensslin, D. Reuter, and A. Wieck, *Observation of excited states in a p-type GaAs quantum dot*, Euro Physics Letters, 84 (2008), p. 57004. 73

[190] M. Bartošík, D. Škoda, O. Tomanec, P. Kalousek, R.and Jánský, J. Zlámal, J. Spousta, P. Dub, and T. Šikola, *Role of humidity in local anodic oxidation: A study of water condensation and electric field distribution*, Phys. Rev. B, 79 (2009), p. 195406. 73

[191] M. Yasutake, Y. Ejiri, and T. Hattori, *Modification of Silicon Surface Using Atomic Force Microscope with Conducting Probe*, Japanese Journal of Applied Physics, 32 (1993), pp. L1021–L1023. 76

[192] T. Hattori, Y. Ejiri, K. Saito, and M. Yasutake, *Fabrication of nanometer-scale structures using atomic force microscope with conducting probe*, Journal of Vacuum Science & Technology A, 12 (1994), pp. 2586–2590. 76

[193] H. Sugimura, N. Kitamura, and H. Masuhara, *Modification of n-Si(100) Surface by Scanning Tunneling Microscope Tip-Induced Anodization under Nitrogen Atmosphere*, Japanese Journal of Applied Physics, 33 (1994), pp. L143–L145. 76

[194] K. Hennessy, C. Högerle, E. Hu, A. Badolato, and A. Imamoğlu, *Tuning photonic nanocavities by atomic force microscope nano-oxidation*, Applied Physics Letters, 89 (2006), p. 041118. 77

[195] C. J. Summers, E. Graugnard, D. P. Gaillot, T. Yamashita, C. W. Neff, and J. Blair, *Tuning of photonic crystal band properties by atomic layer deposition*, Journal of Nonlinear Optical Physics & Materials, 17 (2008), pp. 1–14. 80

[196] W.-Y. Chen, M.-J. Chen, C.-C. Cheng, T. M. Hsu, C.-J. Wang, and J.-I. Chyi, *Imaging resonant modes in photonic crystal nanocavity by atomic force microscope nano-oxidation*, Applied Physics Letters, 98 (2011), p. 191110. 80

[197] P. Vettiger, M. Despont, U. Drechsler, U. Durig, W. Haberle, M. I. Lutwyche, H. E. Rothuizen, R. Stutz, R. Widmer, and G. K. Binnig, *The "Millipede"—More than thousand tips for future AFM storage*, IBM Journal of Research and Development, 44 (2000), pp. 323–340. 85

[198] M. Nooney, V. Liberman, M. Xu, A. Ludviksson, and R. Martin, *Reaction of HCl with the GaAs(100) surface*, Surface Science, 302 (1994), pp. 192–204. 99

[199] S. J. Gibson, J. P. Boulanger, and R. R. LaPierre, *Opportunities and pitfalls in patterned self-catalyzed GaAs nanowire growth on silicon*, Semiconductor Science and Technology, 28 (2013), p. 105025. 102

[200] *Optical Etaloning in Charge Coupled Devices (CCD).*, Accessed July 2021. 111

[201] A. Takamori, S. Sugata, K. Asakawa, E. Miyauchi, and H. Hashimoto, *Cleaning of MBE GaAs Substrates by Hydrogen Radical Beam Irradiation*, Japanese Journal of Applied Physics, 26 (1987), pp. L142–L144. 117

[202] Z. R. Wasilewski, J.-M. Baribeau, M. Beaulieu, X. Wu, and G. I. Sproule, *Studies of oxide desorption from GaAs substrates via Ga_2O_3 to Ga_2O conversion by exposure to Ga flux*, Journal of Vacuum Science & Technology B, 22 (2004), pp. 1534–1538. 117

[203] Y. Asaoka, *Desorption process of GaAs surface native oxide controlled by direct Ga-beam irradiation*, Journal of Crystal Growth, 251 (2003), pp. 40–45. Proceedings of the Twelfth International Conference on Molecular Beam Epitaxy. 117

[204] M. Yamada, Y. Masamichi, and I. Yuichi, *Anomalous behaviors observed in the isothermal desorption of GaAs surface oxides*, Surface science, 339 (1995), pp. L914–L918. 117

[205] P. Atkinson and O. Schmidt, *Gallium-assisted deoxidation of patterned substrates for site-controlled growth of InAs quantum dots*, Journal of Crystal Growth, 311 (2009), pp. 1815–1818. International Conference on Molecular Beam Epitaxy (MBE-XV). 117

[206] L. Li, E. Linfield, R. Sharma, and A. Davies, *In-assisted desorption of native GaAs surface oxides*, Applied Physics Letters, 99 (2011), p. 061910. 117

[207] T. Xia, Y. Cho, M. Cotrufo, I. Agafonov, F. van Otten, and A. Fiore, *In-assisted deoxidation of GaAs substrates for the growth of single InAs/GaAs quantum dot emitters*, Semiconductor Science and Technology, 30 (2015), p. 055009. 117

[208] S. Hussain, A. Pozzato, M. Tormen, V. Zannier, and G. Biasiol, *Site-Control of InAs/GaAs Quantum Dots with Indium-Assisted Deoxidation*, Materials, 9 (2016), p. 208. 117, 186

[209] B. Brennan and G. Hughes, *Identification and thermal stability of the native oxides on InGaAs using synchrotron radiation based photoemission*, Journal of Applied Physics, 108 (2010), p. 053516. 125

[210] J. Martín-Sánchez, P. Alonso-González, J. Herranz, Y. González, and L. González, *Site-controlled lateral arrangements of InAs quantum dots grown on GaAs(001) patterned substrates by atomic force microscopy local oxidation nanolithography*, Nanotechnology, 20 (2009), p. 125302. 140

[211] D. Fuster, L. Ginés, Y. González, J. Herranz, and L. González, *Low temperature oxide desorption in GaAs (111)A substrates*, Thin Solid Films, 537 (2013), pp. 70–75. 141

[212] A. Huggenberger, C. Schneider, T. Heindel, M. Kamp, S. Reitzenstein, S. Höfling, L. Worschech, and A. Forchel, *Site-controlled In(Ga)As quantum dots with narrow emission linewidth for integration into nanophotonic devices*, 2011 International Quantum Electronics Conference IQEC and CLEO., (2011), pp. 216–218. 143, 188

[213] M. Nakayama, K. Suyama, and H. Nishimura, *Biexciton formation in GaAs/AlAs type-II superlattices under extremely low excitation powers*, Physical Review B, 51 (1995), pp. 7870–7873. 170

[214] L. Seravalli, G. Trevisi, P. Frigeri, D. Rivas, G. Muñoz-Matutano, I. Suárez, B. Alén, J. Canet-Ferrer, and J. P. Martínez-Pastor, *Single quantum dot emis-*

sion at telecom wavelengths from metamorphic InAs/InGaAs nanostructures grown on GaAs substrates, Applied Physics Letters, 98 (2011), p. 173112. 170

[215] J. Canet-Ferrer, G. Munoz-Matutano, J. Herranz, D. Rivas, B. Alen, Y. Gonzalez, D. Fuster, L. Gonzalez, and J. Martínez-Pastor, *Exciton and multiexciton optical properties of single InAs/GaAs site-controlled quantum dots*, Applied Physics Letters, 103 (2013), p. 183112. 171

[216] A. Zunger and G. Bester, *Theory of excitons, charged excitons, exciton fine-structure and entangled excitons in self-assembled semiconductor quantum dots*, Physica E: Low-dimensional Systems and Nanostructures, 21 (2004), pp. 204–210. 171

[217] R. Seguin, A. Schliwa, S. Rodt, K. Pötschke, U. W. Pohl, and D. Bimberg, *Size-Dependent Fine-Structure Splitting in Self-Organized* InAs/GaAs *Quantum Dots*, Physical Review Letters, 95 (2005), p. 257402. 171

[218] S. Stufler, P. Ester, A. Zrenner, and M. Bichler, *Power broadening of the exciton linewidth in a single InGaAs/GaAs quantum dot*, Applied Physics Letters, 85 (2004), pp. 4202–4204. 176

[219] M. Helfrich, P. Schroth, D. Grigoriev, S. Lazarev, R. Felici, T. Slobodskyy, T. Baumbach, and D. M. Schaadt, *Growth and characterization of site-selective quantum dots*, Physica Status Solidi A, 209, pp. 2387–2401. 180

This page intentionally left blank

A | Appendix

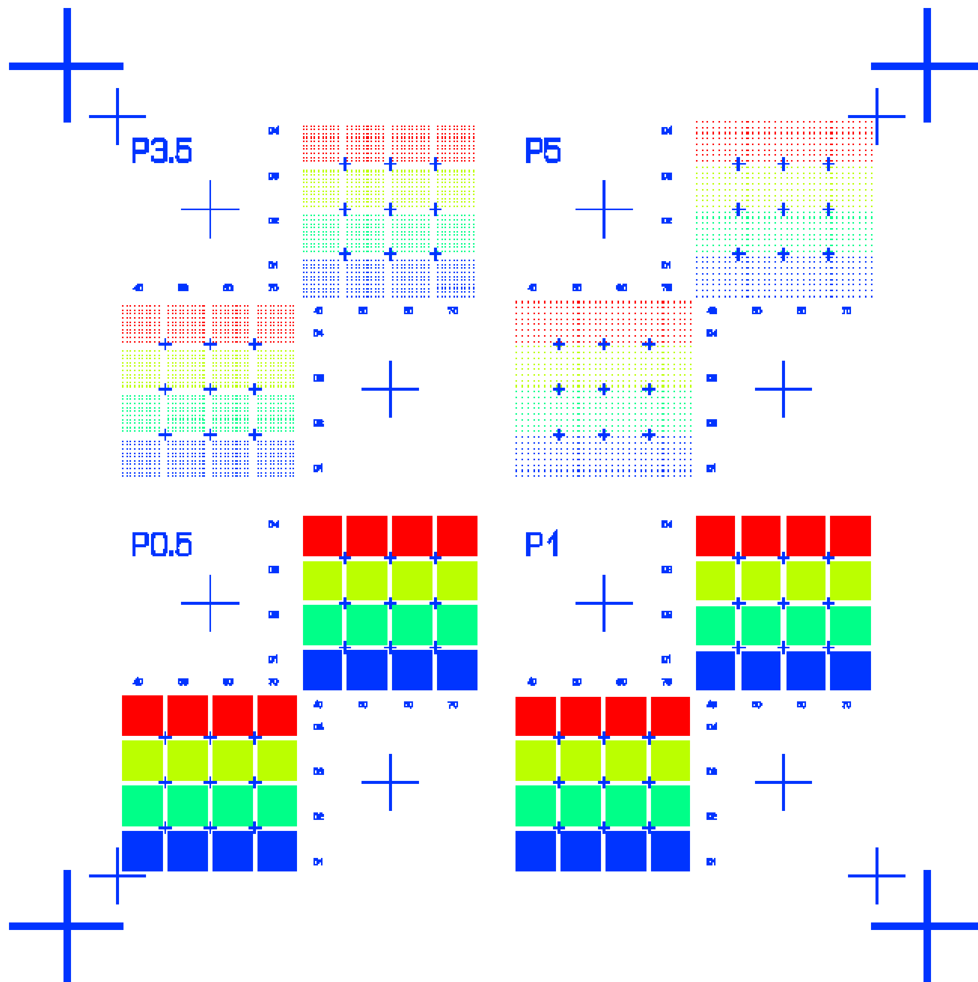

Figure A-1. EBL pattern 2. The four areas labelled P0.5, P1, P3.5 and P5 are each at a different nanohole pitch corresponding to 0.5 μm, 1.0 μm, 3.5 μm, and 5.0 μm . The dose and drawn size was varied for each pitch. Alignment crosses of various sizes, suitable for AFM, μPL, and EBL alignment, are present across the pattern. Drawn size ranges between 40 nm and 70 nm and dose varies between 0.6 and 5.8 times base dose.

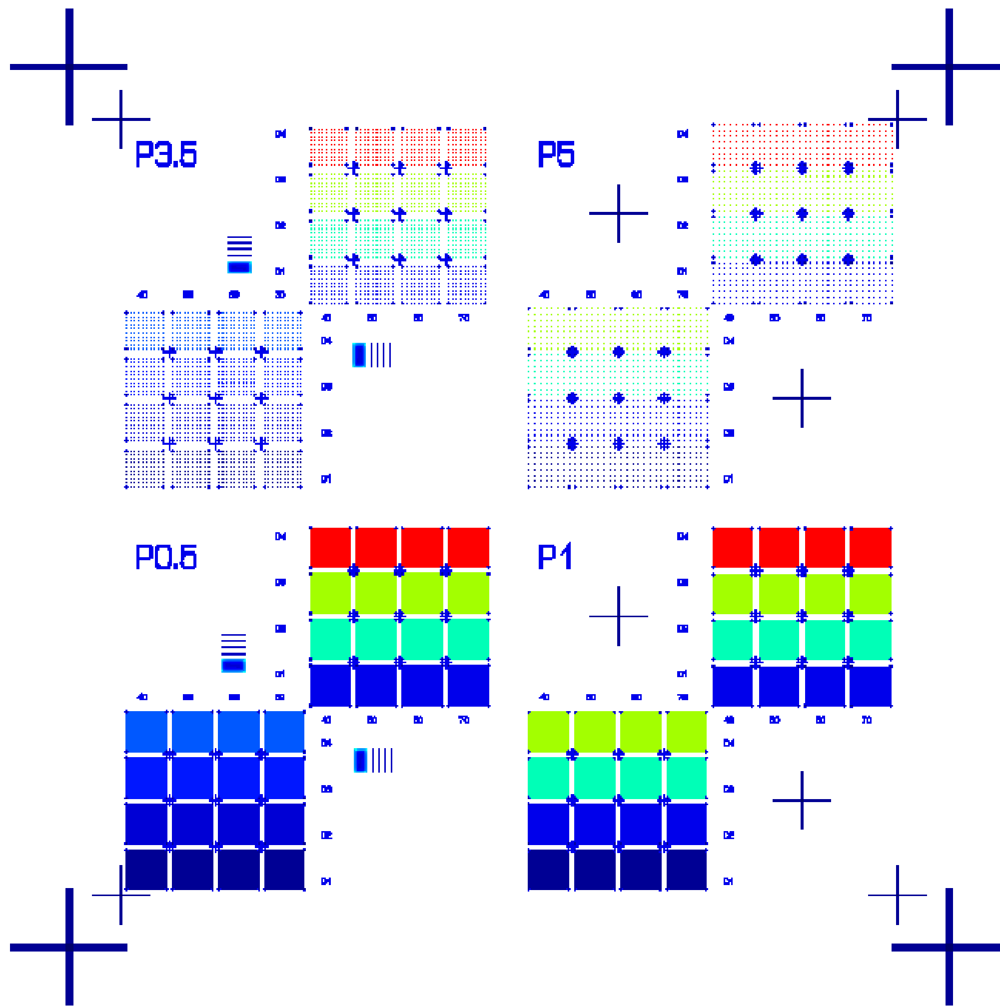

Figure A-2. EBL pattern 3 shows the same basic design as pattern 2. Updates included drawn size ranges from 32 nm to 70 nmand some crosses were replaced with lines that allowed larger featurer etch depths to be measured.

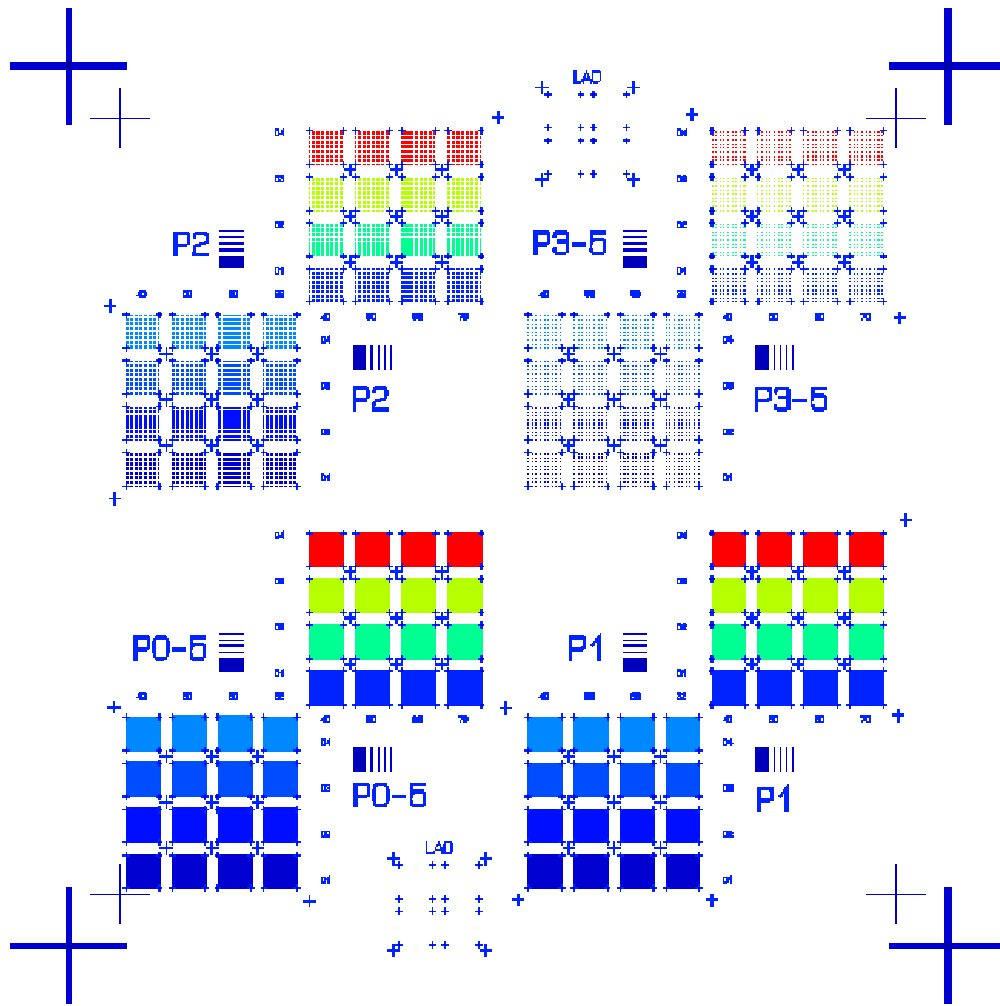

Figure A-3. EBL pattern 4. Updates included all crosses were replaced with etch measurement lines, alignment marks specifically for LAO fabrication were added, induvidual arrays were slightly reduced in size, which made alignment crosses more easily destinguishable during Pl measurements, and pitch was changed to 0.5 μm, 1.0 μm, 2.0 μm, 3.5 μm.

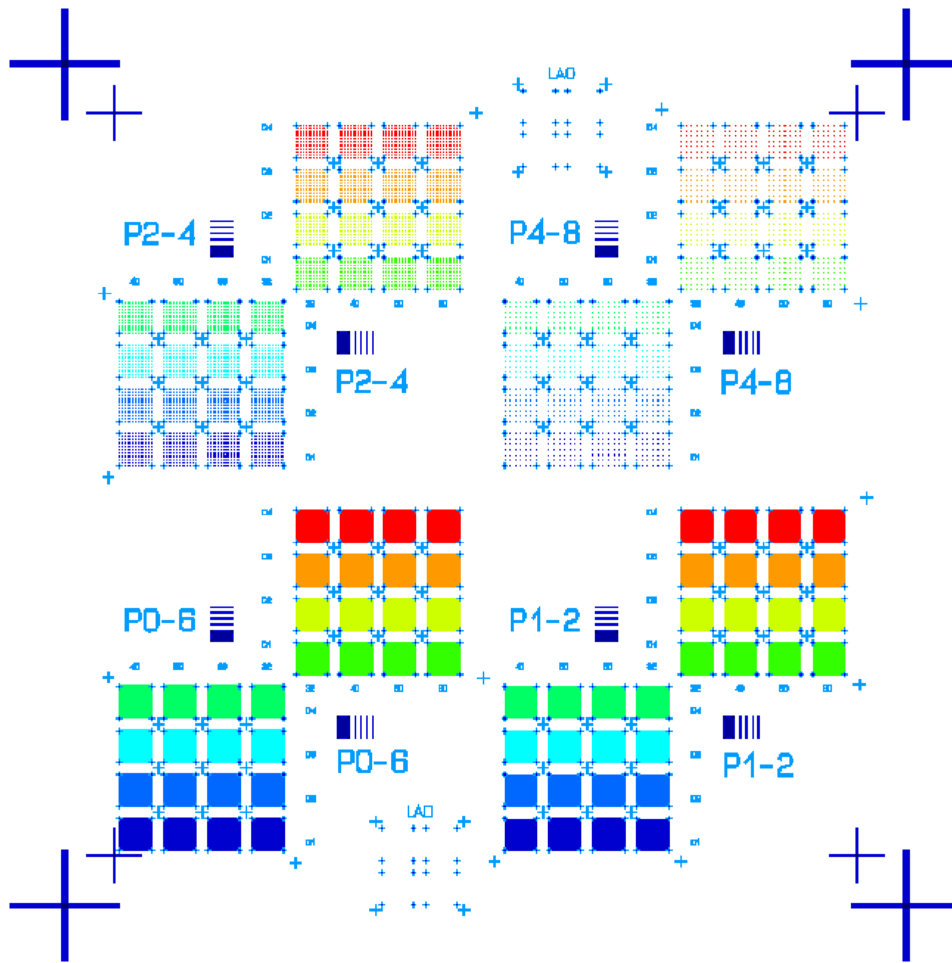

Figure A-4. EBL pattern 5. Updates included reduction in the dose range from 0.6 to 2.7 times the base dose, and pitch was changed to 0.6 μm, 1.2 μm, 2.4 μm, and 4.8 μm.

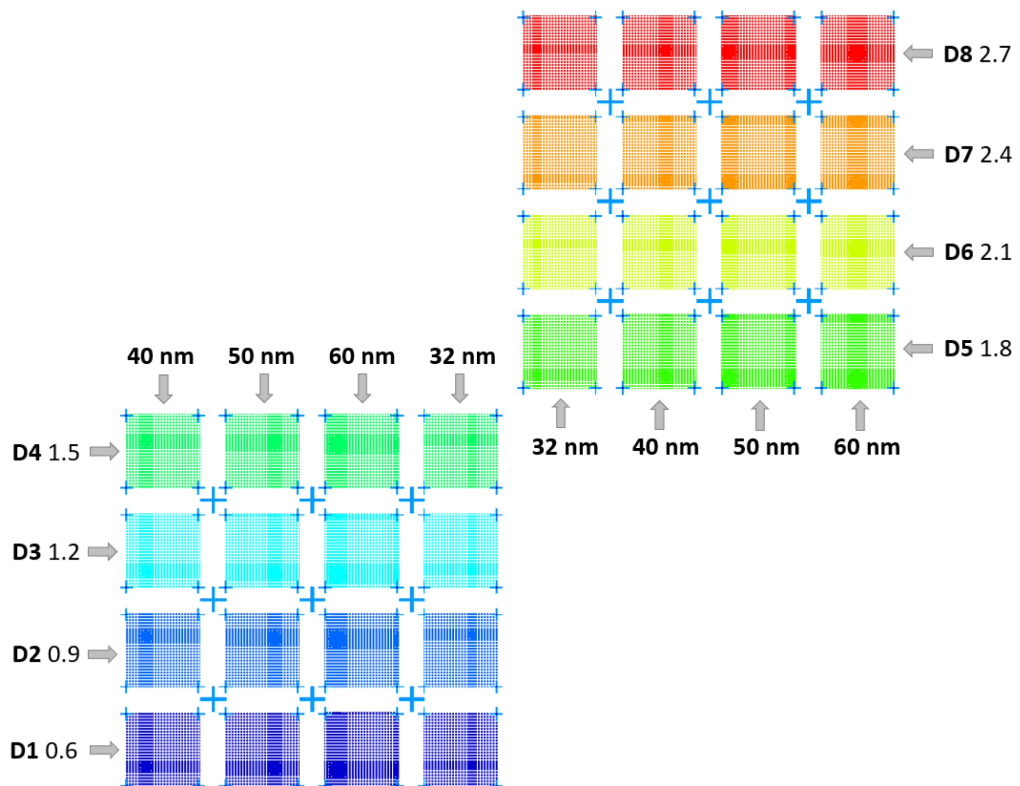

Figure A-5. Zoom in of nanohole arrays labelled with the EBL dose and drawn size for EBL pattern 5, pitch 0.6 μm.

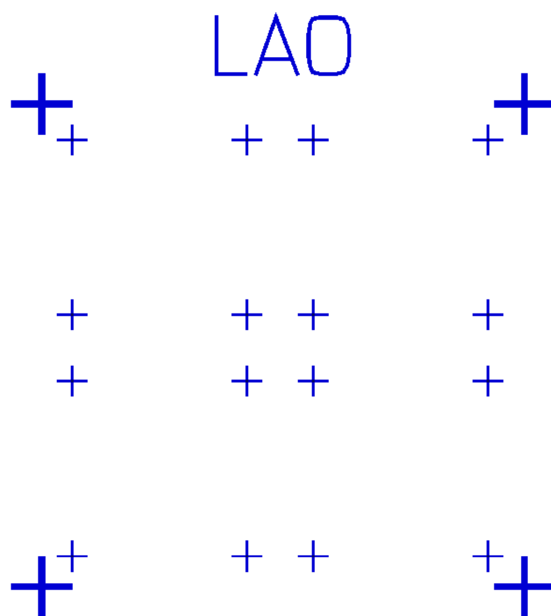

Figure A-6. Zoom in on LAO alignment marks, EBL pattern 4 and 5.

Table A.1. A list of positively and negatively charged and ion and fragment species in SIMS spectra.

m/z	Positive	Negative	m/z	Positive	Negative
1	H	H	59	Co, C_3H_7O, (CH_3)2SiH	AlO2, CHSiO, CH_3COO, BO_3, C_3H7O
7	Li		60	Ni	SiO2, C_5
9	Be, Al		61		SiO2H, C_5H
10	Be, Al		62		NO_3
11	Be, Al		63	Cu	PO_2
12	C	C	64	Zn, TiO	SO_2, S_2
13	CH	CH	65	Cu	
14	CH_2, N	CH_2, N	66	Zn, TiO	C_3NO
15	CH_3		67	C_5H_7	
16	O	O	68	Zn	
17		OH	69	Ga, CF_3, C_4H_5O, CrOH	
18	H_2O		70	C_5H_9	
19	H_3O	F	71	Ga, C_5H11	
20	Ca		72	Ge	C_6
23	Na		73	(CH_3)3Si, FeOH, $H_3O(H_2O)_3$	C_6H, C_2H_5COO, C_4H_9O
24	Mg, C_2	C_2	74	Ge	
25	C_2H	C_2H	75	As	As, CH_3SiO_2
26	C_2H_2	CN	76		SiO_3
27	Al, C_2H_3	BO	77	C_6H_5	SiO_3H
28	Si, CHNH, CO, N_2	Si	78	Se	Se
29	SiH, C_2H_5	Si	79	C_6H_7	Br, PO_3
30	CH_3NH	Si	80	Se	SO_3, SeBr, SO_3H
31	P, CF, CH_3O	P, CH_3O	81	ZnOH, C_6H_9	
32	O_2	S, O_2	83	C_6H_{11}	
33		SH	84		CrO_2
35		Cl	85	$C_4H_5O_2$	CrO_2H, $C_4H_5O_2$, GaO
36		C_3	87		GaO
37	$H_3O(H_2O)$	Cl, CH_3	88	Sr	
38		C2N	89	Y	
39	K, C_3H_3		90	Zr, YH	
40	Ca, Ar, C_2HCN	C_2O	91	C_7H_7, $H_3O(H_2O)_4$	AsO
41	C_3H_5	C_2OH	92	Mo	
42		CNO, SiN	93	C_3F_3, Nb, C_7H_9	C_7H_9, C_3F_3
43	AlO, C_3H_7, CH_3Si	AlO, BO_2, C_2H_3O	94	Mo	
44		CO_2	95	C_7H_{11}, Mo	PO_4
45	SiOH, Sc, C_2H_5O	CO_2H, C_2H5O	96	Mo	SO_4
46	Na_2	NO_2	97	C_7H_{13}, Mo	SO_4H
47	PO, CFO	PO	98	Mo	
48	Ti	C_4	100	C_2F_4, Mo	CrO
49		C_4H	101		GaO_2
50	CF_2	C_3N	103		GaO_2
51	V		107		AsO_2
52	Cr		113	In	
53	C_4H_5		115	In	
54	Al_2		138		Ga_2
55	Mn, C_4H_7, $H_3O(H_2O)_2$	C_2H_3CO	142		Ga_2
56	Fe		147	$(CH_3)_5SiO_2$	
57	FeH, C_4H_9, CaOH		154		Ga_2O
58	Ni	CNS	158		Ga_2O

Table A.2. A list of SCQD InAs/GaAs development samples, grown on the V-90 MBE (SFXXXX) or DCA MBE (PRXXXX), where capped samples were measured using μPL and uncapped samples were measured using AFM.

Sample	EBL pattern	Indium coverage (ML)	Percent of 2D to 3D time (%)	QD growth rate (ML/s)	QD growth temperature (°C)	Buffer growth temperature (°C)	Cap	Purpose
SF1457	1	1.60	94	0.01	475	475	No	SCQD growth
SF1458	1	1.60	94	0.01	475	475	No	
SF1475	1	1.60	94	0.01	475	475	Yes	
SF1535	1	1.53	90	0.01	475	475	Yes	
SF1558	2	1.50	88	0.01	475	475	No	
SF1559	2	1.41	83	0.01	475	475	No	
PR0026	NA	1.70	100	0.02	470	500	Yes	AHC investigation
PR0027	NA	1.70	100	0.02	470	500	Yes	
PR0028	NA	1.70	100	0.02	470	500	Yes	
PR0029	NA	1.70	100	0.02	470	500	Yes	
PR0063	3	1.59	93.5	0.01	500	500	No	SCQD growth
PR0064	3	1.59	93.5	0.01	500	500	No	
PR0065	3	1.59	93.5	0.01	500	500	Yes	
PR0066	3	1.59	93.5	0.01	500	500	Yes	
PR0074	3	NA	NA	NA	NA	500	No	HABS current optimisation
PR0075	3	NA	NA	NA	NA	500	No	
PR0076	3	NA	NA	NA	NA	500	No	
PR0082	4	NA	NA	NA	NA	500	No	Buffer temperature optimisation
PR0083	4	NA	NA	NA	NA	580	No	
PR0084	4	NA	NA	NA	NA	537	No	
PR0085	4	NA	NA	NA	NA	515	No	
PR0092	5	1.56	92	0.01	500	537	No	SCQD growth
PR0093	5	1.58	93	0.01	500	537	No	
PR0094	5	1.55	91	0.01	500	537	No	
PR0095	5	1.57	92.5	0.01	500	537	No	
PR0097	5	1.56	92	0.01	500	537	Yes	
PR0098	5	1.53	90	0.01	500	537	Yes	
PR0099	5	1.55	91	0.01	500	537	Yes	
PR0100	5	1.55	91	0.01	500	537	No	